frontiers | Research Topics

Complex networks in interdisciplinary research: From theory to applications

Edited by
Xiyun Zhang, Ye Wu, Thomas Peron and Cong Li

Published in
Frontiers in Physics
Frontiers in Chemistry

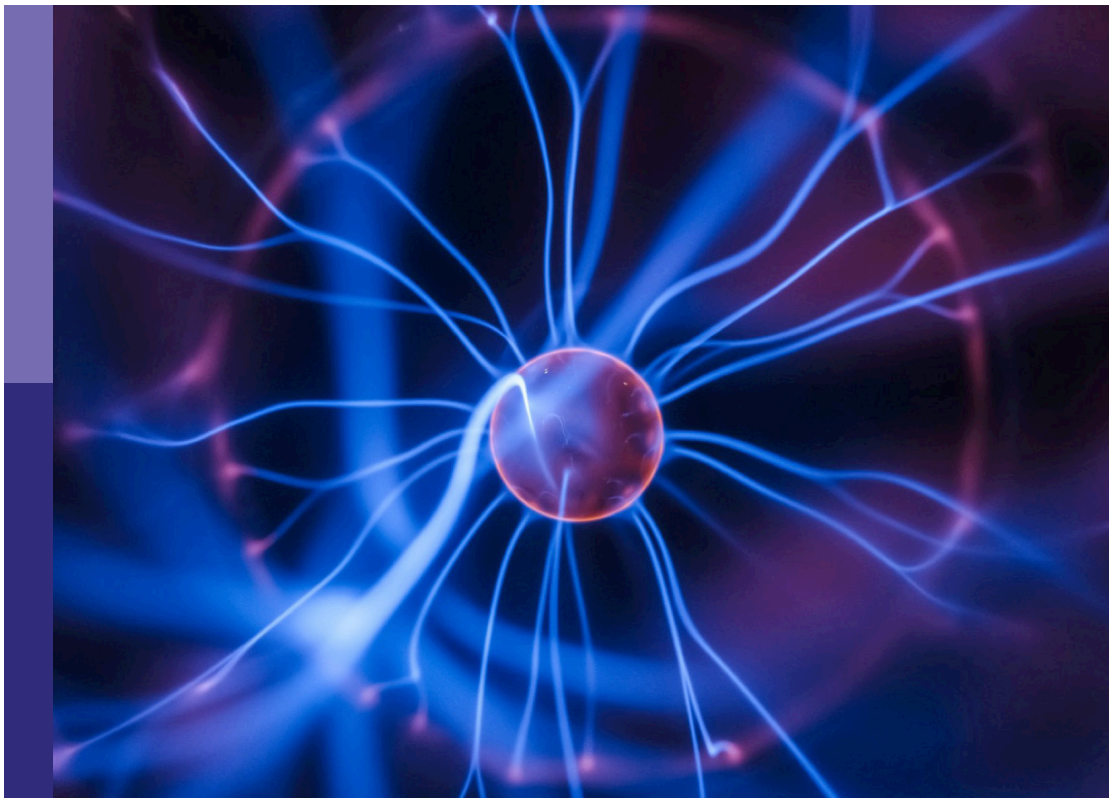

ISSN 1664-8714
ISBN 978-2-8325-4141-8
DOI 10.3389/978-2-8325-4141-8

About Frontiers

Frontiers is more than just an open access publisher of scholarly articles: it is a pioneering approach to the world of academia, radically improving the way scholarly research is managed. The grand vision of Frontiers is a world where all people have an equal opportunity to seek, share and generate knowledge. Frontiers provides immediate and permanent online open access to all its publications, but this alone is not enough to realize our grand goals.

Frontiers journal series

The Frontiers journal series is a multi-tier and interdisciplinary set of open-access, online journals, promising a paradigm shift from the current review, selection and dissemination processes in academic publishing. All Frontiers journals are driven by researchers for researchers; therefore, they constitute a service to the scholarly community. At the same time, the *Frontiers journal series* operates on a revolutionary invention, the tiered publishing system, initially addressing specific communities of scholars, and gradually climbing up to broader public understanding, thus serving the interests of the lay society, too.

Dedication to quality

Each Frontiers article is a landmark of the highest quality, thanks to genuinely collaborative interactions between authors and review editors, who include some of the world's best academicians. Research must be certified by peers before entering a stream of knowledge that may eventually reach the public - and shape society; therefore, Frontiers only applies the most rigorous and unbiased reviews. Frontiers revolutionizes research publishing by freely delivering the most outstanding research, evaluated with no bias from both the academic and social point of view. By applying the most advanced information technologies, Frontiers is catapulting scholarly publishing into a new generation.

What are Frontiers Research Topics?

Frontiers Research Topics are very popular trademarks of the *Frontiers journals series*: they are collections of at least ten articles, all centered on a particular subject. With their unique mix of varied contributions from Original Research to Review Articles, Frontiers Research Topics unify the most influential researchers, the latest key findings and historical advances in a hot research area.

Find out more on how to host your own Frontiers Research Topic or contribute to one as an author by contacting the Frontiers editorial office: frontiersin.org/about/contact

Complex networks in interdisciplinary research: From theory to applications

Topic editors

Xiyun Zhang — Jinan University, China

Ye Wu — Beijing Normal University, China

Thomas Peron — University of São Paulo, Brazil

Cong Li — Fudan University, China

Citation

Zhang, X., Wu, Y., Peron, T., Li, C., eds. (2023). *Complex networks in interdisciplinary research: From theory to applications*. Lausanne: Frontiers Media SA.

doi: 10.3389/978-2-8325-4141-8

Table of contents

frontiers | Frontiers in Physics

TYPE Original Research
PUBLISHED 25 August 2022
DOI 10.3389/fphy.2022.967870

OPEN ACCESS

EDITED BY
Ye Wu,
Beijing Normal University, China

REVIEWED BY
Deniz Eroglu,
Kadir Has University, Turkey
Ping Li,
Southwest Petroleum University, China

*CORRESPONDENCE
Peng Ji,
pengji@fudan.edu.cn
Marc Barthelemy,
marc.barthelemy@ipht.fr

SPECIALTY SECTION
This article was submitted to Interdisciplinary Physics, a section of the journal Frontiers in Physics

RECEIVED 13 June 2022
ACCEPTED 25 July 2022
PUBLISHED 25 August 2022

CITATION
Ye J, Hu Q, Ji P and Barthelemy M (2022), The effect of interurban movements on the spatial distribution of population.
Front. Phys. 10:967870.
doi: 10.3389/fphy.2022.967870

The effect of interurban movements on the spatial distribution of population

Jiachen Ye[1,2,3], Qitong Hu[1,4], Peng Ji[1,2,3]* and Marc Barthelemy[5,6]*

[1]Institute of Science and Technology for Brain-Inspired Intelligence, Fudan University, Shanghai, China, [2]Key Laboratory of Computational Neuroscience and Brain-Inspired Intelligence (Fudan University), Ministry of Education, Shanghai, China, [3]MOE Frontiers Center for Brain Science, Fudan University, Shanghai, China, [4]School of Mathematical Sciences, Shanghai Jiao Tong University, Shanghai, China, [5]Institut de Physique Théorique, Université Paris Saclay, CEA, CNRS, Paris, France, [6]Centre d'Analyse et de Mathématique Sociales, (CNRS/EHESS), Paris, France

Understanding how interurban movements can modify the spatial distribution of the population is important for transport planning but is also a fundamental ingredient for epidemic modeling. We illustrate this on vacation trips for all transportation modes in China during the Lunar New Year and compare the results for 2019 with the ones for 2020 where travel bans were applied for mitigating the spread of a novel coronavirus (COVID-19). We first show that inter-urban travel flows are broadly distributed and display both large temporal and spatial fluctuations, making their modeling very difficult. When flows are larger, they appear to be more dispersed over a larger number of origins and destinations, creating *de facto* hubs that can spread an epidemic at a large scale. These movements quickly induce (in about a week for this case) a very strong population concentration in a small set of cities. We characterize quantitatively the return to the initial distribution by defining a pendular ratio which allows us to show that this dynamics is in general very slow and even stopped for the 2020 Lunar New Year due to travel restrictions. Travel restrictions obviously limit the spread of the diseases between different cities, but have thus the counter-effect of keeping high concentration in a small set of cities, *a priori* favoring intra-city spread, unless individual contacts are strongly limited. These results shed some light on the statistics of interurban movements and how they modify the national distribution of populations, a crucial ingredient for devising effective control strategies at a national level.

KEYWORDS

COVID-19, interurban movements, spatial distribution, transportation modes, baidu qianxi

Introduction

The 2020 Chinese Lunar New Year period witnessed the outbreak of a novel coronavirus (COVID-19) in Wuhan, China, which quickly infected other countries before becoming a pandemic [1]. The proximity of this outbreak with the Chinese Spring Festival, a period of travel with high traffic loads, provided terrible conditions for the spread of this disease. With an

increasing amount of confirmed cases, more attention has been devoted to modeling the spread of COVID-19 from various aspects such as determining the value of the reproductive number [2–7], of the incubation period [8–10]. In general, analytical modeling plays of course an important role in the prediction of the spread and allows in particular to test control strategies [11], which was verified in this case too [12–22]. Particularly important was the estimatimation of probability to export the disease in other countries [19, 23, 24], and were how effective travel restrictions inside China [19].

Demographic information and mobility, either under the form of data or given by transportation models (see for example the review [25]), are crucial for modeling infectious diseases [26], including this COVID-19. This sort of data is also useful for transport planning [27], city livability [28], for congestion analysis and prediction. Mobility in general concerns either the global scale with movements between countries [18–21], or the national scale between cities, or even inside cities [20–22]. Here we will mostly focus on inter-urban mobility for all types of transport modes, and in contrast with most of the epidemiological studies, we will not model the spread of the disease and instead but will focus on two –interrelated– aspects. First we will focus on statistical properties of movements between cities (in a holiday period) and how the population distribution is affected by these large scale seasonal migrations. This leads us to the second aspect that we will consider, namely, the possible impact of these movements on the epidemic spread between cities. More precisely, we will investigate the statistical properties of traffic flows between cities during the Chinese Spring Festival in 2020 and in 2019. These movements are essentially due to workers coming back to their hometown for the new year holidays and must not be confused with interurban migration where individuals change their town residence. An important point to note is that the comparison of the traffic flows for 2019 and for 2020, where travel restrictions took place, gives us an opportunity to uncover some fundamental properties of mobility. This knowledge is fundamental for understanding and modeling mobility at the national scale. Additionally, it is worth to note that network measure for spatial-temporal weighted networks could also provide fundamental information and deserves future attention [29, 30].

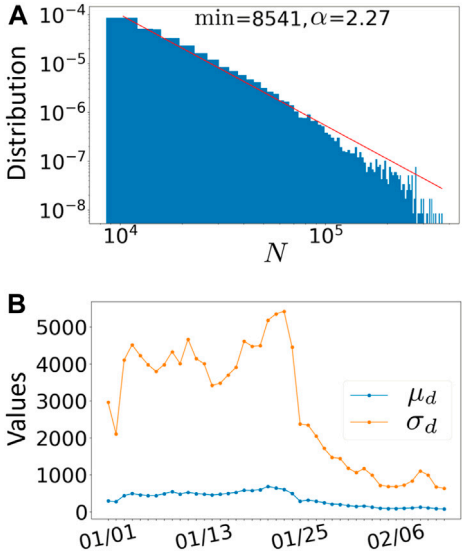

FIGURE 1
Statistics of interurban flows. **(A)** Distribution of all traffic flows $N(i, j, d)$ in loglog. The line is a power law fit of the form $N^{-\alpha}$ with exponent $\alpha = 2.27$ with fitting method described in [29]. **(B)** Average and standard deviation of the flows $N(i, j, d)$ averaged over traffic flows versus the date d (from 1st January to 12th February).

Results

Statistics of interurban flows

We will first study standard statistical properties of interurban flows, obtained from migration data provided by Baidu Qianxi (see Material and Methods). This dataset enables us to monitor the traffic flows between cities. For each day d ($d = 1, 2, \ldots, T$), we extract the number of individuals $N(i, j, d)$ going from city i to city j with any travel mode. The migration data can thus be taken as a directed, weighted network of flows between the set of $n = 296$ cities of China whose populations are also known (see Material and Methods). We collected the data for the Spring Festival of 2020 (from Jan. 1st to Feb. 12th, 2020), and for assessing the impact of travel bans, we also collected the data for the Spring Festival of 2019 (which according to the Chinese lunar calendar takes place from Jan. 12th to Feb. 23rd, 2019).

Large heterogeneity of flows

We first consider the distribution of all flows of individuals $N(i, j, d)$ for all cities i and j and all days d, as shown in Figure 1A. The maximum flow is of order 10^5 and the average of order 10^3 indicates a broad distribution. A power law fit is consistent with this picture with an exponent $\alpha \approx 2.3$ (Figure 1A). This heterogeneity is confirmed in Figure 1B which shows both the average value μ_d and the standard deviation σ_d computed over all inter-city flows (for each day d). For most days, the relative dispersion σ_d/μ_d is of order 5–10. This heterogeneity is probably due to the large diversity of cities, which serve as origins or destinations of flows (see below for further analysis). An important feature that Figure 1B exhibits the sharp drop of the standard deviation after Jan. 25th, the Lunar New Year (LNY), which is mainly due to the travel ban (Supplementary Figures S1, S3 in the Supplementary Material (SM) for a detailed discussion) as shown below.

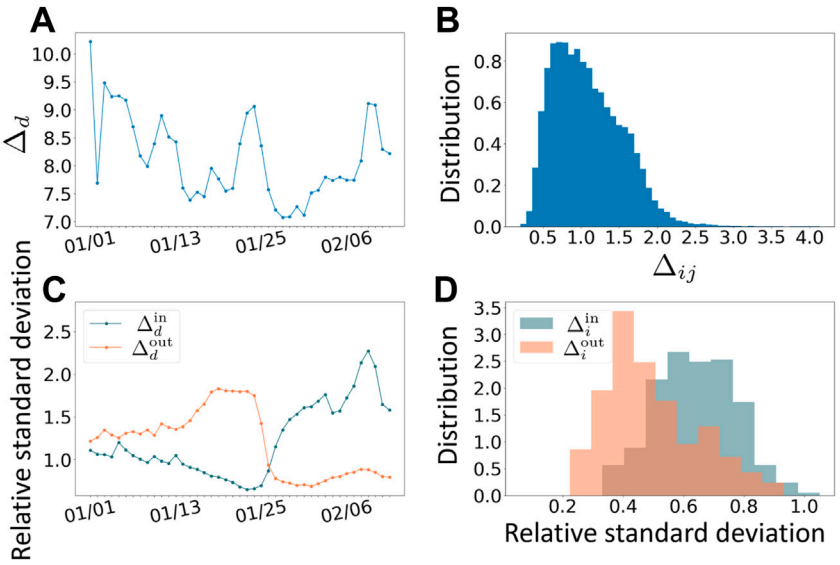

FIGURE 2
Temporal versus spatial fluctuations. **(A)** Relative standard deviation of the flows N averaged over traffic flows and represented here versus time. **(B)** Distribution of the relative standard deviation of N averaged over time. **(C)** Relative standard deviation of $N_{\text{in}}(i, d)$ and $N_{\text{out}}(i, d)$ averaged over cities and shown here versus time. **(D)** Distribution of the relative standard deviation of N_{in} and N_{out} averaged over time.

Temporal versus spatial fluctuations

In order to understand the nature of the different fluctuations affecting the flows N (i, j, d), we compute the relative standard deviation $\Delta_{ij} = \frac{\sigma_{ij}}{\mu_{ij}}$, where μ_{ij} and σ_{ij} are the average and standard deviation computed over time, and the relative standard deviation $\Delta_d = \frac{\sigma_d}{\mu_d}$, average over all flows, for a given day d. We show on Figure 2A the spatial dispersion Δ_d versus time and in Figure 2B the distribution of Δ_{ij}. We observe that the spatial dispersion is of order 8.3, while the temporal dispersion is less (mainly concentrated around 1). The main reason for heterogeneity thus lies in the flow fluctuations between different origins and destinations, while temporal fluctuations are smaller but not negligible. These two sources of heterogeneity clearly represent a challenge for modeling these flows, especially with very simplified models. Our results indicate that the first modeling step would be to describe the spatial heterogeneity of flows and then to consider temporal variations.

The next natural quantities, which can be computed over this network, are the incoming flows $N_{\text{in}}(i, d)$ and outgoing flows N_{out} (i, d) defined by

$$\begin{cases} N_{\text{in}}(i,d) = \sum_{j=1}^{n} N(j,i,d) \\ N_{\text{out}}(i,d) = \sum_{j=1}^{n} N(i,j,d) \end{cases} \quad (1)$$

respectively. We measure in the same way as above various measures of fluctuations, either averaged over cities or over time, leading to the quantities $\Delta_d^{\text{in (out)}}$, $\Delta_i^{\text{in (out)}}$. As these quantities are sums of random variables, we expect smaller relative dispersions than for N (i, j, d) which is indeed what we observe (Figures 2C,D, with typical values of relative dispersion of order 1 (Supplementary Figures S4, S5 for additional details). In order to get first insights about the influence of travel bans, we compare the incoming flows and outgoing flows versus city population in 2019 and 2020 with days $N_{\text{in, out}}^{\text{before}}$ before and $N_{\text{out, in}}^{\text{after}}$ after LNY. We first observe that (Supplementary Figure S2 in SM) basically the number of outgoing individuals before LNY corresponds approximately to the number of incoming individuals after LNY with $N_{\text{in (out)}}^{\text{before}} \approx N_{\text{out (in)}}^{\text{after}}$ (and vice-versa). These relations thus correspond roughly to the conservation of the number of individuals traveling during the Chinese Spring Festival.

Structure of incoming and outgoing flows

The value of incoming or outgoing flows gives information about the volume of migrations, but not about the number of important origins or destinations. In order to characterize the dispersion over different cities, we denote by $\mathcal{O}(i, d)$ and $\mathcal{D}(i, d)$, the sets of origin of flows incoming in city i and destinations of flows from city i (for the day d), respectively. We then use Gini indices [30] that capture the dispersion of incoming and outgoing flows and are given by

$$G_{\text{in}}(i,d) = \frac{1}{2O^2 \bar{N}_{\text{in}}(i,d)} \sum_{p,q \in \mathcal{O}(i,d)} |N(p,i,d) - N(q,i,d)| \quad (2)$$

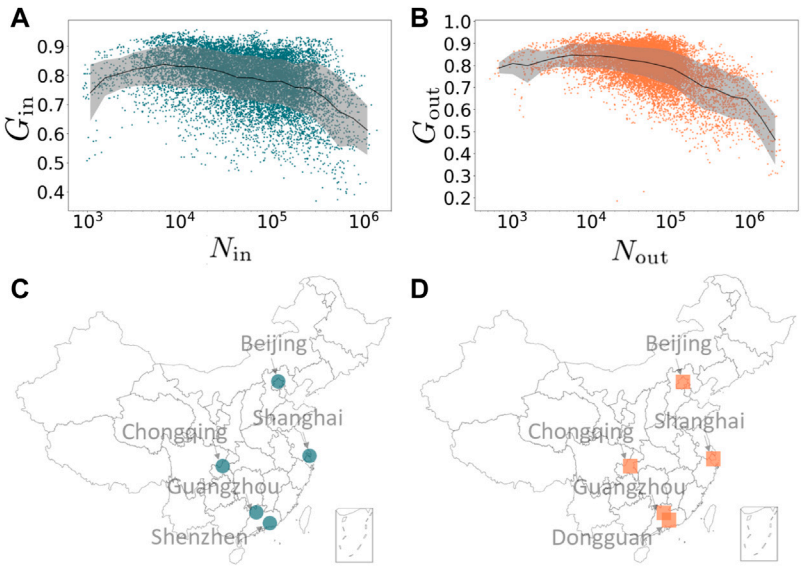

FIGURE 3
Relationship between Gini index and incoming/outgoing flows. **(A)** G_{in} versus N_{in} for all cities and days. **(B)** G_{out} versus N_{out} for all cities and days (shown in loglog). The thick line indicates the average of G_{in} (G_{out}) versus of N_{in} (N_{out}) and the shaded area represents the standard deviation of the average. Top 5 critical cities for **(C)** incoming flows and **(D)** outgoing flows.

$$G_{out}(i,d) = \frac{1}{2D^2\bar{N}_{out}(i,d)} \sum_{p,q\in\mathcal{D}(i,d)} |N(i,p,d) - N(i,q,d)| \quad (3)$$

where O and D represent the number of elements of the sets $\mathcal{O}(i,d)$ and $\mathcal{D}(i,d)$. The quantity $\bar{N}_{in}(i,d) = \frac{N_{in}(i,d)}{|\mathcal{O}(i,d)|}$ is the average incoming flows and $\bar{N}_{out}(i,d) = \frac{N_{out}(i,d)}{|\mathcal{D}(i,d)|}$ the average outgoing flows. Intuitively, if all traffic flows to city i are from one single origin city on day d, the Gini index $G_{in}(i,d)$ will be 1, while if traffic flows to city i are all equal, the Gini index $G_{in}(i,d)$ will be 0 (and similarly for $G_{out}(i,d)$).

We plot these Gini indices computed for each city versus the traffic flows to or from this city. These Figures 3A,B show that on average the larger the traffic flows are, the more dispersed they are over a larger number of origins or destinations. In terms of epidemic control, it is clear that cities with a large flow N_{in} and a small Gini index G_{in} is the most critical, in the sense that many people from many different cities are converging to the same place. Equally, cities with a large N_{out} and a small G_{out} should be particularly monitored, since they can act as hubs in spreading the disease over the inter-city network. Figures 3C,D show the top 5 critical cities, including Beijing, Shanghai, Chongqing and Guangzhou for both the incoming and outgoing flows, Shenzhen for the incoming flows, and Dongguan for the outgoing flows.

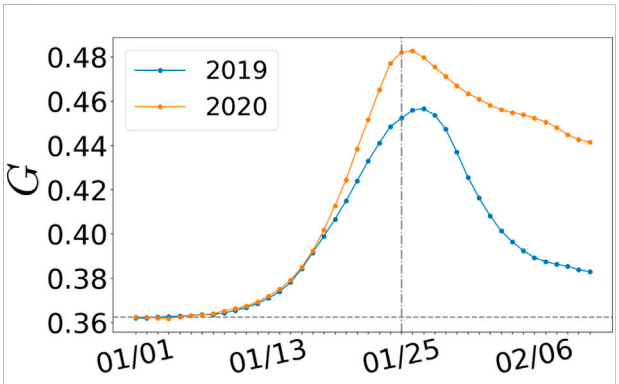

FIGURE 4
Variation of the Gini index. Temporal variations around the Spring Festival holidays of the population Gini index for 2019 and 2020. The horizontal dotted line represents the value "at rest". The vertical line indicates the day of the LNY.

Statistical structure of the national population

An important effect of incoming and outgoing flows is that they change the population structure. Some cities will receive a large number of individuals while for others we expect a decrease of their population. Migration thus affects the statistical structure of the national population and in this section we will characterize this effect.

Temporal evolution of population structure

In order to characterize the disparity of the population distribution and how it varies during seasonal migrations, we consider the population of city i at time d given by

$$P(i,d) = P_0(i) + \sum_{d' \leqslant d} N_{\text{in}}(i,d') - \sum_{d' \leqslant d} N_{\text{out}}(i,d'), \quad (4)$$

where $P_0(i)$ represents the population of city i without incoming and outgoing flows. The Gini index for the city population of the whole country at day d is then given by

$$G(d) = \frac{1}{2n^2\bar{P}(d)} \sum_{i,\ j=1}^{n} |P(i,d) - P(j,d)|, \quad (5)$$

where $\bar{P}(d) = \frac{1}{n}\sum_{i=1}^{n} P(i,d)$ is the average population of all cities at day d. Intuitively, if all people gather in one city, G will be 1, while if people spread evenly across all cities, G will be 0. For comparison, we also define the Gini index at rest as

$$G_{\text{rest}} = \frac{1}{2n^2\bar{P}_0} \sum_{i,\ j=1}^{n} |P_0(i) - P_0(j)|. \quad (6)$$

This quantity captures the degree of population concentration without any traffic flows, where $\bar{P}_0 = \frac{1}{n}\sum_{i=1}^{n} P_0(i)$ is the average population of all cities without any traffic flows. We show in Figure 4 the variation of the Gini coefficient when we take into account migration flows.

We plot both the results for 2019 and 2020. In both cases we see an important increase of the Gini index in a short time (about a week): When the LNY is approaching, people go back from workplaces to hometowns for reunion with families. A smaller set of cities concentrates these meetings with the number of important cities reaching its minimum and the Gini index reaching its peak on the LNY. Based on the Gini index, we estimate the number of "important" cities where the concentration takes place through $[n\ (1 - G)]$, where $[\cdot]$ denotes the integer part (Supplementary Material for details where we show in Supplementary Figure S6 this number versus time and indeed observe an important drop when approaching the LNY). After the LNY (Jan. 25th), individuals are going back home and the Gini coefficient relaxes back to its original value, but much slower. We observe that in 2020, the increase of the Gini index is larger and, due to travel bans, the decrease even slower than normal. The reason may be that after the outbreak of COVID-19, almost all regions have deferred the time of resuming works and classes after the Spring Festival holiday. For example, Shanghai proposed that companies not crucial to the nation should not resume works before Feb. 10th and that schools should provide online classes. At this point, the population structure at the national level is far from being back to normal. These different results show that these seasonal movements induce a strong concentration of individuals in a relative small set of cities, and that travel bans tend to keep this situation of high concentration.

Return to "equilibrium": Pendular ratio

We observe in Figure 4 that after the LNY there is a decrease of the Gini index indicating a return to normal state characterized by a lower concentration of individuals. In order to characterize quantitatively this return to the original state (before holidays), we measure the gap between individuals going out from a city before the LNY and coming back after it. This gap defines a 'pendular ratio' given by

$$R(i,d_f) = \frac{\sum_{\hat{d}<d\leqslant\hat{d}+d_f} N_{\text{in}}(i,d)}{\sum_{\hat{d}-d_f\leqslant d<\hat{d}} N_{\text{out}}(i,d)}, \quad (7)$$

where d_f is a range of days around the LNY $\hat{d}$. If this ratio is much larger than 1, it means that for this city there is a large incoming flow while for the opposite situation $R(i, d_f) \ll 1$, a large number of individuals are going out (compared to the incoming flows). At large times d_f, we expect that $R \simeq 1$ since most of the individuals have come back. We divide cities into three categories according to the value of $R(i, 1)$: If the value is larger than 1.5, we classify city i as a "receiver" city. If the

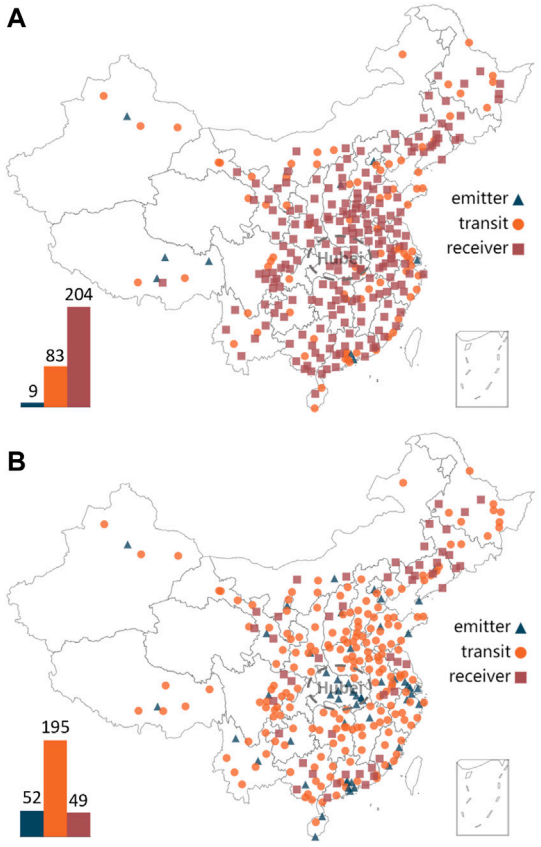

FIGURE 5
Spatial distribution of different categories of cites. **(A)** Emitter, receiver and transit cities according to the value of $R(i, 1)$ for 2019 with the number of three categories of cites at lower left corner. **(B)** Emitter, receiver and transit cities according to the value of $R(i, 1)$ for 2020 with the number of three categories of cites at lower left corner.

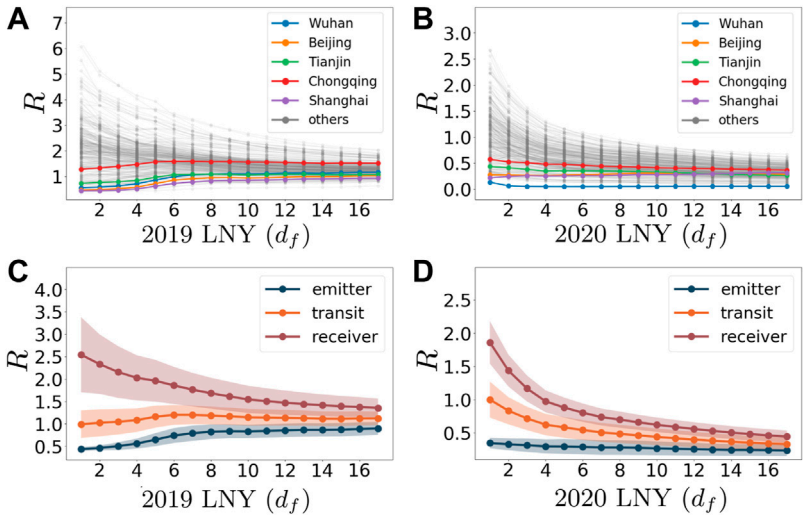

FIGURE 6
Pendular ratio comparison. **(A)** Pendular ratio for all cities versus days d_f from LNY in 2019. We highlight five important cities. **(B)** Pendular ratio for all cities versus days d_f from LNY in 2020 with highlight of 5 cities. **(C)** Average values of the pendular ratio over cities according to the classification (receiver, emitter or transit cities) versus days from LNY in 2019. The colored areas correspond to one standard deviation. **(D)** Mean value of the pendular ratio over cities according to the classification versus days from LNY in 2020 with the shaded area representing the corresponding standard deviation.

value is less than 0.5, we classify city i as an "emitter" city. Finally, if the value is between 0.5 and 1.5, we classify city i as a "transit" city. We represent on Figure 5 the cities of different types on the map of China. We observe that both receiver and transit cities are homogeneously distributed in China. In contrast, emitters cities are in general located in developed regions, e.g., Beijing, Shanghai, Guangzhou, and so on, as shown in Figures 5A,B. It is interesting to note that cities of the Hubei province (within the dashed circle in the figure) are emitters cities in 2020, essentially due to travel restrictions that prevented individuals to come back to Wuhan. This is an important difference compared to the year of 2019 that appears here in the spatial structure of emitters and receivers.

We show in Figures 6A,B the pendular ratio for 2019 and 2020 for all cities and we highlight 5 cities: Wuhan, Beijing, Tianjin, Chongqing, and Shanghai, corresponding to the origin place of COVID-19 and four province-level municipalities. We note here that the curve corresponding to Wuhan is at the bottom of all cities in Figures 6B, reflecting the success of sealing off Wuhan from all outside contact to stop the spread of the disease since Jan. 23rd.

In Figures 6C,D, we show this pendular ratio for 2019 and 2020 for the different types of cities (we average over cities in a given category, emitter, receiver or transit). Results show that the standard deviation is small for the three groups adding credit to their definition. In addition, compared to 2019, the values of R (i, 1) corresponding to 2020 are much smaller. In 2019, the pendular ratio of all the three types of cities returns to 1, meaning that the majority of individuals who went away for the holidays came back. The situation for 2020 is very different with a pendular ratio for all types of cities that converges to a value less than 1 (even less than 0.5), indicating that the majority of people who went away for the holidays did not come back yet. This result remains consistent with the conclusion of Gini index (Figure 3) about a larger concentration in cities and the effect of travel bans.

Finally, we note here that we additionally implemented our whole analysis at the province level (Supplementary Material) and the results obtained are similar to those obtained at the city level.

Discussion

Our findings thus concern four different aspects. First, the traffic flows between cities are very heterogeneous not only spatially but also from a temporal perspective. Such a large heterogeneity could be induced by the large flows observed during this particular period of the Spring Festival and also by travel bans. We note here that similar results apply also to an aggregated level, i.e. the incoming and outgoing flows for provinces also display important heterogeneities. This

heterogeneity aspect is crucial for understanding and modeling epidemic spreading for which we know its importance [31, 32] and more generally for most processes on networks [33]. We quantify the dispersion of origins/destinations of the incoming/outgoing flows showing that for larger flows we have a larger variety of origins and destinations. We also show that during these seasonal migrations of the Spring Festival, the national structure of population changes quickly with a larger concentration in a small set of cities. This concentration decays normally in time after the festivities but travel bans slow down this return to the initial state. It is natural to try to stop the geographical spread of the disease by interurban movements, but on the other hand, large concentration in cities can favor the spread at the city level and increase the number of infected cases. This concentration can be compensated by a more important control at the individual contact level which is what was done in cities such as Wuhan. These results are in line with epidemic modeling results [21], where travel quarantine is effective only when combined with a large reduction of intra-community transmission.

The study presented here focuses on this particular and very important event of the Chinese Lunar New Year, and it would be interesting to test these properties for other events and for other countries where a large fraction of the population moves within the country. Our results highlight the importance of mobility studies for modeling a variety of processes and in particular for understanding and modeling the spread of epidemics. Effective mitigating strategies need to take into account the change of population structure that we exhibited here.

Methods

Data

We obtained the migration data from Baidu Qianxi (http://qianxi.baidu.com), by using Baidu Location Based Services, and Baidu Tianyan, for all transportation modes. It provides the following two datasets: Migration index reflecting the size of the population moving into or out from a city/province, and migration ratio capturing the proportion of each origins and destination. We collected the data during Chinese Spring Festival period of 2020 (from Jan. 1st to Feb. 12th, 2020). For parallel comparison, the migration index during the same period of 2019 (re-scaled according to Chinese lunar calendar, from Jan. 12th to Feb. 23rd, 2019) is also used.

In addition to the migration data, we collected the demographic from China Statistical Yearbook (http://www.statsdatabank.com), an annual statistical publication, which reflects comprehensively economic and social development of China. It covers key statistical data in recent years at both the city level and the province level. We collected the data of population of 31 province-level regions and 296 city-level regions from China Statistical Yearbook 2019, the latest edition provided.

Data availability statement

The original contributions presented in the study are included in the article/Supplementary Material, further inquiries can be directed to the corresponding author.

Author contributions

PJ and MB designed the study, QH collected the data, and JY performed calculations. PJ and MB analyzed and interpreted the data and wrote the manuscript.

Acknowledgments

PJ acknowledges National Science and Technology Innovation 2030 Major Program (2021ZD0204500, 2021ZD0204504), National Natural Science Foundation of China (62076071), and Shanghai Municipal Science and Technology Major Project (No. 2018SHZDZX01). MB thanks the cityof Paris (Paris 2030) for funding.

Conflict of interest

The authors declare that the research was conducted in the absence of any commercial or financial relationships that could be construed as a potential conflict of interest.

Publisher's note

Supplementary material

The Supplementary Material for this article can be found online at: https://www.frontiersin.org/articles/10.3389/fphy.2022.967870/full#supplementary-material

References

1. Hernández Jc Wee S, McNeil DG. *W.h.o. declares global emergency as wuhan coronavirus spreads*. The New York Times (2020).

2. Cao Z, Zhang Q, Lu X, Pfeiffer D, Jia Z, Song H, Zeng DD. *Estimating the effective reproduction number of the 2019-ncov in China*. medRxiv (2020).

3. Tang B, Wang X, Qian L, Tang S, Xiao Y, Wu J. Estimation of the transmission risk of the 2019-ncov and its implication for public health interventions. *J Clin Med* (2020) 9(2):462. doi:10.3390/jcm9020462

4. Riou J, Althaus CL. Pattern of early human-to-human transmission of wuhan 2019 novel coronavirus (2019-ncov), december 2019 to january 2020. *Eurosurveillance* (2020) 25(4):2020. doi:10.2807/1560-7917.es.2020.25.4.2000058

5. Zhao S, Lin Q, Ran J, Musa SS, Yang G, Wang W, et al. *Preliminary estimation of the basic reproduction number of novel coronavirus (2019-ncov) in China, from 2019 to 2020: A data-driven analysis in the early phase of the outbreak*. International Journal of Infectious Diseases (2020).

6. Park SW, Champredon D, Earn DJD, Li M, Weitz JS, Grenfell BT, Dushoff J. *Reconciling early-outbreak preliminary estimates of the basic reproductive number and its uncertainty: A new framework and applications to the novel coronavirus (2019-ncov) outbreak*. medRxiv (2020). doi:10.1098/rsif.2020.0144

7. Zhang J, Litvinova M, Wang W, Wang Y, Deng X, Chen X, et al. *Evolving epidemiology of novel coronavirus diseases 2019 and possible interruption of local transmission outside hubei province in China: A descriptive and modeling study*. medRxiv (2020).

8. Backer JA, Klinkenberg D, Wallinga J. Incubation period of 2019 novel coronavirus (2019-ncov) infections among travellers from wuhan, China, 20–28 january 2020. *Eurosurveillance* (2020) 25(5):2000062. doi:10.2807/1560-7917.es.2020.25.5.2000062

9. Read JM, JessicaBridgen RE, DerekCummings AT, Ho A, Jewell CP. *Novel coronavirus 2019-ncov: Early estimation of epidemiological parameters and epidemic predictions*. medRxiv (2020).

10. Liu T, Hu J, Kang M, Lin L, Zhong H, Xiao J, et al. *Transmission dynamics of 2019 novel coronavirus (2019-ncov)* (2020).

11. Heesterbeek H, Anderson RM, Andreasen V, Bansal S, Angelis D, Dye C, et al. Modeling infectious disease dynamics in the complex landscape of global health. *Science* (2015) 347(6227):aaa4339. doi:10.1126/science.aaa4339

12. Liang Y, Xu D, Fu S, Gao K, Huan J, Xu L, Jia-da L. *A simple prediction model for the development trend of 2019-ncov epidemics based on medical observations* (2020). *arXiv preprint arXiv:2002.00426*.

13. Chen Y, Cheng J, Jiang Y, Liu K. *A time delay dynamical model for outbreak of 2019-ncov and the parameter identification* (2020). *arXiv preprint arXiv: 2002.00418*.

14. Ming W-K, Huang J, Zhang CJP. *Breaking down of healthcare system: Mathematical modelling for controlling the novel coronavirus (2019-ncov) outbreak in wuhan, China*. bioRxiv (2020).

15. Majumder M, Mandl KD. *Early transmissibility assessment of a novel coronavirus in wuhan, China*. China (2020). p. 2020.

16. Chen Z, Zhang W, Lu Y, Guo C, Guo Z, Liao C, et al. *From sars-cov to wuhan 2019-ncov outbreak: Similarity of early epidemic and prediction of future trends*. CELL-HOST-MICROBE-D-20-00063 (2020).

17. Li J. *A robust stochastic method of estimating the transmission potential of 2019-ncov* (2020). *arXiv preprint arXiv:2002.03828*.

18. Wu JT, Leung K, Leung GM. Nowcasting and forecasting the potential domestic and international spread of the 2019-ncov outbreak originating in wuhan, China: A modelling study. *The Lancet* (2020) 395. doi:10.1016/S0140-6736(20)30260-9

19. Chinazzi M, Jessica T, Gioannini C, Litvinova M, Pastore A, Rossi L, et al.*Preliminary assessment of the international spreading risk associated with the 2019 novel coronavirus (2019-ncov) outbreak in wuhan city*. USA: Center for Inference and Dynamics of Infectious Diseases (2020).

20. Lai S, Bogoch I, Watts A, Khan K, Li Z, Tatem A. *Preliminary risk analysis of 2019 novel coronavirus spread within and beyond China* (2020).

21. Chinazzi M, JessicaDavis T, Ajelli M, Gioannini C, Litvinova M, Merler S, et al. The effect of travel restrictions on the spread of the 2019 novel coronavirus (2019-ncov) outbreak. *Science* (2020).

22. Qian X, Sun L, Ukkusuri SV. *Scaling of contact networks for epidemic spreading in urban transit systems* (2020). *arXiv preprint arXiv: 2002.03564*.

23. Pullano G, Pinotti F, Valdano E, Boëlle P, Poletto C, Colizza V. Novel coronavirus (2019-ncov) early-stage importation risk to Europe, january 2020. *Eurosurveillance* (2020) 25(4):2020. doi:10.2807/1560-7917.es.2020.25.4.2000057

24. Gilbert M, Pullano G, Pinotti F, Valdano E, Poletto C, Boëlle P-Y, et al. Preparedness and vulnerability of african countries against importations of Covid-19: A modelling study. *The Lancet* (2020) 395. doi:10.1016/S0140-6736(20)30411-6

25. Barbosa H, Barthelemy M, Ghoshal G, James CR, Lenormand M, Louail T, et al.Human mobility: Models and applications. *Phys Rep* (2018) 734:1–74. doi:10.1016/j.physrep.2018.01.001

26. Balcan D, Colizza V, Gonçalves B, Ramasco J, Vespignani A. Multiscale mobility networks and the spatial spreading of infectious diseases. *Proc Natl Acad Sci U S A* (2009) 106(51):21484–9. doi:10.1073/pnas.0906910106

27. Black J. *Urban transport planning: Theory and practice*, 4. Routledge (2018).

28. Bassolas A, Barbosa-Filho H, Dickinson B, Dotiwalla X, Paul E, Gallotti R, et al. Hierarchical organization of urban mobility and its connection with city livability. *Nat Commun* (2019) 10(1):4817–0. doi:10.1038/s41467-019-12809-y

29. Alstott J, Bullmore E, Powerlaw DP. A Python package for analysis of heavy-tailed distributions. *Plos One* (2014) 9:e85777. doi:10.1371/journal.pone.0085777

30. Dixon PM, Weiner J, Mitchell-Olds T, Woodley R. Bootstrapping the gini coefficient of inequality. *Ecology* (1987) 68(5):1548–51. doi:10.2307/1939238

31. Pastor-Satorras R, Vespignani A. Epidemic spreading in scale-free networks. *Phys Rev Lett* (2001) 86(14):3200–3. doi:10.1103/physrevlett.86.3200

32. Barthélemy M, Barrat A, Pastor-Satorras R, Vespignani A. Velocity and hierarchical spread of epidemic outbreaks in scale-free networks. *Phys Rev Lett* (2004) 92(17):178701. doi:10.1103/physrevlett.92.178701

33. Barrat A, Barthelemy M, Vespignani A. *Dynamical processes on complex networks*. Cambridge University Press (2008).

frontiers | Frontiers in Chemistry

TYPE Original Research
PUBLISHED 13 September 2022
DOI 10.3389/fchem.2022.985001

OPEN ACCESS

EDITED BY
Xiyun Zhang,
Jinan University, China

REVIEWED BY
Hongjie Bi,
Okinawa Institute of Science and Technology Graduate University, Japan
Wei Wang,
Chongqing Medical University, China

*CORRESPONDENCE
Ricai Luo,
hcxylor@126.com

SPECIALTY SECTION
This article was submitted to Theoretical and Computational Chemistry, a section of the journal Frontiers in Chemistry

RECEIVED 03 July 2022
ACCEPTED 04 August 2022
PUBLISHED 13 September 2022

CITATION
Wei Y and Luo R (2022), The wiener index of the zero-divisor graph for a new class of residue class rings. *Front. Chem.* 10:985001. doi: 10.3389/fchem.2022.985001

The wiener index of the zero-divisor graph for a new class of residue class rings

Yinhu Wei and Ricai Luo*

School of Mathematics and Physics, Hechi University, Yizhou, China

The zero-divisor graph of a commutative ring R, denoted by $\Gamma(R)$, is a graph whose two distinct vertices x and y are joined by an edge if and only if $xy = 0$ or $yx = 0$. The main problem of the study of graphs defined on algebraic structure is to recognize finite rings through the properties of various graphs defined on it. The main objective of this article is to study the Wiener index of zero-divisor graph and compressed zero-divisor graph of the ring of integer modulo p^sq^t for all distinct primes p, q and $s, t \in \mathbb{N}$. We study the structure of these graphs by dividing the vertex set. Furthermore, a formula for the Wiener index of zero-divisor graph of $\Gamma(R)$, and a formula for the Wiener index of associated compressed zero-divisor graph $\Gamma_E(R)$ are derived for $R = \mathbb{Z}_{p^sq^t}$.

KEYWORDS

wiener index, zero-divisor graphs, compressed zero-divisor graph, residue class rings, equivalence classification

Introduction

The study of graphs defined on algebraic structures has been an active topic of research in the last few decades. The main question in the area is to recognize finite rings through the properties of various graphs defined on it. The notion of the zero-divisor graph of a commutative ring was introduced by I. Beck in (Beck, 1988), where he considered the set of zero divisors including zero and introduced the concepts such as diameter, grith and clique number of a zero divisor graph. Then later on in (Anderson and Livingston, 1999), Anderson and Livingston changed the vertex set of the zero-divisor graph, they considered only the vertices of the non-zero zero-divisors. For more details, one may see the survey (Singh and Bhat, 2020) and the references therein for the vast literature on the study of zero-divisor graphs.

The Wiener index is one of the important graph indices, and has a variety of applications in pharmaceutical science and in the structure of nanotubes. For results and applications of Wiener index, see (Devillers and Balaban, 1999; Dobrynin et al., 2001; Dehmer and Emmert-Streib, 2014; Dobrynin and Iranmanesh, 2020). There are some works of the Wiener index were done for the ring of integers modulo n. Let us review some of the work done on the topological indices of the zero-divisor graphs. Let p, q be distinct prime numbers. Ahmadi et al. (Ahmadi and Nezhad, 2011) in 2011 has provided an algorithm to determining the Wiener index of $\mathbb{Z}_n$ for $n = p^2, pq$. In 2018, Mohammad et al. (Mohammad and Authman, 2018) has extended

the result by determining the Wiener index of a zero-divisor graph of $\Gamma(\mathbb{Z}_n)$ for $n = p^m$ and p^mq, where $m \in \mathbb{Z}$ and $m \geq 2$ using the Hosoya polynomial. Pirzada et al. (Pirzada et al., 2020) in 2020 determined the Wiener index of a zero-divisor graph and a compressed zero-divisor of $\mathbb{Z}_{p^m}$ for $m \in \mathbb{N}$. In (Asir and Rabikka, 2021), recently a constructed method to calculate the Wiener index of zero-divisor graph of $\mathbb{Z}_n$ for any positive integer n is determined. The authors of (Asir and Rabikka, 2021) calculated the complete formula through restrict n as product of distinct primes and the remaining cases. In 2022, Selvakumar et al. (Selvakumar et al., 2022) visualized the zero-divisor graph $\Gamma(R)$ as a generalized composition of suitable choices of graphs and derived a formula for the Wiener index of the graph $\Gamma(\mathbb{Z}_n)$.

In this paper, we are interested in the parameter Wiener index of graphs for the rings of integers modulo p^sq^t. Although the formulas in the general case for the rings of $\mathbb{Z}_n$ have been obtained in literatures (Asir and Rabikka, 2021) and (Selvakumar et al., 2022), compared with their results, our formula is more direct and convenient for calculation the Wiener index $W(\Gamma(\mathbb{Z}_{p^sq^t}))$. We also get the formula for compressed zero-divisor graph.

Preliminaries

Throughout this paper we assume that R denotes a commutative ring with identity, $Z(R)$ be its set of zero-divisors, the (nonempty) set of nonzero zero-divisors and unit elements denoted by $Z(R)^*$ and $U(R)$. We use $\mathbb{Z}$ to note the ring of integers.

Definition 1. *Let G be a graph and let u and v be two vertices of G. The distance between u and v, denoted by $d_G(u, v)$, is defined to be the length of the shortest path between u and v. The Wiener index of the graph G, denoted by $W(G)$, is defined to be the sum of all distanced between any two vertices of G.*

Let $d_G(v)$ denote the sum of distances of the vertex v from all the vertices of G, then the Wiener index can be redefined as

$$W(G) = \frac{1}{2}\sum_{v\in V(G)} d_G(v).$$

Let R be an arbitrary finite commutative ring with unity. We define an equivalence relation $\sim$ on $Z(R)^*$ as follows. For $x, y \in Z(R)^*$, define $x \sim y$ if and only if $ann(x) = ann(y)$ where $ann(x) = \{r \in R | rx = 0\}$. We call these classes the equiv-annihilator classes of the zero-divisor graph $\Gamma(R)$.

We write $d(x, y)$ to denote the distance between x and y in $Z(R)^*$, and write $x \sim y$ to denote x and y are adjacent, otherwise $x \nsim y$. Let U, V be subsets of the vertex of $\Gamma(R)$, the $U \leftrightarrow V$ shall denote that each vertex of U is adjacent to every vertex of V, and $U \nleftrightarrow V$ denotes that no vertex of U is adjacent to every vertex of V.

The so-called compressed zero-divisor graph of a ring was first defined by the Spiroff et al. in (Spiroff and Wickham, 2011).

Definition 2. *For a commutative ring R with $1 \neq 0$, a compressed zero-divisor graph of a ring R is the undirected graph $\Gamma_E(R)$ with vertex set $Z(R_E) - [0] = R_E - \{[0], [1]\}$ defined by $R_E = \{[x] | x \in R\}$, where $[x] = \{y \in R | ann(x) = ann(y)\}$ and two distinct vertices $[x]$ and $[y]$ are adjacent if and only if $[x][y] = [0] = [xy]$, that is, if and only if $xy = 0$.*

In what follows, we use the graph-theoretic notions from (Douglas, 2001).

Main results

In this section, we first give a structure of $R = \mathbb{Z}_{p^sq^t}$ using the method of equivalence classification.

Let p, q be distinct prime numbers and $s, t \in \mathbb{N}$, the vertex set of $R = \mathbb{Z}_{p^sq^t}$ be divided into disjoint subsets $V_{00}, \ldots, V_{ij}, \ldots, V_{st}$, where

$$V_{ij} = \begin{cases} \{kp^iq^j \in \mathbb{Z}_n | p \nmid k \text{ and } q \nmid k\} & if\ i < s \text{ and } j < t \\ \{kp^iq^t \in \mathbb{Z}_n | p \nmid k\} & if\ i < s \text{ and } j = t \\ \{kp^sq^j \in \mathbb{Z}_n | q \nmid k\} & if\ i = s \text{ and } j < t. \end{cases} \quad (1)$$

We noted that $V_{st} = \varnothing$ and $V_{00} \nsubseteq Z(\mathbb{Z}_{p^sq^t})^*$. For the convenience of presentation, we always assumes that V_{00} and V_{st} are empty sets in the following, unless otherwise specified. Therefore

$$V\left(\Gamma\left(\mathbb{Z}_{p^sq^t}\right)\right) = \bigcup_{0\leq i\leq s}\left(\bigcup_{0\leq j\leq t} V_{ij}\right).$$

Example 1. *Consider the ring $R = \mathbb{Z}_{2^2\times 3^2}$. The vertex set of $\Gamma(\mathbb{Z}_{2^2\times 3^2})$ is*

$$\begin{aligned} V(\Gamma(\mathbb{Z}_{2^2\times 3^2})) &= V_{01} \bigcup V_{02} \bigcup V_{10} \bigcup V_{11} \bigcup V_{12} \bigcup V_{20} \bigcup V_{21} \\ &= \{3, 15, 21, 33\} \bigcup \{9, 27\} \bigcup \{2, 10, 14, 22, 26, 34\} \\ &\quad \bigcup \{6, 30\} \bigcup \{18\} \bigcup \{4, 8, 16, 20, 28, 32\} \bigcup \{12, 24\}. \end{aligned}$$

It is not difficult to see that V_{ij} be the equiv-annihilator classes of $\Gamma(\mathbb{Z}_{p^sq^t})$, where $0 \leq i \leq s$ and $0 \leq j \leq t$. If $i < s$ and $j < t$, for any $x, y \in V_{ij}$. Let $z \in ann(x)$, then $z = k'p^{s-i}q^{t-j}$. So $yz = (kp^iq^j)(k'p^{s-i}q^{t-j}) = kk'p^sq^t$, that is, $z \in ann(y)$. If $i < s$ and $j = t$, for any $x, y \in V_{ij}$. Let $z \in ann(x)$, then $z = k'p^{s-i}$. So $yz = (kp^iq^t)(k'p^{s-i}) = kk'p^sq^t$, that is, $z \in ann(y)$. If $i = s$ and $j < t$, for any $x, y \in V_{ij}$. Let $z \in ann(x)$, then $z = k'q^{t-j}$. So $yz = (kp^sq^j)(k'q^{t-j}) = kk'p^sq^t$, that is, $z \in ann(y)$. Thus $ann(x) = ann(y)$ for any $x, y \in V_{ij}$.

Next, we prove some elementary properties of the vertex subsets V_{ij}.

Lemma 1. *For distinct prime numbers p, q, let $n = p^sq^t$ for some $s, t \in \mathbb{N}$ and V_{ij} be the equiv-annihilator classes of $\Gamma(\mathbb{Z}_n)$ where $0 \leq i \leq s$ and $0 \leq j \leq t$. Then*

(1) $|V_{ij}| = \begin{cases} (p-1)p^{s-i-1}(q-1)q^{t-j-1} & if\ i \neq s \text{ and } j \neq t \\ (q-1)q^{t-j-1} & if\ i = s \\ (p-1)p^{s-i-1} & if\ j = t. \end{cases}$

(2) *$V_{ij} \leftrightarrow V_{i'j'}$ if and only if $i + i' \geq s$ and $j + j' \geq t$.*

Proof. (1) we consider the following cases.

Case 1: $i \neq s$ and $j \neq t$.

Let S_{ij} be the set of all the elements that can be divisible by p^iq^j in $\mathbb{Z}_n$. By the inclusion-exclusion principle,

$$|V_{ij}| = |S_{ij}| - |pS_{ij}| - |qS_{ij}| + |pqS_{ij}|.$$

Note that $|S_{ij}| = |\{kp^iq^j|0 \leq k < p^{s-i}q^{t-j}\}| = p^{s-i}q^{t-j}$. Since

$$|pS_{ij}| = |\{kp^{i+1}q^j|0 \leq k < p^{s-i-1}q^{t-j}\}| = p^{s-i-1}q^{t-j}$$
$$|qS_{ij}| = |\{kp^iq^{j+1}|0 \leq k < p^{s-i}q^{t-j-1}\}| = p^{s-i}q^{t-j-1}$$

And

$$|pqS_{sj}| = |\{kp^{i+1}q^{j+1}|0 \leq k < p^{s-i-1}q^{t-j-1}\}| = p^{s-i-1}q^{t-j-1}.$$

Then

$$|V_{ij}| = p^{s-i}q^{t-j} - p^{s-i-1}q^{t-j} - p^{s-i}q^{t-j-1} + p^{s-i-1}q^{t-j-1}$$
$$= (p-1)p^{s-i-1}(q-1)q^{t-j-1}.$$

Case 2: $i = s$.

Since

$$|S_{sj}| = |\{kp^sq^j|0 \leq k < q^{t-j} \text{ and } q \nmid k\}|$$

Then

$$|S_{sj}| = q^{t-j} - q^{t-j-1} = (q-1)q^{t-j-1}.$$

Case 3: $j = t$.

Since

$$|S_{it}| = |\{kp^iq^t|0 \leq k < p^{s-i} \text{ and } p \nmid k\}|$$

Then

$$|S_{it}| = p^{s-i} - p^{s-i-1} = (p-1)p^{s-i-1}.$$

(2) Let $x = k_{ij}p^iq^j \in V_{ij}$, $y = k_{i'j'}p^{i'}q^{j'} \in V_{i'j'}$. If $i + i' \geq s$ and $j + j' \geq t$, then

$$xy = k_{ij}k_{i'j'}p^{i+i'}q^{j+j'} = k_{ij}k_{i'j'}p^{i+i'-s}q^{j+j'-t}n \equiv 0 (mod n).$$

So x is adjacent to y.

Conversely, suppose $V_{ij} \leftrightarrow V_{i'j'}$. If $i + i' < s$ or $j + j' < t$. We have $xy = k_{ij}k_{i'j'}p^{i+i'}q^{j+j'}$ can't be a multiple of n, a contradiction.

The following result characterized the distance between the equiv-annihilator classes.

Proposition 1. *For distinct prime numbers p, q, let $x, y \in V(\Gamma(\mathbb{Z}_{p^sq^t}))$ for some $s, t \in \mathbb{N}$. Then $d(x, y) = 1$, 2 or 3.*

Proof. Let $V_{01}, V_{10}, \cdots, V_{s,t-1}, V_{s-1,t}$ be the equiv-annihilator classes of $\Gamma(\mathbb{Z}_{p^sq^t})$, where V_{ij} defined by (1). For $x \in V_{i_1j_1}$ and $y \in V_{i_2j_2}$, where $0 \leq i_1, i_2 \leq s$ and $0 \leq j_1, j_2 \leq t$.

If $i_1 + i_2 \geq s$ and $j_1 + j_2 \geq s$, then $x \sim y$ and $d(x, y) = 1$ by lemma 1. So we only need to consider the cases of $i_1 + i_2 < s$ or $j_1 + j_2 < s$ in the following, that is, $x \nsim y$. Without loss of generality,we may assume that $i_1 + i_2 < s$. Consider the following cases.

Case 1: $0 < i_1, i_2 < s$.

Let $i = s - min\{i_1, i_2\}, j = t$. We have $i_1 + i \geq s$ and $j_1 + j \geq t$, also $i + i_2 \geq s$ and $j + j_2 \geq t$. Then $V_{i_1j_1} \leftrightarrow V_{ij} \leftrightarrow V_{i_2j_2}$. Hence, $d(x, y) = 2$.

Case 2: $i_1 = 0$ and $i_2 = 0$.

Let $i = s, j = t - min\{j_1, j_2\}$. We have $i_1 + i \geq s$ and $j_1 + j \geq t$, also $i + i_2 \geq s$ and $j + j_2 \geq t$. Then $V_{i_1j_1} \leftrightarrow V_{ij} \leftrightarrow V_{i_2j_2}$. Hence, $d(x, y) = 2$.

Case 3: $i_1 = 0$ and $i_2 \neq 0$. Consider the following subcases.

Subcase3.1: If $j_2 = 0$. Let $i_3 = s$, $i_4 = s - i_2$, $j_3 = t - j_1$, and $j_4 = t$. We have

$$i_1 + i_3 = s,\ i_2 + i_4 = s,\ i_3 + i_4 = s + (s - i_2) > s$$

And

$$j_1 + j_3 = t,\ j_2 + j_4 = t,\ j_3 + j_4 = (t - j_1) + t > t.$$

Thus $V_{i_1j_1} \leftrightarrow V_{i_3j_3} \leftrightarrow V_{i_4j_4} \leftrightarrow V_{i_2j_2}$.

Since

$$i_1 + i_4 = 0 + (s - i_2) < s,\ j_3 + j_2 = (t - j_1) + 0 < t,$$

Then $V_{i_1j_1} \nleftrightarrow V_{i_4j_4}$ and $V_{i_3j_3} \nleftrightarrow V_{i_2j_2}$. Therefore, $d(x, y) = 3$.

Subcase3.2: If $j_2 \neq 0$. Let $i = s$ and $j = t - min\{j_1, j_2\}$. We have

$$i_1 + i = s,\ j_1 + j \geq t$$

And

$$i + i_2 > s,\ j + j_2 \geq t.$$

Thus $V_{i_1j_1} \leftrightarrow V_{ij} \leftrightarrow V_{i_2j_2}$. Therefore, $d(x, y) = 2$.

Case 4: $i_1 \neq 0$ and $i_2 = 0$. A similar argument as in Case 3 shows that $d(x, y) = 2$ *or* 3.

We have already shown that in any case, $d(x, y) = 1$, 2 *or* 3.

Now, we can calculate the Wiener index of $\Gamma(\mathbb{Z}_{p^sq^t})$.

Theorem 1. *For distinct prime numbers p, q, and some $s, t \in \mathbb{N}$. The Wiener index*

$$W\left(\Gamma\left(\mathbb{Z}_{p^sq^t}\right)\right) = \sum_{i=0}^{\left\lceil \frac{s}{2}\right\rceil -1}\sum_{j=0}^{t}|V_{ij}|\left(|V_{ij}|-1\right)+\sum_{i=0}^{s}$$
$$\times \sum_{j=0}^{\left\lceil \frac{t}{2}\right\rceil -1}|V_{ij}|\left(|V_{ij}|-1\right)-\sum_{i=0}^{\left\lceil \frac{s}{2}\right\rceil -1}$$
$$\times \sum_{j=0}^{\left\lceil \frac{t}{2}\right\rceil -1}|V_{ij}|\quad\left(|V_{ij}|-1\right)+\sum_{i=\left\lceil \frac{s}{2}\right\rceil}^{s}$$
$$\times \sum_{j=\left\lceil \frac{t}{2}\right\rceil}^{t}\frac{|V_{ij}|\left(|V_{ij}|-1\right)}{2}+2\sum_{i=0}^{s}$$
$$\times \sum_{j=0}^{t}|V_{ij}|\quad\left(\sum_{j'=j+1}^{t}|V_{ij'}|+\sum_{i'=i+1}^{s}\sum_{j'=0}^{t}|V_{i'j'}|\right)$$
$$-\sum_{i=\left\lceil \frac{s}{2}\right\rceil}^{s}\sum_{j=0}^{t}|V_{ij}|\quad\left(\sum_{j'=max\{t-j,j+1\}}^{t}|V_{ij'}|\right)-\sum_{i=0}^{s-1}$$
$$\times \sum_{j=0}^{t}|V_{ij}|\left(\sum_{i'=max\{s-i,i+1\}}^{s}\sum_{j'=t-j}^{t}|V_{i'j'}|\right)\quad+\sum_{j=0}^{t}$$
$$\times \sum_{i'=0}^{s}|V_{0j}\|V_{i'0}|-|V_{s0}\|V_{0t}|$$

where

$$|V_{ij}| = \begin{cases}(p-1)p^{s-i-1}(q-1)q^{t-j-1} & if\ i\neq s\ and\ j\neq t\\ (q-1)q^{t-j-1} & if\ i=s\\ (p-1)p^{s-i-1} & if\ j=t.\end{cases}$$

Proof. Let $n = p^sq^t$, we have V_{01}, V_{10}, …, $V_{s-1,t}$, $V_{s,t-1}$ is the partition of $V(\Gamma(\mathbb{Z}_{p^sq^t}))$,where V_{ij} defined by (1). For any two different elements x, y in V_{ij}. By the proof of Proposition 1, there are the following cases.

Case 1: $0\le i\le\lceil\frac{s}{2}\rceil-1$ or $0\le j\le\lceil\frac{t}{2}\rceil-1$.

In this case, we have $d(x, y) = 2$. Then

$$\sum_{x,y\in V_{ij}}d(x,y)=\sum_{k=2}^{|V_{ij}|}d(x_1,x_k)+\sum_{k=3}^{|V_{ij}|}d(x_2,x_k)+\cdots+d\left(x_{|V_{ij}|-1},x_{|V_{ij}|}\right)$$
$$=2\left(|V_{ij}|-1\right)+2\left(|V_{ij}|-2\right)+\cdots+2$$
$$=|V_{ij}|\left(|V_{ij}|-1\right).$$

Case 2: $\lceil\frac{s}{2}\rceil\le i\le s$ and $\lceil\frac{t}{2}\rceil\le j\le t$.

In this case, $d(x, y) = 1$. Then

$$\sum_{x,y\in V_{ij}}d(x,y)=\sum_{k=2}^{|V_{ij}|}d(x_1,x_k)+\sum_{k=3}^{|V_{ij}|}d(x_2,x_k)+\cdots+d\left(x_{|V_{ij}|-1},x_{|V_{ij}|}\right)$$
$$=\left(|V_{ij}|-1\right)+\left(|V_{ij}|-2\right)+\cdots+1$$
$$=\frac{|V_{ij}|\left(|V_{ij}|-1\right)}{2}.$$

Let x and y be the elements in the two different equiv-annihilator classes, V_{ij} and $V_{i'j'}$, respectively. Consider the following cases.

Case 3: $i + i' \ge s$ and $j + j' \ge t$.

By Lemma 1, $d(x, y) = 1$. Then

$$\sum_{x\in V_{ij}}\sum_{y\in V_{i'j'}}d(x,y)=|V_{ij}\|V_{i'j'}|.$$

Case 4: $0 < i + i' < s$ or $0 < j + j' < t$.

Subcase **4.1:** $i = 0$ and $j' = 0$.

In this case, we have $d(x, y) = 3$. Hence

$$\sum_{x\in V_{ij}}\sum_{y\in V_{i'j'}}d(x,y)=3|V_{ij}\|V_{i'j'}|.$$

Subcase 4.2: $i' = 0$ and $j = 0$.

In this case, $d(x, y) = 3$. Hence

$$\sum_{x\in V_{ij}}\sum_{y\in V_{i'j'}}d(x,y)=3|V_{ij}\|V_{i'j'}|.$$

Subcase 4.3: If i, j' are not both equal to 0, and i', j are not both equal to 0.

In this case, $d(x, y) = 2$. Hence

$$\sum_{x\in V_{ij}}\sum_{y\in V_{i'j'}}d(x,y)=2|V_{ij}\|V_{i'j'}|.$$

In conclusion, the Weiner index is

$$W\left(\Gamma\left(\mathbb{Z}_{p^sq^t}\right)\right)=\sum_{i=0}^{s}\sum_{j=0}^{t}\left(\sum_{x,y\in V_{ij}}d(x,y)\right)+\sum_{i,i'=0}^{s}$$
$$\times\sum_{j,j'=0}^{t}\left(\sum_{x\in V_{ij}}\sum_{y\in V_{i'j'}}d(x,y)\right)$$
$$=\sum_{i=0}^{\left\lceil\frac{s}{2}\right\rceil-1}\sum_{j=0}^{t}|V_{ij}|\left(|V_{ij}|-1\right)+\sum_{i=0}^{s}\sum_{j=0}^{\left\lceil\frac{t}{2}\right\rceil-1}|V_{ij}|\left(|V_{ij}|-1\right)$$
$$-\sum_{i=0}^{\left\lceil\frac{s}{2}\right\rceil-1}\sum_{j=0}^{\left\lceil\frac{t}{2}\right\rceil-1}|V_{ij}|\quad\left(|V_{ij}|-1\right)+\sum_{i=\left\lceil\frac{s}{2}\right\rceil}^{s}$$
$$\times\sum_{j=\left\lceil\frac{t}{2}\right\rceil}^{t}\frac{|V_{ij}|\left(|V_{ij}|-1\right)}{2}+2\sum_{i=0}^{s}$$
$$\times\sum_{j=0}^{t}|V_{ij}|\quad\left(\sum_{j'=j+1}^{t}|V_{ij'}|+\sum_{i'=i+1}^{s}\sum_{j'=0}^{t}|V_{i'j'}|\right)$$
$$-\sum_{i=\left\lceil\frac{s}{2}\right\rceil}^{s}\sum_{j=0}^{t}|V_{ij}|\quad\times\left(\sum_{j'=max\{t-j,j+1\}}^{t}|V_{ij'}|\right)-\sum_{i=0}^{s}$$
$$\times\sum_{j=0}^{t}|V_{ij}|\left(\sum_{i'=max\{s-i,i+1\}}^{s}\sum_{j'=t-j}^{t}|V_{i'j'}|\right)\quad+\sum_{j=0}^{t}$$
$$\times\sum_{i'=0}^{s}|V_{0j}\|V_{i'0}|-|V_{s0}\|V_{0t}|.$$

Therefore the result holds, by Lemma 1.

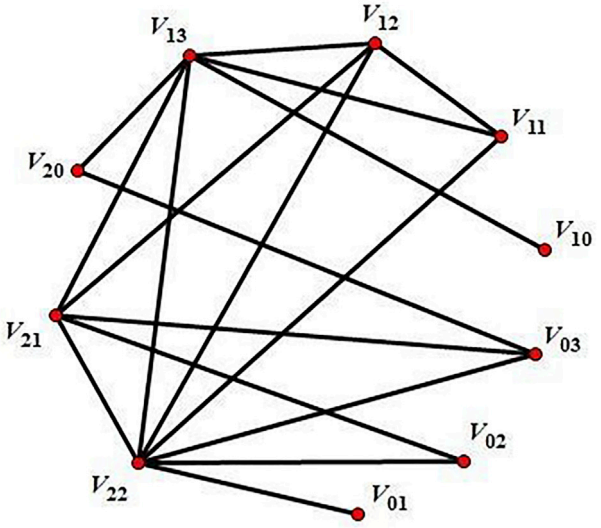

FIGURE 1
the compressed zero-divisor graph $\Gamma_E(\mathbb{Z}_{2^2\times3^3})$.

The following Table gives the exact value of $W(\Gamma(\mathbb{Z}_n))$ for $n = 2^s3^t$, where $1 \le s \le 3$ and $1 \le t \le 3$.

The compressed zero-divisor graph of $\mathbb{Z}_{p^sq^t}$ can be obtained by treating the set V_{ij}, $0 \le i \le s$, $0 \le j \le t$, as a single vertex. To illustrate, let's give an example in the following.

Example 2. *Consider the ring $R = \mathbb{Z}_{2^2\times3^3}$, the vertex set of $\Gamma(\mathbb{Z}_{2^2\times3^3})$ is divided into 10 sets V_{01}, V_{02}, V_{03}, V_{10}, V_{11}, V_{12}, V_{13}, V_{20}, V_{21}, V_{22}. Then the associated compressed zero-divisor graph $\Gamma_E(\mathbb{Z}_{2^2\times3^3})$ is shown in* Figure 1.

Before proving the next result we need the following lemma.

Lemma 2. *For distinct prime numbers p, q, let $n = p^sq^t$ for some $s, t \in \mathbb{N}$ and $G = \Gamma_E(\mathbb{Z}_n)$ be the compressed zero-divisor graph of $\mathbb{Z}_n$. Then*

(1) $V(G) = \{V_{ij} | 0 \le i \le s, 0 \le j \le t\}$.

(2) $$d_G(V_{ij}) = \begin{cases} 2(s+1)(t+1)+s-j-6 & if\ i=0\ and\ 0<j<t \\ 2(s+1)(t+1)+s-t-7 & if\ i=0\ and\ j=t \\ 2(s+1)(t+1)+t-i-6 & if\ 0<i<t\ and\ j=0 \\ 2(s+1)(t+1)+t-s-7 & if\ i=s\ and\ j=0 \\ 2(s+1)(t+1)-(i+1)(j+1)-4 & if\ i\ge\left\lceil\frac{s}{2}\right\rceil\ and\ j\ge\left\lceil\frac{t}{2}\right\rceil \\ 2(s+1)(t+1)-(i+1)(j+1)-5 & otherwise. \end{cases}$$

Proof. (1) Note that

$$Z(\mathbb{Z}_n)^* = \{up^iq^j \in \mathbb{Z}_n | u \in U(\mathbb{Z}_n)\ and\ (i,j) \ne (0,0), (s,t)\},$$

where $U(\mathbb{Z}_n)$ be the units set of $\mathbb{Z}_n$.

Let $x = u_1p^iq^j, y = u_2p^{i'}q^{j'} \in Z(\mathbb{Z}_n)^*$, such that $ann(x) = ann(y)$. Assume that $(i, j) \ne (i', j')$. Without loss of generality, we may let $i < i'$. There are the following cases.

Case 1: $i < i' < s$.

Since $z = up^{s-i'}q^t \in ann(y)$. But $xz = u_1up^{s-i'+i}q^{t+j}$ is not divisible by n, a contradiction. therefore, $(i, j) = (i', j')$ and $[x] = [y] = V_{ij}$.

Case 2: $i < s < i'$.

Since $z = up^{s-i-1}q^t \in ann(y)$. But $xz = u_1up^{s-1}q^{t+j}$ is not divisible by n, a contradiction. therefore, $(i, j) = (i', j')$ and $[x] = [y] = V_{ij}$.

Case 3: $s < i < i'$.

In this case, we have $j < t$ and $j' < t$. If $j \ne j'$, then $z = uq^{min\{t-j,t-j'\}} \in ann(x)$ or $z = uq^{min\{t-j,t-j'\}} \in ann(y)$ but not both. A contradiction. therefore, $j = j'$ and $[x] = [y] = V_{sj}$.

Then the result is holds.

(2) Let $d_G^k(V_{ij})$ denote the sum of distances of the vertex V_{ij} from the vertices of G with a distance of k, where $k = 1$, 2 or 3 by Proposition 1. Then

$$d_G(V_{ij}) = d_G^1(V_{ij}) + d_G^2(V_{ij}) + d_G^3(V_{ij}).$$

There are the following cases.

Case 1: $i = 0$ and $0 < j < t$.

By Lemma 1 there are $V_{ij} \leftrightarrow V_{i'j'}$ if and only if $i + i' \ge s$ and $j + j' \ge t$. So in this case $d_G^1(V_{ij}) = j$ because $i' = s$ and $j' = t - 1, \ldots, t - j$. By the proof of Proposition 1, $d(V_{ij}, V_{i'j'}) = 3$ if and only if $i' = 1, 2, \ldots, s$ and $j' = 0$. So $d_G^3(V_{ij}) = 3s$. therefore

$$\begin{aligned} d_G^2(V_{ij}) &= 2\left(|V(G)| - d_G^1(V_{ij}) - \frac{1}{3}d_G^3(V_{ij}) - |\{V_{00}, V_{ij}, V_{st}\}|\right) \\ &= 2((s+1)(t+1) - j - s - 3). \end{aligned}$$

Hence, $d_G(V_{ij}) = 2(s + 1)(t + 1) + s - j - 6$.

Case 2: $i = 0$ and $j = t$.

As case 1, $d_G^1(V_{ij}) = t$ because $i' = s$ and $j' = t - 1, t - 2, \ldots, 0$. Since $d(V_{ij}, V_{i'j'}) = 3$ if and only if $i' = 1, 2, \ldots, s - 1$ and $j' = 0$. Then $d_G^3(V_{ij}) = 3(s - 1)$. Therefore

$$\begin{aligned} d_G^2(V_{ij}) &= 2\left(|V(G)| - d_G^1(V_{ij}) - \frac{1}{3}d_G^3(V_{ij}) - |\{V_{00}, V_{ij}, V_{st}\}|\right) \\ &= 2((s+1)(t+1) - t - (s-1) - 3). \end{aligned}$$

Hence, $d_G(V_{ij}) = 2(s + 1)(t + 1) + s - t - 7$.

Case 3: $0 < i < s$ and $j = 0$.

A similar argument as in Case 1 shows that, $d_G(V_{ij}) = 2(s + 1)(t + 1) + t - i - 6$.

Case 4: $i = s$ and $j = 0$.

A similar argument as in Case 2 shows that, $d_G(V_{ij}) = 2(s + 1)(t + 1) + t - s - 7$.

Case 5: $0 < i \le \lceil\frac{s}{2}\rceil - 1$ and $j \ne 0$, or $0 < j \le \lceil\frac{t}{2}\rceil - 1$ and $i \ne 0$.

Since $d(V_{ij}, V_{i'j'}) = 1$ if and only if $i' = s, s - 1, \ldots, s - i$ and $j' = t, t - 1, \ldots, t - j$ except V_{st}. So $d_G^1(V_{ij}) = (i + 1)(j + 1) - 1$. In this case, $d_G^3(V_{ij}) = 0$. Therefore

TABLE 1 The Wiener index of $\Gamma(\mathbb{Z}_n)$ for $n = 2^s3^t$.

$\mathbb{Z}_n$	2×3	$2^2 \times 3$	$2^3 \times 3$	2×3^2	$2^2 \times 3^2$	$2^3 \times 3^2$	2×3^3	$2^2 \times 3^3$	$2^3 \times 3^3$
$W(\Gamma(\mathbb{Z}_n))$	4	38	210	109	504	2294	1267	5152	22136

$$d_G^2(V_{ij}) = 2\left(|V(G)| - d_G^1(V_{ij}) - \frac{1}{3}d_G^3(V_{ij}) - |\{V_{00}, V_{ij}, V_{st}\}|\right)$$
$$= 2((s+1)(t+1) - ((i+1)(j+1)-1) - 3)$$

Hence, $d_G(V_{ij}) = 2(s+1)(t+1) - (i+1)(j+1) - 5$.

Case 6: $i \geq \lceil \frac{s}{2} \rceil$ and $j \geq \lceil \frac{t}{2} \rceil$.

Since $d(V_{ij}, V_{i'j'}) = 1$ if and only if $i' = s, s-1, \ldots, s-i$ and $j' = t, t-1, \ldots, t-j$ except V_{st}, V_{ij}. So $d_G^1(V_{ij}) = (i+1)(j+1) - 2$. In this case, $d_G^3(V_{ij}) = 0$. Therefore

$$d_G^2(V_{ij}) = 2\left(|V(G)| - d_G^1(V_{ij}) - \frac{1}{3}d_G^3(V_{ij}) - |\{V_{00}, V_{ij}, V_{st}\}|\right)$$
$$= 2((s+1)(t+1) - ((i+1)(j+1)-2) - 3)$$

Hence, $d_G(V_{ij}) = 2(s+1)(t+1) - (i+1)(j+1) - 4$.

This completes the proof of the lemma.

Remark 1. *From the above lemma, it can be easily seen that the cardinalities of the vertex set of G,* that is, $|V(G)| = (s+1)(t+1) - 2$. *So* $|V(\mathbb{Z}_{2^2\times3^3})| = 10$ *as shown in Example 1.*

The following theorem gives the Wiener index of $\Gamma_E(\mathbb{Z}_{p^sq^t})$.

Theorem 2. *For distinct prime numbers p, q, and some* $s, t \in \mathbb{N}$. *The Wiener index of the compressed zero-divisor graph* $\Gamma(\mathbb{Z}_{p^sq^t})$ *is*

$$W\left(\Gamma_E\left(\mathbb{Z}_{p^sq^t}\right)\right) = \frac{1}{2}(2(s+1)(t+1)(s+t+st)$$
$$-\frac{1}{2}s(s+1) - \frac{1}{2}t(t+1)$$
$$-\frac{s(s+3)t(t+3)}{4} \quad -4st + \left(s - \left\lceil \frac{s}{2} \right\rceil + 1\right)\left(t - \left\lceil \frac{t}{2} \right\rceil + 1\right)$$
$$-7(s+t)+1).$$

Proof. Let $n = p^sq^t$, and $G = \Gamma_E(\mathbb{Z}_n)$. we have $V_{01}, V_{10}, \ldots, V_{s-1,t}, V_{s,t-1}$ are all the vertices of G by Lemma 2, where V_{ij} defined by (1). Then

$$W(G) = \frac{1}{2}\left(\sum_{j=1}^{t} d_G(V_{0j}) + \sum_{i=1}^{s} d_G(V_{i0}) + \sum_{i=1}^{s}\sum_{j=1}^{t} d_G(V_{ij}) - d_G(V_{st})\right)$$
$$= \frac{1}{2}\left(\sum_{j=1}^{t}[2(s+1)(t+1) + s - j - 6] + \sum_{i=1}^{s}[2(s+1)(t+1) + t - i - 6] - 2\right.$$
$$\left. + \sum_{i=1}^{s}\sum_{j=1}^{t}[2(s+1)(t+1) - (i+1)(j+1) - 5] + \sum_{i=\lceil \frac{s}{2} \rceil}^{s}\sum_{j=\lceil \frac{t}{2} \rceil}^{t} 1 - [(i+1)(j+1) - 4]\right)$$
$$= \frac{1}{2}\left(2(s+1)(t+1)(s+t+st) - \frac{1}{2}s(s+1) - \frac{1}{2}t(t+1) - \frac{s(s+3)t(t+3)}{4} - 4st\right.$$
$$\left. + \left(s - \left\lceil \frac{s}{2} \right\rceil + 1\right)\left(t - \left\lceil \frac{t}{2} \right\rceil + 1\right) - 7(s+t) + 1\right).$$

Example 3. *Consider the ring* $R = \mathbb{Z}_{2^2\times3^3}$. *The Wiener index of the compressed zero-divisor graph* $\Gamma_E(\mathbb{Z}_{2^2\times3^3})$ *is*

$$W(\Gamma_E(\mathbb{Z}_{2^2\times3^3})) = 78$$

By Theorem 2.

Conclusion

In this paper, we have described the structure of the graph $\Gamma(\mathbb{Z}_{p^s\times q^t})$ for all distinct primes p, q and $s, t \in \mathbb{N}$ by partition of the vertex set. Consider the partition of the vertex set into the subsets $V_{01}, V_{10}, \ldots, V_{ij}, \cdots, V_{s-1,t}, V_{s,t-1}$ as seen (1). Then $V_{ij} \leftrightarrow V_{i'j'}$ if and only if $i + i' \geq s$ and $j + j' \geq t$. Based on this structure, we proved that the distance of two vertices of $\Gamma(\mathbb{Z}_{p^s\times q^t})$ are contained in the set {1, 2, 3}, and derived an explicit formula for Wiener index of the graph in Theorem 1 using the basic counting principles.

In addition, we run the formula obtained through MATLAB software and get the data in Table 1. Then, we studied the structure of the compressed zero-factor graph of $\mathbb{Z}_{p^sq^t}$ by treating the set V_{ij} as a single vertex of the compressed zero-divisor graph $\Gamma_E(\mathbb{Z}_{p^sq^t})$. We showed that the degree of vertex V_{ij} generally includes six cases, with the number of the vertices of the graph be $(s+1)(t+1) - 2$. Finally we derive the corresponding formula for Wiener index $W(\Gamma_E(\mathbb{Z}_{p^sq^t}))$ in Theorem 2. Of course, we can also implement it in software if needed.

Data availability statement

The original contributions presented in the study are included in the article/supplementary material, further inquiries can be directed to the corresponding author.

Author contributions

RL conceived of the presented idea, and WY developed the theory and performed the computations, verified the analytical methods. RL investigated and supervised the findings of this work. All authors discussed the results and contributed to the final manuscript.

Funding

The authors are very grateful to the referee for careful reading of the manuscript and helpful suggestions. This work was supported by the National Science Foundation of China (11961021 and 11561019), Guangxi Natural Science Foundation (2020GXNSFAA159084), Hechi University Research Fund for Advanced Talents (2019GCC005) and Hechi University Research Fund (2018XJQN007).

Conflict of interest

The authors declare that the research was conducted in the absence of any commercial or financial relationships that could be construed as a potential conflict of interest.

Publisher's note

All claims expressed in this article are solely those of the authors and do not necessarily represent those of their affiliated organizations, or those of the publisher, the editors and the reviewers. Any product that may be evaluated in this article, or claim that may be made by its manufacturer, is not guaranteed or endorsed by the publisher.

References

Ahmadi, M. R., and Nezhad, R. J. (2011). Energy and Wiener index of zero-divisor graphs. *Iran. J. Math. Chem.* 2 (1), 45–51. doi:10.22052/ijmc.2011.5166

Anderson, D. F., and Livingston, P. S. (1999). The zero-divisor graph of a commutative ring. *J. Algebra* 217 (2), 434–447. doi:10.1006/jabr.1998.7840

Asir, T., and Rabikka, V. (2021). The Wiener index of the zero-divisor graph of Z_n. *Discrete. Appl. Math.* 319, 461–471. doi:10.1016/j.dam.2021.02.035,

Beck, I. (1988). Coloring of commutative rings. *J. Algebra*. 116, 116 208–226. doi:10.1016/0021-8693(88)90202-5

Dehmer M and Emmert-Streib F (Editors) (2014). *Quantitative graph theory: Mathematical foundations and applications* (Florida, United States: CRC Press).

J. Devillers and A. T. Balaban (Editors) (1999). *Topological indices and related descriptors in QSAR and QSPR* (Amsterdam: Gordon and Breach Science Publishers).

Dobrynin, A., Entringer, R., and Gutman, I. (2001). Wiener index of trees: Theory and applications. *Acta Appl. Math.* 66 (3), 211–249. doi:10.1023/a:1010767517079

Dobrynin, A., and Iranmanesh, A. (2020). Wiener index of edge thorny graphs of catacondensed benzenoids. *Mathematics* 8 (4), 467. doi:10.3390/math8040467

Douglas, B. (2001). *West, introduction to graph theory*. 2nd Ed. Singapore: Pearson Education.

Mohammad, H. Q., and Authman, M. N. (2018). Hosoya polynomial and wiener index of zero-divisor graph of Z_n. *AL-Rafidain J. Comput. Sci. Math.* 12 (1), 47–59. doi:10.33899/csmj.2018.163570$\mathbb{Z}_{n}$

Pirzada, S., Aijaz, M., and Imran Bhat, M. (2020). On the divisor graphs of the Rings Zn. *Afr. Mat.* 31, 31 727–737. doi:10.1007/s13370-019-00755-3

Selvakumar, K., Gangaeswari, P., and Arunkumar, G. (2022). The Wiener index of the zero-divisor graph of a finite commutative ring with unity. *Discrete. Appl. Math.*, 311, 72–84. doi:10.1016/j.dam.2022.01.012

Singh, Pradeep, and Bhat, Vijay Kumar (2020). Zero-divisor graphs of finite commutative rings: A survey. *Surv. Math. Appl.*, 15 371–397.

Spiroff, S., and Wickham, C. (2011). A zero-divisor graph determined by equivalence classes of zero-divisors. *Commun. Algebra* 39 (7), 2338–2348. doi:10.1080/00927872.2010.488675

frontiers | Frontiers in Physics

TYPE Original Research
PUBLISHED 29 September 2022
DOI 10.3389/fphy.2022.1018844

OPEN ACCESS

EDITED BY
Xiyun Zhang,
Jinan University, China

REVIEWED BY
Min Lin,
Sichuan Normal University, China
Zhidan Zhao,
Shantou University, China
Jiaxing Shang,
Chongqing University, China

*CORRESPONDENCE
Bin Peng,
pengbin@cqmu.edu.cn
Wei Wang,
wwzqbx@hotmail.com,
wwzqbc@cqmu.edu.cn

SPECIALTY SECTION
This article was submitted to Interdisciplinary Physics, a section of the journal Frontiers in Physics

RECEIVED 14 August 2022
ACCEPTED 12 September 2022
PUBLISHED 29 September 2022

CITATION
Li W, Ni L, Zhang Y, Su S, Peng B and Wang W (2022), Immunization strategies for simplicial irreversible epidemic on simplicial complex. *Front. Phys.* 10:1018844. doi: 10.3389/fphy.2022.1018844

Immunization strategies for simplicial irreversible epidemic on simplicial complex

Wenjie Li[1], Linghao Ni[1], Yue Zhang[1], Sheng Su[2,3], Bin Peng[1]* and Wei Wang[1]*

[1]School of Public Health, Chongqing Medical University, Chongqing, China, [2]School of Information and Software Engineering, University of Electronic Science and Technology of China, Chengdu, China, [3]Yangtze Delta Region Institute of University of Electronic Science and Technology of China, Huzhou, China

Higher-order networks can be used to describe the interaction of multiple entities in real-world collective behaviors such as dining, conference attendance, and public transportation use. Collective behavior is often one of the main reasons for "super-spreading events" during epidemics. How to propose effective immunization strategies is a Frontier research topic in network science and public health. To the best of our knowledge, there is a lack of systematic research on immunization strategies for epidemics on higher-order networks. We use synthetic networks and real-world networks as underlying structures to construct simplicial complexes to describe higher-order interaction networks, including pairwise and group interactions, and then propose a simplicial irreversible epidemic spreading model (i.e., simplicial Susceptible-Infected-Removed model). The temporal evolution process of nodes in different states in the system is described by extending the Microscopic Markov Chain Approach. Based on the node degree index and betweenness index, immunization strategies are proposed on the higher-order networks. Through theoretical analysis and numerical simulations, we discuss the effects of different higher-order infection rates, immunization ratios, and immunization strategies on the simplicial irreversible epidemic spread. Under some specific parameter configurations, we observe continuous growth, discontinuous growth, reduction of outbreak threshold, *etc.*

KEYWORDS

immunization strategy, simplicial irreversible epidemic, simplicial complex, higher-order network, epidemic spread

1 Introduction

With the rapid expansion of computer science and data science in recent years, the research on the spread of network epidemics has entered a golden era, garnering significant interest from academics in mathematics, physics, and public health [1–3].

Complex network theory provides a good framework for studying the structure and dynamics of complex interactive systems, can effectively demonstrate the essential characteristics of real-world social systems, demonstrates excellent mathematical

performance, and is capable of performing rigorous mathematical calculations [4–7]. In 2001, Pastor-Satorras et al. [8] utilized complex networks to study for the first time the dynamic spread process of computer viruses. This new epidemiological framework ushered in the era of complex network epidemic spread dynamics and received a great deal of scholarly interest domestically and internationally. Since then, complex network-based epidemiological spread research has been the dominant approach in the field of epidemiological spread research [9–12]. However, the majority of past research has focused on the spread process of epidemics on complex networks in order to provide quantitative analysis for policy-making in the field of public health.

The Susceptible-Infected-Removed (SIR) model is one of the classic models of epidemic spread. It is frequently applied to epidemics with irreversible spread processes, such as chickenpox, measles, whooping cough, *etc.* After the treatment of such epidemics, patients can develop lifelong immunity, which is prevalent in the actual world [13]. Nesteruk [14] predicted the coronavirus epidemic in South Korea using the SIR model. Guo et al. [15] investigated the impact of discontinuous treatment strategies on the spread dynamics of SIR epidemics.

The majority of previous studies on network epidemic spread dynamics are based on simple networks (i.e., classical complex networks), but an increasing number of studies have demonstrated that higher-order network structures have a substantial effect on the epidemic spread process [16–18]. For instance, Althouse et al. [19] discovered that the collective behavior in higher-order networks is the primary cause of "super spreading events" during the Covid-19. Higher-order networks can be used to describe the interaction of multiple entities in real-world collective behaviors such as dining, conference attendance, and public transportation use. Numerous attempts have been made by scientists to describe networks with both pairwise and higher-order interactions. Newman et al. [20] attempted to use a bipartite graph to describe, and other researchers attempted to use clique expansion and the threshold model to describe [21–24], but neither method produced satisfactory results. To better characterize higher-order network structures, scientists propose simplicial complex, which describe higher-order interactions by sets of interactions as opposed to pairs of edges [25–27]. A simplicial complex Z is consisted of several simplexes, and if a simplex θ is contained within Z, then all the sub-simplexes $\sigma \subset \theta$ of simplex θ are also included in Z [28,29].

The purpose of studying the pathogenesis and spread rules of epidemics is to control the wanton spread of epidemics, so as to reduce or avoid the harm caused by them. The spread of epidemics depends to a large extent on the structure of population contact networks. The strategy of how to screen out some key points for immunization based on network information (local or global), so as to suppress the large-scale spread of epidemics is called immunization strategy. Immunization is a crucial topic in the field of epidemiology and has been investigated for a variety of epidemiological models in complex networks [30–34].

Pastor-Satorras et al. [35] were the pioneers in investigating immunization strategies in uniform and scale-free networks. For a uniform network, the nodes are roughly equivalent, so they proposed a simple and effective immunization strategy, random immunization, in which each node in the network has the same probability of being immune, and disease cannot continue to spread in the network when the immunization ratio exceeds a certain critical value. For a scale-free network with an uneven degree distribution of nodes, the random immunization strategy is currently invalid. They proposed a another effective immunization strategy, target immunization, which involves selecting the network nodes with the higher degree for immunization [36]. Target immunization needs to obtain the global information of the network, and it is often difficult to obtain the global information of the real population exposure network, which severely limits the practical application of this method. By randomly selecting a certain proportion of nodes as auxiliary nodes and then randomly selecting a neighboring node for immunization for each auxiliary node, a new immunization strategy known as acquaintance immunization was proposed by Cohen et al. [30]. The acquaintance immunization strategy does not require global network information and is simple to implement, but its immune effect is not the best. Gallos et al. [37] enhanced the acquaintance immunization strategy, which is to randomly select a certain proportion of individuals and then, for each individual, select the individual whose degree in the neighbor node is greater than its own or greater than a given threshold as the final immune object. The structure of the contact network often determines the efficacy of the immunization strategy. Bridge nodes are the two end nodes that connect the edges of different modules in a network; bridge nodes do not necessarily have a high degree value, so the degree-based target immunization strategy or the acquaintance immunization strategy may fail [38]. Considering that bridge nodes often have high betweenness, Freeman [39] proposed another effective immunization strategy, betweenness immunization, that is, selecting nodes with larger network betweenness values for immunization. In addition, Newman [40] proposed a random walk-based node-centricity immunization strategy, Salathe et al. [41] proposed the Community-Bridge-Find algorithm, and a novel utility model of vaccination game was formulated by Jin et al. [42], *etc.*

The development of higher-order networks has aroused great interest in the research community. Jhun [43] investigated the spread of epidemics on hypergraphs and proposed an immunization strategy for hyperedges with high simultaneous infection rate (SIP), i.e., the probability that all nodes in a hyperedge are in the infected state, which is derived from individual-based mean-field theory. To the best of our knowledge, there is a scarcity of systematic study on

epidemiological immunization strategies on higher-order networks.

The main contributions of this paper are as follows: 1) We characterize higher-order networks by constructing simplicial complex and present a simplicial model for the spread of irreversible epidemic on simplicial complex. 2) On the basis of this model, we validate and compare the performance of traditional random immunization, target immunization, and betweenness immunization strategies, and we investigate the impact of higher-order network structures on their immune effects.

This paper is structured as follows: In Section 2, we describe how to construct simplicial complex using synthetic (heterogeneous network) and real-world networks, and then we present a simplicial irreversible epidemic spread model on the simplicial complex. Next, we perform numerical simulations in Section 3 to investigate the influence of higher-order network topologies on the spread process and the immune effects of various immunization strategies. In addition, we introduce the theoretical model framework in Section 4 and derive the temporal evolution equations of individuals in different states in the network. Conclusions are drawn and discussed in Section 5.

2 Model description

In this paper, a simplicial complex is constructed to characterize higher-order networks containing both pairwise interactions (i.e., 1-simplex) and higher-order interactions (e.g., 2-simplex), and a simplicial irreversible epidemic spread model is proposed on it. Next, we first introduce the basic concepts of simplicial complex, and then describe how to build simplicial complex with synthetic and real-world networks as the underlying network structures. Finally, to describe the spread dynamics of irreversible epidemics and explore the impact of higher-order network structure on the immune effect of different immunization strategies, a new spread model is proposed on the higher-order network based on the simplicial complex.

2.1 Simplicial complex

A simplicial complex Z is specified by two parameters (N, M), where N is the set of nodes and M is the set of simplexes constituting Z. A m-simplex $\theta \subset Z$ is made up of a filled clique of a set of $m+1$ nodes (i.e., $\theta = [n_0, n_1, \ldots n_m]$), which defines a $(m+1)$-body interaction. Specifically, a m-simplex describes the simultaneous interaction between $m+1$ nodes, where a 0-simplex designates an separate node without any interaction (e.g $[n_0]$, $[n_1]$,... $[n_m]$), a 1-simplex illustrates the pairwise interaction between two nodes (e.g $[n_0, n_1]$, $[n_0, n_m]$), a 2-simplex describes three nodes connected pairwisely by edges and form a 'full' triangle (e.g., $[n_0, n_1, n_m]$), and so on, as shown in Figure 1A. A simplicial complex Z consisted of a set of nodes is a set of simplexes, matching the following requirements: If a simplex $\theta \subset Z$, then any simplex σ composed of subsets of simplex θ are also included in Z, e.g., a 2-simplicial complex Z is a collection of 0-, 1- and 2-simplexes.

2.2 Synthetic simplicial complex

We build a simplicial complex with heterogeneous network and real-world network as the underlying network structure, respectively. The Random Simplicial Complex (RSC) model permits the formation of simplicial complex with a specified average degree [29], we initially employed this model to construct synthetic simplicial complex. Using the RSC model to generate a K-simplicial complex requires $K+1$ parameters, which are N vertices and K probabilities $\{p_1, \ldots, p_K\}$ p_1 and p_K govern the creation of 1-simplex and K-simplex, respectively. In this paper, $K = 2$, hence the generation of a 2-simplicial complex necessitates three parameters (N, p_1, p_2). For a given collection V of N nodes, 1-simplexes are constructed by linking any pair of nodes $o, p \in V$ with probability $p_1 \in [0, 1]$, where the average degree of the 1-simplexes is $k^{\star} = (N-1)p_1$. Then, 2-simplexes are constructed by linking any three nodes o, p, $q \in V$ with probability $p_2 \in [0, 1]$, where the average degree of 2-simplexes is $k^{*} = (N-1)(N-2)p_2/2$ (i.e., the average amount of 'full' triangles connecting to a node). Since the 2-simplicial complex is composed of 1-simplexes and 2-simplexes, the average degree κ of the final network is jointly determined by $k^{\star}$ and k^{*}, $k \approx (N-1)p_1 + 2k^{*}(1-p_1)$.

2.3 Real-world simplicial complex

Using a publicly available dataset that depict face-to-face interactions between individuals collected by the SocioPatterns Collaboration [44], we then design a real-world simplicial complex. We use data collected from two real social scenarios: a conference (SFHH) and a workplace (InVS15). Every 20 seconds, face-to-face interaction data is gathered for each scenario. We begin by aggregating the data using a sliding time window with a period of $\Delta t = 5$ min, then search for 2- and 3-cliques in each window and weight them according to the frequency with which they occur. Then, 20% of the most frequent simplexes are preserved and aggregated to produce the 2-simplicial complex. The size of each real simplicial complex is 403 and 214, with the average degree of 2-simplexes $\kappa^{*} = 9.4, 5.8$ and the average degree of 2-simplicial complex $\kappa = 26.6, 20.8$.

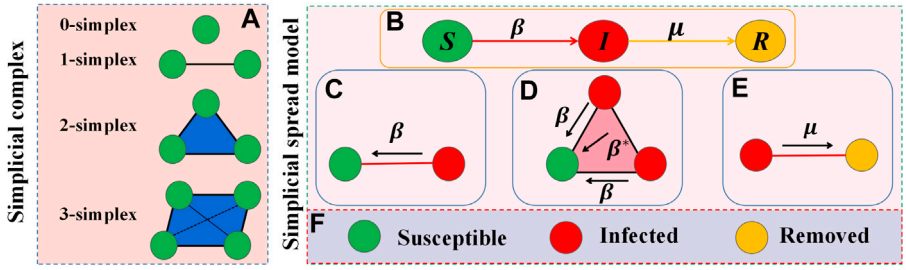

FIGURE 1
Illustration of the model description. The composition of the simplicial complex is shown in **(A)**. **(B)** Depicts the classic SIR model. Epidemic infection and recovery processes are shown in **(C–E)**. The "full" triangle denotes the 2-simplex structure, while the green, red, and yellow circles indicate susceptible, infected, and removed individuals, respectively, as shown in **(F)**.

2.4 Simplicial spread model

Peer effects and reinforcement effects are extremely prevalent in social contagion, from which emerge higher-order network interactions. With this in mind, we propose an epidemic spread model on the simplicial complex, assuming that the spread of the disease conforms to the Susceptible-Infected-Removed (SIR) model. There are three possible states for a node in the network: Susceptible state S, infected state I and removed state R, as shown in Figure 1B. The spread of the epidemic is controlled by two parameters β and $\beta^{\star}$. Initially, a proportion ρ^0 of nodes are infected. If a node o is in S state, an infected neighbor p can infect it *via* their pairwise interaction (o, p) with rate β, as shown in Figure 1C. Node o can also get infection from node p and q *via* a 2-simplex (o, p, q) with rate $\beta^{\star}$, where both node p and q are in the infected state, and this event can be seen as a synergistic reinforcing effect, as shown in Figure 1D. In addition, infected nodes can recover to the removed state with rate μ, as shown in Figure 1E. Individuals who reverted to the R state are immune to future infections.

3 Numerical simulation

Taking into account the varying average degrees of 1-simplexes and 2-simplexes across networks, we combine $k^{\bigstar}$, $k^{\star}$, β, $\beta^{\star}$, and μ into a single infection rate parameter. Specifically, there are $\lambda = \beta k^{\bigstar}/\mu$ and $\lambda^{\star} = \beta^{\star}k^{\star}/\mu$. λ and $\lambda^{\star}$ denote the 1-simplex infection rate and 2-simplex infection rate, respectively. Next, based on the simplicial complex constructed from heterogeneous network and real-world networks, we investigate the effect of higher-order interactions on the process of irreversible epidemic spread and the immune effects of various immunization strategies. We stipulate that every node joining the network chooses $M = 4$ vertices to connect links, up until the network size N reaches 500, when building simplicial complex based on heterogeneous network. Set $k^{\bigstar} = 20$ and $k^{\star} = 6$ to change the connection probability p_1 and p_2. Finally, the average degree of the network κ is determined to be 20.

In this study, epidemic spread from initial infection seed density of $\rho^0 = 0.02$, and we set the recovery rate $\mu = 0.02$. The final infection density $\rho^{\star}$ in the figure represents the density of nodes in the R state in the network when the spread process reaches the ultimate state. The symbols in the figures represent the average results of 200 numerical simulations, and the solid lines represent the theoretical results calculated from Eq. 9. Due to a shortcoming intrinsic to the theoretical approach, the results of theory and simulation cannot match precisely. We employed the Microscopic Markov Chain Approach, which assumes that the probability of two neighbors infecting the same individual is independent and disregards the dynamical correlations between the states of nodes. Higher-order interactions serve to exacerbate these dynamical correlations, making it difficult for theory to represent the simulation process in its entirety. The observable phenomena in the figures is primarily demonstrated by theoretical results in our explanation.

3.1 The effect of 2-simplex infection rates

To study the effect of higher-order interactions on the irreversible epidemic spread process, we investigate the epidemic final infection density $\rho^{\star}$ as a function of the 1-simplex infection rate λ on synthetic and real-world simplicial complex, as shown in Figure 2. This figure displays both continuous and discontinuous growth. In addition, the 2-simplex infection rate exerts varying degrees of effect on the spread process in different ranges of 1-simplex infection rate. As depicted by the red solid lines and circles in the figure, we first conduct theoretical analysis and numerical simulations on the heterogeneous network. As illustrated in Figures 2A,B,C, when the 2-simplex infection rate is relatively low, the growth of $\rho^{\star}$

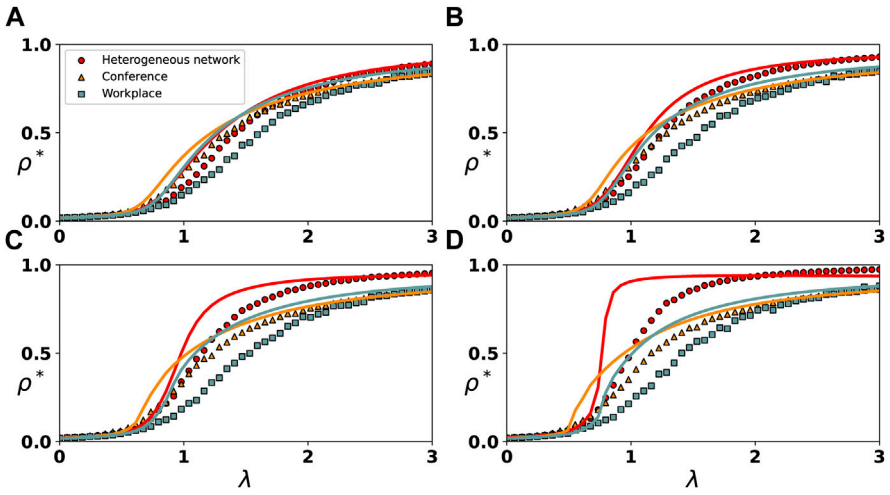

FIGURE 2
Evolution of the final infection density ρ^* with λ under varying rates of 2-simplex. The spread of the epidemic on the heterogeneous network and two real-world networks are represented by circles, triangles and squares, respectively. For the spread on the heterogeneous network, we set $\lambda^* = 0.5$ in **(A)**, $\lambda^* = 3.5$ in **(B)**, $\lambda^* = 6.5$ in **(C)** and $\lambda^* = 12$ in **(D)**. For the spread on the real-world networks, we set $\lambda^* = 0.5$ in **(A)**, $\lambda^* = 1.5$ in **(B)**, $\lambda^* = 2.5$ in **(C)** and $\lambda^* = 4.5$ in **(D)**.

with λ is always continuous. As depicted in Figure 2D, when the 2-simplex infection rate is high, there is a discontinuous increase in the growth of ρ^* with λ. In particular, as demonstrated by Figure 2D, when $\lambda^* = 12$ and $0 < \lambda < 0.5$, the growth of ρ^* with λ is continuous. When $0.5 < \lambda < 1$, growth of ρ^* with λ goes from continuous to discontinuous as λ increases. We also find that as λ^* increases, the outbreak threshold of the epidemic decreases, as shown in Figures 2A–D. For instance, when $\lambda^* = 0.5$, λ needs to increase to around 3 for the epidemic to break out, as shown in Figure 2A. When $\lambda^* = 12$, λ only has to increase to about 1 for the outbreak of the epidemic, as shown in Figure 2D.

In addition, we find that the 2-simplex infection rate exerts varying degrees of effect on the spread process of the epidemic in different ranges of λ. When the 1-simplex infection rate is small (e.g., $\lambda = 0.5$), the increase in the 2-simplex infection rate has almost no effect on the spread process, as shown in Figures 2A–D. When $0.5 < \lambda < 1.5$, the 2-simplex infection rate has the greatest impact on the spread process, which causes the growth of ρ^* with λ to gradually become discontinuous with the increase of λ^*, as shown in Figures 2A–D. When $1.5 < \lambda < 3$, the 2-simplex infection rate has less of an impact on the spread process, as shown in Figures 2A–D.

Next, we repeat the same investigation on real-world simplicial complex constructed from a conference and workplace, respectively, and observe similar phenomena as on synthetic simplicial complex. Due to the small size and complex structure of real-world networks, a high 2-simplex infection rate leads to large error fluctuations in the simulation results. On the real-world networks, we reduce the 2-simplex infection rate, so no obvious discontinuous growth is observed.

3.2 The effect of immunization strategies

Then, we investigate the impact of higher-order interactions on epidemic spread under various immunization strategies. Based on the node degree index and betweenness index, we categorize network nodes. First, we select 10% of the nodes at random for immunization, which is the random immunization strategy (Random). Select 10% of the nodes with the greatest degree, the smallest degree, the greatest betweenness, and the smallest betweenness for immunization, i.e., the maximum degree strategy (Degree _ max), the minimum degree strategy (Degree _ min), the maximum betweenness strategy (Betweenness _ max), and the minimum betweenness strategy (Betweenness _ min). Figure 3 shows the evolution of ρ^* with λ under different immunization strategies and 2-simplex infection rates.

We first perform theoretical analysis and numerical simulations on the heterogeneous network, as shown in Figures 3A–D. We find that the immunization strategy based on node degree has the same immune effect as the betweenness immunization strategy. When selecting the node with the highest degree and betweenness for immunization, the effect is definitely superior to when selecting the node with the lowest degree and betweenness for immunization, however the effect of the random immunization strategy is intermediate. Furthermore, in some special parameter scenarios, we observe similar phenomena to those in Figure 2. When the node with the smallest degree or betweenness of 10% is selected for immunization, the increase in the 2-simplex infection rate has a significant impact on the spread of the epidemic. When the 2-simplex rate is large enough, there is an obvious discontinuous growth in the growth of ρ^* with λ, as

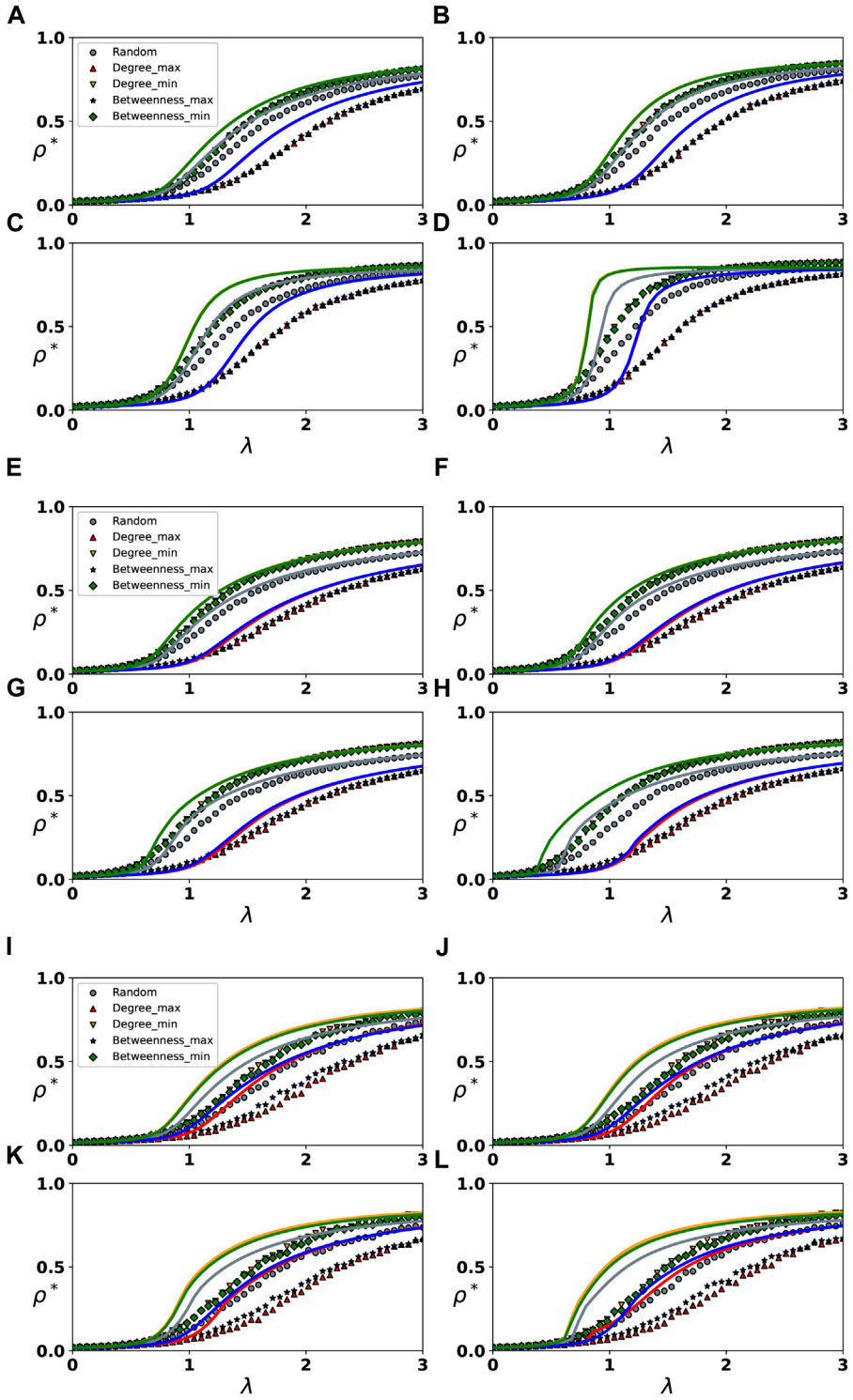

FIGURE 3
Evolution of the final infection density ρ^* with λ under varying 2-complex infection rates and immunization strategies. Subgraphs **(A–D)**, **(E–H)** and **(I–L)** represent the spread of epidemics on the synthetic network and two real-world networks, respectively. Different colors and symbols have been used to depict different immunization strategies. For the spread on the heterogeneous network, we set $\lambda^* = 0.5$ in **(A)**, $\lambda^* = 3.5$ in **(B)**, $\lambda^* = 6.5$ in **(C)** and $\lambda^* = 12$ in **(D)**. For the spread on the real-world networks, we set $\lambda^* = 0.5$ in **(E)** and **(I)**, $\lambda^* = 1.5$ in **(F)** and **(J)**, $\lambda^* = 2.5$ in **(G)** and **(K)**, $\lambda^* = 4.5$ in **(H)** and **(L)**.

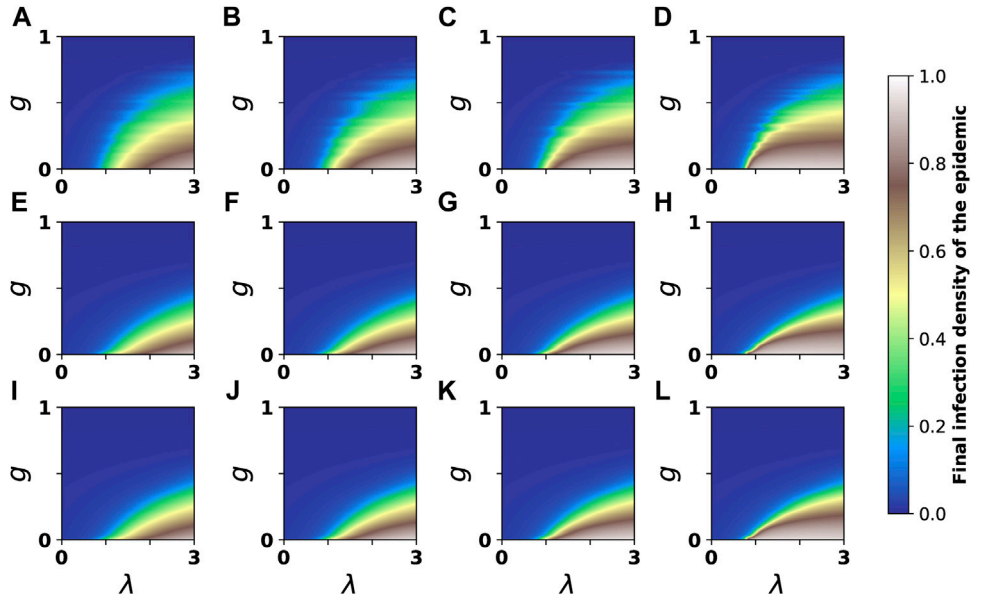

FIGURE 4
Evolution of the final infection density with λ and g under varying 2-simplex infection rates. g represents the ratio of immune nodes. Colors indicate theoretical results for final infection density. Four subgraphs **(A–D)** at the top represent random immunization strategy, four subgraphs **(E–H)** in the middle represent the maximum degree immunization strategy, and four subgraphs **(I–L)** at the bottom represent the maximum betweenness immunization strategy. From the left to the right, λ^* corresponds to 0.5, 3.5, 6.5 and 12.

shown by the green and yellow lines in Figures 3A–D. When 10% of nodes are randomly selected for immunization, the effect of the increase in the 2-simplex rate on the spread of the epidemic is diminished, and the growth of ρ^* with λ gradually becomes discontinuous, as illustrated by the gray lines in Figures 3A–D. When the node with the largest degree and betweenness of 10% is selected for immunization, the increase in 2-simplex infection rate has no discernible effect on the spread of the epidemic, and the growth process of ρ^* with λ is always continuous, as depicted by the red and blue lines in Figures 3A–D. Regardless of the immunization strategy, an increase in the 2-simplex infection rate leads to a reduction in the outbreak threshold of the epidemic. Similar to the phenomenon depicted in Figure 2, the increase in the infection rate of the 2-simplex has varying degrees of impact on the spread process of the epidemic in various λ ranges. Furthermore, when λ is small (e.g., $\lambda = 0.5$), the epidemic cannot break out under either immunization strategy. When $2 < \lambda < 3$, $\lambda^* = 12$, the epidemic spread under different immunization strategies has the same spread size. In other words, when both the 1-simplex rate and the 2-simplex rate are large and 10% of the nodes are selected for immunization, alternative immunization strategies have the same effect, as shown in Figure 3D.

Likewise, we conduct research on two real-world networks, a conference and workplace, and observe similar phenomena. However, as shown in Figures 3H,L, when the infection rates of 1-simplex and 2-simplex are both large, the spread size of epidemics under various immunization strategies varies, which may be related to the ratio of immunized nodes and the network structure. Furthermore, since we set the 2-simplex infection rate relatively small on real-world networks, we do not observe obvious discontinuous growth.

3.3 The effect of immunization ratios

Finally, to further investigate the effect of different immunization strategies on the spread of the epidemic on higher-order networks, we examine the effect of different immunization strategies on the spread size of the epidemic under different 2-simplex infection rates and different immunization ratios on the simplex complex constructed based on the heterogeneous network. Figure 4 depicts the evolution of final infection density ρ^* as a function of immune ratio g and 1-simplex infection rate λ for various 2-simplex infection rates λ^*. We first investigate the case of random immunization strategy, as shown in Figures 4A–D. We discover that when g is small (about less than 0.3), the increase of λ^* will cause the growth of ρ^* to become discontinuous with the increase of λ, hence decreasing the outbreak threshold. When both g and λ^* are small, the interval between different colors is large, and the growth of final infection density with λ is continuous, as shown in Figures 4A–C. When g is small and λ^* is large, brown is squeezed toward blue, and the interval between different colors becomes smaller. At this time, the growth of final infection density with λ is discontinuous, and a slight change in λ can lead to the

outbreak of the epidemic. When g exceeds around 0.3, the increase of λ^* has little effect on the increase of ρ^* with λ. In addition, we discover that the epidemic cannot spread when g is approximately 0.8 or when λ is small (approximately less than 0.5).

Next, we discuss the case of the maximum degree strategy and the maximum betweenness strategy, as demonstrated in Figures 4E–L. Similar phenomena are observed as with the random immunization strategy. When g is relatively small, the increase of λ^* will cause the process of ρ^* to grow discontinuously with λ, as shown in Figure 4H. When g is relatively large, an increase in λ^* will have little effect on the process of increasing ρ^* with λ, as shown in Figures 4E–H. Compared with the random immunization strategy, the g required to fully sustain the epidemic outbreak with the maximum degree immunization strategy is smaller, about 0.5. When g is small (about 0.1) and both λ^* and λ are large, different immunization strategies have the same immune effect and have less impact on the spread size of the epidemic, as shown in Figures 4D,H,L when $\lambda^* = 12$ and $\lambda = 3$. In addition, the maximum degree immunization strategy and the maximum betweenness immunization strategy have the same immune effect.

4 Theoretical method

To the best of our knowledge, existing studies mostly use Mean-Field theory to study the dynamics of epidemic spread on higher-order networks. This method regards the individuals in the network as equivalent nodes, which ignores the heterogeneity between individuals, cannot fully reflect the complete structural information of the contact network, and cannot track the evolution of individual nodes. In order to more accurately describe the irreversible epidemic spread process on higher-order networks and track the state evolution of each node in the network, we use the Microscopic Markov Chain Approach to construct the theoretical model [45–47].

As mentioned in Section 2, our model contains a total of N nodes, each node has three possible existence states (S, I, R) at any time. The spread process can be performed by 1-simplex or 2-simplex. We use $p_i^T(t), T \in \{S, I, R\}$ to denote the probability that a node i is in state T at time t. The temporal evolution process of $p_i^T(t)$ is as follows:

$$p_i^S(t+1) = p_i^S(t)(1-m_i)\hbar_i(t)\hbar_i^t(t) \tag{1}$$

$$p_i^I(t+1) = p_i^I(t)(1-m_i)(1-\mu) + p_i^S(t)(1-m_i)\left[1-\hbar_i(t)\hbar_i^t(t)\right] \tag{2}$$

$$p_i^R(t+1) = p_i^R(t)(1-m_i) + p_i^I(t)(1-m_i)\mu \tag{3}$$

The left side of Eq. 1 represents the probability that a node i in the system is in the S state at time $t+1$, the right side represents the probability that a node i is in the S state at time t and is not infected and immune. $\hbar_i(t)$ and $\hbar_i^t(t)$ represent the probability that an S state node i is not infected by an I state node through the 1-simplex and 2-simplex at time t, respectively. m_i is the immunization coefficient, $m_i = 1$ when node i is selected as the immune node, otherwise $m_i = 0$. For Eq. 2, the left side represents the probability that a node i in the system is in the I state at time $t+1$, the first term on the right side represents the probability that the node i is in the I state at time t and has not recovered and been immune, the second term represents the probability that an S state node i is not immune but is infected at time t. For Eq. 3, the left side represents the probability that a node i in the system is in R state at time $t+1$, the first term on the right side represents the probability that node i is in R state at time t and is not immune, the second term represents the probability that a node i in state I is not immune at time t but returns to state R. The expressions for $\hbar_i(t)$ and $\hbar_i^t(t)$ are as follows:

$$\hbar_i(t) = \prod_{m\in\tau_i}\left[1-\beta p_m^I(t)\right] \tag{4}$$

$$\hbar_i^t(t) = \prod_{m,n\in\Delta_i}\left[1-\beta^t p_m^I(t) p_n^I(t)\right] \tag{5}$$

For Eq. 4, the right side represents the probability that an S state node i is not infected by its I state neighbor node m through 1-simplex at time t, τ_i represents the set of neighbor nodes connected by node i through 1-simplex. For Eq. 5, the right side represents the probability that an S state node i is not infected by its two I state neighbors m and n through a 2-simplex at time t, and Δ_i represents the set of neighbor nodes connected by node i through 2-simplex.

When N is large enough, we define $\rho^T(t)$ to represent the proportion of individuals who are in state T at time t in the system, which can be approximated as the average of the probability that individuals are in state T, $T \in \{S, I, R\}$ $\rho^T(t)$ can be expressed as:

$$\rho^T(t) = \frac{1}{N}\sum_{i=1}^{N} p_i^T(t) \tag{6}$$

Correspondingly, the proportion of nodes in the S, I and R state in the system at time t can be expressed as:

$$\rho^S(t) = \frac{1}{N}\sum_{i=1}^{N} p_i^S(t) \tag{7}$$

$$\rho^I(t) = \frac{1}{N}\sum_{i=1}^{N} p_i^I(t) \tag{8}$$

$$\rho^R(t) = \frac{1}{N}\sum_{i=1}^{N} p_i^R(t) \tag{9}$$

When $t \to \infty$, the system reaches the final state, we denote $\rho(t \to \infty)$ as ρ, at this time, $\rho^I = 0$.

5 Conclusion

In this work, we construct simplicial complex to represent higher-order networks and propose a simplicial irreversible

epidemic spread model (SIR) on it. On the basis of the degree index and betweenness index of nodes, we compare and analyze the impacts of five different immunization strategies on the spread of the epidemic using this model. We first construct simplicial complex containing both pairwise interactions and higher-order interactions on synthetic networks and real-world networks. By extending the Microscopic Markov Chain theoretical analysis model, the temporal evolution equations of nodes in three distinct states are then determined. Finally, the effects of 1-simplex infection rate, 2-simplex infection rate, and different immunization strategies on the epidemic spread process are examined by numerical simulations.

We first investigate the effect of different 2-simplex infection rates on the process of epidemic spread in the absence of immunization strategies. We discover that when λ^* is relatively small, the growth of ρ^* with λ is always continuous. When λ^* is relatively large, there is a discontinuous growth of ρ^* along with the growth of λ. As λ^* increases, the outbreak threshold of the epidemic decreases. In addition, we discover that the 2-simplex infection rate exerts variable degrees of effect on the spread process of the epidemic in different ranges of λ.

Then we discuss the impact of higher-order interactions on the spread of the epidemic under five different immunization strategies with a fixed immunization ratio of 10%. We find that the immunization strategy based on the node degree index has the same immune effect as the one based on the node betweenness index. Selecting the node with the largest degree and betweenness for immunization has the best effect, followed by the random immunization strategy, and finally the immunization strategy with the smallest degree and betweenness. When nodes with a ratio of 10% are selected for immunization, the increase in 2-simplex infection rate has a significant impact on the spread of epidemics under the degree and betweenness minimum immunization strategy, resulting in discontinuous growth in the system. The impact on the epidemic spread under the random immunization strategy is weakened, and there is no significant impact on the epidemic spread under the degree and betweenness maximum immunization strategy. Regardless of the immunization strategy, an increase in the 2-simplex infection rate leads to a reduction in the outbreak threshold of the epidemic.

Finally, we examine the evolution of the final infection density with the immunization ratio and the 1-simplex infection rate for various 2-simplex infection rates. We find that when the immunization ratio and 2-simplex infection rate are both small, the growth of the final infection density is always continuous with 1-simplex infection rate. When the ratio of immune is small and the infection rate of 2-simplex is large, there will be a discontinuous growth in the growth of final infection density with the 1-simplex infection rate. Compared with the random immunization strategy, the ratio of immunization required to fully sustain the outbreak of the epidemic is smaller when the degree and betweenness maximum immunization strategies are adopted. When the immunization ratio is small and both the 2-simplex and 1-simplex infection rate are large, different immunization strategies have the same immune effect and have less impact on the spread size of the epidemic.

In summary, this paper investigates the effects of different immunization strategies, 2-simplex and 1-simplex infection rates on the spread of the irreversible epidemic on higher-order networks. This research has certain practical significance for epidemic prevention and control. For example, in the early stage of an outbreak, when vaccines are lacking, it is more effective to immunize a large number of exposed persons than to randomly choose individuals for immunization. This work has limitations as well. Our conclusions are primarily supported by theoretical analysis. However, due to the inherent limits of the theoretical method, our theoretical results do not precisely correspond to the simulation results. How to develop a more accurate theoretical method to simulate the spread process is a direction worthy of consideration.

Data availability statement

The raw data supporting the conclusion of this article will be made available by the authors, without undue reservation.

Author contributions

WL wrote the original draft of this opinion manuscript. BP, SS and WW provided feedback on the manuscript. LN and YZ edited the final manuscript. All authors approved for the final version of the manuscript.

Funding

This research was supported by the Social Science Foundation of Chongqing (No. 2021PY53), National Natural Science Foundation of China (No. 61903266), Natural Science Foundation of Chongqing (No. cstc2021jcyj-msxmX0132), Natural Science Foundation of Yuzhong District, Chongqing (No.20210117), Science and Technology Research Program of Chongqing Municipal Education Commission (No. KJQN202200429).

Conflict of interest

The authors declare that the research was conducted in the absence of any commercial or financial relationships that could be construed as a potential conflict of interest.

Publisher's note

References

1. Zhang R-x., Jin Z, Li S-p. Epidemic spreading with time delay on complex networks. *Acta Math Appl Sin Engl Ser* (2016) 32:319–26. doi:10.1007/s10255-016-0554-1

2. Qu J, Tang M, Liu Y, Guan S. Identifying influential spreaders in reversible process. *Chaos, Solitons & Fractals* (2020) 140:110197. doi:10.1016/j.chaos.2020.110197

3. Malik HAM, Abid F, Wahiddin MR, Waqas A. Modeling of internal and external factors affecting a complex dengue network. *Chaos, Solitons & Fractals* (2021) 144:110694. doi:10.1016/j.chaos.2021.110694

4. Albert R, Barabási A-L. Statistical mechanics of complex networks. *Rev Mod Phys* (2002) 74:47–97. doi:10.1103/revmodphys.74.47

5. Newman ME. The structure and function of complex networks. *SIAM Rev Soc Ind Appl Math* (2003) 45:167–256. doi:10.1137/s003614450342480

6. Salfenmoser L, Obermayer K. Nonlinear optimal control of a mean-field model of neural population dynamics. *Front Comput Neurosci* (2022) 90:931121. doi:10.3389/fncom.2022.931121

7. Chen P, Guo X, Jiao Z, Liang S, Li L, Yan J, et al. Effects of individual heterogeneity and multi-type information on the coupled awareness-epidemic dynamics in multiplex networks. *Front Phys* (2022) 689. doi:10.3389/fphy.2022.964883

8. Pastor-Satorras R, Vespignani A. Epidemic spreading in scale-free networks. *Phys Rev Lett* (2001) 86:3200–3. doi:10.1103/physrevlett.86.3200

9. Liu Z, Hu B. Epidemic spreading in community networks. *Europhys Lett* (2005) 72:315–21. doi:10.1209/epl/i2004-10550-5

10. Saumell-Mendiola A, Serrano MÁ, Boguná M. Epidemic spreading on interconnected networks. *Phys Rev E* (2012) 86:026106. doi:10.1103/physreve.86.026106

11. Stegehuis C, Van Der Hofstad R, Van Leeuwaarden JS. Epidemic spreading on complex networks with community structures. *Sci Rep* (2016) 6:29748–7. doi:10.1038/srep29748

12. Qu J-Y, Tang M, Liu Y, Guan S-G. The relative importance of structure and dynamics on node influence in reversible spreading processes. *Front Phys (Beijing)* (2021) 16:51503–10. doi:10.1007/s11467-021-1082-9

13. Pastor-Satorras R, Castellano C, Van Mieghem P, Vespignani A. Epidemic processes in complex networks. *Rev Mod Phys* (2015) 87:925–79. doi:10.1103/revmodphys.87.925

14. Nesteruk I. *Estimations of the coronavirus epidemic dynamics in South Korea with the use of sir model*. ResearchGate (2020). Preprint.

15. Guo Z, Huang L, Zou X. Impact of discontinuous treatments on disease dynamics in an sir epidemic model. *Math Biosci Eng* (2012) 9:97–110. doi:10.3934/mbe.2012.9.97

16. Battiston F, Cencetti G, Iacopini I, Latora V, Lucas M, Patania A, et al. Networks beyond pairwise interactions: Structure and dynamics. *Phys Rep* (2020) 874:1–92. doi:10.1016/j.physrep.2020.05.004

17. Li W, Xue X, Pan L, Lin T, Wang W. Competing spreading dynamics in simplicial complex. *Appl Maths Comput* (2022) 412:126595. doi:10.1016/j.amc.2021.126595

18. Wang W, Li W, Lin T, Wu T, Pan L, Liu Y. Generalized k-core percolation on higher-order dependent networks. *Appl Maths Comput* (2022) 420:126793. doi:10.1016/j.amc.2021.126793

19. Althouse BM, Wenger EA, Miller JC, Scarpino SV, Allard A, Hébert-Dufresne L, et al. Superspreading events in the transmission dynamics of sars-cov-2: Opportunities for interventions and control. *Plos Biol* (2020) 18:e3000897. doi:10.1371/journal.pbio.3000897

20. Newman ME, Strogatz SH, Watts DJ. Random graphs with arbitrary degree distributions and their applications. *Phys Rev E* (2001) 64:026118. doi:10.1103/physreve.64.026118

21. Palla G, Derényi I, Farkas I, Vicsek T. Uncovering the overlapping community structure of complex networks in nature and society. *nature* (2005) 435:814–8. doi:10.1038/nature03607

22. Kahle M. Topology of random clique complexes. *Discrete Math* (2009) 309:1658–71. doi:10.1016/j.disc.2008.02.037

23. Czaplicka A, Toral R, San Miguel M. Competition of simple and complex adoption on interdependent networks. *Phys Rev E* (2016) 94:062301. doi:10.1103/physreve.94.062301

24. Sizemore AE, Giusti C, Kahn A, Vettel JM, Betzel RF, Bassett DS. Cliques and cavities in the human connectome. *J Comput Neurosci* (2018) 44:115–45. doi:10.1007/s10827-017-0672-6

25. Perc M. Does strong heterogeneity promote cooperation by group interactions? *New J Phys* (2011) 13:123027. doi:10.1088/1367-2630/13/12/123027

26. Millán AP, Torres JJ, Bianconi G. Synchronization in network geometries with finite spectral dimension. *Phys Rev E* (2019) 99:022307. doi:10.1103/physreve.99.022307

27. Skardal PS, Arenas A. Abrupt desynchronization and extensive multistability in globally coupled oscillator simplexes. *Phys Rev Lett* (2019) 122:248301. doi:10.1103/physrevlett.122.248301

28. Kee KF, Sparks L, Struppa DC, Mannucci M. Social groups, social media, and higher dimensional social structures: A simplicial model of social aggregation for computational communication research. *Commun Q* (2013) 61:35–58. doi:10.1080/01463373.2012.719566

29. Iacopini I, Petri G, Barrat A, Latora V. Simplicial models of social contagion. *Nat Commun* (2019) 10:2485–9. doi:10.1038/s41467-019-10431-6

30. Cohen R, Havlin S, Ben-Avraham D. Efficient immunization strategies for computer networks and populations. *Phys Rev Lett* (2003) 91:247901. doi:10.1103/physrevlett.91.247901

31. Chen Y, Paul G, Havlin S, Liljeros F, Stanley HE. Finding a better immunization strategy. *Phys Rev Lett* (2008) 101:058701. doi:10.1103/physrevlett.101.058701

32. Matamalas JT, Arenas A, Gómez S. Effective approach to epidemic containment using link equations in complex networks. *Sci Adv* (2018) 4:eaau4212. eaau4212. doi:10.1126/sciadv.aau4212

33. Costa GS, Ferreira SC. Nonmassive immunization to contain spreading on complex networks. *Phys Rev E* (2020) 101:022311. doi:10.1103/physreve.101.022311

34. Shim E. Optimal allocation of the limited Covid-19 vaccine supply in South Korea. *J Clin Med* (2021) 10:591. doi:10.3390/jcm10040591

35. Pastor-Satorras R, Vespignani A. Immunization of complex networks. *Phys Rev E* (2002) 65:036104. doi:10.1103/physreve.65.036104

36. Pastor-Satorras R, Vespignani A. *Handbook of graphs and networks*. Berlin: Wiley VCH (2003). Epidemics and immunization in scale-free networks.

37. Gallos LK, Liljeros F, Argyrakis P, Bunde A, Havlin S. Improving immunization strategies. *Phys Rev E* (2007) 75:045104. doi:10.1103/physreve.75.045104

38. Morris M, Podhisita C, Wawer MJ, Handcock MS. Bridge populations in the spread of hiv/aids in Thailand. *AIDS (London, England)* (1996) 10:1265–71. doi:10.1097/00002030-199609000-00013

39. Freeman LC. Centrality in social networks conceptual clarification. *Social networks* (1978) 1:215–39. doi:10.1016/0378-8733(78)90021-7

40. Newman ME. A measure of betweenness centrality based on random walks. *Soc networks* (2005) 27:39–54. doi:10.1016/j.socnet.2004.11.009

41. Salathé M, Jones JH. Dynamics and control of diseases in networks with community structure. *Plos Comput Biol* (2010) 6:e1000736. doi:10.1371/journal.pcbi.1000736

42. Jin X, An T, Wang J, Cui G, Zhao J. Impact of strategy conformity on vaccination behaviors. *Front Phys* (2022) 735. doi:10.3389/fphy.2022.972457

43. Jhun B. Effective epidemic containment strategy in hypergraphs. *Phys Rev Res* (2021) 3:033282. doi:10.1103/physrevresearch.3.033282

44. SocioPatterns. *Featured: Infectious sociopatterns poster* (2008). Available at: http://www.sociopatterns.org/ [Accessed on September 10, 2021].

45. Gómez S, Arenas A, Borge-Holthoefer J, Meloni S, Moreno Y. Discrete-time Markov chain approach to contact-based disease spreading in complex networks. *Europhys Lett* (2010) 89:38009. doi:10.1209/0295-5075/89/38009

46. Granell C, Gómez S, Arenas A. Dynamical interplay between awareness and epidemic spreading in multiplex networks. *Phys Rev Lett* (2013) 111:128701. doi:10.1103/physrevlett.111.128701

47. Soriano-Paños D, Lotero L, Arenas A, Gómez-Gardeñes J. Spreading processes in multiplex metapopulations containing different mobility networks. *Phys Rev X* (2018) 8:031039. doi:10.1103/physrevx.8.031039

frontiers | Frontiers in Physics

TYPE Original Research
PUBLISHED 12 October 2022
DOI 10.3389/fphy.2022.1021245

OPEN ACCESS

EDITED BY
Ye Wu,
Beijing Normal University, China

REVIEWED BY
Peng Ji,
Fudan University, China
Gang Chen,
Xi'an Jiaotong University, China

*CORRESPONDENCE
Hongfu Liu,
Liuliuhongfu@nudt.edu.cn
Jing Chen,
chenjing001@vip.sina.com

SPECIALTY SECTION
This article was submitted to Interdisciplinary Physics, a section of the journal Frontiers in Physics

RECEIVED 17 August 2022
ACCEPTED 22 September 2022
PUBLISHED 12 October 2022

CITATION
Chen L, Wang C, Zeng C, Wang L, Liu H and Chen J (2022), A novel method of heterogeneous combat network disintegration based on deep reinforcement learning.
Front. Phys. 10:1021245.
doi: 10.3389/fphy.2022.1021245

A novel method of heterogeneous combat network disintegration based on deep reinforcement learning

Libin Chen[1], Chen Wang[1], Chengyi Zeng[1], Luyao Wang[2], Hongfu Liu[1]* and Jing Chen[1]*

[1]College of Intelligence Science and Technology, National University of Defense Technology, Changsha, China, [2]College of Systems Engineering, National University of Defense Technology, Changsha, China

Modern war is highly dependent on intelligent, unmanned combat systems. Since many intelligent, unmanned combat systems have network attributes, it is meaningful to research combat systems from the perspective of complex network. Heterogeneous network provides a suitable model to describe real combat network. Previous studies of combat network only concentrate on homogeneous networks. However, on the real battlefield, military networks are composed of a large number of heterogeneous nodes and edges with different functions. In the paper, a superior, intelligent, heterogeneous combat network disintegration strategy (HDGED) are obtained by DQN, which embeds heterogeneous networks into a low-dimensional representation vector as input, rather than ignore the differences of the nodes and their connections. A method of heterogeneous graph embedding is first introduced, which adopts type encoding and aggregation. Besides, a normalized combat capability index was designed, which could assess the performance of the dynamic heterogeneous combat networks. On this basis, HDGED was experimented on networks with uneven node combat capabilities and the results show that HDGED has improved disintegration effectiveness for heterogeneous networks of different sizes compared with traditional methods. Our work provides a new approach to realize the disintegration of heterogeneous combat networks by deep reinforcement learning, which is of great significance for optimizing the command operation process, and deserves further study.

KEYWORDS

heterogeneous combat network, graph embedding, combat capability, network disintegration, deep reinforcement learning

1 Introduction

Complex network is a research paradigm that represents a complex system as a network structure, in which nodes represent objects in a complex system, and edges represent the relationship between objects. The traditional complex network predominantly takes the homogeneous network as the research object. However, the ubiquitous networks in the real world, such as citation networks in [1], social networks in [2], recommendation systems in [3], cybersecurity in [4] and military combat networks, are heterogeneous networks composed of various types of entities and relationships which can more accurately describe different types of entities and relationships in the network.

Compared with the homogeneous network, the heterogeneous network has multiple types of entities and relationships, and contains rich structural information and semantic information, which provides a way to discover the deeply hidden information in the network. However, due to the heterogeneity of objects and relationships, many homogeneous network analysis methods cannot be directly applied to heterogeneous networks, which complicates the study of heterogeneous networks. First, the complex structure of heterogeneous networks makes data processing and semantic mining more difficult. Second, how to represent different types of entities and relationships and how to integrate heterogeneous information is a considerable challenge. Third, current studies on heterogeneous networks mainly focus on downstream tasks such as classification [5], clustering [6], link prediction [7], and so on, and studies on heterogeneous network disintegration and heterogeneous network performance evaluation are insufficient.

The heterogeneous network disintegration such as terrorist networks, disease transmission networks, and military warfare networks has important practical significance. The performance of these complex networks is mainly affected by a small number of critical nodes, and the removal of these critical nodes will significantly weaken certain network functions. Therefore, the core of complex network disintegration is to find an optimal set of critical nodes. It is proved that the network disintegration problem is a typical NP-hard problem [8]. If a network contains many nodes, it will be tough to find the optimal network disintegration strategy directly. At present, the research of complex network disintegration mainly focuses on homogeneous networks. According to the algorithm principle, it can be divided into four kinds: 1) The method based on node centrality uses the centrality ordering of nodes to solve the network disintegration strategy. Firstly, the centrality indexes of various nodes are defined, then the critical nodes in the current network are mined according to the centrality ranking of nodes, and finally, the network is disintegrated by removing the nodes with high centrality first. The methods based on node centrality mainly include: Romualdo Pastor-Satorras et al. proposed HDA (High Degree Adaptive) method [9]. Proposed an algorithm called CI (Collective influence) to measure the influence of nodes [10]. By defining a specific influence range, the direct and indirect neighbors of each node in the range were used to describe the influence value of nodes quantitatively. Then the node is removed based on the descending order of the node influence value. The centrality index calculation of this kind of method is complicated, so it is difficult to apply to large-scale networks. 2) The method based on optimal breakage aims to remove all the rings in the network with the least number of nodes so that the network is broken down into small modules, mainly including Alfredo et al. proposed a third-order Min-sum algorithm [11], and proposed a probability model called BPD (Belief Propagation guided Decimation) to measure the removal probability of each node in the current network [12]. Nodes are removed based on the probability of removal. Lenka et al. proposed the CoreHD algorithm to disintegrate the network [13]. The algorithm's core is to strip all first-order nodes of the network based on the K-core decomposition mechanism and then remove the remaining nodes in the network in descending order according to the node degree sequence. This method completely disintegrates the network and does not apply to the universal network disintegration. 3) The main idea of the method based on graph segmentation is to divide the graph into two or more pieces of equal size with the least number of points, and then continue to decompose the graph with the same method, and finally wholly divide the graph, mainly including the RatioCut method proposed by Lars Hagen obtains the final solution by calculating the eigenvector corresponding to the second smallest eigenvalue of the unnormalized Graph Laplacian matrix [14]. The GND method proposed by Xiao-long Ren deals with the graph attack problem with node removal cost by adding the information of point weight to the Graph Laplace matrix in RatioCu [15]. However, this method takes the second smallest eigenvalue of Tulapras matrix as the solution has some limitations. 4) Meta-heuristic-based algorithms view the network tiling problem as a combined optimization problem with different objective functions and constraints, mainly including Deng Ye proposed an optimal disintegration strategy based on tabu search [16]. This approach is mainly limited by computing power.

The above methods are limited to homogeneous networks, and the computational performance limits the disintegration effect. Moreover, most of the methods are designed only for a certain problem scenario. Therefore, there is still a lack of an efficient heterogeneous network disintegration solution framework. In recent years, some work has tried to use deep neural networks to study heterogeneous network representation learning [17–19]. Among them, the shallow

model decomposed the heterogeneous network into single networks, respectively represented these networks, and then integrated the information. For example, HERec uses meta path to extract multiple homogeneous networks from heterogeneous networks, represents these homogeneous networks and aggregates them [3]. The model based on autoencoder aims to use a neural network to construct the encoder learning node attribute representation while maintaining the network structure characteristics. For example, SHINE obtained feature representations by compressed coding of heterogeneous information in social networks, sentiment networks, and pictorial networks, respectively, and fused them by aggregation functions [20]. The core of the generative adversarial network-based approach is to obtain robust node representations using games between generators and discriminators. The method proposed by uses relational perception to train discriminator and generators, and improves negative sampling by learning the potential distribution of nodes [21]. The deep model based on deep reinforcement learning focuses on the meta-path selection dilemma and optimizes the overall framework by taking the downstream task performance as a reward, so as to learn the node representation while avoiding the meta-path selection. For example, transformed the node representation learning of the star network into a Markov decision process, where the action is to select a specific type of link for learning or termination of training, and the state is the order of the selected link types [22]. The key of heterogeneous graph neural network is how to design an appropriate aggregation function to capture the semantics contained in the neighborhood, including structure2vec [23], GCN [24], GraphSAGE [25], GAT [26], GIN [27], etc., Among them, use machine learning to learn network dismantling [28]. First proposed the FINDER operator based on the framework of graph neural network, and applied the combination of graph neural network and deep reinforcement learning to find the critical nodes in the network to solve the optimal disintegration strategy [29]. But this research object was still homogeneous network.

In summary, to make up for the shortcomings of traditional network disintegration methods in solving the heterogeneous network disintegration problem, this paper first presents the Heterogeneous network Disintegration strategy based on Graph Embedding *via* DQN, called HDGED to solve the heterogeneous network disintegration problem. The method is not restricted by the problem scenario and can make full use of the heterogeneous information and network structure information of the heterogeneous network to find the critical nodes in the heterogeneous combat network more effectively to achieve the optimal network disintegration.

The structure of this paper is as follows: the second section summarizes the work related to the modeling of combat networks. The third section introduces the optimal disintegration strategy for heterogeneous operational networks, HDGED, proposed in this paper. The fourth section shows the comparison experiment between HDGED and the baseline algorithm and provides a detailed analysis of the experimental results. Finally, the fifth section discusses the conclusions and future work.

2 Modeling

2.1 Heterogeneous network

As shown in Figure 1, heterogeneous networks are composed of different types of entities (i.e., nodes) and different types of relationships (i.e., edges), which are defined as follows.

Definition1: Heterogeneous Networks (or Heterogeneous Graphs) [17]. Let $G = (V, E)$ be a heterogeneous network, where V and E represent node sets and edge sets, respectively. Each node $v \in V$ and each edge $e \in E$ is associated with its function $\phi(v)$: $V \rightarrow A$ and $\varphi(e)$: $E \rightarrow R$, A and R represent node type and edge type respectively, where $|A| + |R| > 2$.

2.2 Heterogeneous combat network model

The combination of different types of combat entities with various capabilities required for combat forms a heterogeneous

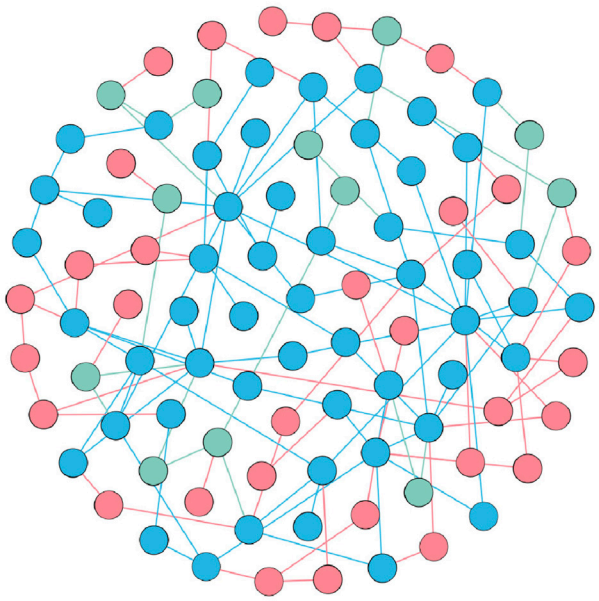

FIGURE 1
An example of a heterogeneous network. Different colors represent different types of nodes and edges.

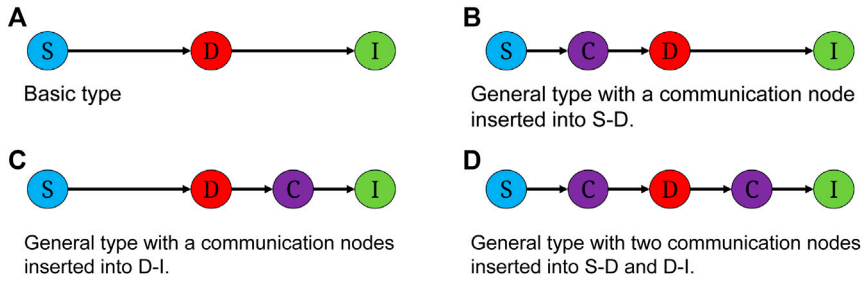

FIGURE 2
Heterogeneous operational chain. As shown in Figure, the OC can be divided into basic type and general type. The basic type, as shown in **(A)**, consists of sensor operation unit, decision operation unit and influence operation unit directly connected. Since any combat unit can also act as an intermediary for information transfer, we extend the basic type to a general type with mediated communication nodes, i.e., **(C)**.Considering the timeliness of operational information, we only consider here the case where there is a one-hop intermediary in the SD and DI information transfer process, and the general type of OC is shown in **(B–D)**.

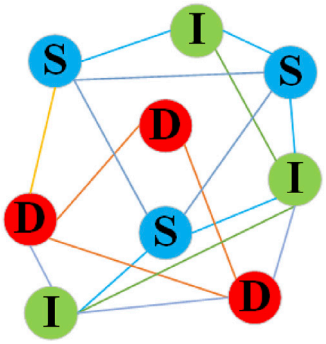

FIGURE 3
Heterogeneous combat network. Node S denotes the sensor entity, node D denotes the decision entity, and node I denotes the impact entity.

combat network (HCN). In this paper, we mainly study the problem of how to quickly dismantle the combat network of the defender from the attacker's point of view, without considering the attacker's entities, so we adopt the model of FINC proposed in [30] by Dekker to classify the combat forces on the battlefield into three categories. Based on the roles of various entities in the combat process, the entities in the weaponry system can be classified into the following three categories.

1) Sensor entities (S): Reconnaissance, surveillance, and early warning equipment, such as reconnaissance satellite, unmanned reconnaissance aircraft, early warning aircraft, radar, and other operating equipment for early warning, detection, and reconnaissance missions.

2) Decider entities (D): Communication and command and control equipment entity, such as command and control system, communication system, data chains, aerospace information system, command vehicle, etc.,

3) Influential entities (I): Joint fire attack and interference entities, such as missiles, cruise missiles, ships, aircraft, attack helicopters, tanks, network attack, and electronic interference, etc.,

In military operations, sensor entities are responsible for detecting enemy targets and transmitting intelligence about enemy targets to decision entities. The decision entity performs data fusion and information analysis of target information from the sensor entity or other decision entities, makes operational decisions and orders the influence entity to conduct an attack. The influence entity receives orders from the decision entity and conducts strikes on enemy targets. The entire combat process forms a chain, called the operational chain.

2.2.1 Operational chain

In this paper, the operational chain (OC) is used to represent the information flow between entities involving various types of functions.

Definition 2: Operational Chain (OC) [6]. In order to accomplish a specific combat mission, sensor entities, decision entities, and influence entities cooperate with each other in an orderly manner to construct an operational chain (OC). According to the different types and numbers of entities, this paper mainly studies the following four operational chains, which can be divided into basic type and general type. The basic type, as shown in Figure 1, consists of the direct connection of sensor entity, decision entity and impact combat unit. Since any combat unit can act as an intermediary for information transfer, we extend the basic type into a general type with intermediary communication nodes. Considering the timeliness of combat information, we only consider the case where there is a one-hop intermediary node in the information transfer process of S-D and D-I. The general type of OC is shown in Figure 1.

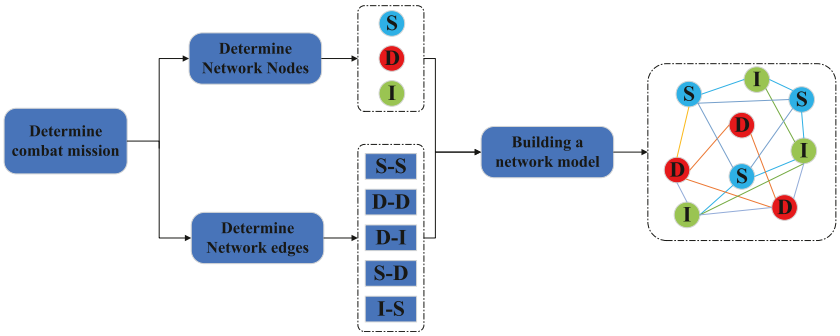

FIGURE 4
Modeling steps of heterogeneous combat network. Firstly, determining the combat objectives according to the combat tasks and determining the nodes and edges of the combat network. Finally, the combat network model is generated from the nodes and the edges identified by the information flow.

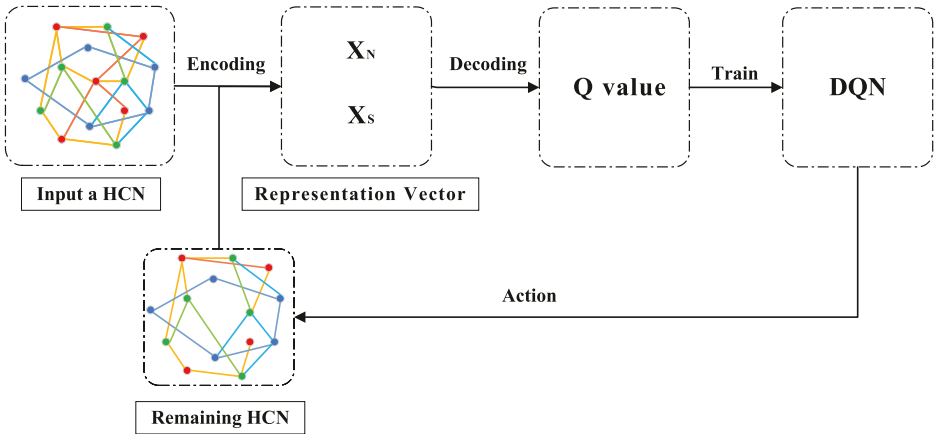

FIGURE 5
Framework of the HDGED.

The Operational Chain can be divided into basic type and general type. The basic type, as shown in Figure 2A, consists of a sensor combat unit, a decision-making combat unit, and an impact combat unit directly connected. Since any combat unit can act as an intermediary for information transmission, we extend the basic type to a general type with an intermediary communication node. Considering the timeliness of operational information, only the presence of a hop intermediary node in the process of information transmission is considered here, and the general type of OC is shown in Figures 2B–D.

The belligerents in a war establish OCs with enemy entities as targets, and the operation chains intertwine to form an operational network eventually. Figure 3 shows the heterogeneous combat network built by combat chains.

2.2.2 Heterogeneous combat network modeling

Consisting of different types of nodes and edges, heterogeneous combat networks (HCN) are used to represent various information flows among sensor entities, decision entities, and influence entities.

Definition 3 Heterogeneous Combat Network (HCN) [6]: a $G = (V, E)$ where $V = S \cup D \cup I = \{v_1, v_2, v_3 \cdots, v_n\}$ represents node set and edge set $E = \{e_1, e_2, e_3, \ldots, e_w\} \subseteq V \times V$ represents information flow between functional entities. Specifically, all functional entities are divided into a set of sensor entities $S = \{v_1^S, v_2^S, v_3^S, \ldots, v_k^S\}$, a set of decision entities $D = \{v_1^D, v_2^D, v_3^D, \ldots, v_l^D\}$, and a set of influence entities $I = \{v_1^I, v_2^I, v_3^I, \ldots, v_p^I\}$. The variable $N = |V|$ and $W = |E|$ denote the number of nodes and edges in the combat network, and $K = |S|$, $L = |D|$, $P = |I|$ respectively the number of sensor entities, the number of decision entities, and the number of influence entities. Different

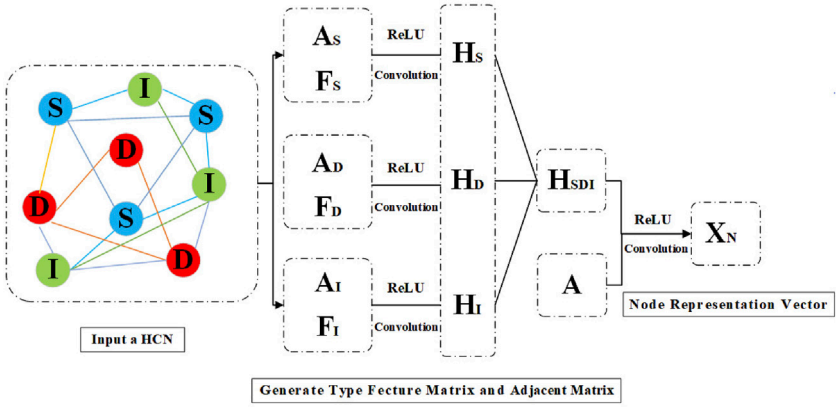

FIGURE 6
Framework of node representation vector encoding.

types of nodes provide different functions during combat. The operational capabilities of the sensor entity, decision entity, and impact entity are denoted as CA_S, CA_D and CA_I. The modeling steps of the heterogeneous combat network model are shown in Figure 4.

3 Optimal disintegrating strategy of heterogeneous combat network

This paper first proposes the Heterogeneous network Disintegration strategy based on Graph Embedding *via* DQN, called HDGED. Furthermore, we combine graph embedding with deep reinforcement learning to solve the optimal disintegrating strategy of heterogeneous networks. Among them, the graph embedding part contains two parts: encoding and decoding. In the encoding part, we embedded different types of nodes in the way of type encoding and designed a multi-layer GCN network to aggregate the structural features and type features of nodes so as to obtain the representation vectors and graph representation vectors of different types of nodes. The decoding process is designed as a deep Q network, and the encoded representation vector is decoded into the Q value of deep reinforcement learning. Then, we train the optimal disintegrating strategy based on the computed Q value through deep reinforcement learning. The overall framework is shown in Figure 5.

3.1 Heterogeneous network encoding

First, we encode the current heterogeneous combat network, and we take the removal of nodes as the executive action and the remaining graph after the removal of nodes as the state. An action (remove node) and a state (remaining graph) is represented as a set of representation vectors. These representation vectors capture the structural information, type information and connections between other nodes of this node and are used to efficiently estimate the expected future benefits $Q(s, a)$ of current action for this state.

The key to heterogeneous network encoding is to solve the following two problems:

1) Node heterogeneity. How to design node feature encoding for different nodes with heterogeneous information in heterogeneous networks is a tough problem.

2) Fusion of heterogeneous neighbor feature information representation. It is also a challenge to obtain a comprehensive node representation considering the influence of different node types in aggregating heterogeneous neighbor feature information.

For problem 1), we first encode the heterogeneous features of different types of nodes by using one-hot representation. The length of the vector of one-hot representation is the number of node types, where the corresponding type component is 1 and the rest components are 0. This encoding approach is concise and effective in adding discrete type features to the node feature vector. Secondly, in order to maintain the graph structure information, we add the structural features of the nodes into the node feature vectors, which finally form the node feature vectors.

For problem 2), in the process of aggregating heterogeneous neighbor feature information, we convolve the adjacency matrix and feature matrix of different types of neighbor nodes separately to obtain the representation of each type of neighbor node. Then, we aggregate the representations of different types of neighbors by nonlinear functions. Finally, in order to maintain the neighborhood structure information of different types of nodes, we convolve the aggregated representation matrices

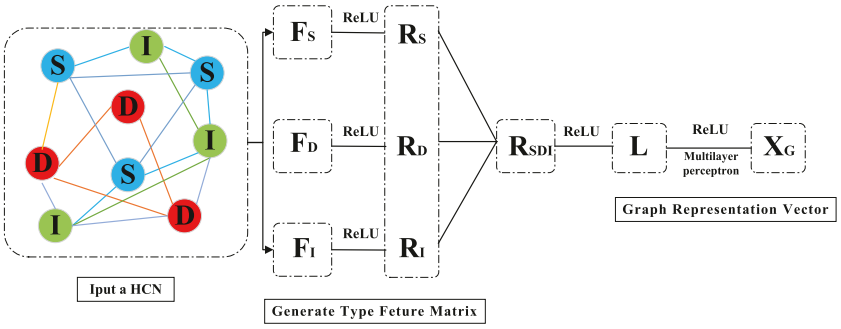

FIGURE 7
Framework of graph representation vector encoding.

with the adjacency matrices to obtain the final representation vector.

3.1.1 Node representation vector

Figure 6 is the overall framework of the node representation vector. Firstly, the type adjacency matrix is calculated respectively according to S, D, and I node types, i.e., A_S, A_D, A_I. Secondly, the feature matrixs of three node types S, D, and I are constructed respectively according to the type features and structural features of nodes:F_S, F_D, F_I. The feature matrix contains the structure information and type information of the node. We convolve the type adjacency matrix with the feature matrix, after that, we take the result of the convolution through the nonlinear activation function. In order to maintain the neighborhood structure information of different types of nodes, the results are convolved with the adjacency matrix again, and finally obtain the node representation vector through the nonlinear activation function, which is the action representation vector X_N in the deep reinforcement learning process. In addition, if the node is weighted, we need to multiply the weight of the node when getting the embedding vector. As shown in Eq. 1.

$$\begin{cases} H_j = \sigma\left[gcn_1\left(A_j, F_j\right)\right], j = S, D, I \\ X_N = \sigma\left[gcn_2\left(A, H_S \| H_D \| H_I\right)\right] \end{cases} \tag{1}$$

Where, A_j, $j = S, D, I$ are the adjacency matrices of nodes of S, D and I, F_j, $j = S, D, I$ are the feature matrix of nodes of S, D and I, σ is the activation function, A is the adjacency matrix of the whole graph, $\|$ is the stitching operation, and X_N is the node representation vector.

3.1.2 Graph representation vector

Figure 7 is the overall framework of the graph representation vector. The graph representation vector represents the current state of the graph and contains heterogeneity information and structure information. We obtain the type feature vector R_j, $j = S, D, I$ by nonlinear aggregation of each of the three type node feature matrices F_j, $j = S, D, I$. After that, we connect the type feature vectors and map them nonlinearly to a latent space to obtain the graph feature vector L. Finally, we let the graph feature vector L through the multilayer perceptron and get the graph representation vector X_G. As shown in Eq. 2.

$$\begin{cases} R_j = \sigma\left(W_j F_j + b_j\right), j = S, D, I \\ L = \sigma\left[W_k \left(R_S \| R_D \| R_L\right)\right] \\ X_G = \sigma\left[W_m \sigma\left(W_n L + b_n\right) + b_m\right] \end{cases} \tag{2}$$

Where, F_j, $j = S, D, I$ is node feature matrix, R_j, $j = S, D, I$ is type feature vector, L is graph feature vector, and X_G is graph representation vector. The algorithm flow of the encoding is shown in Algorithm 1.

Input:
Heterogeneous network: $G = (V, E)$;
Node type adjacency matrix,A_j, $j = S, D, I$;
Node feature matrix,F_j, $j = S, D, I$;
Learning parameters:W_S,W_D,W_I,W_k,W_m,W_n,b_S,b_D,b_I,b_m,b_n;
Output:
Node representation vector, X_N;
Graph representation vector, X_G;
for $i = 1$ *to* 3 ***do***
  Node type adjacency matrix convolve with feature matrix.
  $h_i = \mathrm{Relu}\left(\mathrm{gcn}_1\left(A_i, F_i\right)\right)$
The result convolve with the adjacency matrix.
$X_N = \mathrm{Relu}\left(\mathrm{gcn}_2\left(A, h\right)\right)$
Feature matrix nonlinear mapping.
$R_S = \mathrm{Relu}\left(W_S * F_S + b_S\right)$
$R_D = \mathrm{Relu}\left(W_D * F_D + b_D\right)$
$R_I = \mathrm{Relu}\left(W_I * F_I + b_I\right)$
Connect type feature vectors and nonlinearly mapping.
$R = \mathrm{Relu}\left(W_k * concatenate\left(R_S, R_D, R_I\right)\right)$
multilayer perceptron.
$X_G = \mathrm{Relu}\left(W_m * \mathrm{Relu}\left(W_n R + b_n\right) + b_m\right)$.
return X_N, X_G.

Algorithm 1. Heterogeneous network encoding.

3.2 Heterogeneous network decoding

In the decoding stage, we decode the graph state representation vector X_G and node action representation vector X_N into the value Q in DQN, that is, the mapping of state-action (X_G, X_N) to $Q(X_G, X_N)$. $Q(X_G, X_N)$ can predict the maximum cumulative benefit of the action X_N performed in

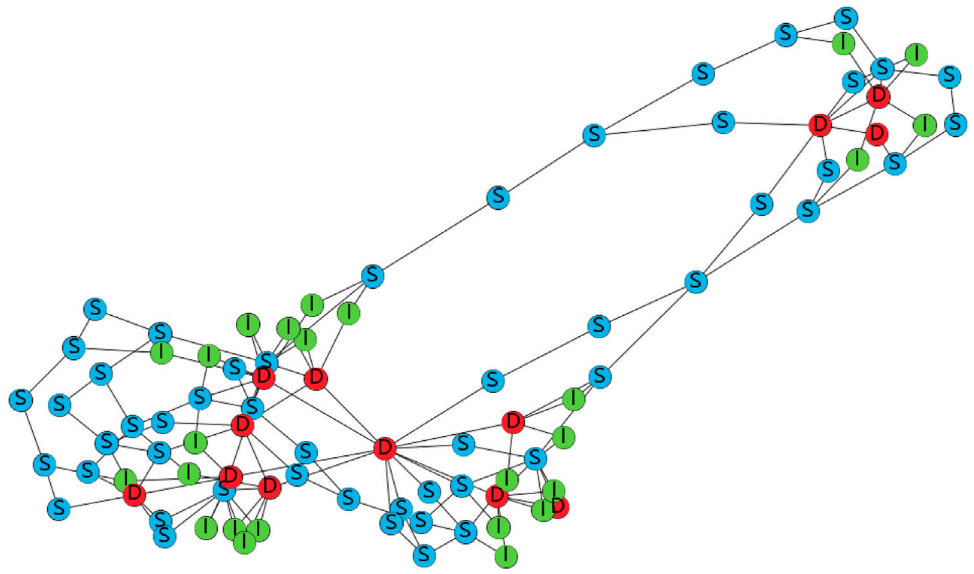

FIGURE 8
Topology diagram of the typical military network: FINC.

the state X_G. We use multilayer perceptrons to parameterize the Q function. More specifically, it is defined as Eq. 3:

$$Q(X_G, X_N) = W_h \sigma\left(X_N^T \cdot X_G \cdot W_i\right) \tag{3}$$

Where,$Q(X_G, X_N)$ is the Q value obtained by decoding, σ is the activation function, X_G is the vector representing graph state, and X_N is the vector representing node action. The algorithm of the decoding is shown in Algorithm 2.

Input:
Heterogeneous network: $G = (V, E)$;
Graph state represent vector,X_G;
Node action represent vector,X_N;
Learning parameters:W_h,W_i.
Output:
Action value, Q.
$X = X_N^T * X_G$
Nonlinear mapping.
$X_Q = \mathrm{Relu}\,(X * W_i)$
$Q = W_h * X_Q$
return Q.

Algorithm 2. Heterogeneous network decoding.

3.3 Heterogeneous network performance evaluation

For heterogeneous networks, the evaluation metrics of homogeneous networks, such as gaint connected component size do not accurately reflect the characteristics of heterogeneous networks. For heterogeneous combat networks, we need to evaluate not only the connectivity of the network but also the operational capability of the network. Therefore, in this paper, based on the "Rescaling Combat Capability Index" in [6], we propose the normalized operational capability index R to evaluate the operational performance of heterogeneous combat networks based on the characteristics of heterogeneous combat networks.

First, we define the combat capabilities of the three types of entities. Since the battlefield environment is dynamic and the performance of various types of weapons and equipment is constantly changing, we believe that the performance of weapons and equipment is closely related to the network structure, and in a complete combat network, each combat entity cooperates with each other and can give full play to the capabilities of each entity. On the contrary, if the combat network is attacked, the capabilities played by the combat entities will be limited accordingly. Therefore, in order to model the combat capabilities of individual entities more realistically and accurately, we define combat capabilities as CA_i, $i = S, D, I$, where i is the entity type. Suppose l_i is a operational chain OC, including sensor entity $S = \{s_j\}$, decision entity $D = \{d_j\}$and influence entity $I = \{i_j\}$ l_i can be calculated as Eq. 4:

$$U(l_j) = \frac{1}{|l_j|} \sum_{s_j \in S} CA_S(s_j) \sum_{d_j \in D} CA_D(d_j) \sum_{i_j \in I} CA_I(i_j) \tag{4}$$

Where, $CA_S(s_j), CA_D(d_j), CA_I(i_j)$ represents the detection ability of the sensor entity, the decision-making ability of the decision entity and the attack ability of the influence entity respectively in the weapon system, and $|l_j|$ represents the length of the operational chain.

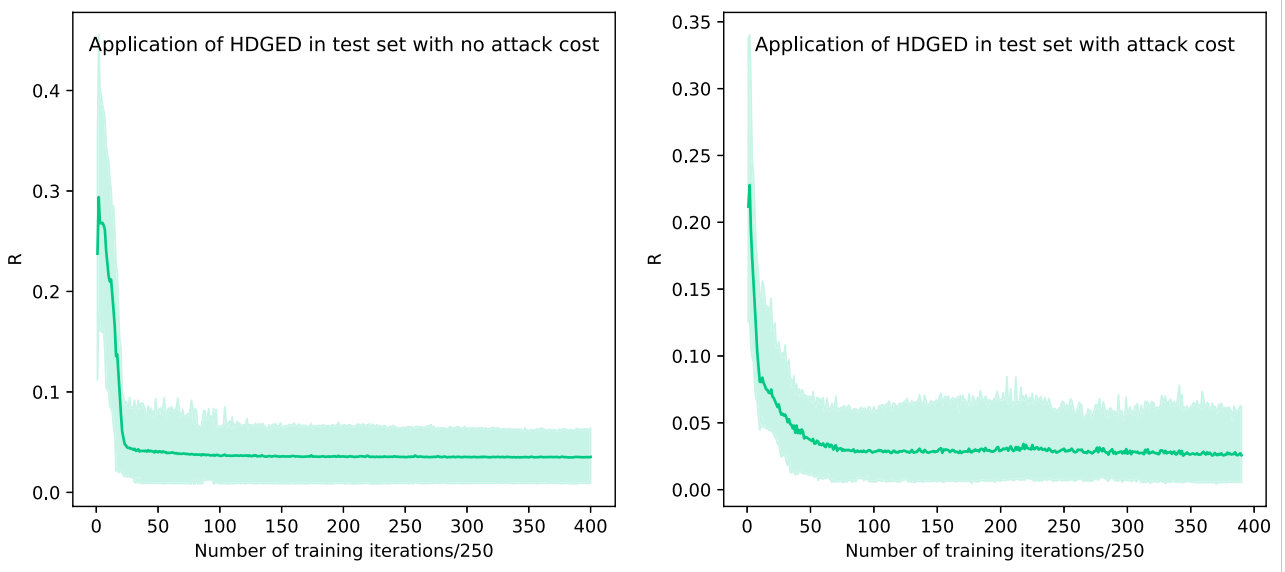

FIGURE 9
The performance of HDGED on the test set under two scenarios as the training progresses. The reward function is represented by the *R* value.

In this paper, we assume that the attacker has complete information about the defender's operational network and the attack is a node attack, if a node is attacked, the edges it is connected to will be removed together. If $\tilde{V} \in V$ denotes the set of nodes attacked and $\tilde{E} \in E$ denotes the set of edages removed, then the network obtained after the node attack is $\tilde{G} = (V - \tilde{V}, E - \tilde{E})$. We define the ratio $f_N = |\tilde{V}|/N \in [0, 1]$ as the attack intensity.

For a heterogeneous combat network G, and a group of operational chains OCs, $L_G = \{l_k\}, \quad k = 1, 2, \ldots, m$, the combat capability can be expressed as Eq. 5:

$$O(G) = \sum U(l_k) \tag{5}$$

Among them, $O(G)$ is the combat capability index known as G. When the node sequence $\tilde{V} = \{v_1, v_2, \ldots, v_j\}$ is removed, we normalize $O(G)$ as shown in Eq. 6 to represent the connectivity performance of the attacked network,

$$P(\tilde{V}) = P(v_1, v_2, \ldots, v_j) = \frac{O(G\backslash\{v_1, v_2, \ldots, v_j\})}{O(G)} \tag{6}$$

One of the key issues related to attack strategies is an evaluation method for attack effectiveness. We used to calculate the mean value R of the combat capability index after being attacked to assess the attack efficiency of the attack strategy on the heterogeneous combat network. We draw on the evaluation method of network robustness and propose a heterogeneous network combat cumulative normalized combat effectiveness as the evaluation index of the strategy. Our goal is to learn an optimal node removal sequence to make the network disintegrates rapidly, i.e., to minimize the R value as shown in Eq. 7:

$$R(v_1, v_2, \ldots, v_N) = \frac{1}{N}\sum_{j=1}^{N} P(\tilde{V}) = \frac{1}{N}\sum_{j=1}^{N} \frac{O(G\backslash\{v_1, v_2, \ldots, v_j\})}{O(G)} \tag{7}$$

Where N is the number of nodes in the G, and $O(G\backslash\{v_1, v_2, \ldots, v_j\})$ is the combat capability index after removing the set of nodes $\{v_1, v_2, \ldots, v_j\}$ from the G.

In some cases, the attack cost (cost of attacking resources, cost of attacking time, etc.,) of different nodes is different. Our formula for defining the weighted R is as Eq. 8:

$$\begin{aligned} R_{cost}(v_1, v_2, \ldots, v_N) &= \frac{1}{N}\sum_{j=1}^{N} P(\tilde{V})c(v_j) \\ &= \sum_{j=1}^{N} \frac{O(G\backslash\{v_1, v_2, \ldots, v_j\})}{O(G)} c(v_j) \end{aligned} \tag{8}$$

Among them, $c(v_k)$ represents the normalized attack cost of the node, $\sum_{j=1}^{N} c(v_j) = 1$.

3.4 Attack strategy learning

After the encoding-decoding is completed, we use the deep Q network algorithm in deep reinforcement learning to find the key nodes in the combat network. We view it as a Markov process: interacting with the environment to produce a series of states,

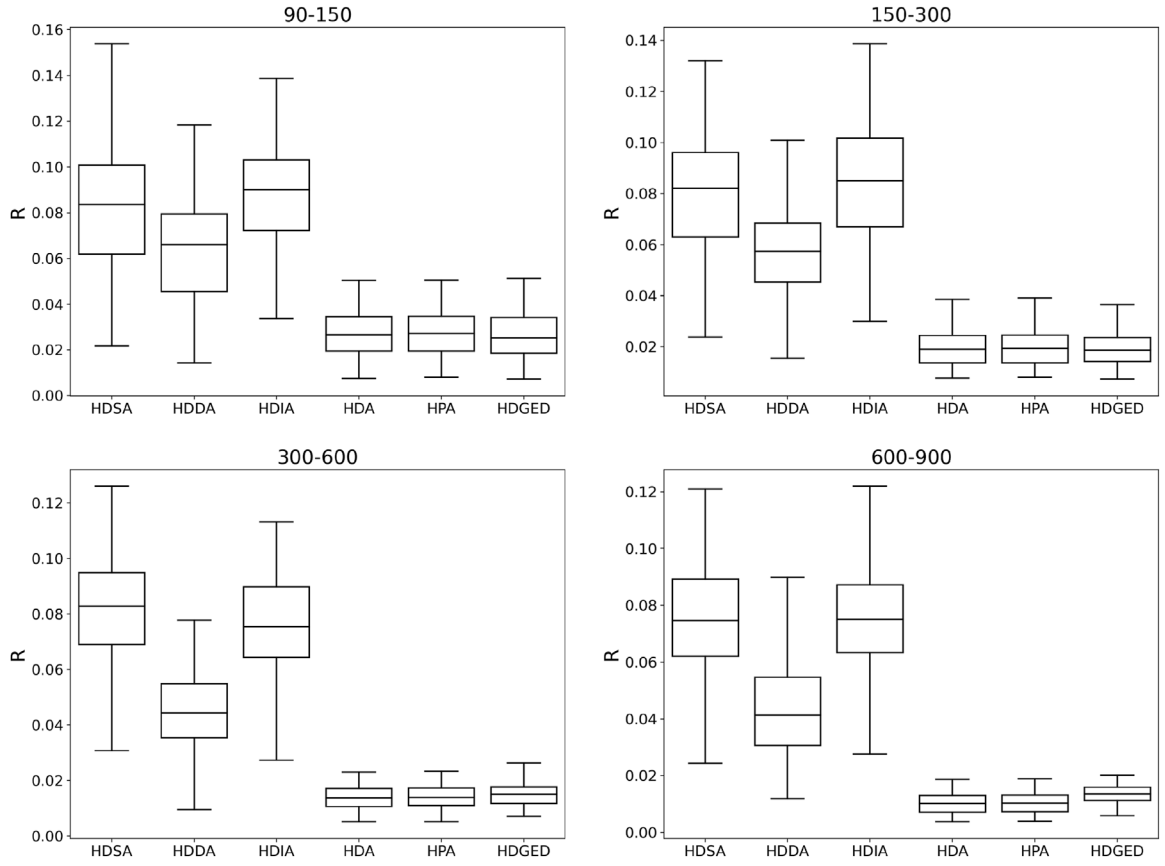

FIGURE 10
Comparison of disintegration capability of HDGED and baseline algorithms on scale-free HCN of four different scales without considering the cost of network attacks.

actions, and rewards. The environment is the input combat network, the state is defined as the remaining network after attacking node, the action is defined as the removal of the critical node under attack, and the reward is defined as the reduction value of the combat network disintegration evaluation index R after taking action.

We decode each vector pair (state, action) into a real Q value, which is used to predict the expected future payoff if this node is selected. Based on the calculated Q value, in the training stage, we adopt the greedy selection strategy ϵ, that is, each time with probability $(1-\epsilon)$ to select the highest Q value of the node, with probability randomly selected node. When a round is over (i.e., the remaining graph become isolated nodes),n transfer tuples are collected, i.e., $(S_i, A_i, R_{(i,i+n)}, S_{(i+n)})$ and $R_{(i,i+n)} = \sum^{i+n} R_k$, into the experience replay pool. At the same time, we update the learning parameters of the encoding process and decoding process through the batch training samples from the experience replay pool. See Algorithm 3 for the algorithm process.

Initialize experience replay pool:D,capacity:M
Initialize Q with random weights Θ.
Initialize the target network $\widehat{Q}$ with $\widehat{\Theta} = \Theta$.
for $episode = 1$ *to* M **do**
  Input $G = (V, E)$.
  Initialize the state $S = ()$.
  for $j = 1$ *to* T **do**
    With probablity ε selet a random action a_t.
    Otherwise select $a_t = \arg\max Q(s_t, a; \Theta)$
    Execute action a_t,observe reward r_t.
    Set $s_{t+1} = s_t, a_t$
    if $t >= n$ **then**
      Store transition $(s_{t-n}, a_{t-n}, r_{t-n,t}, s_t)$ in D.
      Sample random minibatch of transitions $(s_j, a_j, r_{j,j+n}, s_{j+n})$ from D.
      if s_{j+n} *is terminal* **then**
        $y_j = r_{j,j+n}$
      else $y_j = r_{j,j+n} + \gamma \max Q(s_{j+n}, a; \Theta)$
      Perform a gradient descent step to update parameters Θ.
      Every C steps,reset$\widehat{\Theta} = \Theta$.
    end if
  end for
end for

Algorithm 3. DQN training.

We require the embedded vectors can thoroughly learn both the heterogeneous information of the network and make full use of the structural information of the network. Therefore, we design the training loss function as Eq. 9.

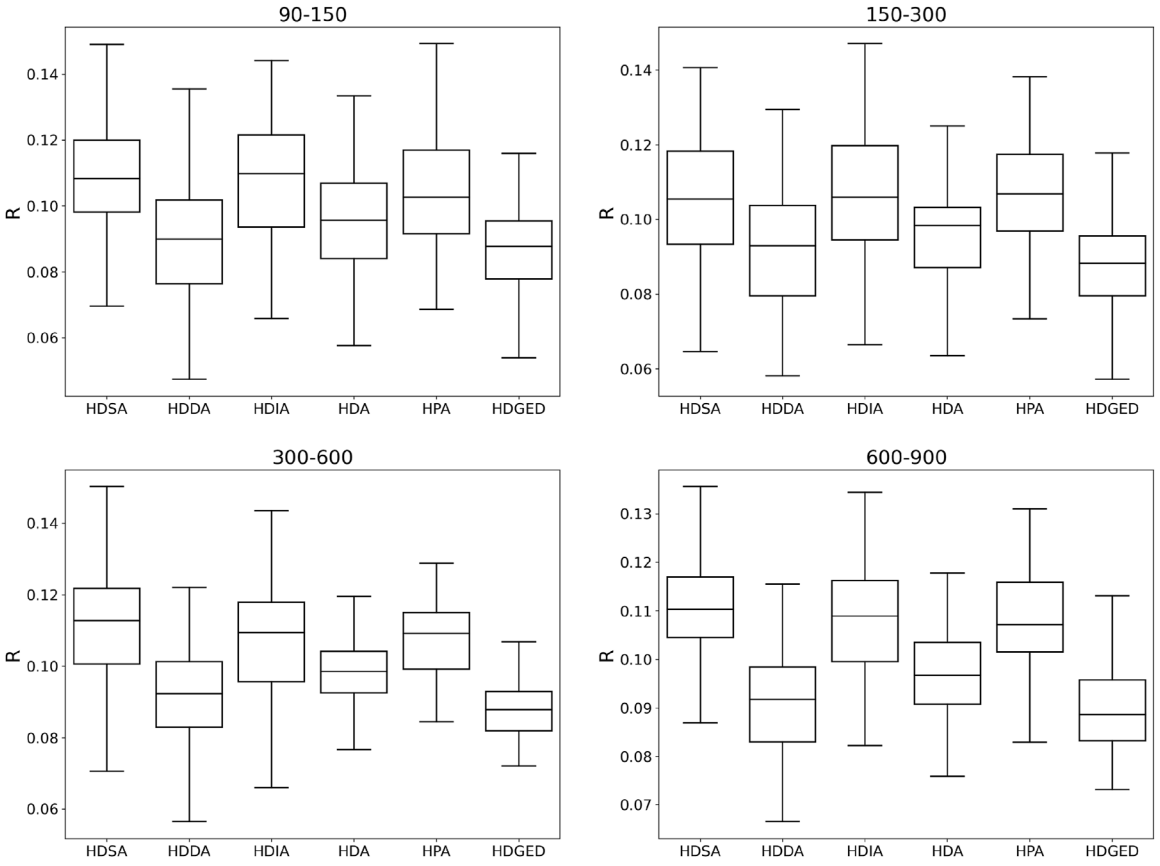

FIGURE 11
Comparison of disintegration capability of HDGED and baseline algorithms on small world HCN of four different scales without considering the cost of network attacks.

$$\begin{cases} L = L_Q + \alpha L_G \\ L_Q = \left(r_{t,t+n} + \gamma \max \hat{Q}(s_{t+n}, \hat{a}) - Q(s_t, a_t)\right)^2 \\ L_G = \sum_{i,j}^{N} s_{i,j} \left\| x_i - x_j \right\|_2^2 \end{cases} \tag{9}$$

Where, L_Q is Q learning loss, $r_{t,t+n}$ is the reward after n steps, $Q(s_t, a_t)$ is the predicted value of Q, L_Q is graph reconstruction loss, and α is weight coefficient.

4 Experimental comparison and analysis

4.1 Experimental setting

Based on the characteristics of military operations, 200 scale-free Heterogeneous Combat Networks (HCNs) of 20–50 nodes are synthesized as training set, where the synthesized networks are generated using the Barabási-Albert (BA) model (Barabási and Albert, 1999). Among them, 100 networks have no weights for nodes, and the nodes of the other 100 networks are randomly assigned weights which represents the attack cost of the nodes. The two groups are trained and applied separately. In order to test the disintegration effect of the algorithm on HCNs of different sizes and the migration ability of the algorithm on different networks, we generated two types of networks as test sets, i.e. scale-free network and small-world network. Four different scales were generated for each type of network, the number of nodes was 90–150, 150–300, 300–600 and 600–900, and 100 networks were randomly generated for each scale, and then evaluate the average performance of the algorithm on these 100 networks. And experiments were carried out on the typical military network, FINC, which is from the paper "An efficient link prediction index for complex military organization" published by [31]. It contains 89 combat entities, including 12 Decider entities (D), 26 Influential entities (I) and 51 Sensor entities (S), and 150 communication links linking the entire military network. The topology of the military network is shown in

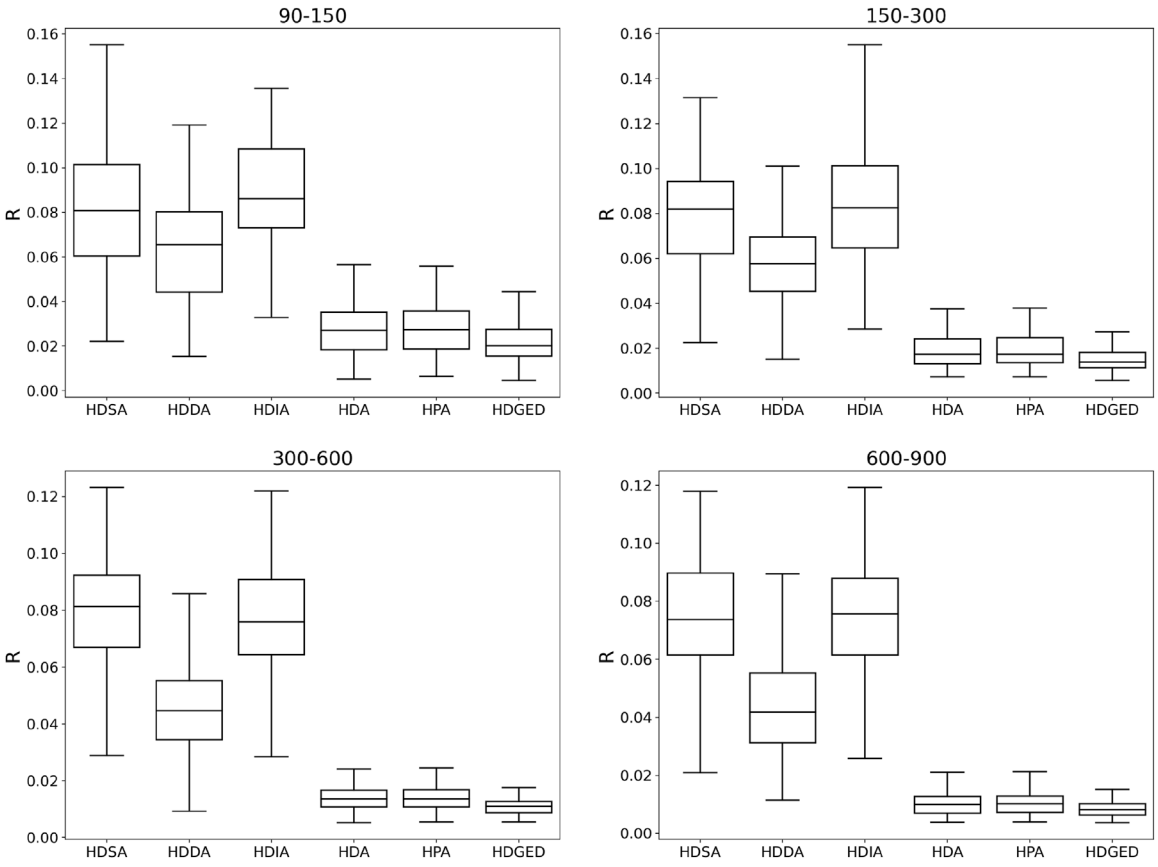

FIGURE 12
Comparison of disintegration capability of HDGED and baseline algorithms on scale-free HCN of four different scales with considering the cost of network attacks.

Figure 8, where the red nodes represent Decider entities (D), the green nodes represent Sensor entities (S), and the yellow nodes represent Influential entities (I). Depending on the information flow on the HCN, the edges of the HCN are classified into five types, including $S-S$, $S-D$, $D-D$, $D-I$, and $I-S$. We set the initial combat capability of each entity to be the same, and CA_S, CA_D and CA_I are both set to 2.

As for the baseline algorithms, considering that there are relatively few researches on disintegration for heterogeneous operational networks, and we evolve some existing attack strategies against homogeneous networks so that they become baseline strategies applicable to heterogeneous operational networks. These include strategies that attack only a single type of node: HDSA (high-degree sensor node adaptive), HDDA (high-degree decision node adaptive) and HDIA (high-degree influential node adaptive). HDA (high degree adaptive) and HPA (high PageRank adaptive) are strategies that rank the networks according to their degree attributes and PageRank attributes.

4.2 Experimental results and analysis

During the training phase, the parameters were stored for every 250 iterations. The value of the loss function gradually tends to be stable as the training progress. We load the parameters recorded every 250 iterations into the HDGED, and then applied HDGED on a test set contains 200 different networks with 60–90 nodes. The R value of each network disintegration during testing is calculated and averaged, which can be regarded as the performance of HDGED. For validation the convergence of the learning process, the results of the reward function obtained each time are drawn into a curve as shown in Figure 9. It can be found that with the progress of training, the average R value obtained by HDGED on the test set became lower and lower until it is stable. This phenomenon shows that the effect of HDGED is getting better and better. Subsequently, we apply the algorithm to other various scenarios as follows.

In Figures 10, 11, we show the HDGED and four baseline algorithms on four scale-free HCNs and small worlds, respectively, without considering the attack cost. Compared with the average

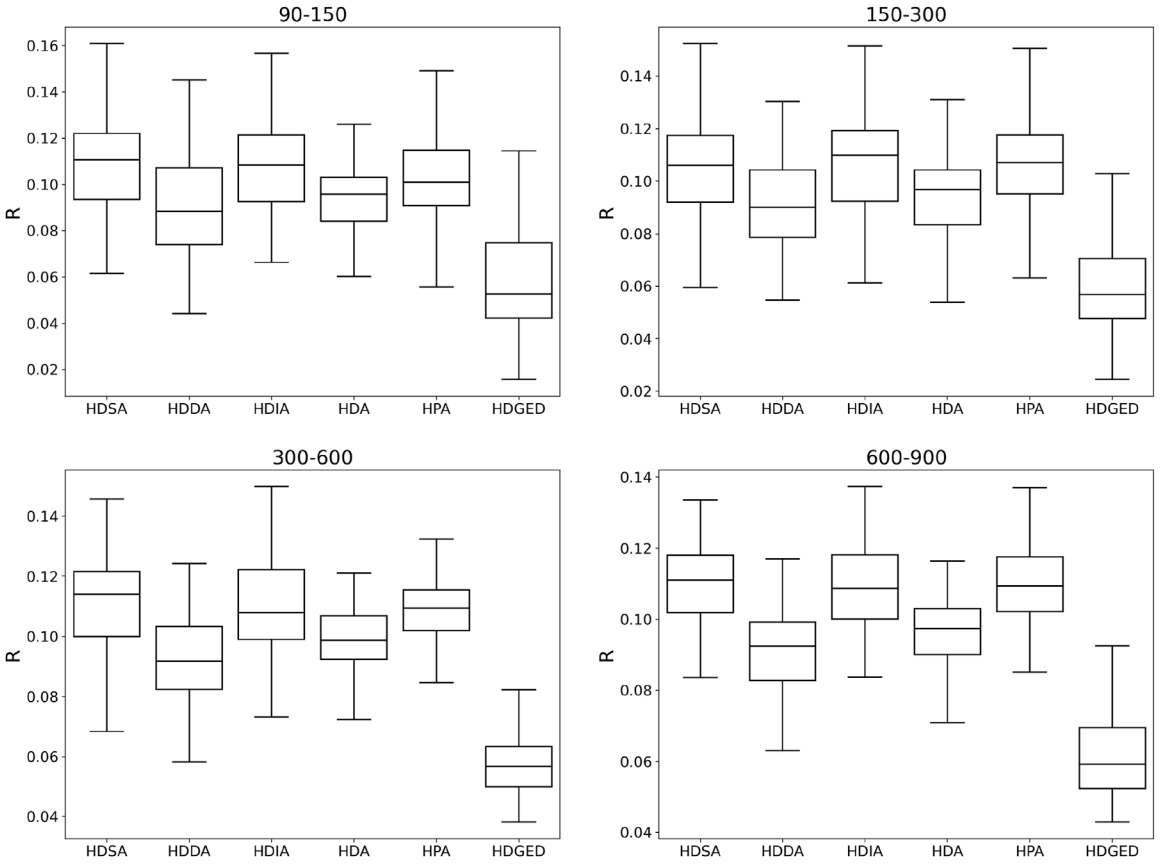

FIGURE 13
Comparison of disintegration capability of HDGED and baseline algorithms on small world HCN of four different scales with considering the cost of network attacks.

effect on HCN, it can be seen that our method has the smallest R value and the smallest variance, and achieves the effect of SOTA on two types of four different scale networks.

In Figures 12, 13, we show the HDGED algorithm and four baseline algorithms on four scale-free HCNs and small-world HCNs, respectively, considering the attack cost. Compared with the average effect on the above, the attack cost here is obtained by random assignment. It can be seen that our method has achieved SOTA in various scenarios.

In order to further verify the algorithm, we conducted experiments on the real military network FINC, as shown in Figure 14, respectively showing the cases where the attack cost is not considered and the attack cost is randomly assigned (node weights are random) effects of the following methods. The X-axis is the attack strength (f_N), and the Y-axis is the normalized combat capability index $P(\tilde{V})$. In the initial stage of decomposition, the curve of the HDGED algorithm declines the fastest, and the curve of the HDSA algorithm declines the slowest. It can be seen that the HDGED decomposition efficiency is the highest. The area enclosed by each curve is the R value of the algorithm. The smaller the area, the better the performance of the algorithm. The results show that under the same conditions, the HDGED algorithm achieves the SOTA effect and has higher decomposition efficiency.

Figure 15 shows the disintegration results of the HDGED algorithm and HDA algorithm on a scale-free heterogeneous combat network of size 97. We can see that the HDGED algorithm finds the critical nodes in the combat network that affect the combat capability and disintegrates them. The results show that the HDGED algorithm disintegrates the network combat capability to 0 after attacking 13 nodes. However, the network structure is heavily damaged after HDA attacks 13 nodes, but the network still has combat capability. Analyzing the reason, the decision nodes in the heterogeneous combat network have more influence on the combat capability of the network than the sensor nodes and the influence nodes, so the HDGED algorithm first disintegrates the decision nodes in the heterogeneous combat network. On the other hand, the HDA algorithm

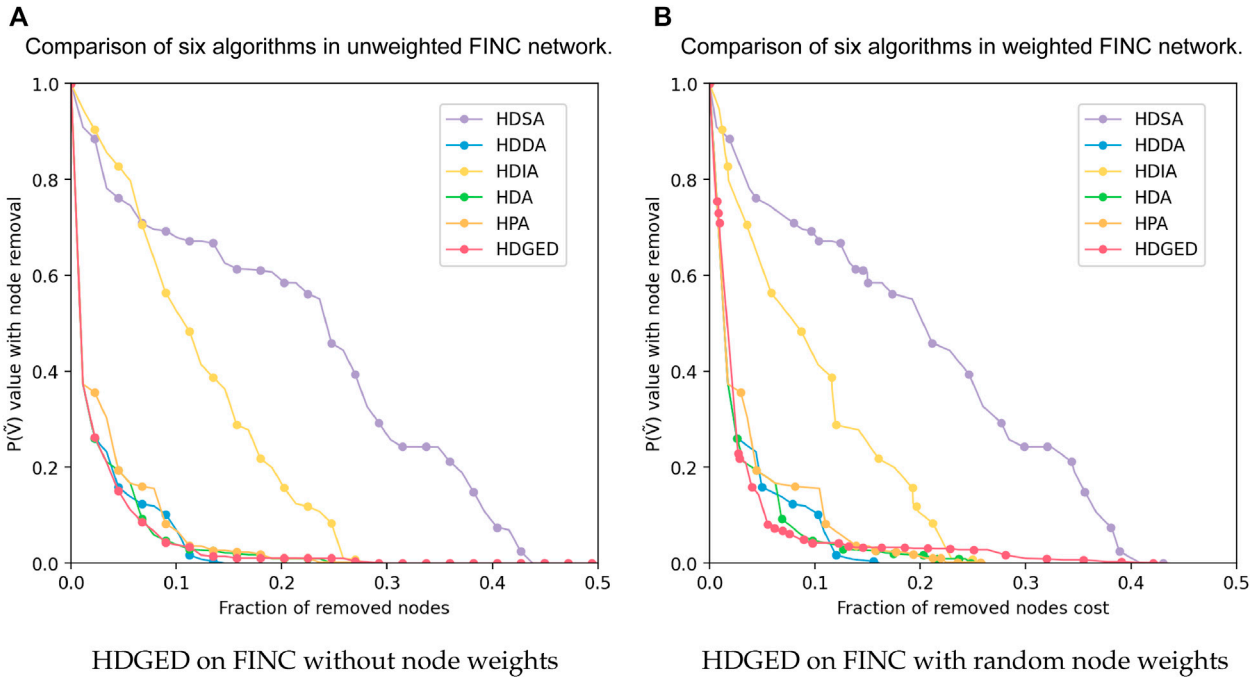

FIGURE 14
The performance of HDGED on the FINC military network without considering the attack cost and considering the attack cost. It can be seen that with the removal of nodes, the network performance gradually decreases. **(A, B)** Shows specifically the degradation of the operational performance of the FINC network when facing HDGED and other baseline strategies.

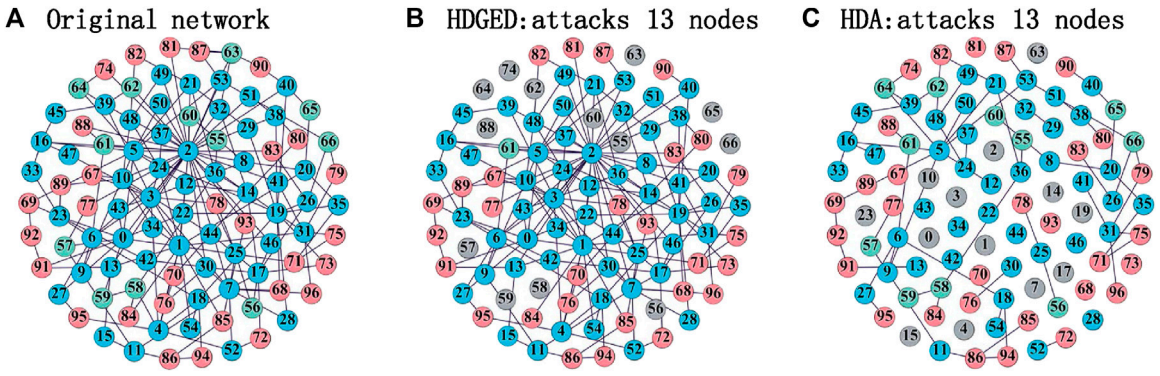

FIGURE 15
Comparison of disintegration capability of HDGED and HDA on a scale-free HCN of scale 97. **(A)** is the HCN of scale 97, in which the blue node is the sensor entity, the green node is the decision entity, the red node is the influence entity, the numbers of the three of them are 55, 12, and 30, respectively. **(B)** shows the result after HDGED attacks the 13 nodes in the original network, and the gray node is the attacked entity, $P(\bar{V}) = 0$. **(C)** shows the result after HDA attacks the 13 nodes in the original network, $P(\bar{V}) = 0.63$.

attacks according to the node degree ranking and does not consider the influence of nodes on the combat capability, so the disintegration efficiency is lower than HDGED.

5 Conclusion

Research on the disintegration of heterogeneous networks such as terrorist networks, disease transmission networks, and military combat networks is of great significance in the real world. However, the current network disintegration strategies are limited to homogeneous networks and cannot be directly applied to heterogeneous networks. Therefore, this paper takes the heterogeneous combat network as the research object to study the heterogeneous network disintegration strategy, and the main contributions are as follows.

Firstly, this paper presents a optimal disintegration strategy of heterogeneous combat networks based on the combination of graph embedding and deep reinforcement learning. Through training, our proposed HDGED algorithm can fully exploit the heterogeneous and structural information of the heterogeneous network and quickly find the critical nodes affecting the network function.

Secondly, our approach can be extended to heterogeneous combat networks of different scales. We have conducted comparative experiments on heterogeneous combat networks of different scales. And experiments were carried out on the FINC network. Our method is able to maintain stable disintegration effects for heterogeneous combat networks of different sizes, and its disintegration effects are all better than the baseline algorithm.

Thirdly, our method has good mobility for heterogeneous combat networks with uneven combat capabilities. Through extensive training for combat networks with uneven combat capabilities, our method can discover the critical nodes that affect the global network combat capabilities without getting caught in a few localized nodes with extensive individual combat capabilities, thus maintaining a stable disintegration effect.

Fourthly, we design the normalized operational capability index to more accurately assess the connectivity and operational capability of the dynamically changing heterogeneous combat network.

Finally, the research in this paper fills the gap in the study of heterogeneous network disintegration, which has some significance for exploring general heterogeneous network disintegration and has necessary guidance for the future intelligent combat. In the future, we will further study the disintegration of HCNs under incomplete information conditions.

Data availability statement

The raw data supporting the conclusion of this article will be made available by the authors, without undue reservation.

Author contributions

All authors contributed to the study conception and design. Material preparation, data collection and analysis were performed by LC, CZ, and HL. The first draft of the manuscript was written by CW and checked by LW and JC. All authors commented on previous versions of the manuscript. All authors read and approved the final manuscript.

Funding

This work is supported by National Natural Science Foundation (NNSF) of China under Grant 62173336; Scientific Research Plan of National University of Defense Technology under Grant No. ZK-20-38; Postgraduate Research and Innovation Project of Hunan Province under Grant CX20210085.

Conflict of interest

The authors declare that the research was conducted in the absence of any commercial or financial relationships that could be construed as a potential conflict of interest.

Publisher's note

All claims expressed in this article are solely those of the authors and do not necessarily represent those of their affiliated organizations, or those of the publisher, the editors and the reviewers. Any product that may be evaluated in this article, or claim that may be made by its manufacturer, is not guaranteed or endorsed by the publisher.

References

1. Yasunaga M, Kasai J, Zhang R, Fabbri AR, Li I, Friedman D, et al. Scisummnet: A large annotated corpus and content-impact models for scientific paper summarization with citation networks. In: *Proceedings of the thirty-third AAAI conference on artificial intelligence and thirty-first innovative applications of artificial intelligence conference and ninth AAAI symposium on educational advances in artificial intelligence*. Honolulu, HI: AAAI Press (2019). AAAI'19/IAAI'19/EAAI'19. doi:10.1609/aaai.v33i01.33017386

2. Tajeuna EG, Bouguessa M, Wang S. Modeling and predicting community structure changes in time-evolving social networks. *IEEE Trans Knowl Data Eng* (2019) 31:1166–80. doi:10.1109/TKDE.2018.2851586

3. Shi C, Hu B, Zhao WX, Yu PS. Heterogeneous information network embedding for recommendation. *IEEE Trans Knowl Data Eng* (2019) 31:357–70. doi:10.1109/TKDE.2018.2833443

4. Hou S, Ye Y, Song Y, Abdulhayoglu M. Hindroid: An intelligent android malware detection system based on structured heterogeneous information network. In: *Proceedings of the 23rd ACM SIGKDD international conference on knowledge discovery and data mining*. New York, NY, USA: Association for Computing Machinery (2017). p. 1507–15. KDD '17. doi:10.1145/3097983.3098026

5. Shi Y, Lei M, Yang H, Niu L. Diffusion network embedding. *Pattern Recognit DAGM* (2019) 88:518–31. doi:10.1016/j.patcog.2018.12.004

6. Li X, Kao B, Ren Z, Yin D. Spectral clustering in heterogeneous information networks. In: *Proceedings of the thirty-third AAAI conference on artificial intelligence and thirty-first innovative applications of artificial intelligence conference and ninth AAAI symposium on educational advances in artificial intelligence*. Honolulu, HI: AAAI Press (2019). AAAI'19/IAAI'19/EAAI'19. doi:10.1609/aaai.v33i01.33014221

7. Yang Y, Lichtenwalter RN, Chawla NV. Evaluating link prediction methods. *Knowl Inf Syst* (2015) 45:751–82. doi:10.1007/s10115-014-0789-0

8. Arulselvan A, Commander CW, Elefteriadou L, Pardalos PM. Detecting critical nodes in sparse graphs. *Comput Oper Res* (2009) 36:2193–200. doi:10.1016/j.cor.2008.08.016

9. Pastor-Satorras R, Vespignani A. Epidemic spreading in scale-free networks. *Phys Rev Lett* (2001) 86:3200–3. doi:10.1103/PhysRevLett.86.3200

10. Morone F, Makse HA. Influence maximization in complex networks through optimal percolation. *Nature* (2015) 524:65–8. doi:10.1038/nature14604

11. Braunstein A, Dall'Asta L, Semerjian G, Zdeborová L. Network dismantling. *Proc Natl Acad Sci U S A* (2016) 113:12368–73. doi:10.1073/pnas.1605083113

12. Mugisha S, Zhou H-J. Identifying optimal targets of network attack by belief propagation. *Phys Rev E* (2016) 94:012305. doi:10.1103/PhysRevE.94.012305

13. Zdeborová L, Zhang P, Zhou H-J. Fast and simple decycling and dismantling of networks. *Sci Rep* (2016) 6:37954–6. doi:10.1038/srep37954

14. Hagen L, Kahng A. New spectral methods for ratio cut partitioning and clustering. *IEEE Trans Comput -Aided Des Integr Circuits Syst* (1992) 11:1074–85. doi:10.1109/43.159993

15. Ren X-L, Gleinig N, Helbing D, Antulov-Fantulin N. Generalized network dismantling. *Proc Natl Acad Sci U S A* (2019) 116:6554–9. doi:10.1073/pnas.1806108116

16. Deng Y, Wu J, Tan Y-J. Optimal attack strategy of complex networks based on tabu search. *Physica A: Stat Mech its Appl* (2016) 442:74–81. doi:10.1016/j.physa.2015.08.043

17. Wang X, Bo D, Shi C, Fan S, Ye Y, Philip SY. A survey on heterogeneous graph embedding: Methods, techniques, applications and sources. *IEEE Trans Big Data* (2022) 1. doi:10.1109/tbdata.2022.3177455

18. Xie Y, Yu B, Lv S, Zhang C, Wang G, Gong M. A survey on heterogeneous network representation learning. *Pattern Recognition* (2021) 116:107936. doi:10.1016/j.patcog.2021.107936

19. Zhang Z, Cui P, Zhu W. Deep learning on graphs: A survey. *IEEE Trans Knowl Data Eng* (2020) 34:249–70. doi:10.1109/tkde.2020.2981333

20. Wang H, Zhang F, Hou M, Xie X, Guo M, Liu Q. Shine: Signed heterogeneous information network embedding for sentiment link prediction. In: *Wsdm 2018*. Marina Del Rey, CA, USA (ACM) (2018). February 5–9, 2018.

21. Hu B, Fang Y, Shi C. Adversarial learning on heterogeneous information networks. In: *Proceedings of the 25th ACM SIGKDD international conference on knowledge discovery & data mining*. New York, NY, USA: Association for Computing Machinery (2019). p. 120–9. KDD '19. doi:10.1145/3292500.3330970

22. Qu M, Tang J, Han J. Curriculum learning for heterogeneous star network embedding via deep reinforcement learning. In: *Proceedings of the eleventh ACM international conference on web search and data mining*. New York, NY, USA: Association for Computing Machinery (2018). p. 468–76. WSDM '18. doi:10.1145/3159652.3159711

23. Dai H, Dai B, Song L. Discriminative embeddings of latent variable models for structured data. In: *Proceedings of the 33rd international conference on international conference on machine learning* - (2016) 48:2702–11. (JMLR.org), ICML'16.

24. Kipf TN, Welling M. *Semi-supervised classification with graph convolutional networks* (2016). arXiv preprint arXiv:1609.02907.

25. Hamilton WL, Ying R, Leskovec J. Inductive representation learning on large graphs. In: *Proceedings of the 31st international conference on neural information processing systems*. Red Hook, NY, USA: Curran Associates Inc. (2017). p. 1025–35. NIPS'17.

26. Veličković P, Cucurull G, Casanova A, Romero A, Liò P, Bengio Y. Graph attention networks. In: *Proceedings of the 6th international conference on learning representations* (2018).

27. Xu K, Hu W, Leskovec J, Jegelka S. How powerful are graph neural networks? In: *Proceedings of the 7th international conference on learning representations* (2019).

28. Grassia M, De Domenico M, Mangioni G. Machine learning dismantling and early-warning signals of disintegration in complex systems. *Nat Commun* (2021) 12:5190–10. doi:10.1038/s41467-021-25485-8

29. Fan C, Zeng L, Sun Y, Liu Y-Y. Finding key players in complex networks through deep reinforcement learning. *Nat Mach Intell* (2020) 2:317–24. doi:10.1038/s42256-020-0177-2

30. Dekker AH. Measuring the agility of networked military forces. *J Battlefield Technology* (2006) 9:19–24. doi:10.3316/informit.111183921111700

31. Fan C, Liu Z, Lu X, Xiu B, Chen Q. An efficient link prediction index for complex military organization. *Physica A: Stat Mech its Appl* (2017) 469:572–87. doi:10.1016/j.physa.2016.11.097

frontiers | Frontiers in Physics

TYPE Original Research
PUBLISHED 09 November 2022
DOI 10.3389/fphy.2022.1017218

OPEN ACCESS

EDITED BY
Cong Li,
Fudan University, China

REVIEWED BY
Xiao-Peng Zhang,
Nanjing University, China
Peng Ji,
Fudan University, China

*CORRESPONDENCE
DaoGuang Wang,
xznuwang@jsnu.edu.cn

SPECIALTY SECTION
This article was submitted to Interdisciplinary Physics, a section of the journal Frontiers in Physics

RECEIVED 11 August 2022
ACCEPTED 28 October 2022
PUBLISHED 09 November 2022

CITATION
Wang D, Wang Y, Lü H, Wu Z and Liang X (2022), Resembling the bottleneck effect in p53 core network including the dephosphorylation of ATM by Wip1: A computational study.
Front. Phys. 10:1017218.
doi: 10.3389/fphy.2022.1017218

Resembling the bottleneck effect in p53 core network including the dephosphorylation of ATM by Wip1: A computational study

DaoGuang Wang[1]*, Yaolai Wang[2], Huaping Lü[1], Zhangqi Wu[1] and Xiaoming Liang[1]

[1]School of Physics and Electronic Engineering, Jiangsu Normal University, Xuzhou, China, [2]School of Science, Jiangnan University, Wuxi, China

As one of the key proteins, wild-type p53 can inhibit the tumor development and regulate the cell fate. Thus, the study on p53 and its related kinetics has important physiological significance. Previous experiments have shown that wild-type p53-transcribed phosphatase one protein Wip1 can maintain the continuous oscillation of the p53 network through post-translational modification. However, the relevant details are still unclear. Based on our previous p53 network model, this paper focuses on the modification of Wip1 dephosphorylated ataxia telangiectasia mutant protein ATM. Firstly, the characteristics and mechanism of p53 network oscillation under different numbers of DNA double strand damage were clarified. Then, the influence of ATM dephosphorylation by Wip1 on network dynamics and its causes are investigated, including the regulation of network dynamics transition by the mutual antagonism between ATM dephosphorylation and autophosphorylation, as well as the precise regulation of oscillation by ATM-p53-Wip1 negative feedback loop. Finally, the cooperative process between the dephosphorylation of ATM and the degradation of Mdm2 in the nucleus was investigated. The above results show that Wip1 interacts with other components in p53 protein network to form a multiple coupled positive and negative feedback loop. And this complex structure provides great feasibility in maintaining stable oscillation. What's more, for the state of oscillation, the bottleneck like effect will arise, especially under a certain coupled model with two or more competitive negative feedback loops. The above results may provide some theoretical basis for tumor inhibition by artificially regulating the dynamics of p53.

KEYWORDS

network, oscillation, feedback loop, kinetics, p53, bottleneck effect, protein

1 Introduction

As the basic unit of life, cells can regulate their own behavior to adapt to intra- and extracellular stress signals, depending on the protein interaction networks [1]. The p53 signaling network, with protein p53 at its core, is one of the key components of the cell, being a popular research topic in physiology for the last 4 decades [2–4]. Studies have shown that p53 is strongly associated with many types of cancer, such as liver, lung, breast, stomach, colon and prostate cancers [4–6]. To mitigate threatens from these troubles, there is an urgent need to improve the understanding of p53. In resting state, the E3 ubiquitin ligase Murine Double Minute 2 (Mdm2) can promote rapid degradation of p53, resulting in low p53 expression levels [7]. Under stressful conditions, such as ionizing radiation, UV irradiation, drug induction or metabolic stress, p53 is activated and maintained at high levels [8–11]. As a multifunctional transcription factor, p53 can induce the expression of various downstream proteins involved in the cell cycle, metabolism or apoptosis [12, 13]. In particular, for cell fate decision, p53 dynamics are showing great effect in different environments [14–16]. Studies have shown that pulsed oscillations in the p53 network are widespread [17, 18], determining the survival probability of cell, and it needs to be studied in detail. Therefore, the generation and maintenance of stable oscillations deserves further investigation. What's more, the related process in oscillation like gene transcription and protein post-translational modifications, which can form coupled multi-feedback loops, still needs to be investigated. In this paper, we focus on the phosphorylation and dephosphorylation of the ataxia-telangiectasia mutated protein (ATM) at site of Ser1981 [19, 20] and provide insight into the dynamics of the associated p53 signaling network.

Induced by ionizing radiation or drugs, undamped periodic oscillations in single cells or cell populations are the typical feature of protein p53, in which the radiation doses are correlated with the number of oscillatory pulses [21, 22]. For this phenomenon, many theoretical models have been established, which are based on the p53-Mdm2 negative feedback loop [22] (NFL). For example, the model designed by [23], including the p53-Mdm2 NFL as the main structure, has investigated the global stability of p53 network. Based on the NFL of p53-Mdm2, some models considered multiple NFLs, such as the models in Refs. [18, 24], which added the NFL of p53-Wip1-ATM to investigate the stable, oscillations and biorhythms in the signaling transduction network; the Yang's model [25], which examined the phosphorylation of the Ser395 site of Mdm2, analyzed the coupled positive feedback loop (PFL) and NFL of p53-Mdm2 and related kinetics; the Ouattara's model [26], which distinguished the nucleus and cytoplasm of p53, found the amplitude and height of p53 were variable, while the peak width and period were less affected by noise. In addition to these deterministic models, stochastic kinetic models have also been widely used, e.g., the model constructed by Ma et al. [27] includes differential equations and stochastic repair processes to reproduce the pulsing release behavior of p53; the model by Xia and Jia [28] includes a p53 oscillation module and a DNA repair module, successfully explained the possible mechanism of ion radiation dose regulation of the p53 pulse number. Another stochastic model [29] introduced the τ-leap algorithm to reproduce the response details of the p53 protein network and discusses the effects of intra/extracellular noise and cellular variability on the stability of oscillations. These models provided a comprehensive analysis of p53-related dynamics and yield important results. However, some details of the network still need to be investigated in depth, e.g., how to regulate the single feedback loop, coupled positive and negative feedback loops [30–33] or coupled double NFLs within the structure of co-existence of multiple feedback loops.

In order to answer these questions, this paper takes the phosphorylation and dephosphorylation processes of ATM as a starting point, and investigates the changes of p53 network dynamics. Basing on a simple p53 network structure, the kinetic equations of the model are given. Then, through numerical analysis, the relationship between the network system and the degree of damage and other parameters is found, and the bifurcation point and the state characteristics of the system are clarified; together with the bifurcation curve, the oscillation region on the two-parameter bifurcation diagram can be determined. Numerical analysis showed that the different response patterns of the cells under UV and IR radiation were closely related to the strength of the positive feedbacks and negative feedbacks [34] on ATM, indicating that dephosphorylation of Wip1 is a critical part of the network and its presence increases the regulatory pathway. The computational results show that the negative feedback of p53-Mdm2 is fundamental to the oscillations of the p53 network, while other feedbacks have a regulatory effect on the p53 oscillations and can maintain the stability of the oscillations. In conclusion, the model demonstrates that the p53 oscillations occur as a result of the coupling and compromise between NFL and PFL/NFL in close proximity to each other. In contrast to the conclusions of other models, we believe that the antagonistic strengths acting on different components of the same loop need to be of the same magnitude, and the strengths of the coupled positive and negative feedbacks in different loops need to be matched, and the formation of a competitive relationship between the coupled double negative feedbacks needs to be coordinated.

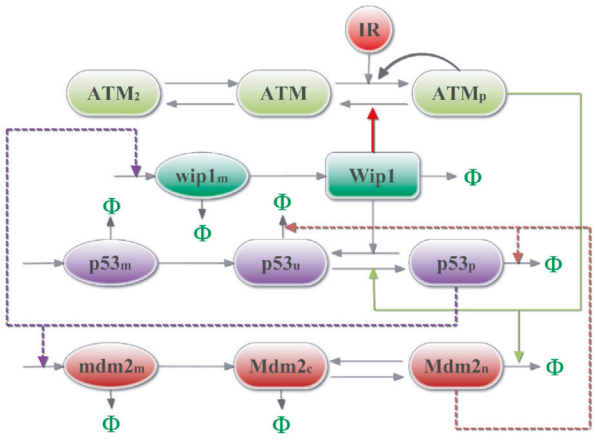

FIGURE 1
Schematic diagram of the p53 protein network model. After irradiation, DNA damage activates ATM, which can phosphorylate and accelerate the degradation of nuclear Mdm2, thereby stabilizing and activating p53 phosphorylation. Then, p53 will induce the production of Mdm2 and Wip1, while Wip1 can dephosphorylate ATM and p53 in turn. The symbol Φ represents the degradation process.

2 Model and methods

2.1 Model

2.1.1 The p53 core network model

Based on previous studies [15, 16, 24, 29], we constructed a simplified model containing the core components associated with p53 oscillations, as shown in Figure 1. The model takes into account the action of ionizing radiation (IR) or DNA damage agents [35] (e.g., etoposide). The DNA double strand break (DSB) occurs and DNA repair proteins are then recruited to repair the damage. At the same time, rapid autophosphorylation of ATM is induced in cells [36], causing the conversion of ATM dimers (ATM_2) into active phosphorylated ATM monomers (ATM_p) [36, 37]. ATM_p further phosphorylates p53 and Mdm2, accelerates the degradation of nuclear Mdm2, and enhances the stability and transcriptional activity of p53 [37]. In non-stressed cells, p53 remains at a low level due to the negative regulation of the E3 ubiquitin ligase Mdm2. However, the p53 protein concentration can be maintained at high levels at this time. Phosphorylation of p53 ($p53_p$) induces the production of Mdm2 and Wip1 [19], while Wip1 dephosphorylates p53 and ATM_p. In the abstract, there are two negative feedbacks and one positive feedback in the model. Practical experiments have shown that p53 oscillations can last for a long time [23]. Considering that DNA damage repair may be defective in some cells, the repair process is not added to the model and the initial number of DNA damages is used as input.

2.1.2 Deterministic equations

The dynamics of the model is described by a system of ordinary differential equations (ODES). The kinetic equations for ATM activation are as follows.

$$\frac{d[ATM_2]}{dt} = k_{dim} \cdot [ATM]^2 - k_{udim} \cdot [ATM_2], \tag{1}$$

$$\begin{aligned}\frac{d[ATM_p]}{dt} = {} & k_{basal} \cdot H^+([ATM], j_{atms}) - k_{deatm} \\ & \cdot H^+([ATM_p], j_{deatm}) + k_{acatm} \cdot [ATM_p] \\ & \cdot \frac{N_{dsb}}{N_{dsb} + j_{dsb}} \cdot H^+([ATM], j_{acatm}) - k_{deatmwip} \\ & \cdot [Wip1] \cdot H^+([ATM_p], j_{deatmwip}).\end{aligned} \tag{2}$$

Where, [−] represents the concentration of the component, the function $H^+(A,B)$ is defined as A/(A+ B). It has been shown that the total amount of ATM does not change much after IR [19], so $[ATM]_{tot} = [ATM] + [ATM_p] + 2[ATM_2]$ is a constant in the model. The binding and dissociation reactions of proteins in the model are described by the law of mass action, while the enzymatic reactions are characterized by Michaelis-Menten kinetics (MM). In undamaged cells, ATM appears as dimers or oligomers. And the ATM dimer can spontaneously polymerize or dissociate into inactive monomers, of which the reaction intensity is reflected by k_{dim} and k_{udim} correspondingly. After DNA damage, ATM dimmers are recruited to the damaged DNA and the ATM autophosphorylation [20] will be accelerated, involving the basal activation and the DNA damages induced activation, of which the strengths are represented by k_{basal} and k_{acatm} respectively. The process is summarized by the first and third term on the righ-hand side of Eq. 2, where N_{dsb} represents the amount of DNA damage.

The p53-related kinetics include the basic transcriptional, translational, phosphorylation and reversible phosphorylation processes, as described below.

$$\frac{d[p53_m]}{dt} = k_{sp53} - k_{dp53m} \cdot [p53_m], \tag{3}$$

$$\begin{aligned}\frac{d[p53_u]}{dt} = {} & k_{rp53} \cdot [p53_m] + k_{wip53s} \cdot [Wip1] \cdot H^+([p53_p], j_{wip53s}) \\ & - k_{dep53} \cdot [p53_u] - k_{acp531} \cdot [ATM_p] \\ & \cdot H^+([p53_u], j_{ap53}) - k_{dp53} \cdot [Mdm2_n] \\ & \cdot H^+([p53_u], j_{p53}),\end{aligned} \tag{4}$$

$$\begin{aligned}\frac{d[p53_p]}{dt} = {} & k_{acp531} \cdot [ATM_p] \cdot H^+([p53_u], j_{ap53}) - k_{dep53s} \cdot [p53_p] \\ & - k_{dp53s} \cdot [Mdm2_n] \cdot H^+([p53_p], j_{p53s}) \\ & - k_{wip53s} \cdot [Wip1] \cdot H^+([p53_p], j_{wip53s}).\end{aligned} \tag{5}$$

The Mdm2-related dynamics are stated as follows:

TABLE 1 Default values of parameters.

Parameter	Values	Parameter	Values	Parameter	Values	Parameter	Values	Parameter	Values
N_{dsb}	175	j_{dsb}	150	$[ATM_{tot}]$	1	k_{acatm}	0.136[a]	$k_{deatmwip}$	0.24
k_{udim}	0.016[a]	k_{dim}	0.008[a]	k_{basal}	0.016[a]	j_{acatm}	0.1[a]	j_{deatm}	0.2[a]
j_{atms}	0.1[a]	k_{deatm}	0.001[a]	$j_{deatmwip}$	0.2[a]	k_{sp53}	0.008[a]	k_{dep53}	0.04[a]
k_{dep53s}	0.0008[a]	k_{dp53}	0.24[a]	k_{dp53s}	0.012[a]	k_{acp531}	0.08[a]	k_{wip53s}	0.004[a]
j_{ap53s}	3.0[a]	j_{wip53s}	0.1[a]	j_{p53}	0.1[a]	j_{p53s}	0.02[a]	k_{swip10}	0.0008[a]
k_{swip1}	0.008[a]	j_{swip1}	0.7[a]	k_{dwip1}	0.096[a]	k_{dp53m}	0.08[a]	k_{rp53}	0.32[a]
k_{smdm20}	0.0016[a]	k_{smdm2}	0.016[a]	j_{smdm2}	1.0[a]	k_{dmdm2c}	0.0064[a]	k_{i}	0.08[a]
k_{o}	0.04[a]	$k_{dmdm2n0}$	0.0032[a]	$k_{dmdm2n1}$	0.096[a]	j_{mdm2n}	1.0[a]	k_{dmdm2m}	0.048[a]
k_{rmdm2}	0.16[a]	k_{dwip1m}	0.048[a]	k_{rwip1}	0.48[a]				

[a]Refs. [26, 27, 29].

$$\frac{d[mdm2_m]}{dt} = k_{smdm20} + k_{smdm2} \cdot H^{(+,4)}([p53^p], j_{smdm2}) - k_{dmdm2m} \cdot [mdm2_m], \tag{6}$$

$$\frac{d[Mdm2_c]}{dt} = k_{rdmdm2} \cdot [mdm2_m] - k_{dmdm2c} \cdot [Mdm2_c] + k_o \cdot [Mdm2_n] - k_i \cdot [Mdm2_c], \tag{7}$$

$$\frac{d[Mdm2_n]}{dt} = k_i \cdot [Mdm2_c] - k_o \cdot [Mdm2_n] - k_{dmdm2n0} \cdot [Mdm2_n] - k_{dmdm2n1} \cdot [ATM_p] \cdot H^{+}([Mdm2_n], j_{mdm2n}). \tag{8}$$

For Mdm2, the model considers Mdm2 in two forms: intracytoplasmic Mdm2 ($Mdm2_c$) and intra-nuclear Mdm2 ($Mdm2_n$). And the p53 transcription of $mdm2_m$ is characterized by the Hill function with the form of $H^{+,n}$ (A,B) defined as $A^n/(A^n + B^n)$, where n indicating the degree of synergy. The nuclear input and output Mdm2 are expressed as linear terms of the rate constant, respectively.

Similarly, the kinetic behavior of Wip1 is described by the following equation, and the transcription of Wip1 by p53 is portrayed by the Hill equation.

$$\frac{d[wip1_m]}{dt} = k_{swip10} + k_{swip1} \cdot H^{(+,3)}([p53_p], j_{swip1}) - k_{dwip1m} \cdot [wip1_m], \tag{9}$$

$$\frac{d[Wip1]}{dt} = k_{rwip1} \cdot [wip1_m] - k_{dwip1} \cdot [Wip1]. \tag{10}$$

The unit of time is minute, while concentrations are divided by some certain standard concentrations, thus being dimensionless. And, all the parameters are listed in Table 1.

2.2 Material and methods

p53 related network in cell lines has rich dynamics with non-linear characteristics, and the bifurcation analysis method is an effective means to probe the reason for such non-linear dynamics behaviors of cells. When the parameters of the system change, the system will undergo sudden changes, such as the transformations from stable to unstable state, the appearance of limit cycle, chaos, and so on. These changes can be called bifurcations. As a typical non-linear system model, p53 core network model has rich and complex dynamics, associating with many types of bifurcation. For example, when the protein is activated, its expression can change from a low level to a stable high level, corresponding to Saddle-Node bifurcation. If stimulated by the external signal, the protein concentration in the cell can transform from a stable equilibrium state to a limit cycle oscillation, suggesting the Hopf bifurcation. Thus, the parameters in the p53 network model can affect the non-linear dynamics greatly. To reveal the principle of how to regulate the p53 network, it is meaningful to make the bifurcation analysis.

For bifurcation analysis, such software as Oscill8 [38] and MatCont [39] are commonly used to draw the trajectory diagram of the variables when the parameters change. In this study, the Oscill8 software is introduced to make one or two parameter bifurcation analysis, while MatCont is used to check the two parameter bifurcation analysis results. In the bifurcation analysis diagrams, this study only shows the results in the case of positive values, such as the reaction rates and protein levels, and discards the negative results, although they are mathematically meaningful.

Given a fixed parameter of external inputs in the model, the time series can be obtained. With the method of peak detection, the amplitude and period can be calculated. Comparing with the Fourier transformation, the oscillation period can be quite accurate. In numerical calculation of the differential equations, the Runge-Kutta method is introduced with a time step of 0.001 s [40].

3 Results

In this part, we first obtain the typical time series diagram and one-dimensional parameter bifurcation diagram of the

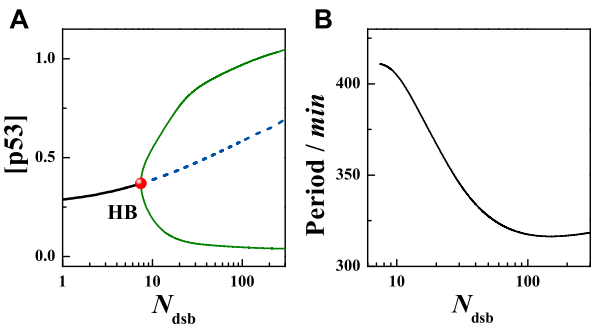

FIGURE 2
Deterministic analysis of the model. **(A)** The bifurcation diagram of total p53 concentration with N_{dsb}, the black solid line and dotted line represent stable and unstable states respectively, the solid circle represents the HB point, and the blue curve represents the maximum and minimum of [p53] in the limit cycle. **(B)** The change of [p53] with N_{dsb}. Here [p53] = [$p53_u$]+[$p53_p$].

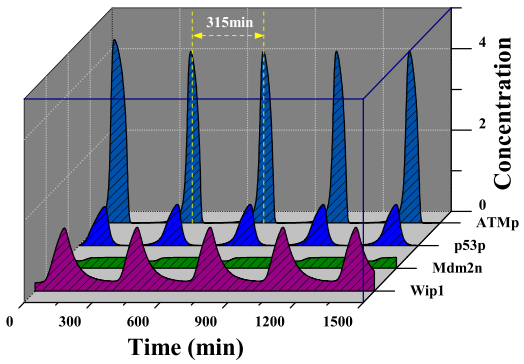

FIGURE 3
Time evolutions of [ATM_p], [$p53_p$], [$Mdm2_n$], [Wip1] with N_{dsb} = 175.

network system, and prove the existence of stable limit cycle oscillation in the system through the phase trajectory. We found that the DNA damage caused by pressure plays an important role in regulating the oscillation. Then, we found the importance of Wip1 dephosphorylation on the network. The one-dimensional and two-dimensional parametric bifurcation diagrams clearly show the complex characteristics of system dynamics. Meanwhile, the possible reasons for the oscillation phenomenon observed in the experiment are also analyzed. We found that in the complex coupled network model, especially in the coupled NFLs model, DNA damage shows a bottleneck-like effect on the oscillatory parameter regions. Finally, by means of biochemical reaction dynamics, we examined the influence of double negative coupling competition effect on oscillation.

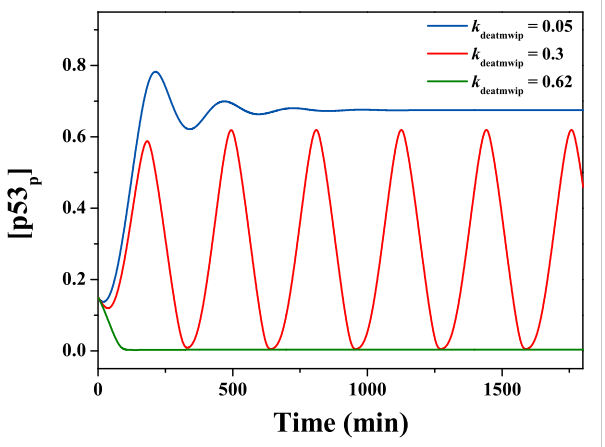

FIGURE 4
Time evolutions of [$p53_p$], with different $k_{deatmwip}$. From top to down, $k_{deatmwip}$ = 0.05, 0.3, 0.62 respectively. The parameter N_{dsb} = 175.

3.1 General overview of p53 dynamics

Considering the above model, the level of DNA damage was investigated firstly. Calculations show that in the absence of damage, i.e., N_{dsb} = 0, the system is in a stable steady state with a low p53 expression level. When N_{dsb} = 8, the system will goes across the Hopf Bifurcation (HB) (Figure 2A). When N_{dsb} > 8, the system destabilizes and then exhibits stable limit cycle oscillations. That means the fixed point of the high-dimensional system changes from a stable focus to an unstable focus surrounded by the limit cycle. The amplitude of the p53 protein increases with the N_{dsb} value, accompanied by a decrease in the period as seen in Figure 2B. In particular, for N_{dsb} = 175 (about 5 Gy IR dose), the period of oscillation was 315 min (5.3 h) (Figure 3), which is in good agreement with the experimental results [18, 23]. Here, a slight DNA damage can cause p53 oscillation, mainly due to the rapid activation of ATM. But, if N_{dsb} is quite small, the positive feedback effect on ATM will be too weak, and a long time is needed for the other components of the network to receive and respond to the stimulus signal, which brings an obvious long time delay, thus generating a larger oscillation period. On the contrary, a higher N_{dsb} can bring about high frequency and low amplitude oscillations. Especially, the flat period range is quite wide with larger N_{dsb} values, showing the high occurring probability of stable oscillation.

3.2 Bifurcation analysis of the negative feedback strength

The classical pathway for the negative regulation of p53 by Wip1 is the dephosphorylation of ATM at the Ser1981 site [18, 19], which corresponds to the parameter $k_{deatmwip}$. That is, the

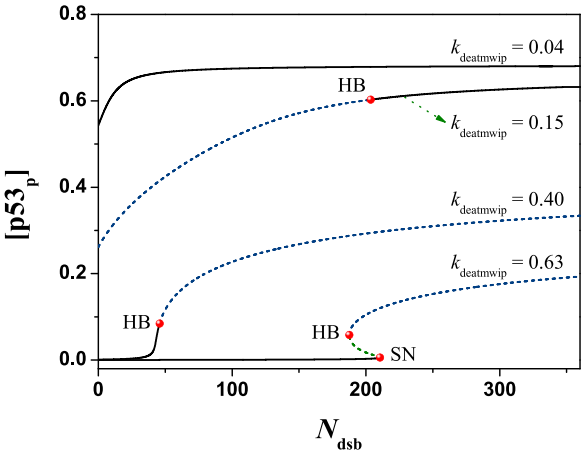

FIGURE 5
The bifurcation diagram of [p53$_p$] with N_{dsb}, the black solid line and dotted line represent stable and unstable states respectively, the symbol 'HB' represents the Hopf bifurcation point, and the symbol 'SN' represents the Saddle-Node bifurcation point. From top to down, $k_{deatmwip}$ = 0.04, 0.15, 0.40, 0.63 respectively. The parameter N_{dsb} = 175.

value of $k_{deatmwip}$ affects the strength of the ATM-p53-Wip1 negative feedback loop. In order to explore the influence of this parameter on the network system, the value of $k_{deatmwip}$ was changed independently. The results show that this parameter exerts great influence on the system state. For example, if $k_{deatmwip}$ is taken as 0.05, 0.3 and 0.62 respectively, the state of the system variable changes significantly. As shown in the Figure 4, the time series of [p53$_p$] can show stable high level, periodic oscillation state and stable low level changes respectively. Here, the parameter N_{dsb} = 175.

Next, in order to obtain a more comprehensive understanding, the one-dimensional parameter bifurcation diagram of the system is calculated by changing the value of N_{dsb}. The calculation results show that the system state changes greatly with N_{dsb}. Regardless of the global solution in mathematics, the case of $N_{dsb} > 0$ is considered here. It is found that the system can present two forms of solutions: steady-state solution or oscillatory solution. Taking different values of $k_{deatmwip}$, the bifurcation diagram changes obviously, as shown in Figure 5. This shows the potential ability of parameter $k_{deatmwip}$ in regulating cell state under different IR doses.

Furthermore, the regulation of parameter $k_{deatmwip}$ on the system state been focused. After numerical analysis, the equilibrium state of [p53$_p$] was obtained in relation to the variation of the parameter $k_{deatmwip}$, i.e., Figure 6. On the bifurcation diagram, three bifurcation points can be observed sequentially with increasing $k_{deatmwip}$: Hopf bifurcation point (HB), Saddle Node bifurcation point (SN) and Saddle Node Homoclinic bifurcation point (SNIC), same as the results in model [25]. The line between HB and SN is the unstable focus and saddle point, the line between SN and SNIC is the unstable saddle point, while the line outside HB and SNIC represents the stable point of the system. What is interesting is that a stable limit cycle can be found in the system, which is located between HB and SNIC, where stable periodic oscillations will occur. Here the [p53$_p$] concentrations changes differently. For example, when N_{dsb} = 175, the bifurcation diagram shows that the parameter $k_{deatmwip}$ is in the (0, HB) interval and the negative feedback strength is relatively weak, [p53$_p$] is in the high state; the parameter $k_{deatmwip}$ is in the (SNIC, + ∞) interval and the negative feedback strength is relatively high, [p53$_p$] is in the low steady state; the parameter $k_{deatmwip}$ is in the (HB, SNIC) interval and the negative feedback strength is relatively weak [p53$_p$] is in the changeable steady state. The parameter $k_{deatmwip}$ was in the (HB, SNIC) interval and produced stable non-decaying periodic oscillations. This indicates that Wip1-mediated negative feedback is important for p53 oscillations, which is consistent with the article [24]. Under different value of N_{dsb}, for instance N_{dsb} = 10, 35, 175, 350, the patterns of bifurcation diagrams vary greatly. This shows that $k_{deatmwip}$ and N_{dsb} can affect the system together.

Here, the synergistic effect of positive and negative feedback is responsible for this change on the bifurcation diagram. When $k_{deatmwip}$ is very small, the positive feedback effect on ATM will be quite strong, which can make ATM activated quickly. As the phosphorylation of p53 is mainly dominated by ATM, thus p53 can rise to a high level quickly, even N_{dsb} is quite small. So there is no oscillation. Next, when $k_{deatmwip}$ increases, the positive feedback effect on ATM is weakened, and the negative feedback effect is strengthened, thus the periodic oscillation appears. The $k_{deatmwip}$ value continues to rise, the positive feedback effect on ATM is weakened too, and the level of p53 rises slowly with N_{dsb}. As the oscillation needs a proper range of [p53$_p$], so the HB moves right at the N_{dsb} axis in Figure 5. If $k_{deatmwip}$ value is very large, the positive feedback effect on ATM will be seriously weakened. So, given a quite large N_{dsb} value can ATM starts to activate and the periodic oscillation begins appear. Meanwhile, with the increasing N_{dsb} value, the equilibrium point of the system may changes from the stable node towards an unstable focus, thus evolving into the SNIC.

The changes of oscillation period can also be obtained with different parameters of $k_{deatmwip}$, which shows a same trend: first is rapid increasing, following with a flat platform and final is rapid increasing (seen in Figure 7). Without losing generality, we select a flat period region with up limit of 332.5 min, and determine the $k_{deatmwip}$ region for oscillation, where a wide range can be seen for high N_{dsb} values. Especially, they are $k_{deatmwip}$ = 0.445 and 0.5273 with N_{dsb} = 175 and 350 respectively. The flat period region means the period value can be observed in the experiment with high probability. For relevant cell experiments, that means a suitable negative feedback strength should be required for a realistic and stable oscillation period.

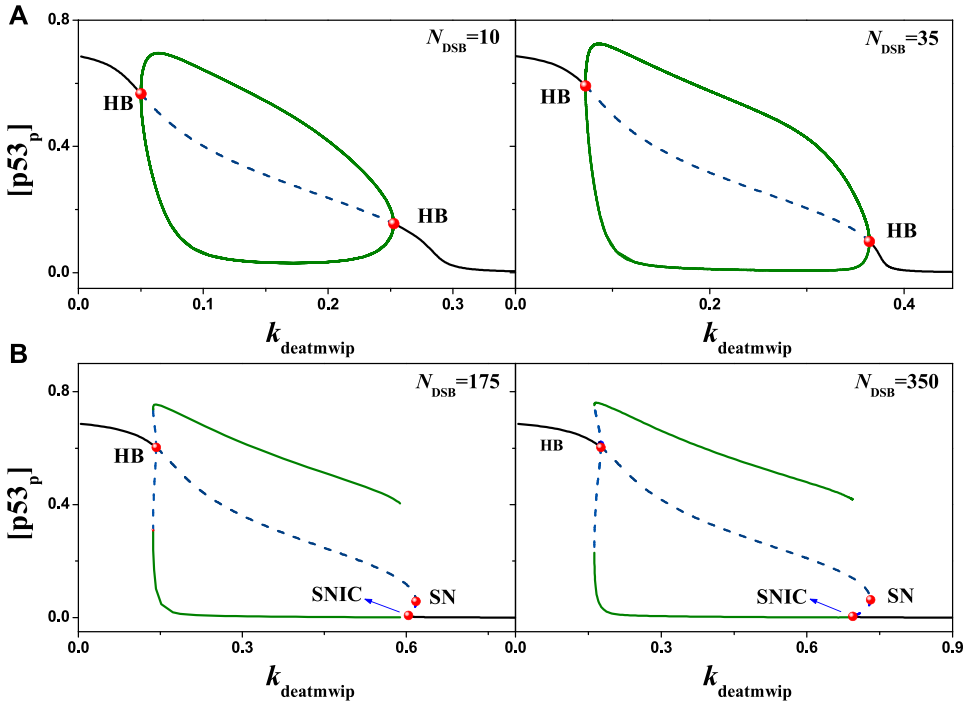

FIGURE 6
The bifurcation diagram of [p53$_p$] with $k_{deatmwip}$, the black solid line and dotted line represent stable and unstable states respectively, the symbol 'HB' represents the Hopf bifurcation point, the symbol 'SN' represents the Saddle-Node bifurcation point, and the symbol 'SNIC' represents the Saddle Node Homoclinic bifurcation point. **(A)** From left to right, N_{dsb} = 10 and 35 respectively. **(B)** From left to right, N_{dsb} = 175 and 350 respectively. Either in **(A)** or **(B)**, the same ordinate system is used for the left and right graphs.

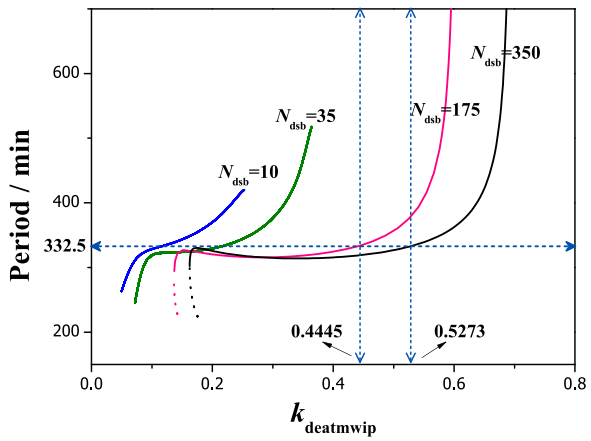

FIGURE 7
The dependence of period on the parameter $k_{deatmwip}$ with different N_{dsb}. From left to right, N_{dsb} = 10, 35, 175, 350 respectively. The horizontal dots line denotes the period of 332.5 min. The vertical dots lines indicate $k_{deatmwip}$ = 0.4445, 0.5273 respectively.

The above results were obtained only for N_{dsb} = 10, 35, 175, 350, but practical experiments [18] indicate that periodic oscillations of p53 can be detected when the iron-radiation dose exceeds a certain threshold, i.e., when the amount of DNA damage is greater than a certain value. A more complete understanding can be obtained by the distribution of network states on a two-dimensional parameter plane. Taking the $k_{deatmwip}$-N_{dsb} two-dimensional parameter space as an example, the relevant bifurcation curves were obtained in Figure 8. In this two-dimensional parameter space there are three states: stable steady state I, stable oscillatory state II and excitable state III. Among them, excitable state III can only be found if $k_{deatmwip}$ and N_{dsb} are above a certain value (0.5246, 80). The results in Figure 8 also show that only if the strength of $k_{deatmwip}$ is appropriate can stable p53 oscillation will appear. If $k_{deatmwip}$ is too low or close to zero, there is no oscillatory state II, which is consistent with the experimental phenomenon in UV-irradiated cells [18], where the Wip1-ATM pathway is not activated. The results in Figure 8 may also provide some theoretical explanation for the experiments of Chen et al [35].

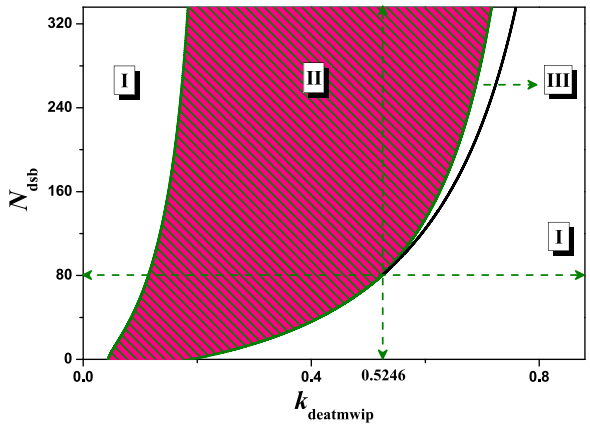

FIGURE 8
The two-parameter bifurcation with respect to $k_{deatmwip}$ and N_{dsb}. The symbols 'I','II' and 'III' represent monostable state, oscillation state and excited state respectively. The vertical dots line indicates $k_{deatmwip}$ = 0.5246.

Namely that the strength of $k_{deatmwip}$ in cells is in a specific range and that p53 oscillations can only occur when the dose of etoposide (amount of DNA damage) is moderate.

3.3 Self-antagonism of the ATM-p53-Wip1 NFL

The above results mainly reflect the situation in the ATM-p53-Wip1 negative feedback loop after changing the strength of a single feedback. In the actual cellular setting, there may be other antagonistic effects in the same loop that are worth considering. For example, in this model the dephosphorylation of Ser1981 by Wip1 on ATM and the phosphorylation of Ser15 by ATM on p53 [41]. In this model, the parameter k_{acp531} is used to represent the strength of ATM phosphorylation on p53. Numerical analysis yielded the equilibrium state of [$p53_p$] in relation to the parameter $k_{deatmwip}$, i.e., in Figure 9. When k_{acp531} = 0.08, with N_{dsb} = 175 the bifurcation diagrams are consistent with

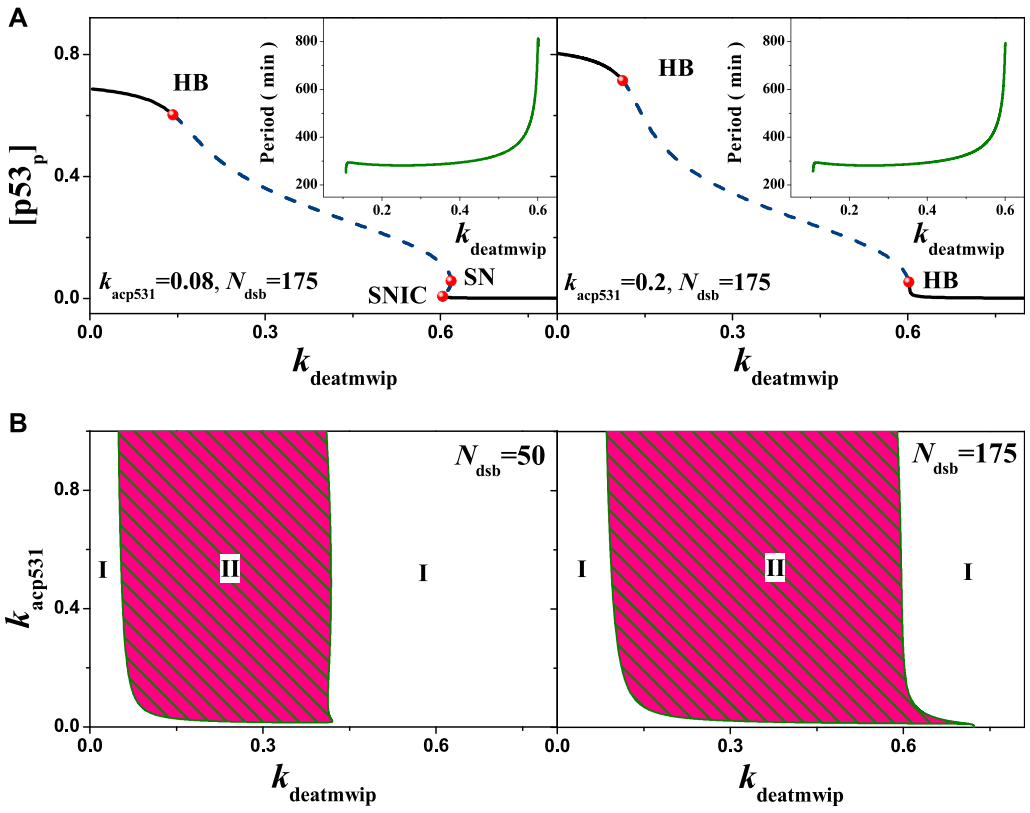

FIGURE 9
Influences of the ATM regulated p53 phosphorylation on the network dynamics with different strengths. **(A)** One parameter bifurcation diagram of [$p53_p$] on the parameter $k_{deatmwip}$. From left to right, k_{acp531} = 0.08 and 0.20 respectively. The schematic diagram shows the relationship between the period and the parameters $k_{deatmwip}$. **(B)** The two-parameter bifurcation with respect to $k_{deatmwip}$ and k_{acp531}. The symbols 'I', 'II' and 'III' represent monostable state, oscillation state and excited state respectively. From left to right, N_{dsb} = 50 and 175 respectively. Either in A or B, the same ordinate system is used for the left and right graphs.

Figure 6. But, when k_{acp531} = 0.2, only two Hopf bifurcation points can be observed as $k_{deatmwip}$ increases, indicating a sudden change in the equilibrium state of the system. As the parameter $k_{deatmwip}$ increases, the period exerts the same tends as in Figure 7 when N_{dsb} = 175.

The above changes can be interpreted from the relevant dynamics in detail. When the parameter $k_{deatmwip}$ is in the range (0,HB), indicating relative low negative feedback strength, which may benefit the high level of p53 phosphorylation, thus there is only stable equilibrium state. On contrary, when $k_{deatmwip}$ is in the range (SNIC, +∞) (k_{acp531} = 0.08) or the range (HB, +∞) (k_{acp531} = 0.2), the p53 phosphorylation will be suppressed, the system will also go to stable equilibrium state. Only when $k_{deatmwip}$ is in the range (HB, SNIC) or (HB, HB), the stable oscillation can appears. This may indicate the importance of the appropriate feedback strength for p53 oscillation. And the emergence of SNIC when k_{acp531} = 0.08 suggests that the antagonism increases the complexity of the same feedback loop. When k_{acp531} = 0.2, the $k_{deatmwip}$ range for p53 oscillation becomes larger, suggesting that the increased phosphorylation on p53 at Ser15 may contribute to the arise of stable oscillatory states. It is worth nothing to mention that, due to the nonlinear synergistic effect, with a higher phosphorylation strength on p53, the a stable limit loop will surround an unstable focus instead of unstable node, which causes the change from SNIC to HB, as in Figure 9A.

Furthermore, a more clear understanding can be obtained by two-dimensional bifurcation diagram. Within different DNA damage, the $k_{deatmwip}$-k_{acp531} bifurcation diagram can be obtained by extending each bifurcation point, i.e., Figure 9B. For N_{dsb} = 50, the system oscillation state II corresponds to a smaller value of $k_{deatmwip}$ and a larger range of k_{acp531} values, indicating that the amount of Ser15 phosphorylation of p53 is important, i.e., a stable periodic oscillation can also be maintained by weak Ser15 phosphorylation of p53. At N_{dsb} = 175, the parameter range of systemic oscillation state II was relatively broadened, indicating a high correlation between the amount of DNA damage and the stable oscillation state. Comparing the above results, a more plausible explanation is that DNA damage acts directly on ATM, and ATM can phosphorylate p53, as DNA damage amplifies the signal through positive feedback from ATM, which facilitating the emergence of oscillations, in consist with the findings in the study [25, 31, 32, 42]. These founds also indicate the need of coordinated mutual antagonism in the same feedback loop in order to maintain stable periodic oscillations.

3.4 Synergies of coupled PFL and NFL

Different from the above discussion in the same feedback loop, we further analyzed a pair of opposite effect on the same protein, e.g., the phosphorylation and dephosphorylation on ATM. In this

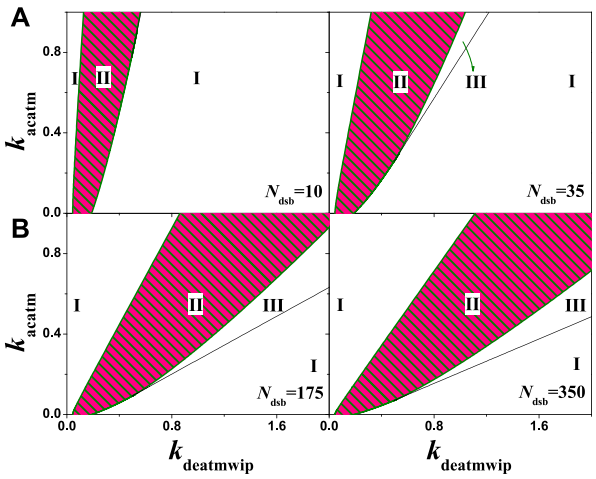

FIGURE 10
The two-parameter bifurcation with respect to $k_{deatmwip}$ and k_{acatm}. The symbols 'I','II', and 'III' represent monostable state, oscillation state and excited state respectively. **(A)** From left to right, N_{dsb} = 10,35 respectively. **(B)** From left to right, N_{dsb} = 175, 350 respectively. Either in A or B, the same ordinate system is used for the left and right graphs.

model, the ATM autophosphorylation is considered, different from the phosphorylation of Mdm2 at Ser395 [25], as in research it is confirmed that ATM autophosphorylation happens more often, which can accelerate the ATM activation to a higher level quickly [36], forming a PFL. To test whether DNA damage amplifies the signal through ATM's PFL more conducive to oscillations, we make a test by comparison. Generally, in coupled PFL and NFL, oscillation is dominated by NFL, and PFL exerts a gain effect on NFL [32]. In this model, p53-Wip1-ATM and p53-Mdm2 NFLs coexist. Numerical analysis shows that the value range of the oscillation parameter $k_{deatmwip}$ of the system becomes wider by increasing of the positive feedback strength parameter k_{acatm}, as shown in Figure 10. Although the value of k_{acatm} is zero representing no phosphorylation on p53, the oscillation range can also be found with proper $k_{deatmwip}$ values, indicating that the oscillation is dominated by p53-Mdm2 loop. In the two-parameter bifurcation diagram, the oscillable $k_{deatmwip}$ interval widens with the increase of k_{acatm}, indicating that the increase of positive feedback amplifies the signal and is conducive to p53 oscillation.

The more damage, the more oscillating region will appear in the system, as well as the excitable state III. The possible reason is that DNA damage directly acts on substrate ATM, which changes the positive feedback intensity of ATM. The change of positive feedback strength leads to the change of equilibrium property of the system, causing the change of system state. That means the positive feedback increases the complexity of system state. Since the appearance of the oscillating state requires a specific range of positive and negative feedback intensity, it also indicates that the

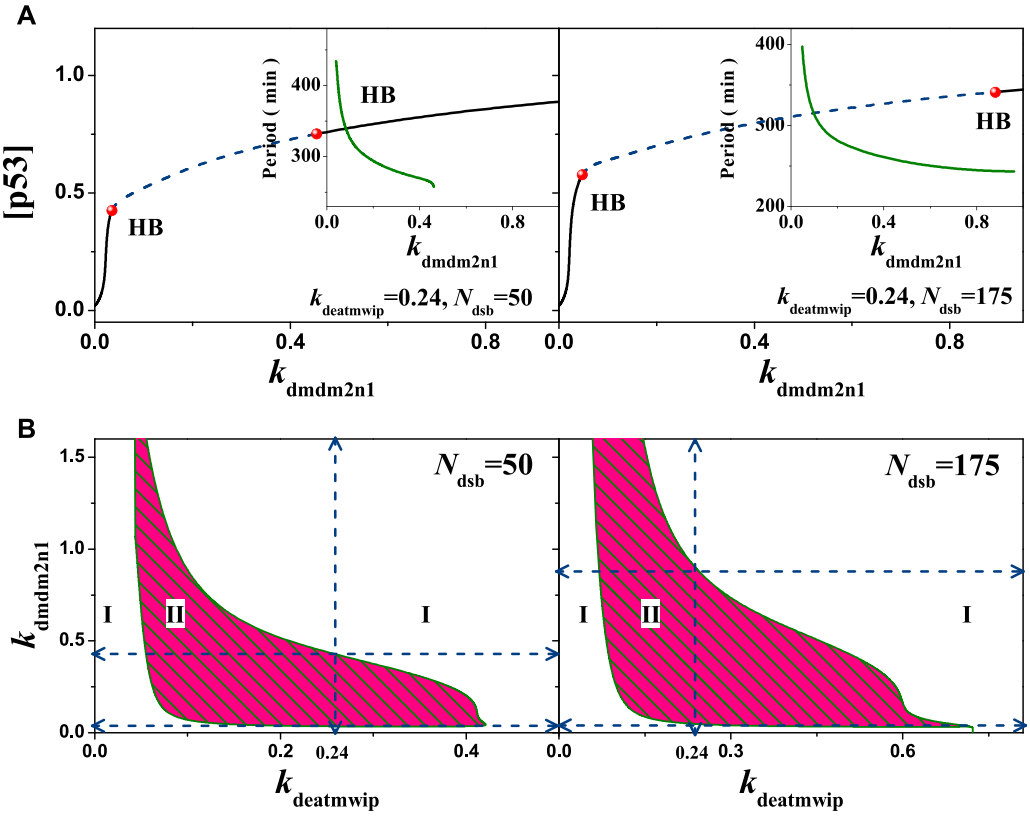

FIGURE 11
Influences of the ATM regulated Mdm2n degradation on the network dynamics with different strengths. **(A)** One parameter bifurcation diagram of [p53] on the parameter $k_{dmdm2n1}$. From left to right, $k_{deatmwip}$ = 0.15 and 0.24 respectively. The schematic diagram shows the relationship between the period and the parameters $k_{dmdm2n1}$. **(B)** The two-parameter bifurcation with respect to $k_{deatmwip}$ and $k_{dmdm2n1}$. The symbols 'I','II' and 'III' represent monostable state, oscillation state and excited state respectively. From left to right, N_{dsb} = 50 amd 175 respectively. Either in A or B, the same ordinate system is used for the left and right graphs.

oscillation is the result of the coordination of positive and negative feedback. General research models also confirm [31, 32, 42] that the network model coupled with PFLs and NFLs has better robustness and better response in the p53 network.

3.5 Bottleneck like effect of p53-Wip1-ATM and p53-Mdm2 NFLs

Further, in addition to the coupled PFL and NFL in a single loop discussed above, there are also coupled NFLs in this system, deserving much attentions. For example, the negative feedback collaboration between p53-Wip1-ATM and p53-Mdm2. Here, we first paid special attention to the degradation of intranuclear Mdm2 regulated by phosphorylated ATM, which essentially constitutes a nested ATM-Mdm2-p53-Wip1 NFL that partially overlaps with the pathway of the p53-Wip1-ATM and p53-Mdm2 NFL. In contrast to the previous use of the Mdm2 inhibitor Nutlin-3 to activate the p53 signaling pathway [43], here, regulating the coupled NFLs to achieve state transition can be a new try. In this model, the strength of Mdm_n degradation by ATM is reflected in the key parameter $k_{dmdm2n1}$. Within different conditions, the 1-D bifurcation diagrams of $k_{dmdm2n1}$ can be obtained. As shown in Figure 11A, the parameter range of the scalable $k_{dmdm2n1}$ was found to change significantly after fixing the intensity of dephosphorylation of ATM by Wip1, and the corresponding oscillation period varied in the same trend with $k_{dmdm2n1}$. The scalable $k_{dmdm2n1}$ range was larger for smaller values of $k_{deatmwip}$ ($k_{deatmwip}$ = 0.15) and smaller for larger $k_{deatmwip}$ ($k_{deatmwip}$ = 0.24), indicating their mutually exclusive nature. Thus, the competitive involution may cause the limitation of oscillation, showing a bottleneck like effect on N_{dsb}. In the $k_{deatmwip}$-$k_{dmdm2n1}$ two dimensional bifurcation diagrams, this effect was very obvious. For different N_{dsb}, e.g., N_{dsb} = 50 and 175 respectively, oscillation regions tending to be concave towards the origin, as in Figure 11B. This change in the oscillable parameter region reflects the competing effects of

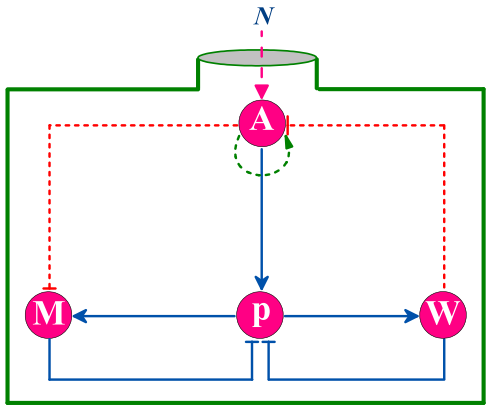

FIGURE 12
Simplified system network structure diagram. *N* represents the DNA damage number.

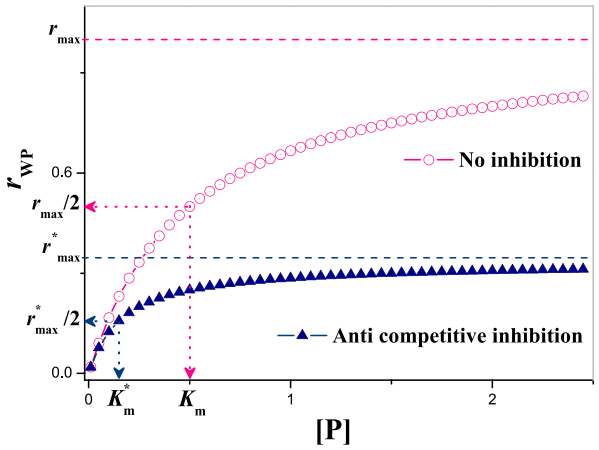

FIGURE 13
The dependence of r_{PM} on [P] under anti-competitive inhibition. Without losing generality, $K_m = 0.5$, $r_{max} = 1.0$, $K_M = 0.5$ and [M] = 1.0. So, $K^*_m = 0.167$, $r^*_{max} = 0.333$.

the two NFLs. The scalable parameter region is different, indicating that the amount of DNA damage dominates the neck of p53 oscillation.

This bottleneck like effect is most likely due to the fact that ATM-promoted degradation of Mdm2, in which larger values of $k_{dmdm2n1}$ implying higher levels of p53, when the system is prone to oscillation or instability. The higher dephosphorylation on ATM tends to disrupt the equilibrium, thus lowering the p53 expression and making the system monostable, also the lower dephosphorylation intensity on ATM tends to raise the p53 expression and make the system tends to the other extreme. Only when the two are coordinated can stable oscillations be generated. For $N_{dsb} = 50$, the oscillatory region in the two dimensional bifurcation diagram has no intersection with either axis, indicating that the p53-Mdm2 pathway and the p53-Wip1-ATM pathway are equally important for oscillations. So, this nested coupling of the dual NFls constrains each other and creates a competitive effect, limiting the scale of the parameters region.

3.6 Theoretical analysis

In this subsection, we further conduct a theoretical analysis on the above results, aim at revealing the underlying physical mechanism. As far as we know, such feedback loops as coupled PFL and NFL have been widely studied in the literature. Here, we are more concerned with the special pathway of coupled NFLs. By simplifying the biochemical reaction process between different proteins, we obtained the abstract structural diagram of p53 core network, as shown in Figure 12.

For such a simplified network model, we can infer that its responding capacity for stress signals depends on the short board in the signaling pathway, e.g., the node with the weakest interaction ability, reflecting as the bottleneck effect on strength. Assuming that each node protein in the network can equally participate in the reaction, the core node protein, as the busiest one, is easier to become a short board. In this coupled NFLs model, considering the reaction process that p53 actually participates in, we introduced anti-competitive inhibition dynamics to analogize the related dynamics. The mechanism of anti-competitive inhibition can be expressed as,

$$\mathrm{W} + \mathrm{P} \underset{k_{-1}}{\overset{k_{+1}}{\rightleftharpoons}} [\mathrm{WP}] \overset{k_{+2}}{\rightarrow} \mathrm{W} + \mathrm{P}'$$

$$[\mathrm{WP}] + \mathrm{M} \underset{k_{-3}}{\overset{k_{+3}}{\rightleftharpoons}} [\mathrm{WMP}]$$

where, W,P and M can represents Wip1, p53 and Mdm2 respectively.

Based on the steady-state assumption, the following equations can be listed:

$$\frac{d[\mathrm{WP}]}{\mathrm{d}t} = k_{+1}[\mathrm{W}][\mathrm{P}] - (k_{-1} + k_{+2})[\mathrm{WP}] = 0, \tag{11}$$

$$\frac{d[\mathrm{WMP}]}{\mathrm{d}t} = k_{+3}[\mathrm{WP}][\mathrm{M}] - (k_{-3})[\mathrm{WMP}] = 0, \tag{12}$$

$$[\mathrm{W}_0] = [\mathrm{W}] + [\mathrm{WP}] + [\mathrm{WMP}], \tag{13}$$

$$r_{\mathrm{WP}} = k_{+2}[\mathrm{WP}], \tag{14}$$

After integration, one can get

$$r_{\mathrm{WP}} = \frac{r_{\max}[\mathrm{P}]}{K_{\mathrm{m}} + [\mathrm{P}] + [\mathrm{P}][\mathrm{M}]/K_{\mathrm{M}}} = \frac{r^{\star}_{\max}[\mathrm{P}]}{K^{\star}_{\mathrm{m}} + [\mathrm{P}]}, \tag{15}$$

where,

$$K^{\star}_{\mathrm{m}} = \frac{K_{\mathrm{m}}}{1 + [\mathrm{M}]/K_{\mathrm{M}}}, \quad r^{\star}_{\max} = \frac{r_{\max}}{1 + [\mathrm{M}]/K_{\mathrm{M}}}. \tag{16}$$

Here, K_m^* is the apparent Michaelis constant in the presence of inhibitors, K_M is the dissociation constant of inhibitor, r_{max} is the maximum initial rate without inhibitor, and K_m is the apparent Michaelis constant without inhibitors. It can be seen from the Eq. 15 that when [M] increases or K_M decreases, K_m^* will increase, thereby inhibiting the decline of substrate P reaction rate. The relationship between reaction rate r_{PM} and substrate concentration P is shown in Figure 13. It can be seen that with the increasing substrate concentration [P], the degree of competitive inhibition will decrease, but it will gradually show a saturated state.

In order to reflect the inhibition degree of the inhibitor on the reaction, we define a physical quantity: i,

$$i = \frac{r_P - r_{PM}}{r_P} \cdot 100\%, \tag{17}$$

where, $r_P = r_{max}$ [P]/(K_m + [P]) is the production rate of P' without inhibitor.

For this model, it has

$$i = \frac{[P][M]}{K_M([P] + K_m) + [P][M]} \cdot 100\%. \tag{18}$$

So, from the Eq. 18 it can be inferred that the inhibition degree of inhibitors can be reduced by increasing [P] and the competitive oscillations can be mitigated. But increasing [P] can only alleviate the inhibition in a certain range. As, given larger [P] the oscillation will be destroyed. Through comparison, it can be seen that without the inhibitor [M], the NFL of AMT-p53-Wip1 can run well, e.g., the oscillation of a single negative feedback loop network seems to have more control advantages, but the disadvantages are also obvious: poor robustness. Therefore, we suggest that adding multiple positive feedback pathways to this p53 network may be a better choice.

4 Discussion

Classical theories suggest that multiple NFLs in the cell network combined with time delays in such process as gene transcription, protein translation and protein entry or exit from the nucleus, are the main causes of oscillations in the p53 protein network [21]. And it also demonstrated that positive feedback regulates the gain of negative feedback, which can be used to regulate this present model. In contrast to the positive feedback between p53 and Mdm2 mentioned in the article [25], the positive feedback in this model comes from the phosphorylation of ATM. The positive feedback of ATM up-regulates the p53-Mdm2 negative feedback loop, thus facilitating the threshold effect on the amount of DNA damage. The coupled positive-negative or negative-negative feedback enriches the kinetic behavior of the p53 protein network. What's more, the bottleneck effect caused by coupled NFLs firstly proposed by us in this model is still deserves further attention. Whether this effect only appears in p53 network or in other networks needs further confirmation. It is undeniable that the appearance of this coupled NFLs motif limits the overall response range, and new methods need to be considered for improvement, as it is still an effective way in clinical medicine to achieve tumor inhibition by regulating p53 network and related components [44, 45]. In any case, the understanding from the details of this model can be more generalizable for other network models with feedback loops. In addition, it is worth nothing that the system of ordinary differential equations and the Hill function in the deterministic model can only characterize the statistical behaviour of proteins in subcellular levels. To achieve more, molecular-level modelling is required, as well as the corresponding molecular dynamics methods. What's more, from an abstract perspective, p53 network consists of nodes, edges, and typical topological motifs, which can form a small scale-free network. Stimulated by the external signals, the self-dynamics and interaction dynamics of p53 network will change accordingly, reflecting the adaptability of cells. Understanding the spatiotemporal signal propagation [46–48] in this network with perturbations ideas may bring some inspiration.

5 Conclusion

In summary, this paper focuses on the dephosphorylation of ATM by Wip1 and discusses the this modification process on ATM, p53 and Mdm2, as well as the p53 oscillation phenomenon in detail. After constructing a mathematical model of the p53 protein network in accordance with the classical understanding, we investigated the regulation of p53 network oscillations by Wip1 dephosphorylation on ATM using the ordinary differential equations as the main concern for parametric bifurcation analysis. The results showed that: 1) the Wip1-ATM-p53 loop, where Wip1 dephosphorylation and p53 phosphorylation can form an internal mutual antagonism, is necessary to maintain stable limit cycle oscillations. And the different intensity of Wip1 dephosphorylation can provide a partial explanation for the response of p53 protein under UV or IR radiation; 2) the PFL of ATM autophosphorylation is coupled with the Wip1-ATM-p53 NFL, which can increase the gain of the NFL [32], ensuring robust oscillations; 3) the p53-Wip1-ATM loop and the p53-Mdm2 loop can form a coupled double NFL, which resists each other and suppresses the expansion of the oscillable parameter region, creating an Bottleneck-like effect. In order to alleviate this constraint, we suggest adding a positive feedback signal pathway to achieve better oscillation stability. Overall, this paper shows that either antagonism of the same loop or coupling of different loops can regulate the p53 network, and that periodic oscillations are the result of the coordination of various strengths in the structure of the coupled network. This conclusion has implications for other network models where oscillations occur. In addition, the downstream related genes and proteins of the p53 protein network are closely related to cell cycle, apoptosis and cellular senescence [13], is worth further

analysis. It is also hoped that the results of this study will provide a useful reference for researches on related cellular diseases.

Data availability statement

The original contributions presented in the study are included in the article/supplementary material, further inquiries can be directed to the corresponding author.

Author contributions

DW and ZW completed the result analysis and wrote the first draft of the manuscript. YW and XL participated in manuscript design and results analysis. DW and HL contributed to conception and design of the study. DW, HL, and XL was responsible for manuscript writing and revision. All authors contributed to manuscript revision, read, and approved the submitted version.

Funding

This work was supported by the National Natural Science Foundation of China (Grant Nos. 11804123 and 12175087) and the special program of the National Natural Science Foundation of China (Grant No. 11547025).

Acknowledgments

We sincerely thank all the reviewers, editors, and frontiers editorial staff for their constructive advices and excellent work.

Conflict of interest

The authors declare that the research was conducted in the absence of any commercial or financial relationships that could be construed as a potential conflict of interest.

Publisher's note

References

1. Vogelstein B, Lane D, Levine AJ. Surfing the p53 network. *Nature* (2000) 408: 307–10. doi:10.1038/35042675

2. Linzer DI, Levine AJ. Characterization of a 54k Dalton cellular sv40 tumor antigen present in sv40-transformed cells and uninfected embryonal carcinoma cells. *Cell* (1979) 17:43–52. doi:10.1016/0092-8674(79)90293-9

3. Levine AJ. p53: 800 million years of evolution and 40 years of discovery. *Nat Rev Cancer* (2020) 20:471–80. doi:10.1038/s41568-020-0262-1

4. Vousden KH, Lane DP. p53 in health and disease. *Nat Rev Mol Cel Biol* (2007) 8:275–83. doi:10.1038/nrm2147

5. Jackson SP, Bartek J. The dna-damage response in human biology and disease. *Nature* (2009) 461:1071–8. doi:10.1038/nature08467

6. Che Z, Sun H, Yao W, Lu B, Han Q. Role of post-translational modifications in regulation of tumor suppressor p53 function. *Front Oral Maxillofac Med* (2020) 2: 1–11. doi:10.21037/fomm.2019.12.02

7. Kubbutat MH, Jones SN, Vousden KH. Regulation of p53 stability by mdm2. *Nature* (1997) 387:299–303. doi:10.1038/387299a0

8. Guo L, Liew H, Camus S, Goh A, Chee L, Lunny D, et al. Ionizing radiation induces a dramatic persistence of p53 protein accumulation and dna damage signaling in mutant p53 zebrafish. *Oncogene* (2013) 32:4009–16. doi:10.1038/onc.2012.409

9. Kahlert C, Melo SA, Protopopov A, Tang J, Seth S, Koch M, et al. Identification of double-stranded genomic dna spanning all chromosomes with mutated kras and p53 dna in the serum exosomes of patients with pancreatic cancer. *J Biol Chem* (2014) 289:3869–75. doi:10.1074/jbc.C113.532267

10. Berkers CR, Maddocks OD, Cheung EC, Mor I, Vousden KH. Metabolic regulation by p53 family members. *Cell Metab* (2013) 18:617–33. doi:10.1016/j.cmet.2013.06.019

11. Maddocks OD, Berkers CR, Mason SM, Zheng L, Blyth K, Gottlieb E, et al. Serine starvation induces stress and p53-dependent metabolic remodelling in cancer cells. *Nature* (2013) 493:542–6. doi:10.1038/nature11743

12. Shaltiel IA, Aprelia M, Saurin AT, Chowdhury D, Kops GJ, Voest EE, et al. Distinct phosphatases antagonize the p53 response in different phases of the cell cycle. *Proc Natl Acad Sci U S A* (2014) 111:7313–8. doi:10.1073/pnas.1322021111

13. Garcia-Barros M, Paris F, Cordon-Cardo C, Lyden D, Rafii S, Haimovitz-Friedman A, et al. Tumor response to radiotherapy regulated by endothelial cell apoptosis. *Science* (2003) 300:1155–9. doi:10.1126/science.1082504

14. Hafner A, Bulyk ML, Jambhekar A, Lahav G. The multiple mechanisms that regulate p53 activity and cell fate. *Nat Rev Mol Cel Biol* (2019) 20:199–210. doi:10.1038/s41580-019-0110-x

15. Zhang XP, Liu F, Cheng Z, Wang W. Cell fate decision mediated by p53 pulses. *Proc Natl Acad Sci U S A* (2009) 106:12245–50. doi:10.1073/pnas.0813088106

16. Zhang XP, Liu F, Wang W. Two-phase dynamics of p53 in the dna damage response. *Proc Natl Acad Sci U S A* (2011) 108:8990–5. doi:10.1073/pnas.1100600108

17. Purvis JE, Karhohs KW, Mock C, Batchelor E, Loewer A, Lahav G. p53 dynamics control cell fate. *Science* (2012) 336:1440–4. doi:10.1126/science.1218351

18. Batchelor E, Mock CS, Bhan I, Loewer A, Lahav G. Recurrent initiation: A mechanism for triggering p53 pulses in response to dna damage. *Mol Cel* (2008) 30: 277–89. doi:10.1016/j.molcel.2008.03.016

19. Shreeram S, Demidov ON, Hee WK, Yamaguchi H, Onishi N, Kek C, et al. Wip1 phosphatase modulates atm-dependent signaling pathways. *Mol Cel* (2006) 23:757–64. doi:10.1016/j.molcel.2006.07.010

20. Bakkenist CJ, Kastan MB. Dna damage activates atm through intermolecular autophosphorylation and dimer dissociation. *Nature* (2003) 421:499–506. doi:10.1038/nature01368

21. Lev Bar-Or R, Maya R, Segel LA, Alon U, Levine AJ, Oren M. Generation of oscillations by the p53-mdm2 feedback loop: A theoretical and experimental study. *Proc Natl Acad Sci U S A* (2000) 97:11250–5. doi:10.1073/pnas.210171597

22. Lahav G, Rosenfeld N, Sigal A, Geva-Zatorsky N, Levine AJ, Elowitz MB, et al. Dynamics of the p53-mdm2 feedback loop in individual cells. *Nat Genet* (2004) 36: 147–50. doi:10.1038/ng1293

23. Geva-Zatorsky N, Rosenfeld N, Itzkovitz S, Milo R, Sigal A, Dekel E, et al. Oscillations and variability in the p53 system. *Mol Syst Biol* (2006) 2:2006.0033. doi:10.1038/msb4100068

24. Wang DG, Zhou CH, Zhang XP. The birhythmicity increases the diversity of p53 oscillation induced by dna damage. *Chin Phys B* (2017) 26:128709. doi:10.1088/1674-1056/26/12/128709

25. Yang HL, Liu N, Yang LG. Influence of mdm2-mediated positive feedback loop on the oscillation behavior of p53 gene network. *Acta Phys Sin* (2021) 70(13): 138701–9. doi:10.7498/aps.70.20210015

26. Ouattara DA, Abou-Jaoudé W, Kaufman M. From structure to dynamics: Frequency tuning in the p53-mdm2 network. ii: Differential and stochastic approaches. *J Theor Biol* (2010) 264:1177–89. doi:10.1016/j.jtbi.2010.03.031

27. Ma L, Wagner J, Rice JJ, Hu W, Levine AJ, Stolovitzky GA. A plausible model for the digital response of p53 to dna damage. *Proc Natl Acad Sci U S A* (2005) 102: 14266–71. doi:10.1073/pnas.0501352102

28. Jun-Feng X, Ya J. A mathematical model of a p53 oscillation network triggered by dna damage. *Chin Phys B* (2010) 19:040506. doi:10.1088/1674-1056/19/4/040506

29. Wang DG, Wang S, Huang B, Liu F. Roles of cellular heterogeneity, intrinsic and extrinsic noise in variability of p53 oscillation. *Sci Rep* (2019) 9:5883. doi:10.1038/s41598-019-41904-9

30. Wang YL, Liu F. Transcription apparatus: A dancer on a rope. *Acta Phys Sin* (2020) 69:248702. doi:10.7498/aps.69.20201631

31. Wang LS, Li NX, Chen JJ, Zhang XP, Liu F, Wang W. Modulation of dynamic modes by interplay between positive and negative feedback loops in gene regulatory networks. *Phys Rev E* (2018) 97:042412. doi:10.1103/PhysRevE.97.042412

32. Huang B, Tian X, Liu F, Wang W. Impact of time delays on oscillatory dynamics of interlinked positive and negative feedback loops. *Phys Rev E* (2016) 94: 052413. doi:10.1103/PhysRevE.94.052413

33. Li X, Liu F, Shuai JW. Dynamical studies of cellular signaling networks in cancers. *Acta Phys Sin* (2016) 65:178704. doi:10.7498/aps.65.178704

34. Li X, Li Z, Yang W, Wu Z, Wang J. Bidirectionally regulating gamma oscillations in wilson-cowan model by self-feedback loops: A computational study. *Front Syst Neurosci* (2022) 16:723237–13. doi:10.3389/fnsys.2022.723237

35. Chen X, Chen J, Gan S, Guan H, Zhou Y, Ouyang Q, et al. Dna damage strength modulates a bimodal switch of p53 dynamics for cell-fate control. *BMC Biol* (2013) 11:73–11. doi:10.1186/1741-7007-11-73

36. Kozlov SV, Graham ME, Jakob B, Tobias F, Kijas AW, Tanuji M, et al. Autophosphorylation and atm activation: Additional sites add to the complexity. *J Biol Chem* (2011) 286:9107–19. doi:10.1074/jbc.M110.204065

37. Shiloh Y, Ziv Y. The atm protein kinase: Regulating the cellular response to genotoxic stress, and more. *Nat Rev Mol Cel Biol* (2013) 14:197–210. doi:10.1038/nrm3546

38. Wang HY, Zhang XP, Wang W. Regulation of epithelial-to-mesenchymal transition in hypoxia by the hif-1α network. *FEBS Lett* (2022) 596:338–49. doi:10.1002/1873-3468.14258

39. Dhooge A, Govaerts W, Kuznetsov YA. Matcont: A matlab package for numerical bifurcation analysis of odes. *ACM Trans Math Softw* (2003) 29:141–64. doi:10.1145/779359.779362

40. Zingg DW, Chisholm TT. Runge–Kutta methods for linear ordinary differential equations. *Appl Numer Math* (1999) 31:227–38. doi:10.1016/S0168-9274(98)00129-9

41. Thanasoula M, Escandell JM, Suwaki N, Tarsounas M. Atm/atr checkpoint activation downregulates cdc25c to prevent mitotic entry with uncapped telomeres. *EMBO J* (2012) 31:3398–410. doi:10.1038/emboj.2012.191

42. Zhang T, Brazhnik P, Tyson JJ. Exploring mechanisms of the dna-damage response: p53 pulses and their possible relevance to apoptosis. *Cell Cycle* (2007) 6: 85–94. doi:10.4161/cc.6.1.3705

43. Christian T, James R, Zoran F, Brian H, Kenneth K, Holly H, et al. Small-molecule mdm2 antagonists reveal aberrant p53 signaling in cancer: Implications for therapy. *Proc Natl Acad Sci U S A* (2006) 103:1888–93. doi:10.1073/pnas.0507493103

44. Suarez OJ, Vega CJ, Sanchez EN, González-Santiago AE, Rodríguez-Jorge O, Alanis AY, et al. Pinning control for the p53-mdm2 network dynamics regulated by p14arf. *Front Physiol* (2020) 11:976. doi:10.3389/fphys.2020.00976

45. Duffy MJ, Synnott NC, Grady SÓ, Crown J. Targeting p53 for the treatment of cancer. *Semin Cancer Biol* (2022) 79:58–67. doi:10.1016/j.semcancer.2020.07.005

46. Hens C, Harush U, Haber S, Cohen R, Barzel B. Spatiotemporal signal propagation in complex networks. *Nat Phys* (2019) 15:403–12. doi:10.1038/s41567-018-0409-0

47. Bao X, Hu Q, Ji P, Lin W, Kurths J, Nagler J. Impact of basic network motifs on the collective response to perturbations. *Nat Commun* (2022) 13:5301–8. doi:10.1038/s41467-022-32913-w

48. Ji P, Lin W, Kurths J. Asymptotic scaling describing signal propagation in complex networks. *Nat Phys* (2020) 16:1082–3. doi:10.1038/s41567-020-1025-3

frontiers | Frontiers in Physics

TYPE Original Research
PUBLISHED 14 December 2022
DOI 10.3389/fphy.2022.1076314

OPEN ACCESS

EDITED BY
Xiyun Zhang,
Jinan University, China

REVIEWED BY
Ruiqi Li,
Beijing University of Chemical Technology, China
Li Chen,
Shaanxi Normal University, China

*CORRESPONDENCE
Gui-Yuan Shi,
sgy@bnu.edu.cn

SPECIALTY SECTION
This article was submitted to Interdisciplinary Physics, a section of the journal Frontiers in Physics

RECEIVED 21 October 2022
ACCEPTED 25 November 2022
PUBLISHED 14 December 2022

CITATION
Wu R-J, Kong Y-X, Zhang Y-C and Shi G-Y (2022), Analytical results of the k-core pruning process on multiplex networks.
Front. Phys. 10:1076314.
doi: 10.3389/fphy.2022.1076314

Analytical results of the k-core pruning process on multiplex networks

Rui-Jie Wu[1], Yi-Xiu Kong[2], Yi-Cheng Zhang[3] and Gui-Yuan Shi[1]*

[1]International Academic Center of Complex Systems, Beijing Normal University, Zhuhai, China, [2]School of Science, Beijing University of Posts and Telecommunications, Beijing, China, [3]Department of Physics, University of Fribourg, Fribourg, Switzerland

Multiplex networks are generally considered as networks that have the same set of vertices but different types of edges. Multiplex networks are especially useful when describing systems with several kinds of interactions. In this paper, we study the analytical solution of the **k**-core pruning process on multiplex networks. *k*-Core decomposition is a widely used method to find the dense core of the network. Previously, the Non-Backtracking Expansion Branch (NBEB) has been found to be able to easily derive the exact analytical results in the *k*-core pruning process. Here, we further extend this method to solve the **k**-core pruning process on multiplex networks by designing a variation of the method called the Multicolor Non-Backtracking Expansion Branch (MNEB). Our results show that, given any uncorrelated multiplex network, the Multicolor Non-Backtracking Expansion Branch can offer the exact solution for each intermediate state of the pruning process.

KEYWORDS

complex network, complex system, k-core, multiplex network, network theory

1 Introduction

Graphs are often used to model systems that consist of interacting people or entities, where the vertices represent people or entities and the edges represent connections. Nowadays, many graphs are built in this way, from a variety of systems and applications, such as online social networks, e-commerce platforms, and even protein interaction networks. One of the most important tasks in analyzing these graphs is to find the densest part of the network where the vertices are closely related to each other [1–4]. The most commonly used algorithm for this problem is called the k-core decomposition [5], in which the goal is to find the subgraph consisting of the vertices that are left after all vertices whose degrees less than k are removed. *k*-Core decomposition is widely used to identify the important nodes of networks [6–8], help visualize network structures [9,10], understand and explain the collaborative process in social networks [11,12], describe protein functions based on protein–protein networks [13,14], and promote network methods for large text summaries [15].

Previously, many researchers [12,16–18] have focused on solving the *k*-core decomposition problem on a single-layer network. Wu [19] showed that the Non-Backtracking Expansion Branch can be used to obtain the exact results of the *k*-core

10.3389/fphy.2022.1076314

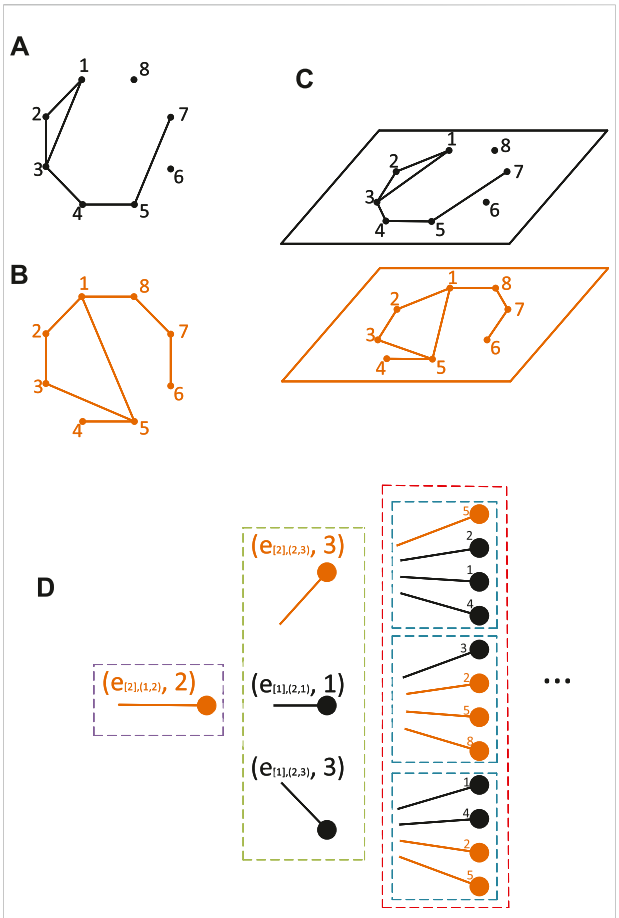

FIGURE 1
Example of a two-layer network. **(A)** First layer; **(B)** second layer; **(C)** two-layer network consists of the two layers **(A)** and **(B)**. **(D)** Multicolor Non-Backtracking Expansion Branch $B(e_{[2],(1,2)}, 2)$of the two-layer network is shown **(B)**. Here, $e_{[h],(i,j)}$ denotes the edge that connects the vertex i and vertex j in the h^{th} layer. The purple, green, and red boxes represent the first, second, and third strata of the MNEB, respectively. It should be noted that the excess neighbor stub set $S(e_{[2],(1,2)}, 2) = \{(e_{[2],(2,3)}, 3), (e_{[1],(2,1)}, 1), (e_{[1],(2,3)}, 3)\}$. The child stubs of the stub $(e_{[2],(1,2)}, 2)$ are all the elements in $S(e_{[2],(1,2)}, 2)$, as shown in the green box. The three blue boxes represent the child stubs of the three corresponding stubs in the second stratum, respectively.

pruning process on single-layer networks. The Non-Backtracking Expansion Branch is an alternative representation to the usual adjacency matrix of a network, which is constructed as an infinite tree having the same local structural information as the given network when observed by non-backtracking walkers.

These findings are important for our understanding of the structure of complex networks. Meanwhile, in real-world scenarios, it is common that we have to deal with systems that consist of many different types of interactions. As a result, systems cannot be represented by a single-layer network. For systems with multiple kinds of connections, we naturally use multiplex networks [20] that have the same set of vertices but different kinds of edges to represent these systems. Multiplex networks are also called multirelational networks, in which the edges between vertices can represent several different types of interactions. These multiplex networks can be used to describe real networks [21] or dynamic processes [22]. In recent years, there has been a trend in network research to study k-kernels on multiplexed networks. Azimi-Tafreshi [23] derived the self-consistent equation, obtained the birth point and relative size of the k-core of the uncorrelated multiplex networks with arbitrary degree distribution, and found hybrid phase transition. Subsequently, by analyzing different real multiplex networks, Osat [24] proposed a new multiplex network model and showed that interlayer correlations are important in characterizing their k-core structure, that is, the organization in the shell layers of nodes with increasing degrees. Radicchi [25]found that for larger numbers of layers, adding new layers increases the robustness of the system by creating redundant interdependencies between layers. Shang [26] revealed that there is a tipping point in the number of layers beyond which the multilayer k-core suddenly collapses. Boccaletti [20] proposed a comprehensive overview of the organization and dynamics between the components (layers) is given and several related issues are covered, ranging from a complete redefinition of fundamental structural measures to understanding how the multilayered nature of networks affects processes and dynamics. In a multiplex network, each kind of connection is represented by a unique layer, and the same vertex is allowed to have different network structures in different layers. Figures 1A–C show a simple example of a multiplex network.

These existing papers show that both intra-layer and inter-layer correlations have important effects on k-core phase transition. For a long time, due to the lack of mathematical tools, theoretical analysis of the k-core process on multiplex networks has been rare. Here, we show that by assigning different colors to distinguish the types of interactions, we can use the Multicolor Non-Backtracking Expansion Branch (MNEB) method to analytically obtain the results of each step in the **k**-core pruning process in a multiplex network.

2 Materials and methods

k-Core decomposition on multiplex networks is used to find the largest subgraph in which the degree of each vertex is at least k_i in the i^{th} layer (here **k** is a non-negative integral vector). In the previous paper [23], the researchers gave the analytical result of the final size of the **k**-core on multiplex networks. Here, we show that the Non-Backtracking Expansion Branch (NBEB) method can be used to obtain the complete solution of **k**-core decomposition on the multiplex, in which not only the final

state but also each intermediate state of the pruning process can be obtained analytically.

Given a multiplex network in which each layer is a simple graph, the standard pruning algorithm for **k**-core decomposition is as follows: for a given sequence of k_i, at each step, we remove these nodes whose degrees in any of these layers are less than the corresponding k. In the following, we analyze, in detail, the pruning process and attempt to give the size of the remaining vertices after each step.

First of all, we introduce the definitions of the terms that are used in the remainder of the paper. Suppose a given multiplex network has R layers. For convenience, we assign each layer with a color c_i to distinguish the edges that belong to different network layers. A "stub" is defined as a combination of an edge $e_{[i]}$ and one of its end vertex V, denoted by $(e_{[i]}, V)$, where the subscript $[i]$ here means that it belongs to the i^{th} layer, and i can be any integer in $[1, R]$. Obviously, the stub $(e_{[i]}, V)$ has the color c_i. We denote by k_i the degree of the vertex V in the i^{th} layer. In the i^{th} layer, we define the neighbor stub set of the vertex V: $S_i(V) = \{(e_{[i],1}, V_{[i],1}), (e_{[i],2}, V_{[i],2}), \ldots (e_{[i],k_i}, V_{[i],k_i})\}$; here, $\{V_{[i],1}, V_{[i],2}, \ldots, V_{[i],k_i}\}$ are the neighbors of V in the i^{th} layer, and $\{e_{[i],1}, e_{[i],2}, \ldots, e_{[i],k_i}\}$ are the edges connecting them to V, and the excess neighbor stub set of any stub $(e_{[i]}, V)$ in the i^{th} layer is found to be the complementary set of $\{(e_{[i]}, V^*)\}$ in $S_i(V)$, which is $S_i(e_{[i]}, V) = S_i(V)/\{(e_{[i]}, V^*)\}$($V^*$ is the neighbor of V *via* $e_{[i]}$).

Consequently, for the whole multiplex network, we define the neighbor stub set of the vertex V as

$$S(V) = \bigcup_{j=1}^{R} S_j(V) \tag{1}$$

and the excess neighbor stub set of $(e_{[i]}, V)$ as

$$S(e_{[i]}, V) = \left(\bigcup_{j=1, j\neq i}^{R} S_j(V) \right) \cup S_i(e_{[i]}, V). \tag{2}$$

It should be noted that the aforementioned expression of the excess neighbor stub set $S(e_{[i]}, V)$ is equivalent to the complementary set of $\{(e_{[i]}, V^*)\}$ in $S(V)$.

Similar to the definition of the Non-Backtracking Expansion Branch (NBEB) in one layer network, starting from any stub $(e_{[i]}, V)$, we can define such a tree-like structure, which we call the Multicolor Non-Backtracking Expansion Branch(MNEB).

The chosen stub $(e_{[i]}, V)$ (with color c_i) is the root of the MNEB, regarded as the first stratum. For any known n^{th} stratum of the MNEB, we can further find the child stubs of each stub in the n^{th} stratum that are all the elements in its excess neighbor stub set, and all these child stubs constitute the $(n+1)^{th}$ stratum of the MNEB. For example, if we have a stub $(e^*_{[i]}, V^*)$ in the n^{th} stratum, its child stubs are all the stubs that belong to $S(e^*_{[i]}, V^*)$. We can continue this process so that we obtain the MNEB of the stub $(e_{[i]}, V)$, denoted by $B(e_{[i]}, V)$. Obviously, there can be different colored stubs in one MNEB. Figure 1D provides an illustration of how the MNEB is constructed.

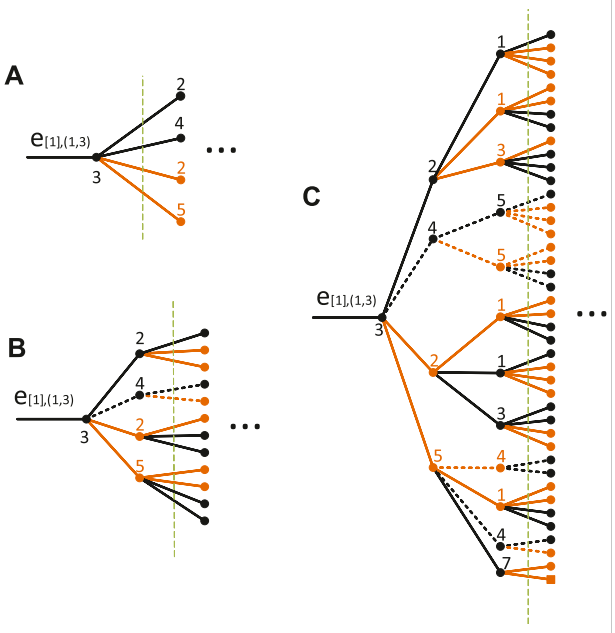

FIGURE 2
Graphic illustration of $Y_{[1],n}$ of the two-layer network shown in Figure 1. The MNEB $B(e_{[1],(1,3)}, 3)$ has the root colored with c_1 = *black*. For example, we perform **k** = (1, 2)-core decomposition on the network. The green dashed line is the indication line of the first n stratum of the MNEB. The solid lines in the MNEB represent the stubs that fulfill condition 2 under the given **k**. The condition that an MNEB belongs to $Y_{[1],n}$ is then decided by whether the MNEB has a solid sub-branch crossing the green dashed indication line. **(A)** shows that $B(e_{[1],(1,3)}, 3) \in Y_{[1],1}$. **(B)** shows that $B(e_{[1],(1,3)}, 3) \in Y_{[1],2}$. **(C)** shows that $B(e_{[1],(1,3)}, 3) \in Y_{[1],3}$. In addition, for **k** = (2, 2), we can also see that $B(e_{[1],(1,3)}, 3) \in Y_{[1],1}$ **(A)** and $B(e_{[1],(1,3)}, 3) \in Y_{[1],2}$ **(B)**. But for $n = 3$, we cannot find such a sub-branch that for each black vertex in the first three strata of this sub-branch, the number of red child vertices is no less than 2, and the number of black child vertices is no less than 1, and for each red vertex in the first three strata of this sub-branch, the number of red child vertices is no less than 1, and the number of black child vertices is no less than 2. Therefore, $B(e_{[1],(1,3)}, 3) \notin Y_{[1],3}$. Here, the discs represent the vertices that have child vertices, and the squares represent the vertices without child vertices.

For a given R-dimensional positive integral vector $\mathbf{k} = (k_1, k_2, \ldots, k_R)$, we can find a set of MNEBs $Y_{[i],n}$ (n is a positive integer) for each $1 \le i \le R$ that meet the following two conditions: 1. the root of the MNEB is colored with c_i; 2. there exists a sub-branch of the MNEB that contains the root stub; for each vertex colored with c_j in the first n strata of this sub-branch, it has at least $k_j - 1$ child vertices colored with c_j and at least k_l child vertices colored with c_l for every $l \neq j (1 \le l \le R)$. Figure 2 shows the details of how to decide whether an MNEB belongs to $Y_{[i],n}$. When $n = 0$, for each $1 \le i \le R$, we define $Y_{[i],0}$ as all the MNEBs whose roots are colored with c_i. Obviously, $Y_{[i],0} \supset Y_{[i],1} \supset \cdots \supset Y_{[i],n} \supset \ldots$. We denote $S_{MNEB}(V)$ as the set of MNEBs of all the stubs in $S(V)$ and $S_{MNEB}(e_{[i]}, V)$ as the set of MNEBs of all the stubs in $S(e_{[i]}, V)$. It is easy to obtain the following theorem from the definition of $Y_{[i],n}$:

Theorem 1. For a stub $(e_{[i]}, V)$ in the i^{th} layer, the MNEB $B(e_{[i]}, V)$ belongs to $Y_{[i],n}$ if and only if among all the MNEBs in $S_{MNEB}(e_{[i]}, V)$, at least k_i-1 MNEBs belong to $Y_{[i],n-1}$ and k_l MNEBs belong to $Y_{[l],n-1}$ for every $l \neq j$ $(1 \leq l \leq R)$.

Let S_n be the set of the remaining vertices after n^{th} pruning, and the following theorem can be established.

Theorem 2. It is denoted by V, a vertex in the network, $V \in S_n$, if and only if among the MNEBs in $S_{MNEB}(V)$, for every $1 \leq l \leq R$, at least k_l MNEBs belong to $Y_{[l],n-1}$.

The proof of Theorem 2 is given in Appendix. An illustration of the five MNEBs in $S_{MNEB}(1)$ of the network from Figure 1 along with a short exemplary analysis using Theorem 2 is presented in Appendix as well.

3 Analysis on large uncorrelated multiplex networks

As a special case, we start with the partly uncorrelated multiplex networks, in which the degrees of vertices are uncorrelated in each layer but the degrees of vertices in different layers are allowed to be interdependent.

For a random vertex V, it has the degree series $(i_1, i_2, \ldots, i_R)$ on a large uncorrelated multiplex network, where $i_1, i_2, \ldots, i_R$ represent the degrees of a vertex in 1, 2, . . ., R layers of the network, respectively. The joint degree distribution probability of the vertex is denoted by $p_{i_1,i_2,\ldots,i_R}$, and the joint excess degree distribution of the vertex in the j^{th} layer is denoted by $q^{[j]}_{i_1,i_2,\ldots,i_R}$, which is the probability that follows a randomly chosen edge in the j^{th} layer, and one of its endpoints has the excess degree k_i, while in the h^{th} layer$(h \neq j)$, its degree is i_h. After that, we can define the following two generating functions:

$$G_0(z_1, z_2, \ldots, z_R) = \sum_{i_1=0}^{\infty} \cdots \sum_{i_R=0}^{\infty} p_{i_1,i_2,\ldots,i_R} z_1^{i_1} \cdot \cdots \cdot z_R^{i_R}, \quad (3)$$

$$G_1^{[j]}(z_1, z_2, \ldots, z_R) = \sum_{i_1=0}^{\infty} \cdots \sum_{i_R=0}^{\infty} q^{[j]}_{i_1,i_2,\ldots,i_R} z_1^{i_1} \cdot \cdots \cdot z_R^{i_R}, \quad (4)$$

where the superscript in the second definition indicates the generating function defined in the j^{th} layer.

These two generating functions are related by

$$G_1^{[j]}(z_1, z_2, \ldots, z_R) = \frac{1}{c_j} \frac{\partial G_0(z_1, z_2, \ldots, z_R)}{\partial z_j}, \quad (5)$$

where c_j is the average degree of the j^{th} layer network. For convenience, we introduce the following denotation:

$$\sum_{\mathbf{i}=\mathbf{x}}^{\mathbf{t}} = \sum_{i_1=x_1}^{t_1} \sum_{i_2=x_2}^{t_2} \cdots \sum_{i_R=x_R}^{t_R},$$

where $\mathbf{x}$ and $\mathbf{t}$ are two fixed integral R dimensional vectors. The aforementioned denotation means to take the sum for $\mathbf{i}$ from the first component to the last component. Of course, there must be $t_j \geq x_j$ for each $1 \leq j \leq R$.

Let $y_{[j],n}$ be the probability that an MNEB whose root is colored with c_j belongs to $Y_{[j],n}$, then from Theorem 1, we can obtain the recursive relationship:

$$\begin{aligned} y_{[j],n} &= \sum_{\mathbf{i}=\mathbf{k}_j}^{\infty} q_{\mathbf{i}}^{[j]} \sum_{\mathbf{m}=\mathbf{k}_j}^{\mathbf{i}} \prod_{l=1}^{R} \binom{i_l}{m_l} \left(y_{[l],n-1}\right)^{m_l} \left(1 - y_{[l],n-1}\right)^{i_l - m_l} \\ &= \sum_{\mathbf{m}=\mathbf{k}_j}^{\infty} \frac{\partial^{(m_1+\cdots+m_R)} G_1^{[j]}}{\partial z_1^{m_1} \ldots \partial z_R^{m_R}}\bigg|_{\mathbf{z}=\mathbf{1}-\mathbf{y}_{n-1}} \prod_{l=1}^{R} \frac{\left(y_{[l],n-1}\right)^{m_l}}{m_l!}, \end{aligned} \quad (6)$$

where $y_{[j],0} = 1$ for every $1 \leq j \leq R$. In the aforementioned equation, it should be noted that the summation indexes $\mathbf{i} = (i_1, i_2 \ldots i_R)$ and $\mathbf{m} = (m_1, m_2 \ldots m_R)$ are vectors. When performing a $\mathbf{k}$-core on the multiplex network ($\mathbf{k}$ is a vector), we define an R-dimensional integral vector $\mathbf{k}_j = (k_1, \ldots, k_{j-1}, k_j-1, k_{j+1} \ldots k_R)$. $\mathbf{y}_{n-1}$ denotes the R-dimensional vector $(y_{[1],n-1}, y_{[2],n-1} \ldots y_{[R],n-1})$. Therefore, $\mathbf{1}-\mathbf{y}_{n-1}$ is the R- dimensional vector $(1 - y_{[1],n-1}, 1 - y_{[2],n-1}, \ldots 1 - y_{[R],n-1})$.

Then, we denote by s_n the probability that a randomly chosen vertex belongs to S_n.

$$\begin{aligned} s_n &= \sum_{\mathbf{i}=\mathbf{k}}^{\infty} p_{\mathbf{i}} \sum_{\mathbf{m}=\mathbf{k}}^{\mathbf{i}} \prod_{l=1}^{R} \binom{i_l}{m_l} \left(y_{[l],n-1}\right)^{m_l} \left(1 - y_{[l],n-1}\right)^{i_l - m_l} \\ &= \sum_{\mathbf{m}=\mathbf{k}}^{\infty} \frac{\partial^{(m_1+\cdots+m_R)} G_0}{\partial z_1^{m_1} \ldots \partial z_R^{m_R}}\bigg|_{\mathbf{z}=\mathbf{1}-\mathbf{y}_{n-1}} \prod_{l=1}^{R} \frac{\left(y_{[l],n-1}\right)^{m_l}}{m_l!}. \end{aligned} \quad (7)$$

In the completely uncorrelated multiplex network, where there exists no correlation in different layers, we have $p_{i_1,\ldots,i_R} = p_{i_1} \cdot p_{i_2} \cdots p_{i_R}$; hence, the generating function can be simplified:

$$G_0(z_1, z_2, \ldots, z_R) = \prod_{j=1}^{R} G_{[j],0}(z_j), \quad (8)$$

$$G_1^{[j]}(z_1, z_2, \ldots, z_R) = G_{[j],1}(z_j) \prod_{h=1, h\neq j}^{R} G_{[h],0}(z_h). \quad (9)$$

Here, $G_{[j],0}(z_j)$ and $G_{[j],1}(z_j)$ are the generating functions of the degree distribution and excess degree distribution of the j^{th} layer network, respectively. Substituting these two generating functions into Eqs 6, 7, we obtain

$$\begin{aligned} y_{[j],n} = &\left[1 - \sum_{m=0}^{k_j-2} \frac{\left(y_{[j],n-1}\right)^m}{m!} G^{(m)}_{[j],1}\left(1 - y_{[j],n-1}\right)\right] \\ &\times \prod_{h=1, h\neq j}^{R} \left[1 - \sum_{m=0}^{k_h-1} \frac{\left(y_{[h],n-1}\right)^m}{m!} G^{(m)}_{[h],0}\left(1 - y_{[h],n-1}\right)\right] \end{aligned} \quad (10)$$

and:

$$s_n = \prod_{h=1}^{R} \left[1 - \sum_{m=0}^{k_h-1} \frac{\left(y_{[h],n-1}\right)^m}{m!} G^{(m)}_{[h],0}\left(1 - y_{[h],n-1}\right)\right]. \quad (11)$$

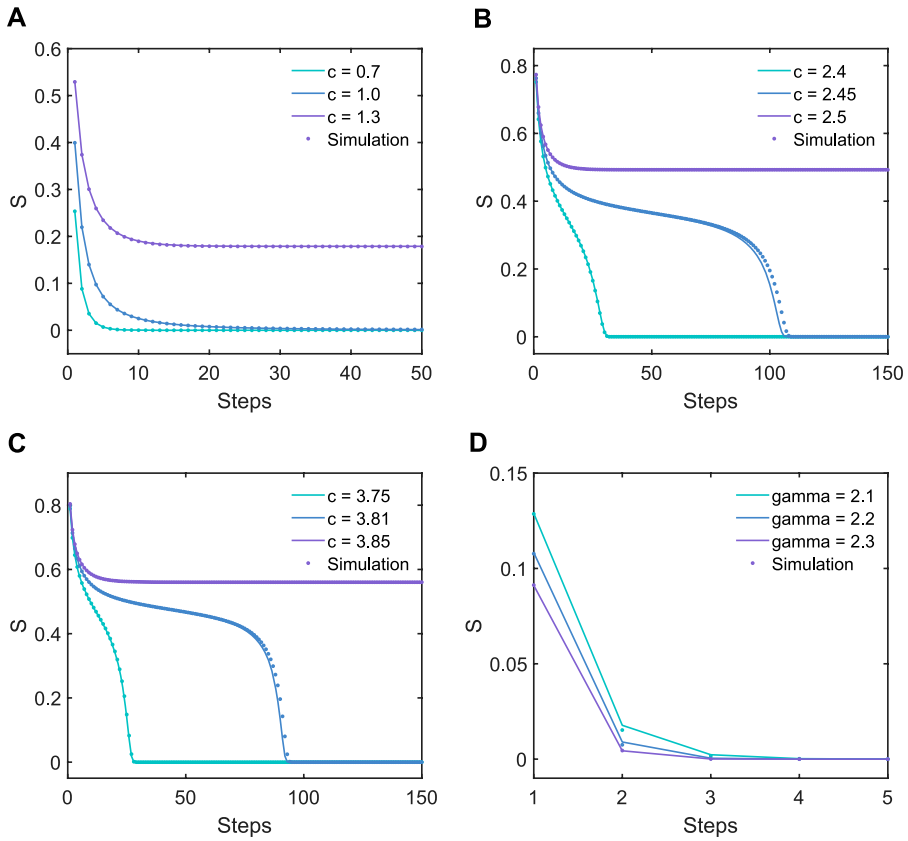

FIGURE 3
Theoretical results (solid lines) and numerical simulation results (dots) for **k**-core decompositions on multiplex networks with identical parameters. All simulations are performed on networks with 10^7 vertices, except that in the simulations of $c = 2.45$ **(B)**, $c = 3.81$ **(C),** and $\gamma = 2.1$ **(D)**, the networks contain 5×10^7 vertices. **(A)** Results of the (1,1)-core pruning process on three different two-layer uncorrelated ER networks. It should be noted that in this case, it shows a continuous phase transition. **(B)** Results of the (1,1,1)-core pruning process on three different three-layer uncorrelated ER networks. In this case, the networks exhibit a discontinuous phase transition. **(C)** Results of the (2,2)-core pruning process on three different two-layer uncorrelated ER networks. It should be noted that in this case, the networks exhibit a discontinuous phase transition, different from the case shown **(A)**. **(D)** Results of the (2,2)-core pruning process on three different two-layer uncorrelated SF networks. In this case, the (2,2)-core does not exist for $\gamma > 2$.

We further perform several numerical simulations to validate the theoretical results, as given in Section 4.

4 Numerical simulations

To validate our method, we perform several **k**-core decompositions on completely uncorrelated multiplex Erdős–Rényi networks (ER networks) and scale-free networks (SF networks). The ER networks are randomly generated with the parameter c to denote the average degree of vertices, and the order of power–law distribution on SF networks is denoted by γ. In the numerical simulation, we build a multiplex network for the same group of vertices, and different layers of the network have different interaction topologies. At each pruning step, we examine the changes of all layers at the same time; as long as the degree of a vertex in a certain layer is less than the corresponding k of that layer, this node will be removed from all layers. The results are shown in Figure 3. It can be observed that our theoretical results are in perfect accordance with the numerical simulations. Figures 3A-D show the theoretical results and numerical results on 4 types of pruning process on several networks. Interestingly, we can find that on ER networks, (1,1)-core pruning is a continuous phase transition. Compared to this, Figure 3B shows that in the three-layer ER network, the phase transition of the k-core near the critical point shows a discontinuous phase transition, which is also reflected in [26], in which it is observed that as the number of layers of the network

increases, the system tends to collapse drastically. In addition, as shown in Figure 3C, discontinuous phase transitions also occur in the (2, 2)-core of the two-layer network. The same is shown in Figure 3B; the k-core pruning process also exhibits rich critical behavior when c is slightly lower than the critical point. The system will go through a long-term transient process and finally collapse, forming a discontinuous phase transition.

5 Conclusion

Overall, in this paper, we derive a new variation of the Non-Backtracking Expansion Branch called the Multicolor Non-Backtracking Expansion Branch, specially designed to solve the **k**-core pruning process on multiplex networks. In a multiplex network, each layer of the network is assigned a unique color, and then, the Multicolor Non-Backtracking Expansion Branch is constructed as an infinite tree having the same local structural information as the given multiplex network, when observed by non-backtracking walkers. We find that with this representation, one can obtain the analytical results of the **k**-core pruning process on any given multiplex network, regardless whether the correlation exists or not. The theoretical results obtained by our method are further validated by numerical simulations. Due to the diversity of edges in multiplex networks, the types of interactions that can be expressed will be much richer than those in a single-layer network. Many characteristic behaviors lacking in single-layer networks emerge in multilayer networks. For example, the phase transition of the k-core in a multi-layer network shows a different behavior compared to that of a single-layer network, as shown in Figure 3, and our method can be used for both single-layer and multi-layer networks and can obtain the analytical results of its k-core. Our method opens new possibilities to analytically solve the **k**-core pruning process on any given multiplex network, which is valuable for both theoretical studies and real-world applications.

Data availability statement

The original contributions presented in the study are included in the article/Supplementary Material; further inquiries can be directed to the corresponding author.

Author contributions

G-YS designed the research; R-JW and G-YS performed the theoretical analysis; Y-XK, G-YS, and Y-CZ designed the figures and performed the numerical experiments. All authors wrote the manuscript.

Conflict of interest

The authors declare that the research was conducted in the absence of any commercial or financial relationships that could be construed as a potential conflict of interest.

Publisher's note

All claims expressed in this article are solely those of the authors and do not necessarily represent those of their affiliated organizations, or those of the publisher, the editors, and the reviewers. Any product that may be evaluated in this article, or claim that may be made by its manufacturer, is not guaranteed or endorsed by the publisher.

References

1. Du N, Wu B, Pei X, Wang B, Xu L. Community detection in large-scale social networks. In: Proceedings of the 9th WebKDD and 1st SNA-KDD 2007 workshop on Web mining and social network analysis (ACM) (2007). p. 16–25.

2. Fortunato S. Community detection in graphs. *Phys Rep* (2010) 486:75–174. doi:10.1016/j.physrep.2009.11.002

3. Papadopoulos S, Kompatsiaris Y, Vakali A, Spyridonos P. Community detection in social media. *Data Min Knowl Discov* (2012) 24:515–54. doi:10.1007/s10618-011-0224-z

4. Weng L, Menczer F, Ahn YY. Virality prediction and community structure in social networks. *Sci Rep* (2013) 3:2522. doi:10.1038/srep02522

5. Kong YX, Shi GY, Wu RJ, Zhang YC. k-core: Theories and applications. *Phys Rep* (2019) 832:1–32. doi:10.1016/j.physrep.2019.10.004

6. Shang F, Chen B, Expert P, Lü L, Yang A, Stanley HE, et al. *Local dominance unveils clusters in networks* (2022). *arXiv preprint arXiv:2209.15497*.

7. Kitsak M, Gallos LK, Havlin S, Liljeros F, Muchnik L, Stanley HE, et al. Identification of influential spreaders in complex networks. *Nat Phys* (2010) 6:888–93. doi:10.1038/nphys1746

8. Li R, Wang W, Di Z. Effects of human dynamics on epidemic spreading in côte d'ivoire. *Physica A: Stat Mech its Appl* (2017) 467:30–40. doi:10.1016/j.physa.2016.09.059

9. Alvarez-Hamelin JI, Dall'Asta L, Barrat A, Vespignani A. Large scale networks fingerprinting and visualization using the k-core decomposition. In: *Advances in neural information processing systems* (2006). p. 41–50.

10. Serrano MÁ, Boguná M, Vespignani A. Extracting the multiscale backbone of complex weighted networks. *Proc Natl Acad Sci U S A* (2009) 106:6483–8. doi:10.1073/pnas.0808904106

11. Goltsev AV, Dorogovtsev SN, Mendes JFF. k-core (bootstrap) percolation on complex networks: Critical phenomena and nonlocal effects. *Phys Rev E* (2006) 73:056101. doi:10.1103/physreve.73.056101

12. Dorogovtsev SN, Goltsev AV, Mendes JFF. K-core organization of complex networks. *Phys Rev Lett* (2006) 96:040601. doi:10.1103/physrevlett.96.040601

13. Altaf-Ul-Amin M, Shinbo Y, Mihara K, Kurokawa K, Kanaya S. Development and implementation of an algorithm for detection of protein complexes in large interaction networks. *BMC bioinformatics* (2006) 7:207. doi:10.1186/1471-2105-7-207

14. Li X, Wu M, Kwoh CK, Ng SK. Computational approaches for detecting protein complexes from protein interaction networks: A survey. *BMC genomics* (2010) 11:S3. doi:10.1186/1471-2164-11-s1-s3

15. Antiqueira L, Oliveira ON, Jr, da Fontoura Costa L, Nunes Md. GV. A complex network approach to text summarization. *Inf Sci* (2009) 179:584–99. doi:10.1016/j.ins.2008.10.032

16. Fernholz D, Ramachandran V. *Cores and connectivity in sparse random graphs*. Austin, TX, USA: The University of Texas at Austin, Department of Computer Sciences (2004). *technical report TR-04-13*.

17. Schwarz J, Liu AJ, Chayes L. The onset of jamming as the sudden emergence of an infinite k-core cluster. *Europhys Lett* (2006) 73:560–6. doi:10.1209/epl/i2005-10421-7

18. Baxter G, Dorogovtsev S, Lee KE, Mendes J, Goltsev A. Critical dynamics of thek-core pruning process. *Phys Rev X* (2015) 5:031017. doi:10.1103/physrevx.5.031017

19. Wu RJ, Kong YX, Di Z, Zhang YC, Shi GY. Analytical solution to the k-core pruning process. *Physica A: Stat Mech its Appl* (2022) 2022:128260. doi:10.1016/j.physa.2022.128260

20. Boccaletti S, Bianconi G, Criado R, Del Genio CI, Gómez-Gardenes J, Romance M, et al. The structure and dynamics of multilayer networks. *Phys Rep* (2014) 544:1–122. doi:10.1016/j.physrep.2014.07.001

21. Szell M, Lambiotte R, Thurner S. Multirelational organization of large-scale social networks in an online world. *Proc Natl Acad Sci U S A* (2010) 107:13636–41. doi:10.1073/pnas.1004008107

22. Li R, Tang M, Hui P. Epidemic spreading on multi-relational networks. *Acta Phys Sin* (2013) 62:168903. doi:10.7498/aps.62.168903

23. Azimi-Tafreshi N, Gómez-Gardenes J, Dorogovtsev S. k–corepercolation on multiplex networks. *Phys Rev E* (2014) 90:032816. doi:10.1103/physreve.90.032816

24. Osat S, Radicchi F, Papadopoulos F. k-core structure of real multiplex networks. *Phys Rev Res* (2020) 2:023176. doi:10.1103/physrevresearch.2.023176

25. Radicchi F, Bianconi G. Redundant interdependencies boost the robustness of multiplex networks. *Phys Rev X* (2017) 7:011013. doi:10.1103/physrevx.7.011013

26. Shang Y. Generalized k-core percolation on correlated and uncorrelated multiplex networks. *Phys Rev E* (2020) 101:042306. doi:10.1103/physreve.101.042306

Appendix

6.1 Proof of Theorem 2

We use mathematical induction to prove the theorem. It is obvious that the theorem holds for $n = 1$. Now, we prove that if the theorem is true for $n-1$, the theorem can be established for n.

First, we prove the sufficiency, that is, for every $1 \le l \le R$, when at least k_l MNEBs in $S_{MNEB}(V)$ belong to $Y_{[l],n-1}$, there must be $V \in S_n$. Since for every $1 \le l \le R$, $Y_{[l],n-1} \subset Y_{[l],n-2}$, we obtain $V \in S_{n-1}$, and in any given layer (for instance, the i^{th} layer), suppose that $\{B(e_{[i],j_1}, V_{j_1}), \ldots, B(e_{[i],j_m}, V_{j_m})\} \subset S_{MNEB}(V)$ belong to $Y_{[i],n-1}$, here $m \ge k_i$; so for each $1 \le r \le m$, in $S_{MNEB}(e_{[i],j_r}, V_{j_r})$, at least k_i-1 MNEBs belong to $Y_{[i],n-2}$, and k_l MNEBs belong to $Y_{[l],n-2}$ for every $l \ne j (1 \le l \le R)$. On the other hand, $B(e_{[i],j_r}, V) \in Y_{[i],n} \subset Y_{[i],n-2}$, so in $S_{MNEB}(V_{j_r})$, for every $1 \le l \le R$, at least k_l MNEBs belong to $Y_{[l],n-2}$. The induction hypothesis gives $V_{j_r} \in S_{n-1}$. Therefore, in $(n-1)^{th}$ pruning, in any given i^{th} layer, at least k_i neighbors of V are retained. We can conclude that V is still retained in the n^{th} pruning.

Next, we prove the necessity. We attempt to prove that when there exists an l in $[1, R]$, which satisfies that at most k_l-1 MNEBs in $S_{MNEB}(V)$ belong to $Y_{[l],n-1}$, there must be $V \notin S_n$. Since for an MNEB $B(e_{[l],r}, V_r)$ whose root is colored with c_l in $S_{MNEB}(V)$ that does not belong to $Y_{[l],n-1}$, from Theorem 1, we know that in $S_{MNEB}(e_{[l],r}, V_r)$, either at most k_l-2 MNEBs belong to $Y_{[l],n-2}$, or there exists $h \ne l$, $1 \le h \le R$ that at most k_h-1 MNEBs belong to $Y_{[h],n-2}$. Therefore, in $S_{MNEB}(V_r)$, there exists $1 \le h \le R$ that at most k_h-1 MNEBs belong to $Y_{[h],n-2}$. From the induction hypothesis, we know that $V_r \notin S_{n-1}$, which means after $(n-1)^{th}$ pruning, in the l^{th} layer, at most k_l-1 neighbors of V survived. So either V has been pruned in $(n-1)^{th}$ pruning or even before, or it survived in the $(n-1)^{th}$ pruning but would be deleted in the n^{th} pruning since its remaining neighbors in the l^{th} layer are less than k_l after the $(n-1)^{th}$ pruning; then, we have $V \notin S_n$.

At this point, sufficiency and necessity are proved, and Theorem 2 can be established.

6.2 An example of Theorem 2

Figure A1 are $B(e_{[1],(1,3)}, 3)$, $B(e_{[1],(1,2)}, 2)$, $B(e_{[2],(1,2)}, 2)$, $B(e_{[2],(1,5)}, 5)$, and $B(e_{[2],(1,8)}, 8)$, respectively. For $\mathbf{k} = (2, 1)$ core decomposition, we can find $B(e_{[1],(1,3)}, 3) \in Y_{[1],\infty}$, $B(e_{[1],(1,2)}, 2) \in Y_{[1],\infty}$, $B(e_{[2],(1,2)}, 2) \in Y_{[2],\infty}$, $B(e_{[2],(1,5)}, 5) \in Y_{[2],\infty}$, and $B(e_{[2],(1,8)}, 8) \notin Y_{[2],1}$. So in $S_{MNEB}(1)$, there are two MNEBs that belong to $Y_{[1],\infty}$ and two MNEBs that belong to $Y_{[2],\infty}$. So we have the vertex $1 \in S_\infty$. For $\mathbf{k} = (2, 2)$, we can find that $B(e_{[1],(1,3)}, 3) \in Y_{[1],2}$, but it does not belong to $Y_{[1],3}$. $B(e_{[1],(1,2)}, 2) \in Y_{[1],3}$, but it does not belong to $Y_{[1],4}$. $B(e_{[2],(1,2)}, 2) \in Y_{[2],3}$, but it does not belong to $Y_{[2],4}$. $B(e_{[2],(1,5)}, 5) \in Y_{[2],1}$, but it does not belong to $Y_{[1],2}$. $B(e_{[2],(1,8)}, 8) \notin Y_{[2],1}$. So we can conclude that vertex 1 survives in the first two steps but will be deleted in the third pruning step.

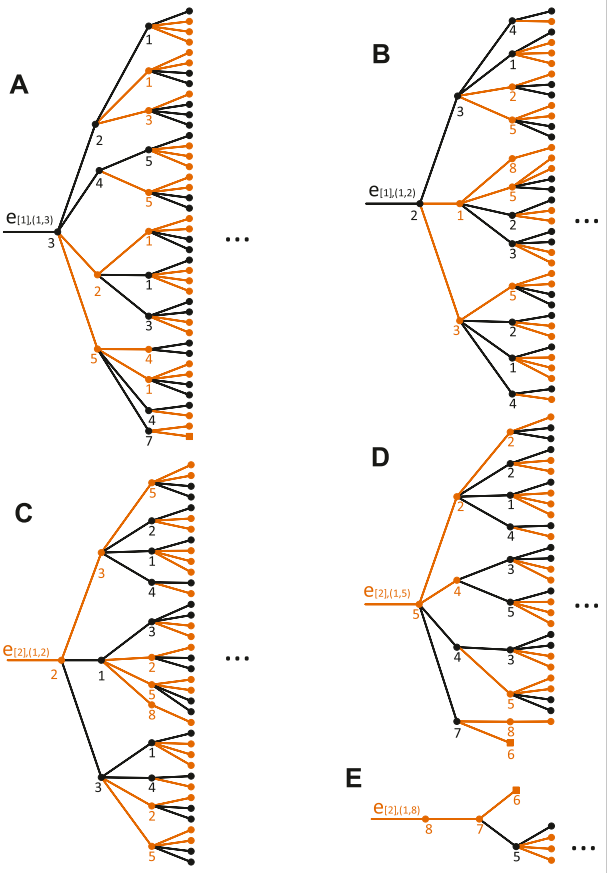

FIGURE A1
All five MNEBs in $S_{MNEB}(1)$ of the network shown in Figure 1. **(A–E)** represent the MBEB of e[1],(1,3), e[1],(1,2), e[2],(1,2), e[2],(1,5), e[1],(1,8), respectively.

frontiers | Frontiers in Physics

TYPE Original Research
PUBLISHED 19 December 2022
DOI 10.3389/fphy.2022.1062554

OPEN ACCESS

EDITED BY
Thomas Peron,
University of São Paulo, Brazil

REVIEWED BY
Wei Wang,
Chongqing Medical University, China
Enrico Schiassi,
University of Arizona, United States

*CORRESPONDENCE
Feng Chen,
fengchen@njmu.edu.cn

SPECIALTY SECTION
This article was submitted to Interdisciplinary Physics, a section of the journal Frontiers in Physics

RECEIVED 06 October 2022
ACCEPTED 30 November 2022
PUBLISHED 19 December 2022

CITATION
Ning X, Li X-A, Wei Y and Chen F (2022), Euler iteration augmented physics-informed neural networks for time-varying parameter estimation of the epidemic compartmental model. *Front. Phys.* 10:1062554. doi: 10.3389/fphy.2022.1062554

Euler iteration augmented physics-informed neural networks for time-varying parameter estimation of the epidemic compartmental model

Xiao Ning[1], Xi-An Li[2], Yongyue Wei[3,4] and Feng Chen[1,4]*

[1]State Key Laboratory of Bioelectronics, School of Biological Science and Medical Engineering, Southeast University, Nanjing, China, [2]Ceyear Technologies Co., Ltd., Qingdao, China, [3]Public Health and Epidemic Preparedness and Response Center, Peking University, Beijing, China, [4]Department of Epidemiology and Biostatistics, Center for Global Health, School of Public Health, Nanjing Medical University, Nanjing, China

Introduction: Differential equations governed compartmental models are known for their ability to simulate epidemiological dynamics and provide highly accurate descriptive and predictive results. However, identifying the corresponding parameters of flow from one compartment to another in these models remains a challenging task. These parameters change over time due to the effect of interventions, virus variation and so on, thus time-varying compartmental models are required to reflect the dynamics of the epidemic and provide plausible results.

Methods: In this paper, we propose an Euler iteration augmented physics-informed neural networks(called Euler-PINNs) to optimally integrates real-world reported data, epidemic laws and deep neural networks to capture the dynamics of COVID-19. The proposed Euler-PINNs method integrates the differential equations into deep neural networks by discretizing the compartmental model with suitable time-step and expressing the desired parameters as neural networks. We then define a robust and concise loss of the predicted data and the observed data for the epidemic in question and try to minimize it. In addition, a novel activation function based on Fourier theory is introduced for the Euler-PINNs method, which can deal with the inherently stochastic and noisy real-world data, leading to enhanced model performance.

Results and Discussion: Furthermore, we verify the effectiveness of the Euler-PINNs method on 2020 COVID-19-related data in Minnesota, the United States, both qualitative and quantitative analyses of the simulation results demonstrate its accuracy and efficiency. Finally, we also perform predictions based on data from the early stages of the outbreak, and the experimental results demonstrate that the Euler-PINNs method remains robust on small dataset.

KEYWORDS

parameter estimation, physics-informed neural network, Euler iteration, SIRD compartmental model, fourier feature mapping

1 Introduction

Mathematical models have proved invaluable to understanding and analyzing the transmission of infectious diseases, and many efforts have been made in epidemiological field [1]. Epidemic compartmental models governed by a system of differential equations can capture epidemiological dynamics and provide highly accurate descriptive and predictive results. Thus, the compartmental models served as the most widely applied modeling approach to analyze the transmission and evolution of infectious diseases [2, 3]. They also play a critical role in evaluating the effectiveness of interventions implemented by authorities in response to epidemic viruses [4]. The coronavirus disease 2019 (COVID-19) has overwhelmingly shocked and shaken the entire world continuously and unexpectedly, the World Health Organization (WHO) declared COVID-19 as a pandemic on 11 March 2020 [5]. Many people become sick, suffer from the Long Covid, and even lost their lives after being infected. Various interventions were implemented to fight the pandemic, specifically to reduce transmission and its impact on healthcare systems [6]. Epidemic compartmental models categorized the population into different compartments based on disease status and subsequently written mathematical equations to model infectious diseases. The basic Susceptible-Infectious-Removed (SIR) model was proposed by Kermack and McKendrick to model the dynamics of the Black Death in London in the year 1927 [7]. Since the start of COVID-19, epidemic compartmental models have been at the forefront of understanding and predicting the situation for supporting decision-making. Various compartmental models have been proposed to characterize the evolution of COVID-19 by adding customized compartments to the classical SIR model, such as the SEIR model with incubation period (E), the SEAIR model with the symptomatic carrier (A), the SEIRS model considering recurrent infection [8–10]. Wang et al use a modelling approach to reconstruct the full-spectrum dynamics of COVID-19 in Wuhan between 1 January and 8 March 2020 across 5 periods defined by events and interventions, identified the high covertness and high transmissibility features of the outbreak [11]. Wei et al. proposed an extended SEIR mode to evaluate how the implementation of clinical diagnostic criteria and universal symptom survey contributed to epidemic control in Wuhan [12].

Once a compartmental model is constructed to simulate a given scenario, the key task is to estimate the related parameters that govern its behavior. Many research efforts focus on parameter estimation of epidemic compartmental models, which fall into two main groups: deterministic and probabilistic, such as maximum likelihood estimation, Markov Chain Monte Carlo (MCMC)-based Bayesian inference [13–15], finite element methods [16], and so on. The deterministic approach uses optimization techniques to find a set of optimal parameters which satisfy the minimization of the difference between simulated and real data. The probabilistic approach especially Bayesian inversion techniques can obtain the probability distribution for each of those parameters to measure the uncertainty [17]. However, these methods suffer from important limitations, such as the problem being non-unique due to the higher number of unknowns than observations, and computational cost increasing exponentially with the complexity of the parameters and models, which hinders their application. Moreover, the fact is that related parameters may change over time in real-world scenarios due to interventions implemented by authorities, population behavioral changes, and/or mutations of the virus. Accordingly, compartmental models require time-varying parameters to capture the evolution of COVID-19 epidemiological attributes including time-varying infection, recovery, and mortality rate. Several research works have attempted to estimate time-varying parameters of the model using complex regression methods [18–20]. These methods for identifying time-varying parameters are in the context of the regression framework in which the time-varying parameters are defined as combinations of basis functions. Such a framework contains numerous parameters and employing intelligent algorithms to determine the parameters can not guarantee an optimal solution. In most instances, finding local optimum can be extremely hard, let alone the global optimum. In addition, the random initialization and following search strategies of such algorithms may lead to different solutions for each execution. Deep learning, also commonly referred to as deep neural networks (DNNs), has been used for dynamical system simulations indicating the strong potential of this computational method to address a wide variety of parameter identification tasks [21]. Neural networks can be viewed as discretizations of continuous dynamical systems, making them well-suited for dealing with dynamic systems. Moreover, the universal approximation theorem guarantees that arbitrary continuous functions can be approximated by neural networks with a sufficient number of hidden units. These two mentioned reasons facilitate DNNs achieved outstanding performance in scientific computation and parameter evaluation. It is important to note that the Physics-informed neural networks (PINNs) framework was originally developed for time-dependent partial differential equations (PDEs) and had been widely used in various domains [22–24]. The PINNs framework perfectly integrates data and mathematical models, it performs accurately and efficiently in the context of the dynamical system when partial spatio-temporal data are available. Recently, exploring the application potential of the PINNs framework in compartmental models has received attention, as many studies have demonstrated the capacity of the PINNs framework to be stable, efficient, and accurate in parameter estimation [25–28]. For example, Kharazmi et al analyze several variations of the classical SIR model through the lens of PINNs to identify time-dependent parameters for

compartmental models [29]. Hu et al proposed a modified PINNs approach to estimate the unknown infected compartment I, and several unknown parameters [30].

In this paper, by skillfully incorporating the idea of Euler iteration and the Physics-informed neural networks, we propose an Euler iteration-based deep neural networks (called Euler-PINNs) to estimate the time-varying parameters for epidemic compartmental models. Firstly, we constructed a susceptible-infected-recovered-deceased (SIRD) compartmental model following the transmission behaviour of COVID-19. Next, several separate deep neural networks are built to express corresponding parameters in the SIRD model, and Euler iteration is applied to solve the equations. Lastly, we define a loss as the discrepancy between the predicted and the observed data of the epidemic in question and try to minimize it. After that, we applied the proposed Euler-PINNs method to the COVID-19 reported data from the state of Minnesota, in the United States. The experimental findings on the synthesized data have revealed that the proposed Euler-PINNs method can estimate reliable time-varying parameters that explicitly depicted the transmission trend of an infectious dynamical system over time. Specifically, both quantitative and qualitative analyses of estimated parameters in the context of the corresponding interventions are consistent with expected dynamics and previous publications. Furthermore, the proposed Euler-PINNs method is applied to predict early outbreaks, demonstrating its reliable prediction as well as robust performance on a small dataset. The main contributions of this paper are as follows:

- We proposed an Euler-PINNs method to estimate the time-vary parameters of the compartmental model. To the best of our knowledge, it is the first method to explore integrating compartmental model and Euler iteration into deep neural networks to model the dynamic of the infectious disease. Different from directly modeling all the compartments and parameters using neural networks, leveraging the Euler iteration in forward process provides more constraints to the network. As a result, this makes the network easier to converge and increases the explainability of the network as well as the plausibility of the results.
- We transform the continuous-time differential equations into discrete-time difference equations and build corresponding neural networks for each time-varying parameter in the equations. Then applying Euler iteration to integrate the neural networks and the differential equations to estimate the time-varying parameters in the equations. In addition, we add Fourier transformation for the input data before feed it to the network, considering that COVID-19 epidemic-related data is from real-world report, which is inherently, stochastic, and noisy.
- We applied the proposed Euler-PINNs method to 2020 COVID-19 data from the state of Minnesota, the United States, to analyze the effectiveness of the interventions. The estimated time-varying parameters of the SIRD compartmental model well explained the COVID-19 evolution under the light of government interventions that were taken, showing consistency in comparison with published works. More importantly, the proposed Euler-PINNs method can provide a reliable prediction for an early outbreak.

The rest of the paper is organized as follows. In Section 2, we briefly introduce Fourier neural networks, including the fundamental theory of neural networks, activation functions and Fourier mapping. Section 3 presents the SIRD compartmental model constructed for a given COVID-19 transmission scenario, and the Eulerian iteration to discretise the model. Moreover, a detailed description of how to integrate the compartmental model and Euler iteration into the neural network and how to design the loss function is provided. In Section 4, we test the proposed Euler-PINNs method with 2020 COVID-19 data from the state of Minnesota, discuss the results obtained and perform prediction for early stage outbreaks. Section 5 wraps up this work with a summary of conclusions, opportunities, and limitations.

2 Fourier induced deep neural networks

2.1 Deep neural networks

This section briefly introduces the relevant concepts and mathematical formulation of DNNs. Mathematically, the DNNs defines a mapping of functions

$$\mathcal{F}: \boldsymbol{x} \in \mathbb{R}^d \Rightarrow \boldsymbol{y} = \mathcal{F}(\boldsymbol{x}) \in \mathbb{R}^c, \tag{1}$$

where d and c are the dimensions of input and output, respectively. At first, a standard neural unit of DNNs with an input $\boldsymbol{x} \in \mathbb{R}^d$ and an output $\boldsymbol{y} \in \mathbb{R}^m$ is in the form of

$$\boldsymbol{y} = \sigma(\boldsymbol{W}\boldsymbol{x} + \boldsymbol{b}) \tag{2}$$

where $\boldsymbol{W} \in \mathbb{R}^{d\times m}$ and $\boldsymbol{b} \in \mathbb{R}^m$ stand for weight matrix and bias vector, respectively. $\sigma(\cdot)$ is an element-wise non-linear unit, generally referred to as the activation function such as sigmoid, rectified linear units, and hyperbolic tangents through the DNNs [31]. The DNNs with L layers can be regarded as the nested composition of sequential standard neural units. Specifically, we let $y_j^{[\ell]}$ represent the j_{th} neuron in ℓ layer, then

$$y_j^{[\ell]} = \sum_{k=1}^{N^{[\ell-1]}} w_{jk}^{[\ell]} \times \sigma^{[\ell-1]}\left(y_k^{[\ell-1]}\right) + b_j^{[\ell]}, \tag{3}$$

where

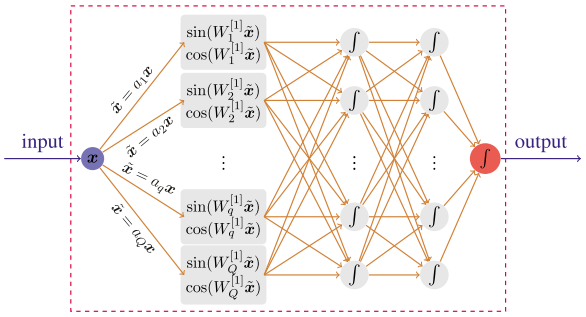

FIGURE 1
Illustration of the representation of Fourier basis in a neural network with 3 hidden layers. $W_q^{[1]}$ represents the weight of the *q–th* hidden units in the first hidden layer.

- $y_k^{[\ell-1]}$: the value of k_{th} neurons in $\ell-1$ layer
- $N^{[\ell-1]}$: the number of neurons in $\ell-1$ layer
- $\sigma^{[\ell-1]}$: the activation function in $\ell-1$ layer
- $w_{jk}^{[\ell]}$: the weights between k_{th} neuron in $\ell-1$ layer and j_{th} neuron in ℓ layer
- $b_j^{[\ell]}$: the bias of j_{th} neuron in ℓ-*1* layer

We denote the output of the DNNs by $\boldsymbol{y}$ $(\boldsymbol{x}; \boldsymbol{\theta})$ with $\boldsymbol{\theta}$ representing the parameter set of all weights and biases. The hyper-parameter $N^{[\ell-1]}$, L and the activation functions $\sigma^{[\ell-1]}$ should be defined before training.

2.2 Activation function

Non-linear activation functions such as ReLU($\boldsymbol{z}$) = max{0, $\boldsymbol{z}$} and tanh($\boldsymbol{z}$) enhance the ability of DNNs to model various non-linear problems such as non-linear PDEs and classification. Therefore, selecting the suitable activation function matters greatly for DNNs applied in all domains. Recent work has shown that Fourier feature mapping as an activation function enables the network to learn the objective function better [32–34]. Since the Fourier feature mapping of sine and cosine can mitigate the spectral bias or frequency preference phenomenon of DNNs [35, 36]. It is

$$\sigma(\boldsymbol{z}) = \begin{bmatrix} \cos(\boldsymbol{\kappa z}) \\ \sin(\boldsymbol{\kappa z}) \end{bmatrix}, \tag{4}$$

where $\boldsymbol{\kappa} = (a_1, a_2, \cdots)$ is a user-specified vector (trainable or untrainable) that is consistent with the number of neural units in the first hidden layer of the DNNs. By performing a Fourier feature mapping of the input data, the input points in Ω may be mapped to the range $[-1, 1]$. Then, the following blocks of the DNNs can nicely handle the feature information, as shown in Figure 1.

Deep neural networks are now consistently used as the non-linear function approximation method and have shown their powerful capacity in the fields of scientific computation and engineering application. Therefore, this paper intends to explore the application of integrating DNNs into epidemic compartmental models for modeling the complex dynamics of COVID-19.

3 Methodology

3.1 Epidemiology model

Epidemic compartmental models enable the simulation of multi-state population transitions by incorporating domain knowledge and mathematical assumptions to characterize the dynamics of the infectious disease. The dynamics of the infection can be described approximately by a variation of the Kermack-McKendrick Eq. 7. We consider a geographical region, assumed as isolated from other regions, and within the such region, we define a time-dependent SIRD model which covers the most important features in modeling the dynamics of COVID-19. The transmission rate determines the dynamic of the epidemic and reflects the effectiveness of the interventions implemented by the authorities. The recovery rate and death rate reflect the capacity of the healthcare system to fight against COVID-19. This hypothesis is a reasonable assumption when interventions are well performed.

$$\begin{aligned} \frac{dS(t)}{dt} &= -\beta\frac{S(t)I(t)}{S(t)+I(t)}, \\ \frac{dI(t)}{dt} &= \beta\frac{S(t)I(t)}{S(t)+I(t)} - \gamma I(t) - \mu I(t), \\ \frac{dR(t)}{dt} &= \gamma I(t), \\ \frac{dD(t)}{dt} &= \mu I(t), \\ N &= S(t)+I(t)+R(t)+D(t) \end{aligned} \tag{5}$$

where $S(t)$, $I(t)$, $R(t)$, $D(t)$ denote the number of susceptible, infected, recovered and deceased individuals over time, respectively. $\beta \geq 0$ represents the *transmission rate* of the disease, which is the average number of contacts of an infected individual per unit of time, multiplied by the probability of disease transmission. $\gamma \geq 0$ represents the *recovery rate*, which is the proportion of infected individual that recover from the disease per unit of time. $\mu \geq 0$ is the *death rate*. Note that $S(t) + I(t) + R(t) + D(t) = N$, where N is the initial population and remains constant in time (e.g., $dN/dt = 0$). The model is initialized at some conventional $t = t_0$ with values $S(t_0) = S_0 > 0$, $I(t_0) = I_0 > 0$, $R(t_0) = R_0 \geq 0$, and $D(t_0) = D_0 \geq 0$. $R(t) + D(t)$ denote the removed individuals that are removed from the susceptible compartment due to death or immunization.

3.2 Euler iteration

Mathematically, the infectious disease transmission dynamics such as (Eq. 5) are generically represented as the following non-linear dynamical system

$$\frac{d\boldsymbol{u}(t)}{dt} = f(\boldsymbol{u}(t), t; \Xi), \tag{6}$$

where $\boldsymbol{u} \in \mathbb{R}^D$ (typically $D \gg 1$) is the state variable and Ξ stands for the parameters of dynamical system. The analytical solution of non-linear different Eq. 6 are hardly obtained or even non-existent in many cases. Alternatively, many numerical simulation algorithms are proposed to deal with the above system by discretizating it with suitable time-stepping Δt, such as forward or backward Euler methods. In the infectious disease transmission scenarios, the real world observed data are time series reported in units of 1 day, so we consider the solutions of SIRD model by the forward Euler method, and take a discretization period of duration 1 day. Then, (Eq. 5) can be expressed as the following discrete-time version:

$$\begin{aligned} S(t+1) &= S(t) - \beta\frac{S(t)I(t)}{S(t)+I(t)}, \\ I(t+1) &= I(t) + \beta\frac{S(t)I(t)}{S(t)+I(t)} - \gamma I(t) - \mu I(t), \\ R(t+1) &= R(t) + \gamma I(t), \\ D(t+1) &= D(t) + \mu I(t), \end{aligned} \tag{7}$$

where $t = t_0, t_0+1, t_0+2, \cdots$. In real-world scenario applications, these parameters are usually time-varying and unknown, which would result in an ill-posed inverse problem. Such an ill-posed inverse problem is a well-known dilemma and poses a significant challenge for traditional methods. Deep learning, specifically deep neural networks, as the non-linear function approximation method has shown its powerful capacity for solving forward-inverse problems. Here, we consider the function expressions for time-varying parameters β, γ and μ utilizing DNNs and provide their high-accuracy estimation relying on the aforementioned Euler iteration method according to the given observed data.

3.3 Overview of Euler-PINNs

To this end, we resort to data-driven surrogate $\beta_{NN}(\cdot, \boldsymbol{\theta}_\beta)$, $\mu_{NN}(\cdot, \boldsymbol{\theta}_\mu)$ and $\gamma_{NN}(\cdot, \boldsymbol{\theta}_\gamma)$ represented by DNNs as the hypothesis spaces (denoted as β_{NN} μ_{NN} and γ_{NN}), then the expression of time-varying parameters β, μ and γ for SIRD model can be obtained by minimizing the following loss function:

$$\begin{aligned} Loss = {} & \omega_s Loss2S + \omega_I Loss2I + \omega_R loss2R + \omega_D Loss2D \\ & + \omega R\left(\boldsymbol{\theta}_\beta, \boldsymbol{\theta}_\gamma, \boldsymbol{\theta}_\mu\right) \end{aligned} \tag{8}$$

with

$$\begin{cases} Loss2S = \frac{1}{N}\sum_{n=0}^{N-1}\left|S_{n+1} - S_n + \beta_{NN}(t_n)\frac{S_n I_n}{S_n + I_n}\right|^2 \\ Loss2I = \frac{1}{N}\sum_{n=0}^{N-1}\left|I_{n+1} - I_n - \beta_{NN}(t_n)\frac{S_n I_n}{S_n + I_n} + \gamma_{NN}(t_n) I_n + \mu_{NN}(t_n) I_n\right|^2 \\ Loss2R = \frac{1}{N}\sum_{n=0}^{N-1}\left|R_{n+1} - R_n - \gamma_{NN}(t_n) I_n\right|^2 \\ Loss2D = \frac{1}{N}\sum_{n=0}^{N-1}\left|D_{n+1} - D_n - \mu_{NN}(t_n) I_n\right|^2 \end{cases}$$

where the observed data for $S(t)$, $I(t)$, $R(t)$ and $D(t)$ at $t = t_0, t_0+1, t_0+2, \cdots$ with a given time interval $[t_0, T]$ are denoted as $S_0, S_1, S_2, \cdots, I_0, I_1, I_2, \cdots, R_0, R_1, R_2, \cdots$, and $D_0, D_1, D_2, \cdots$, respectively. In addition, we introduce five positive relaxing factor ω_S, ω_I, ω_R, ω_D and ω to balance the contribution of *Loss2S*, *Loss2I*, *Loss2R*, *Loss2D* and the regularization sum of network parameter in loss function, respectively. To obtain the ideal $\boldsymbol{\theta}_\beta^\star, \boldsymbol{\theta}_\gamma^\star$ and $\boldsymbol{\theta}_\mu^\star$, optimization methods such as gradient descent (GD) or stochastic gradient descent (SGD) are required during implementation to update the parameters of the DNNs during the training. In this context, the SGD is given by:

$$\boldsymbol{\theta}^{k+1} = \boldsymbol{\theta}^k - \alpha_k \nabla_{\boldsymbol{\theta}^k} L\left(t; \boldsymbol{\theta}^k\right), \quad t \in \{t_0, t_1, t_2, \cdots\},$$

where the *learning rate* α_k decreases with k increasing and $\boldsymbol{\theta} = \{\boldsymbol{\theta}_\beta, \boldsymbol{\theta}_\gamma, \boldsymbol{\theta}_\mu\}$.

Figure 2 describes the schematic of the Euler-PINNs method. In this architecture, three separate deep neural networks are designed to express the corresponding parameters β, γ, and μ in SIRD compartmental model. Next, Euler iteration is introduced to perform the forward process, and then the discrepancy between forward predictions and real-world observations is defined as the loss function which requires to be minimized. Specifically, each neural networks comprise 5 layers, the weight matrix $\boldsymbol{W}_k$ and the bias vector $\mathbf{b}_k$ of the kth layer are: $\boldsymbol{W}_1 \in \mathbb{R}^{1\times35}$, $\boldsymbol{W}_2 \in \mathbb{R}^{35\times50}$, $\boldsymbol{W}_3 \in \mathbb{R}^{50\times30}$, $\boldsymbol{W}_4 \in \mathbb{R}^{30\times30}$, $\boldsymbol{W}_5 \in \mathbb{R}^{30\times20}$ and $\boldsymbol{b}_1 \in \mathbb{R}^{35}$, $\boldsymbol{b}_2 \in \mathbb{R}^{50}$, $\boldsymbol{b}_3 \in \mathbb{R}^{30}$, $\boldsymbol{b}_4 \in \mathbb{R}^{30}$, $\boldsymbol{b}_5 \in \mathbb{R}^{20}$.

4 Application

In this section, we applied the proposed Euler-PINNs method for time-varying parameters estimation of SIRD compartmental model to the real-world data from the state of Minnesota, the United States, and analyzed its performance on both parameter estimation and future prediction.

4.1 Data and implementation

4.1.1 Data source

The proposed Euler-PINNs method was applied to real-world COVID-19 reported data from *The COVID Tracking Project* [37], which covered the confirmed numbers of infected, recovered, and dead cases in the state of Minnesota,

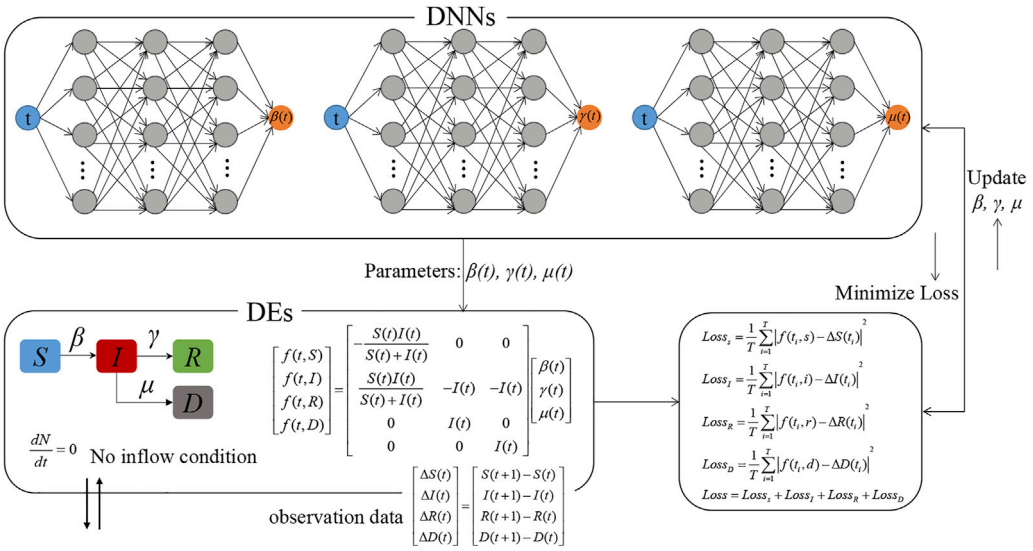

FIGURE 2
The overview of Euler-PINNs for parameters estimation. Each neural networks comprise 5 layers, the weight matrix $\boldsymbol{W}_k$ and the bias vector $\mathbf{b}_k$ of the kth layer are: $\boldsymbol{W}_1 \in \mathbb{R}^{1\times35}$, $\boldsymbol{W}_2 \in \mathbb{R}^{35\times50}$, $\boldsymbol{W}_3 \in \mathbb{R}^{50\times30}$, $\boldsymbol{W}_4 \in \mathbb{R}^{30\times30}$, $\boldsymbol{W}_5 \in \mathbb{R}^{30\times20}$ and $\boldsymbol{b}_1 \in \mathbb{R}^{35}$, $\boldsymbol{b}_2 \in \mathbb{R}^{50}$, $\boldsymbol{b}_3 \in \mathbb{R}^{30}$, $\boldsymbol{b}_4 \in \mathbb{R}^{30}$, $\boldsymbol{b}_5 \in \mathbb{R}^{20}$.

the United States. Accounting for the first dose of COVID-19 vaccine in the United States was administered on 14 December 2020, we selected the time window range 25 March to 13 December of 2020 to avoid any immunity after the vaccination. These time series data $I(t)$, $R(t)$, $D(t)$ are smoothed with a 7-day average due to delays in registering new cases or updating the status of infected individuals over the weekend.

4.1.2 Implementation

We trained the proposed Euler-PINNs method on a personal laptop with an Intel (R) Core (TM) i7-8550U CPU and 1.8GHz, with the Windows 10 operating system. We developed the Euler-PINNs based on Python programming language and using the NumPy [38], Pandas [39] library and the TensorFlow [40] framework. In this numerical experiments, all neural networks are trained by the Adam optimizer, the initial learning rate is 2×10^{-3} with a decay rate 95% for every 2000 epochs. In addition, the regular factors ω is set as 0.0005, max epoch is set as 100000. The entire training process took about 10 min to run 10,000 epochs on all training data, and predictions could be made within seconds.

4.2 Analysis of the results

4.2.1 Quantitative analysis of the results

In this subsection, we present the evaluation of how well the estimated parameters fit the SIRD compartmental model on the available data. Figure 3 shows the fitting of the dynamic of the SIRD model with time-varying parameters to the available data (after 7-day smoothing), which demonstrates that the proposed Euler-PINNs method can accurately fit the different fluctuations in the data. In addition, the performance of mathematical modeling is measured by metrics such as mean absolute errors (MAE) and root means square error (RMSE). The loss function of the proposed Euler-PINNs method is formulated by these metrics, which guarantees it can reflect the convergence of the network and the performance of mathematical models. As can be seen in the Figure 4, the proposed Euler-PINNs method has good convergence.

Moreover, we evaluate how the estimated parameters fit the SIRD compartmental model by comparing the results of previous publications. The findings demonstrate that the proposed Euler-PINNs method yields reliable results that are consistent with those given by other researchers. We compare our results to those obtained using the methodology of the rolling regression framework [19], where the order of magnitude of the time-varying parameters $\beta(t)$, $\gamma(t)$ and $\mu(t)$ is in agreement and the trend is almost identical. It is a sensible note that [41] estimate that the pandemic in the United States presented an estimated ascertainment rate of 21.6% (95% confidence interval:18.9%–25.5%). Asymptomatic and undocumented confirmed cases were not included in our model, which may account for the slightly lower transmission rate we estimated than in paper [19] to some extent. Recovery was defined differently in different states in the United States, in Minnesota it refers to people whose symptoms have improved. This means that asymptomatic cases or individuals suffering from symptoms but not hospitalized nor monitored are not included in the data. As a result, the number of

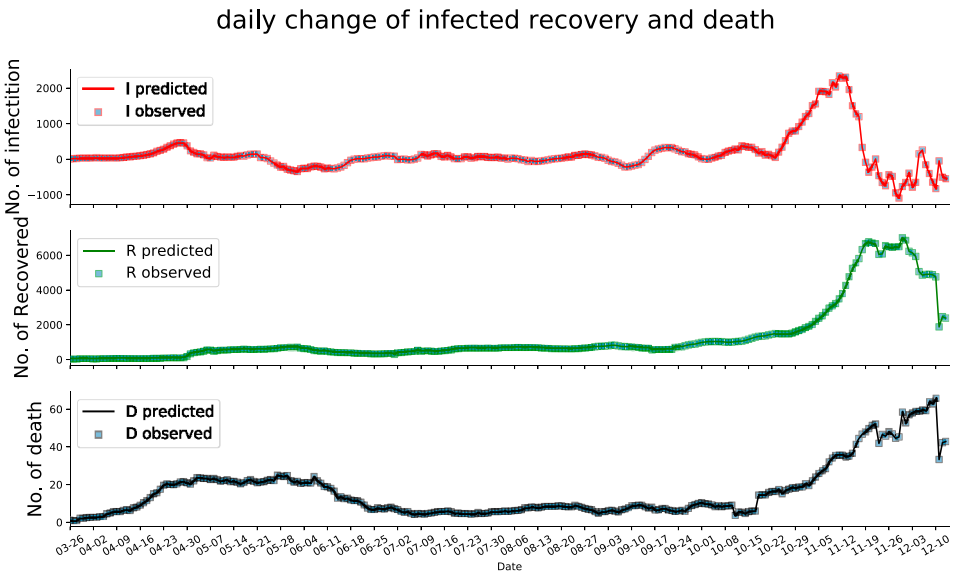

FIGURE 3
The fitting of infection, recovery and deaths during training.The squares represent the observed data and the curves represent the predicted data.

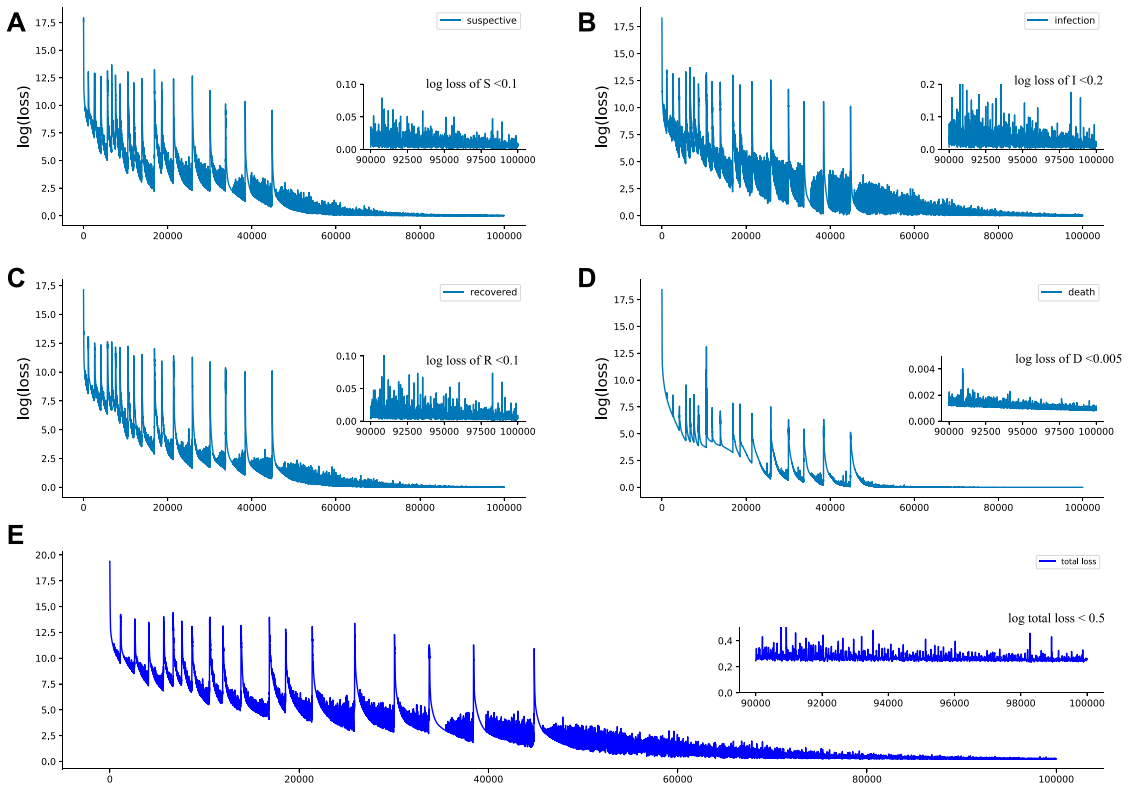

FIGURE 4
Loss of Euler-PINNs method. **(A)**: Loss of susceptible individuals. **(B)**: Loss of infection individuals. **(C)**: Loss of recovery individuals. **(D)**: Loss of death individuals. **(E)**: Total loss of Euler-PINNs.

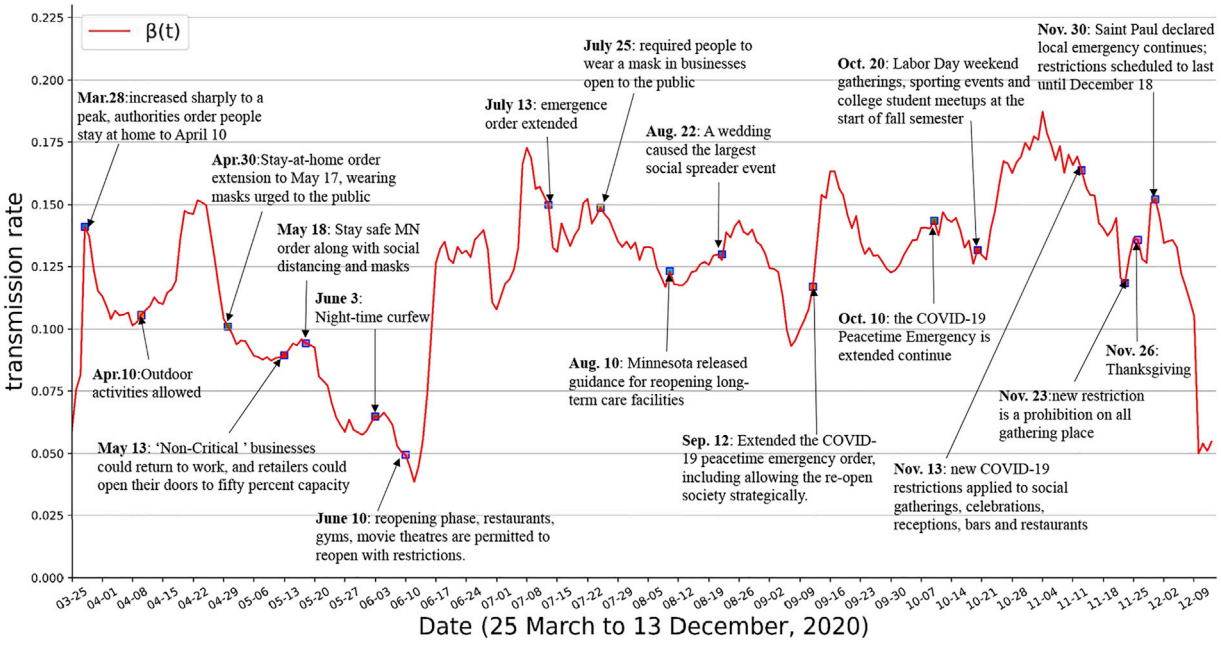

FIGURE 5
Effect of policy implementations and social interactions on $\beta(t)$.

individuals observed as recovered is lower, leading to a lower estimated recovery rate. Consistent with [42], who report values of $\beta(t)$, $\gamma(t)$ and $\mu(t)$ in the United States of orders 10^{-1}, 10^{-2} and 10^{-3}, respectively, around the middle of May. This is also consistent with the orders of magnitude of $\beta(t)$, $\gamma(t)$ and $\mu(t)$ for Minnesota around that time of the year. Consistent with [43], who report that the average time a person is infectious, $1/\gamma(t)$, to be 5 days (i.e., $\gamma(t) \sim 0.2$), our result of $\gamma(t)$ is very close to this estimation. The estimated range of $\mu(t)$ and $\beta(t)$ given by [44] are approximately 10^{-3} and 10^{-1} for the first half of 2020, in the same order with our results.

4.2.2 Qualitative analysis of the results

The epidemiological parameters in compartmental models are sensitive to government policies, people's interactions, medical resources, and so on. In this subsection, we show the evolution of the parameters over time and the corresponding key events during this period. All events and interventions are available from official websites[1] [2] [3]. As shown in Figure 5, the transmission rate $\beta(t)$ can fit well with what would be expected given such events. With the first confirmed cases of COVID-19 detected on March 15 2020, in Minnesota, $\beta(t)$ increased sharply to a peak on March 28. The authorities then ordered people currently living within Minnesota to stay at home from March 28 to April 10. The value of transmission rate $\beta(t)$ kept falling, but started to rise rapidly again after April 10 since all restrictive interventions were lifted. On April 30, the authorities of Minnesota extended the *stay-at-home* order until May 17, and urged people to wear masks in public. On May 13, *Non-Critical* businesses could return to work, and retailers could open their doors to fifty percent capacity. This order affected the average number of contacts among people, with the transmission rate of COVID-19 showing an upward trend after this. On May 18, the new *Stay safe Minnesota* order that contained a series of interventions for controlling the pandemic was issued. *Night-time Curfew* was imposed in all public places within Saint Paul between 10:00 p.m. and 4:00 a.m. on June 3. This new order, along with the effect of masks and social distancing, caused $\beta(t)$ to remain reduced until June 12. However, Minnesota entered reopening phase since June 10, restaurants, gyms, movie theatres, et al. are permitted to reopen with restrictions. The effect of these reopen orders were a surge in $\beta(t)$ a few days later. On July 25, new order required people to wear a mask in businesses open to the public. It is evident that wearing a mask is effective in preventing the transmission of COVID-19, and the transmission rate $\beta(t)$ has started to decrease. On August 10,

1 https://mn.gov/governor/covid-19/news/

2 https://www.stpaul.gov/departments/emergency-management/coronavirus-covid-19

3 https://ballotpedia.org/Documenting_Minnesota%27s_path_to_recovery_from_the_coronavirus_(COVID-19)_pandemic,_2020-2021

the Minnesota released guidance for reopening long-term care facilities, causing a slight surge in transmission rate. In addition, a motorcycle rally was held in western South Dakota during August 7–16, many event-associated cases were identified [45]. On August 22, a late-August wedding in southwestern Minnesota caused the largest social spreader event to date. On September 12, Minnesota extended the COVID-19 peacetime emergency order, including allowing the reopen society strategically. On October 10, the COVID-19 Peacetime Emergency is extended continue. On October 20, surge in cases expected from *Labor Day* weekend gatherings, sporting events and college student meetups at the start of fall semester. Minnesota announced new COVID-19 restrictions on November 11 to curb the spread of the virus, which apply to social gatherings, celebrations, receptions, bars and restaurants from November 13. The new COVID-19 restrictions in Minnesota apply to social gatherings, celebrations and receptions, and bars and restaurants from November 13. Since November 21, a new restriction is a prohibition on all gathering places. However, the impact of these interventions backfired shortly a few days before Thanksgiving on November 26 due to gathering. On November 30, Saint Paul declared that a local emergency continues to exist. The effect of the order of November 23 was a drop in $\beta(t)$ after Thanksgiving activities due to it is scheduled to last until December 18.

Note that the events that have an impact on $\beta(t)$ have to do with people's adaption to preventive interventions and the interactions among individuals, whereas $\mu(t)$ relates to the availability and effectiveness of healthcare, as well as on the resource availability in hospitals. $\gamma(t)$ is known to be disease-specific parameter (inverse of the infectious period) but is also affected by the capacity of the healthcare system to accommodate hospitalization. As far as $\gamma(t)$ and $\mu(t)$, when hospitals and emergency rooms do not working at full capacity they can better look after patients and provide better medical service. This usually results in a decrease in the proportion of individuals that died from the disease (decrease of $\mu(t)$) and in a decrease in the recovery time (increase of $\gamma(t)$). In the context of COVID-19, the hospital's ability to respond to the situation derived from the pandemic had a considerable impact. Hospitals are at full capacity in the first months of the outbreak, and as months went by, healthcare professionals learned more about possible treatments to treat the disease's symptoms and effects. The consequence as shown in Figure 6 and Figure 7, in qualitative terms, was an increasing trend in $\gamma(t)$ and a decreasing trend in $\mu(t)$.

4.3 Forecasting

The compartmental model requires determined initial conditions and model parameters to make predictions. As the initial conditions can be obtained and the model parameters are already calibrated, then predictions for the dynamics of COVID-19 can be made. Modeling results can provide reliable feedback information for the authorities to make future decisions. Therefore, it is critical to identify the epidemic parameters of infectious diseases timely at the beginning of an outbreak. Additionally, to test the performance of the proposed Euler-PINNs method on the small data set, we chose to predict the early-stage dynamics of the COVID-19.

In the prediction part, the value of $\beta(t)$, $\gamma(t)$ and $\mu(t)$ are assumed to be their final value of the training time window. Note that the number of recovered and death state in SIRD model are terminal states, which means that the changes in the number of recovered and death people are always non-decreasing. In turn, the infected people may see periods of increase and decrease due to it is a state of transition. In addition, the number of susceptible state is non-increasing, and therefore the change in this compartment is always non-positive. Training data and 1-week prediction results on the current infected cases, cumulative recovery cases and cumulative death cases and are corresponding ground truth displayed in Figures 8A–C displays the 1-week prediction based on the reported data from March 25—23 April 2020, and Figures 8D–F displays the 1-week prediction based on the reported data from March 25—8 May 2020. The interventions to control the COVID-19 keep adjusting, which may result in uncertainty, simulations illustrate that the proposed Euler-PINNs has the capability to capture the sudden change and give reliable short-term predictions.

4.4 Evaluation metrics

By comparing forecasting results and observations, the performance of the proposed Euler-PINNs can be evaluated. We use four evaluation metrics to make fair and effective comparisons. They are mean absolute error (MAE), average absolute percentage error (MAPE), root mean square error (RMSE) and relative error (REL). The calculation method is shown in Eqs 9–12.

$$MAE = \frac{1}{n}\sum_{i=1}^{n}\left|\hat{y}_i - y_i\right|, \tag{9}$$

$$MAPE = \frac{1}{n}\sum_{i=1}^{n}\left(\frac{\hat{y}_i - y_i}{y_i}\right)*100\%, \tag{10}$$

$$RMSE = \sqrt{\frac{1}{n}\sum_{i=1}^{n}\left(\hat{y}_i - y_i\right)^2}, \tag{11}$$

$$REL = \sum_{i=1}^{n}\frac{\left(\hat{y}_i - y_i\right)^2}{\hat{y}_i^{\,2}}, \tag{12}$$

To test the effect of the proposed Euler-PINNs method in the prediction, we did 3-day, 5-day and 7-day experiments. The experimental results as represented in Table 1 show the highly accurate forecasting capability of the proposed Euler-PINNs method.

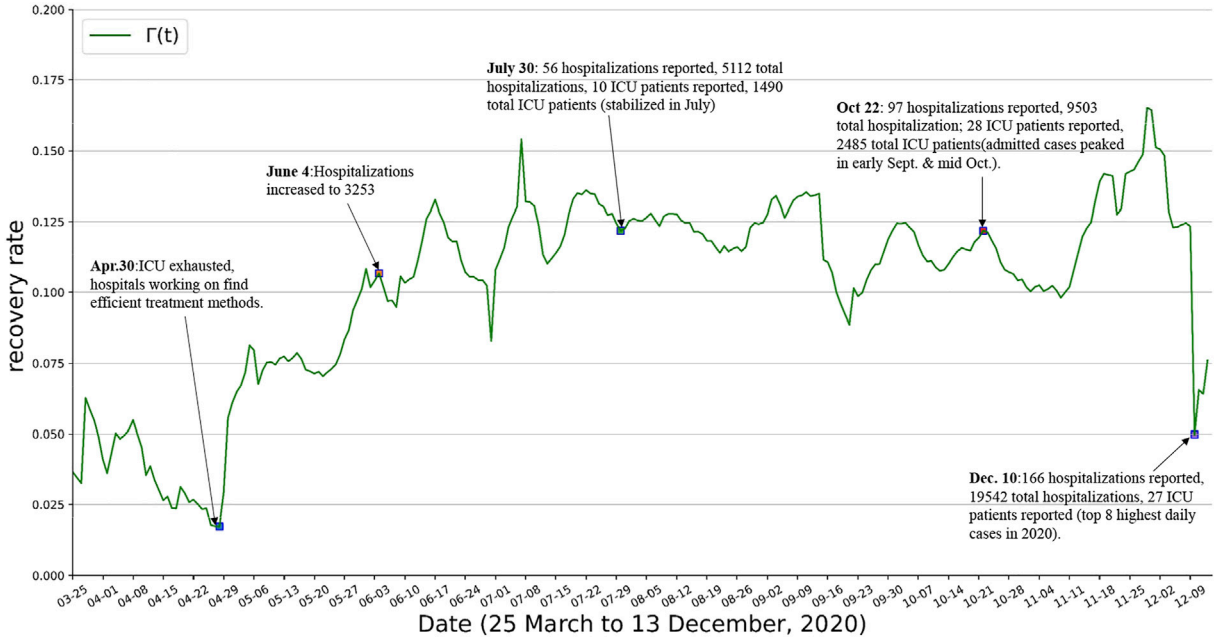

FIGURE 6
Effect of health system and hospitalization rates on $\gamma(t)$.

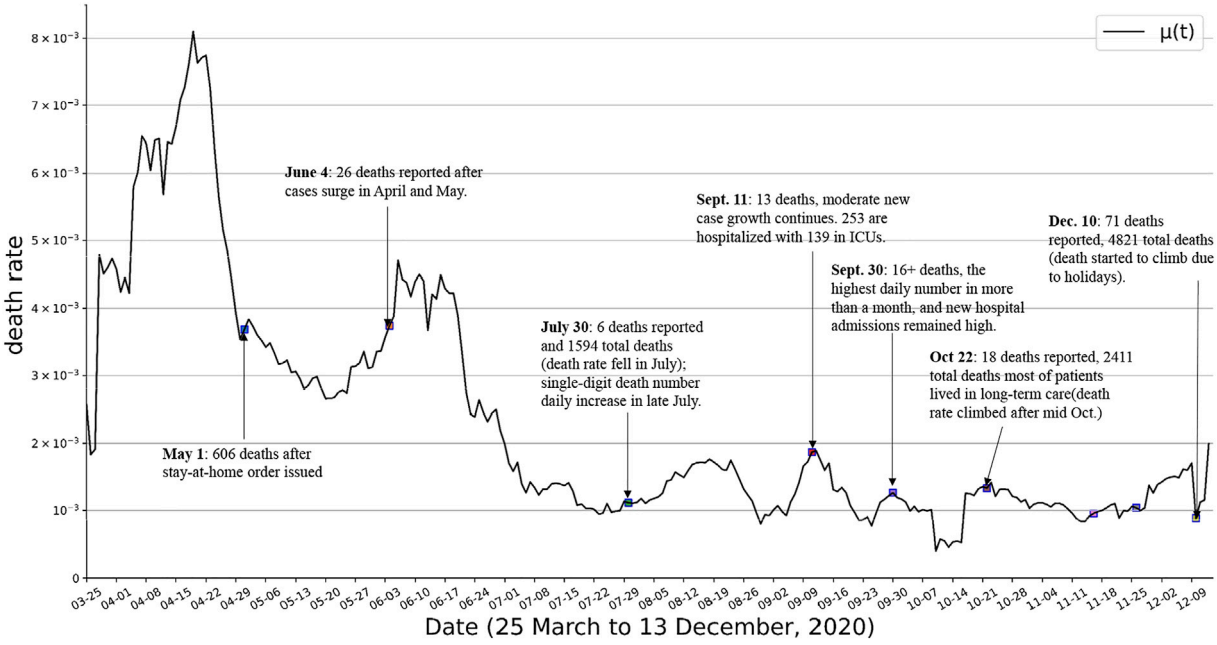

FIGURE 7
Effect of health system and hospitalization rates on $\mu(t)$.

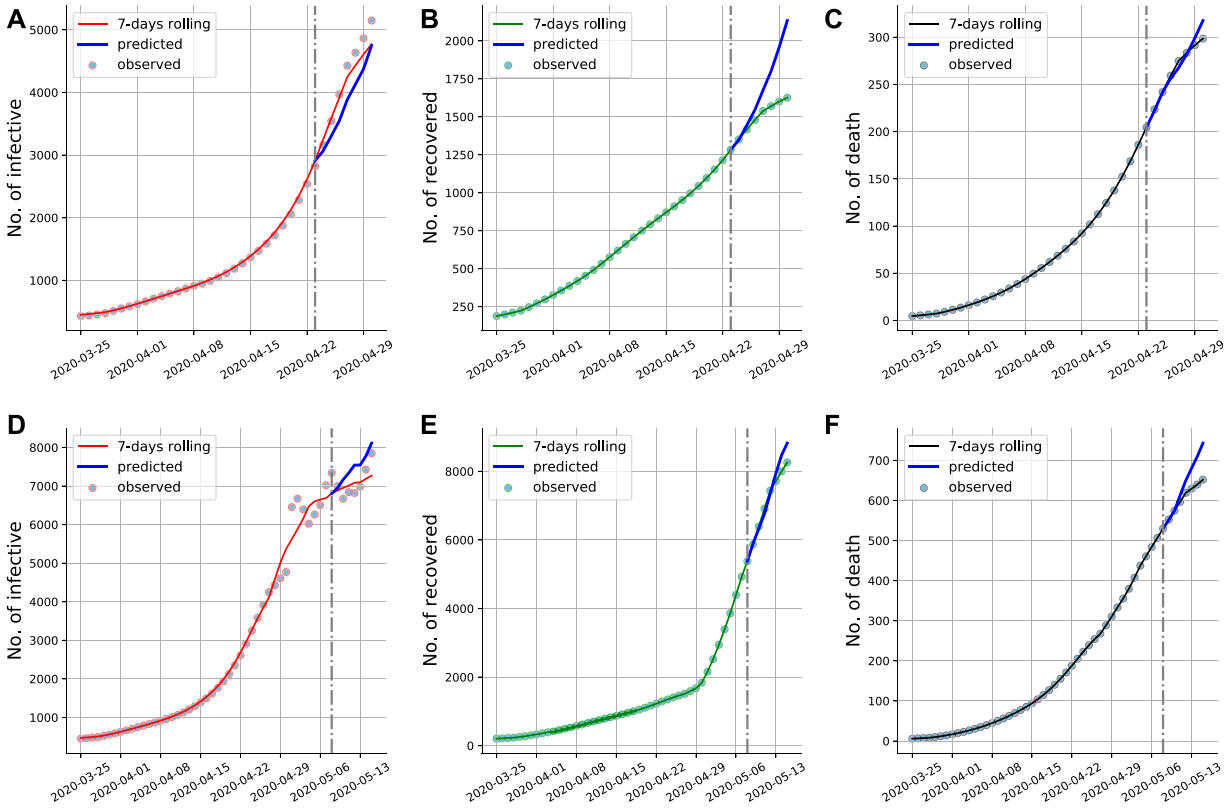

FIGURE 8
Euler-PINNs prediction for the early stage of COVID-19 in Minnesota. The gray vertical line divides the fitting and prediction window. We have included the new available data for the prediction period that were not used in the fitting to show that the predictions are correct. **(A)** and **(D)**: Current infections. **(B)** and **(E)**: Cumulative recovery. **(C)** and **(F)**: Cumulative deaths.

TABLE 1 The prediction performance in 3-day, 5-day and 7-day.

Metrics	After 23 April 2020			After 8 May 2020		
	3-day	5-day	7-day	3-day	5-day	7-day
MAE of I	251.73	359.52	383.61	200.24	300.78	419.99
MAE of R	25.42	75.01	163.23	80.89	110.86	227.0
MAE of D	3.17	7.56	6.88	6.05	20.0	37.33
MAPE% of I	0.0073	0.0104	0.0111	0.0058	0.0088	0.0122
MAPE% of R	0.0007	0.0022	0.0047	0.0024	0.0032	0.0066
MAPE% of D	0.0001	0.0002	0.0002	0.0002	0.0006	0.0011
RMSE of I	285.31	397.03	411.7	228.53	336.04	482.03
RMSE of R	30.31	101.62	225.51	97.05	131.10	298.83
RMSE of D	4.17	9.58	8.56	9.69	27.67	49.36
REL% of I	0.6377	0.9930	0.9159	0.1081	0.2299	0.4646
REL% of R	0.0454	0.4642	2.1383	0.0229	0.0361	0.1688
REL% of D	0.0293	0.1329	0.0958	0.0284	0.2163	0.6549

5 Discussion and conclusion

In this paper, we proposed an Euler-PINNs method to estimate the time-varying parameters of the compartmental model and provide future forecasting based on calibrated parameters. We discretize the time-continuous compartmental model using forward Euler iteration, expressing each parameter in the compartmental model as separate DNNs, and substituting the predicted values of parameters into the equations. The loss function of the proposed Euler-PINNs method is formulated based on the error between prediction and observation, and the Adam optimizer with a dynamic learning rate is applied to minimize it.

Experiment results demonstrate that the time-varying parameters of the SIRD model estimated by the proposed Euler-PINNs method are consistent with previous published works. The transmission rate β determines the dynamics of COVID-19, and the time-varying $\beta(t)$ estimated by proposed Euler-PINNs method can accurately capture the changes in government interventions and individual behaviors, such as mask wearing and social distancing. The recovery rate γ and the death rate μ are expected to increase and decrease, respectively, thanks to the more effective treatments for the disease. The estimated $\gamma(t)$ and $\mu(t)$ by our proposed Euler-PINNs method also fit well with the improved capacity of the healthcare system to fight against COVID-19. The proposed Euler-PINNs method shows that rather than using several stage models with piece-wise constant parameters, it is possible to design one model with time-varying parameters that are capable of representing the overall evolution of the infectious disease. More importantly, applying estimated parameters to the compartmental model to depict the dynamics of COVID-19, the perfect fitting between model predictions and observed data also underscores that parameters yield great fitness.

For different infectious diseases and different transmission scenarios, different compartmental models are required to model the dynamics of infectious diseases. The SIRD compartmental model is not the most complex epidemic model available, dividing more compartments such as breaking down infected people into asymptomatic and symptomatic, adding the virus mutations, or adding the vaccination campaign could be part of a more complex model. In fact, it is impossible to build a state-of-the-art epidemiology model that represents all the intricacies of the current pandemic. Our paper aims to introduce a new intelligent method for estimating time-varying parameters in epidemic models and provide a reliable prediction. The proposed Euler-PINNs method can be implemented easily without any background knowledge about numerical analysis (for example, stability conditions, and *a priori* distribution). Therefore, for applying the Euler-PINNs method to various compartmental models, the practitioner only needs to redefine the transformation matrix for each compartment according to the equations and build DNNs for the relevant parameters. Lastly, deep learning models do not replace conventional computational simulations but could assist them in mitigating some of their common bottlenecks, such as high computational costs. In future work, we are planning to try to test some fast PINN frameworks [46, 47] and to try to approximate the parameters using extreme learning machines (ELM) [48]. More importantly, we would do more validation experiments on various extended compartment models and generalize the proposed method to other infectious diseases.

Data availability statement

The original contributions presented in the study are included in the article/Supplementary Material, further inquiries can be directed to the corresponding author.

Author contributions

XN designed the framwork and developed the code programming by Python and related packages, and X-AL reviewed and improved the code. YW and FC tested the proposed framework and provided critical comments for the application part. XN write the original draft and all the authors reviewed the final manuscript and critically revised it. All authors have read the paper and approved its submission.

Funding

The study was supported by the National Natural Science Foundation of China (82041024 to FC and 81973142 to YW). This study was also partially supported by the Bill & Melinda Gates Foundation (INV-006371).

Conflict of interest

Author X-ALi is employed by Ceyear Technologies Co., Ltd.

The remaining authors declare that the research was conducted in the absence of any commercial or financial relationships that could be construed as a potential conflict of interest.

Publisher's note

References

1. Wei Y, Sha F, Zhao Y, Jiang Q, Hao H, Chen F. Better modelling of infectious diseases: Lessons from Covid-19 in China. *BMJ* (2021) 375:n2365. doi:10.1136/bmj.n2365

2. Guan J, Wei Y, Zhao Y, Chen F. Modeling the transmission dynamics of Covid-19 epidemic: A systematic review. *J Biomed Res* (2020) 34(6):422. doi:10.7555/jbr.34.20200119

3. Mohamadou Y, Halidou A, Kapen PT. A review of mathematical modeling, artificial intelligence and datasets used in the study, prediction and management of Covid-19. *Appl Intell* (2020) 50(11):3913–25. doi:10.1007/s10489-020-01770-9

4. Holmdahl I, Buckee C. Wrong but useful - what covid-19 epidemiologic models can and cannot tell us. *N Engl J Med* (2020) 383(4):303–5. doi:10.1056/nejmp2016822

5. Cucinotta D, Vanelli M. Who declares Covid-19 a pandemic. *Acta Biomed* (2020) 91(1):157–60. doi:10.23750/abm.v91i1.9397

6. Haug N, Geyrhofer L, Londei A, Dervic E, Desvars-Larrive A, Loreto V, et al. Ranking the effectiveness of worldwide Covid-19 government interventions. *Nat Hum Behav* (2020) 4(12):1303–12. doi:10.1038/s41562-020-01009-0

7. Kermack WO, McKendrick AG. A contribution to the mathematical theory of epidemics. *Proc R Soc Lond Ser A, containing Pap a Math Phys character* (1927) 115(772):700–21. doi:10.1098/rspa.1927.0118

8. Maier BF, Brockmann D. Effective containment explains subexponential growth in recent confirmed Covid-19 cases in China. *Science* (2020) 368(6492):742–6. doi:10.1126/science.abb4557

9. Giordano G, Blanchini F, Bruno R, Colaneri P, Di Filippo A, Di Matteo A, et al. Modelling the Covid-19 epidemic and implementation of population-wide interventions in Italy. *Nat Med* (2020) 26(6):855–60. doi:10.1038/s41591-020-0883-7

10. Tian H, Liu Y, Li Y, Wu CH, Chen B, Kraemer MUG, et al. An investigation of transmission control measures during the first 50 days of the Covid-19 epidemic in China. *Science* (2020) 368(6491):638–42. doi:10.1126/science.abb6105

11. Hao X, Cheng S, Wu D, Wu T, Lin X, Wang C. Reconstruction of the full transmission dynamics of Covid-19 in wuhan. *Nature* (2020) 584(7821):420–4. doi:10.1038/s41586-020-2554-8

12. Wei Y, Wei L, Jiang Y, Shen S, Zhao Y, Hao Y, et al. Implementation of clinical diagnostic criteria and universal symptom survey contributed to lower magnitude and faster resolution of the Covid-19 epidemic in wuhan. *Engineering* (2020) 6(10):1141–6. doi:10.1016/j.eng.2020.04.008

13. Jagan M, deJonge MS, Krylova O, Earn DJD. Fast estimation of time-varying infectious disease transmission rates. *Plos Comput Biol* (2020) 16(9):e1008124. doi:10.1371/journal.pcbi.1008124

14. Ge Y, Zhang WB, Wu X, Ruktanonchai CW, Liu H, Wang J, et al. Untangling the changing impact of non-pharmaceutical interventions and vaccination on European Covid-19 trajectories. *Nat Commun* (2022) 13(1):3106–9. doi:10.1038/s41467-022-30897-1

15. Xue L, Jing S, Miller JC, Sun W, Li H, Estrada-Franco J, et al. A data-driven network model for the emerging Covid-19 epidemics in wuhan, toronto and Italy. *Math biosciences* (2020) 326:108391. doi:10.1016/j.mbs.2020.108391

16. Viguerie A, Lorenzo G, Auricchio F, Baroli D, Hughes HJR, Patton A, et al. Simulating the spread of COVID-19 via a spatially-resolved susceptible-exposed-infected-recovered-deceased (SEIRD) model with heterogeneous diffusion. *Appl Maths Lett* (2021) 111:106617. doi:10.1016/j.aml.2020.106617

17. Schiassi E, De Florio M, D'Ambrosio A, Mortari D, Furfaro R. Physics-informed neural networks and functional interpolation for data-driven parameters discovery of epidemiological compartmental models. *Mathematics* (2021) 9(17):2069. doi:10.3390/math9172069

18. Chen YC, Lu PE, Chang CS, Liu TH. A time-dependent sir model for Covid-19 with undetectable infected persons. *IEEE Trans Netw Sci Eng* (2020) 7(4):3279–94. doi:10.1109/tnse.2020.3024723

19. Rubio-Herrero J, Wang Y. A flexible rolling regression framework for the identification of time-varying sird models. *Comput Ind Eng* (2022) 167:108003. doi:10.1016/j.cie.2022.108003

20. Calafiore GC, Novara C, Possieri C. A time-varying sird model for the Covid-19 contagion in Italy. *Annu Rev Control* (2020) 50:361–72. doi:10.1016/j.arcontrol.2020.10.005

21. Raissi M, Perdikaris P, Karniadakis GE. Physics-informed neural networks: A deep learning framework for solving forward and inverse problems involving nonlinear partial differential equations. *J Comput Phys* (2019) 378:686–707. doi:10.1016/j.jcp.2018.10.045

22. Tartakovsky M, Marrero CO, Perdikaris P, Tartakovsky DT, Barajas-Solano D. Physics-informed deep neural networks for learning parameters and constitutive relationships in subsurface flow problems. *Water Resour Res* (2020) 56(5):e2019WR026731. doi:10.1029/2019wr026731

23. Wang N, Chang H, Zhang D. Deep-learning-based inverse modeling approaches: A subsurface flow example. *J Geophys Res Solid Earth* (2021) 126(2):e2020JB020549. doi:10.1029/2020jb020549

24. Zhou Y, He Y, Wu J, Cui C, Chen M, Sun B. A method of parameter estimation for cardiovascular hemodynamics based on deep learning and its application to personalize a reduced-order model. *Numer Methods Biomed Eng* (2022) 38(1):e3533. doi:10.1002/cnm.3533

25. Kevin L, Schafer A, Meng X, Zou Z, Karniadakis GE, Kuhl E. *Bayesian physics-informed neural networks for real-world nonlinear dynamical systems* (2022). *arXiv preprint arXiv:2205.08304*.

26. Nguyen L, Raissi M, Seshaiyer P. Modeling, analysis and physics informed neural network approaches for studying the dynamics of Covid-19 involving human-human and human-pathogen interaction. *Comput Math Biophys* (2022) 10(1):1–17. doi:10.1515/cmb-2022-0001

27. Long J, Khaliq AQM, Furati KM. Identification and prediction of time-varying parameters of Covid-19 model: A data-driven deep learning approach. *Int J Comp Maths* (2021) 98(8):1–16. doi:10.1080/00207160.2021.1929942

28. Cai M, Karniadakis GEM, Li C. Fractional seir model and data-driven predictions of Covid-19 dynamics of omicron variant. *Chaos* (2022) 32(7):071101. doi:10.1063/5.0099450

29. Kharazmi E, Cai M, Zheng X, Zhang Z, Lin G, Karniadakis GEM. Identifiability and predictability of integer- and fractional-order epidemiological models using physics-informed neural networks. *Nat Comput Sci* (2021) 1(11):744–53. doi:10.1038/s43588-021-00158-0

30. Hu H, Kennedy CM, Kevrekidis PG, Zhang HK. A modified pinn approach for identifiable compartmental models in epidemiology with application to Covid-19. *Viruses* (2022) 14(11):2464. doi:10.3390/v14112464

31. Krogh K. What are artificial neural networks? *Nat Biotechnol* (2008) 26(2):195–7. doi:10.1038/nbt1386

32. Wang S, Wang H, Perdikaris P. On the eigenvector bias of Fourier feature networks: From regression to solving multi-scale pdes with physics-informed neural networks. *Comp Methods Appl Mech Eng* (2021) 384:113938. doi:10.1016/j.cma.2021.113938

33. Tancik M, Srinivasan PP, Mildenhall B, Fridovich-Keil S, Raghavan N, Singhal U, et al. *Fourier features let networks learn high frequency functions in low dimensional domains* (2020). *arXiv preprint arXiv:2006.10739*.

34. Li X, Xu ZJ, Zhang L. *Subspace decomposition based dnn algorithm for elliptic-type multi-scale pdes* (2021). *arXiv preprint arXiv:2112.06660*.

35. Xu ZQJ, Zhang Y, Luo T, Xiao Y, Zheng M. Frequency principle: Fourier analysis sheds light on deep neural networks. *CiCP* (2020) 28(5):1746–67. doi:10.4208/cicp.oa-2020-0085

36. Rahaman N, Arpit D, Baratin A, Draxler F, Lin M, Hamprecht FA, et al. On the spectral bias of deep neural networks. In: International Conference on Machine Learning (2019).

37. Wissel D, Van Camp PJ, Kouril M, Weis C, Glauser TA, White PS, et al. An interactive online dashboard for tracking COVID-19 in U.S. counties, cities, and states in real time. *J Am Med Inform Assoc* (2020) 27(7):1121–5. doi:10.1093/jamia/ocaa071

38. Harris C. R., Millman K. J., Van Der Walt F. J., Gommers, R., Virtanen P., Cournapeau D., et al. Array programming with NumPy (2020). *Nature* 585(7825):357–362. Nature Publishing Group.

39. McKinney W. pandas: a foundational python library for data analysis and statistics. *Python high Perform scientific Comput* (2011) 14(9):1–9.

40. Abadi M, Paul B, Chen J, Chen Z, Davis A, Dean J, et al. {TensorFlow}: A system for {Large-Scale} machine learning. In: 12th USENIX symposium on operating systems design and implementation (OSDI 16) (2016). p. 265–83.

41. Pei S, Yamana TK, Kandula S, Galanti M, Shaman J. Burden and characteristics of Covid-19 in the United States during 2020. *Nature* (2021) 598(7880):338–41. doi:10.1038/s41586-021-03914-4

42. Chakraborty A, Chen J, Desvars-Larrive A, Klimek P, Flores Tames E, Garcia D, et al. *Analyzing covid-19 data using sird models*. medRxiv (2020).

43. Bar-On YM, Flamholz A, Phillips R, Milo R. SARS-CoV-2 (COVID-19) by the numbers. *elife* (2020) 9:e57309. doi:10.7554/elife.57309

44. Fernández-Villaverde J, Jones CI. Estimating and simulating a sird model of Covid-19 for many countries, states, and cities. *J Econ Dyn Control* (2022) 140: 104318. doi:10.1016/j.jedc.2022.104318

45. Firestone MJ, Wienkes H, Garfin J, Wang X, Vilen K, Smith KE, et al. COVID-19 outbreak associated with a 10-day motorcycle rally in a neighboring state - Minnesota, august-september 2020. *MMWR Morb Mortal Wkly Rep* (2020) 69(47): 1771–6. doi:10.15585/mmwr.mm6947e1

46. Schiassi E, Furfaro R, Leake C, De Florio M, Johnston H, Mortari D. Extreme theory of functional connections: A fast physics-informed neural network method for solving ordinary and partial differential equations. *Neurocomputing* (2021) 457: 334–56. doi:10.1016/j.neucom.2021.06.015

47. Srinivasan D, Srinivasan B. Physics Informed Extreme Learning Machine (PIELM)-A rapid method for the numerical solution of partial differential equations. *Neurocomputing* (2020) 391:96–118. doi:10.1016/j.neucom.2019.12.099

48. Huang GB, Zhu QY, Siew CK. Extreme learning machine: Theory and applications. *Neurocomputing* (2006) 70(1-3):489–501. doi:10.1016/j.neucom.2005.12.126

frontiers | Frontiers in Physics

TYPE Original Research
PUBLISHED 06 January 2023
DOI 10.3389/fphy.2022.1107338

OPEN ACCESS

EDITED BY
Cong Li,
Fudan University, China

REVIEWED BY
Linying Xiang,
Northeastern University at Qinhuangdao, China
Bo Qu,
Peng Cheng Laboratory, China
Yang Chen,
Fudan University, China

*CORRESPONDENCE
Yong Min,
myong@bnu.edu.cn

SPECIALTY SECTION
This article was submitted to Interdisciplinary Physics, a section of the journal Frontiers in Physics

RECEIVED 24 November 2022
ACCEPTED 21 December 2022
PUBLISHED 06 January 2023

CITATION
Li Z, Zhang J, Xuan Q, Qiu X and Min Y (2023), A novel method detecting controversial interaction in the multiplex social comment network.
Front. Phys. 10:1107338.
doi: 10.3389/fphy.2022.1107338

A novel method detecting controversial interaction in the multiplex social comment network

Zihan Li[1,2], Jian Zhang[3], Qi Xuan[1,2], Xiang Qiu[2] and Yong Min[4,5]*

[1]Institute of Cyberspace Security, Zhejiang University of Technology, Hangzhou, China, [2]The College of Information Engineering, Zhejiang University of Technology, Hangzhou, China, [3]Institute of Cyberspace Security, Hangzhou Dianzi University, Hangzhou, China, [4]The Computational Communication Research Center, Beijing Normal University, Zhuhai, China, [5]School of Journalism and Communication, Beijing Normal University, Beijing, China

With the rise of online social media, users from across the world can participate in opinion formation processes, and some discussions lead to controversial debates around this phenomenon. Controversy detection in social media can help explore public discourse spaces and understand topical issues. Previous controversial detection studies focus more on identifying the opinion or emotional orientation of a comment, while we focus on whether there is a controversial relationship between a comment and its replies. Here, we collect a dataset consisting of 511 news articles, 103,787 comments, and 71,579 users on the Chinese social media platform, Toutiao, and we study the controversial interactions on the subsets of this dataset. Our approach treats news, comments, and users as different types of nodes and constructs multiplex networks connected by user–comment links (i.e., publishing relationship), comment–news links (i.e., comment relationship), and comment–comment links (i.e., replying relationship). Furthermore, we propose a model based on deep learning to detect controversial interactions from these multiplex networks. Our supervised model achieves 83.24% accuracy, with an improvement compared to competitive models. Moreover, we illustrate the applicability of our approach using different ratios of training and testing sets. Our results demonstrate the usefulness of the multiplex networks model for controversial interaction detection and provide a new perspective on controversy detection problems.

KEYWORDS

multiplex network, graph embedding, controversy detection, deep learning, graph neural network

1 Introduction

Online social media such as the Chinese platform, Toutiao[1], have become major channels through which people can easily share their views. In open and free circumstances, the phenomenon of exchanging different opinions probably leads to a fierce discussion and even turns it into a war of words. This situation pollutes the cyber environment. The annoying controversies could be political debates [1, 2] or other topics [3], and the contents of such comments represent a lens of public sentiment. It provides opportunities

1 https://www.toutiao.com

to solve the problems in network governance, such as news topic selection, influence assessment, and polarized views alleviation [4].

As a significant part of the procedure, controversy detection in social media has drawn much attention [2, 5]. For example, Twitter is a central place for online discussions and debates. In addition, Twitter provides support for social and political movements. Due to the wide distribution of Twitter, controversial content needs to be censored before it is posted on Twitter. This strategy protects the online environment and limits the spread of misinformation. However, it is challenging to identify controversies in a robust method because of the way controversy varies with the topic of discussion. For example, during the COVID-19 pandemic, wild extremes of emotion and controversial speech have occurred on Twitter. Controversial opinions and subjective judgments are spreading heavily with Twitter retweets [6]. In such cases, controversy detection would be helpful. For example, users will be warned before viewing such posts to prevent them from being influenced by the content of subjective comments in the post [7].

Controversy detection has been studied on web pages and social media for a long decade [8–10]. As for standard web pages, existing methods mainly exploit the controversy detection on Wikipedia [9, 11–13], Reddit [1, 4, 14], and some political blogs [15, 16]. Early methods of controversy detection are mostly based on statistical analysis, such as user edit history in Wikipedia [17, 18], user revision time [13], and context information [12]. Others incorporate the sentiment-based features [19].

Unlike web pages, online social media consist of more diverse topics and fierce discussion among users. There are many controversial comments under a non-controversial topic or post. This makes controversy detection on social media more challenging. The methods during the development of controversy detection can be divided into three types.

The methods based on the statistics of social media platforms: The statistics of the aimed comments, posts, or topics reflect the importance of such items associated with the controversial comment. For example, Koncar et al. [20] extract textural features such as text length and writing style on controversial comments. Moreover, other methods detect controversy standing on leveraging textural and structural features, such as keywords [21], Twitter-specific features [22], and different aspects of discussions including sentiment and topical cohesiveness [23, 24].

The methods based on the content of comments: Identifying the semantics of the aimed comment is the directed way to solve controversy detection problems. With the development of natural language processing methods, detecting sentiments based on textural information is more accessible. Based on the data collected from social media platforms, some methods detect controversial snapshots containing several comments attached to the same topic based on the contents of comments and external features [25, 26].

The methods based on the network structure: The reply reaction reveals the structural information of social networks. Compared with the traditional homogeneous network, social networks contain different types of entities and relations, rich structural information, and semantic information, which provide a way to discover deeply hidden information for controversy detection. Garimella et al. [2] measured some graph-based features and quantified controversy scores for retweet graphs. In addition, Kumar et al. [27] created a novel LSTM model that combines graph embeddings, user, community, and text features, which gets better prediction results for conflict detection. Hessel et al. [4] integrated the content features with the reply structure and predicted eventual controversy in several Reddit communities. Zhong et al. [14] considered all posts under the same topic using graph-embedding methods. They exploit the information from related posts under the same topic and propose the TPC-GCN and DTPC-GCN models to disentangle both the topic-related and topic-unrelated features and get significant generalizability results on the test datasets.

Graph-embedding techniques have been proven effective in complex network analysis recently. It maps nodes, links, or graphs to low-dimensional dense representations, making it possible to apply machine learning methods for downstream tasks like node classification [28], link prediction [29, 30], and graph classification [31]. Considered as the first work in this area, DeepWalk [32] samples node sequences through random walk and then incorporates skip-gram to learn node embeddings with each node regarded as a word in sentences. To capture both local and global structural features, node2vec [33] extends DeepWalk by employing breadth-first search and depth-first search when sampling node sequences. The sampling strategy is called biased random walk, which improves network representation learning ability. Other random walk-based graph-embedding methods may have similar ideas but adopt different sampling strategies, which focus on different aspects of the network structure [34–36].

Recently, Jiang et al. [37] provided a framework for efficient task-oriented skip-gram-based embeddings. Hu et al. [38] used the generative adversarial networks, which learn node distributions for efficient negative sampling. The emergence of deep learning methods accelerated the growth of this typical research area. Among the variants of graph neural networks (GNN), GCN [39] provided a simplified method to compute the spectral graph convolution to capture the information of the graph structure and node features and transform the structural information between nodes into vectors. GAE [40] designs a decoder for restructuring the relational information of the nodes. The decoder uses the embedding vectors obtained by GCN to reconstruct the graph adjacency matrix, and then perform iteration according to the loss of the reconstructed adjacency matrix and label matrix. In practice, GAE achieves better link prediction results than other algorithms.

Prior work on online controversy detection mainly focuses on comments, topics, or posts [4, 22, 26, 27, 41]. These models are trained to identify the opinion or emotional orientation of a comment, post, or topic. Instead of detecting a controversial comment, our study focuses on the interaction between comments. The controversial comment means this comment probably raises controversy, and the platform's formula determines the score of comments that are likely to be controversial. These definitions may not perfectly characterize whether the current review is prone to controversy because of the limited statics used in the formulation. Controversial interactions are more common than controversial comments in actual social media. In contrast, controversial interaction indicates that a comment's opinion differs from its replies. Compared with quantifying the score of a controversial comment, the controversial interaction can be easily distinguished by the content in the process of labeling.

To detect controversial interactions, we collect information on 103,787 comments and 71,579 users under 511 news and label all of the comments. We treat the users, comments, and news in social media as nodes in multiplex social comment networks. We construct the multiplex networks connected by user–comment links

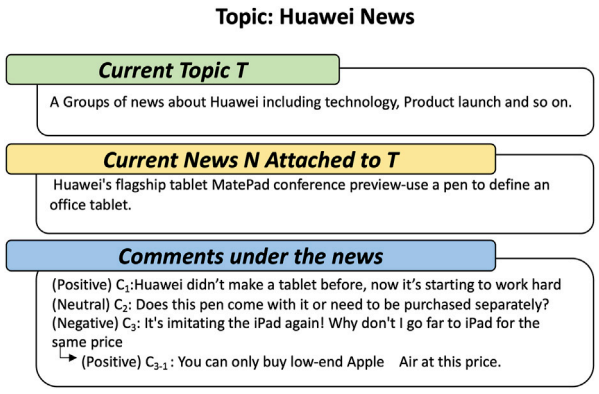

FIGURE 1
A piece of news under the topic of **Huawei** and the comments under the news. Each comment is labeled with positive, negative, or neutral depending on its attitude to the news.

(i.e., publishing relationship), comment–news links (i.e., comment relationship), and comment–comment links (i.e., replying relationship). Then, we propose the news–comment–user graph convolutional network (NCU-GCN) model for detecting controversial interactions. NCU-GCN integrates the graph structure information and the datasets' dynamic features for obtaining the embedding vector of every comment node. After obtaining the embedding vectors, we classify the interactions on two comments based on the embedding vectors and detect the controversial interactions. Extensive experiments demonstrate that our model outperforms existing methods and can exploit features effectively.

The main contributions of this paper are listed as follows:

1. We build a dataset from a real Chinese news portal platform for controversy detection, which consists of 511 news articles, 103,787 comments, and 71,579 users. This dataset covers a large variety of fields under the topic of **Huawei**, such as finance, technology, and entertainment. Such a real-world dataset can help us better understand the generation of controversy between comments in social media and the evolution of controversy under a comment tree.
2. We propose a GCN-based model, NCU-GCN, for controversy detection on the interaction between two comments. The model can integrate the information from heterogeneous graph structures and dynamic features of edges. The dynamic features of edges mainly consist of the posting time of nodes.
3. Extensive experiments on the Toutiao dataset demonstrate the information of temporal and structural can effectively improve the embedding vectors and get a better result in AUC and AP metrics. Moreover, our model performs generalizability under different ratios of training samples.

The remaining of the paper is organized as follows: first, a detailed description is given for the Toutiao dataset in Secion 2 and introduces the proposed NCU-GCN in Section 3. Extensive experiments on Toutiao are presented in Section 4 to show the effectiveness of the proposed methods. Finally, we conclude the paper and highlight some future research directions in Section 5.

2 Dataset analysis

In this section, we first give a detailed description of the dataset and data preprocessing, then conduct preliminary descriptive analyses.

2.1 Data description

The data collected from Toutiao include news, users who commented on the news, and the corresponding comments. This news covers a variety of fields, such as technology, finance, and entertainment. In this paper, we focus on **Huawei**-related news, which were released between 2019-03 and 2019-12. Each piece of news is associated with multiple comments, of which the contents present the attitudes of corresponding viewers toward the news. Thus, the comments could be classified into three categories: positive, neutral, and negative. Figure 1 gives an example of controversy over a certain piece of news. News N belongs to topic T, and it follows multiple comments which show different opinions. As shown in Figure 1, the comments are labeled as positive, neutral, or negative based on their attitudes to the current news, and there exists a situation in C_{3-1} that expresses refutation literally, but it actually supports N. This is because in the comment tree, it refutes to C_3, a refuting comment to N. So, we mark comment C_{3-1} as a positive comment, and in the progress of data preprocessing, we manually specify the labels of each comment according to its content and context. We collect 511 pieces of news with 103,787 comments in total. Moreover, we label all of the comments with an opinion bias. To make the labeling results more accurate, we started with two annotators labeling the same comment. If a disagreement occurs between two annotators, three additional annotators were added to label this comment. The final labeling results were obtained from the average score of these five annotators. In addition, as Figure 2 indicates, there exist several comments without content and published time. We guess the reason is that the users have deleted these comments. For this kind of comment, we can only judge its label based on its replies.

Given such a large amount of data, we would like to focus on the controversies under *sampled* news in this paper. Thus, we sample three subsets of the data for experiments. Specifically, we first find the top two active users who posted the most comments under different news, and we denote them as $u1$ and $u2$. The news commented by $u1$, together with the corresponding comments and the other users, consists of one subset, namely, Toutiao#1. Another subset, Toutiao#2, consists of the news with comments by $u2$ and other comments and users, and the common news, which appears in both Toutiao#1 and Toutiao#2, comes to the third subset, namely, Toutiao#3. The basic statistics of the whole dataset and its extracted subsets are presented in Table 1, where interactions mean the relationship between comments. The definition of these interactions is as follows:

- **Controversial interactions:** Positive and negative.
- **Non-controversial interactions:** Positive and positive, neutral and neutral, and negative and negative.
- **Other interactions:** Neutral and positive and neutral and negative.

Also, we provide statistics on the different relationships of the edges in the dataset. Table 2 shows the number of edges between the three types of nodes and the number of edges between the three

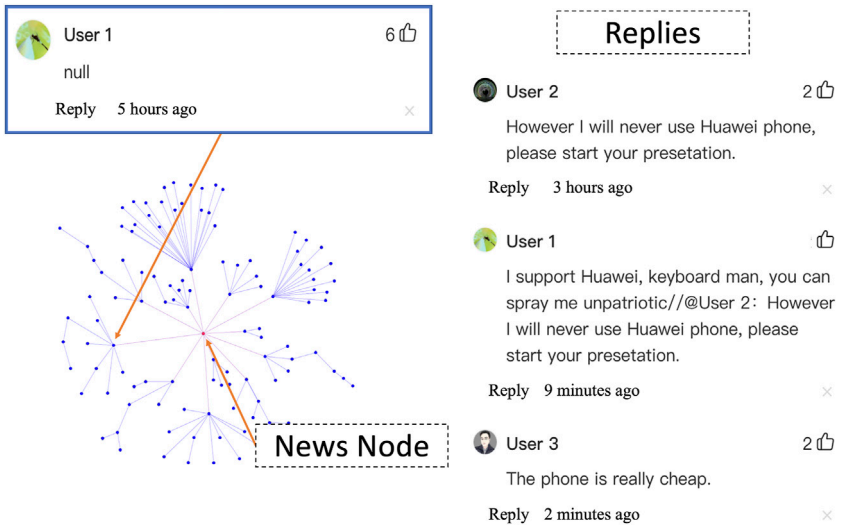

FIGURE 2
Controversial comment tree under one news article of **Huawei**, and one of the comments has been deleted.

TABLE 1 Basic statistics of the Toutiao dataset and its subsets.

	Toutiao	Toutiao#1	Toutiao#2	Toutiao#3
#News	511	11	11	1
#Users	71,579	3,496	5,940	1,573
#Comments	103,787	5,570	10,580	2,466
#Controversial interactions	22,184	2,610	4,570	1,166
#Non-controversial interactions	16,339	1,309	2,976	584
#Interactions	46,536	4,995	9,504	2,294

TABLE 2 Different types of interactions over the Toutiao dataset and its subsets.

Relationship (A–B)	Toutiao	Toutiao#1	Toutiao#2	Toutiao#3
Comment–user	103,787	4,848	9,105	2,178
Comment–news	57,251	575	1,076	172
Comment–comment	46,536	4,995	9,504	2,294
Positive–negative	22,184	2,610	4,570	1,166
Positive–neutral	4,780	440	792	119
Positive–positive	7,873	253	429	20
Neutral–neutral	5,579	691	2,032	327
Neutral–negative	3,233	636	1,166	425
Negative–negative	2,887	365	515	237

types of nodes with different labels. Comment–user, comment–news, and comment–comment represent the edges between the three different types of nodes in the graph, and the remaining six types represent the edges between the three differently labeled comment nodes.

2.2 Analysis from the multiplex social comment network

Despite the content of news and comments, we analyze the contradictory comments from the perspective of the network

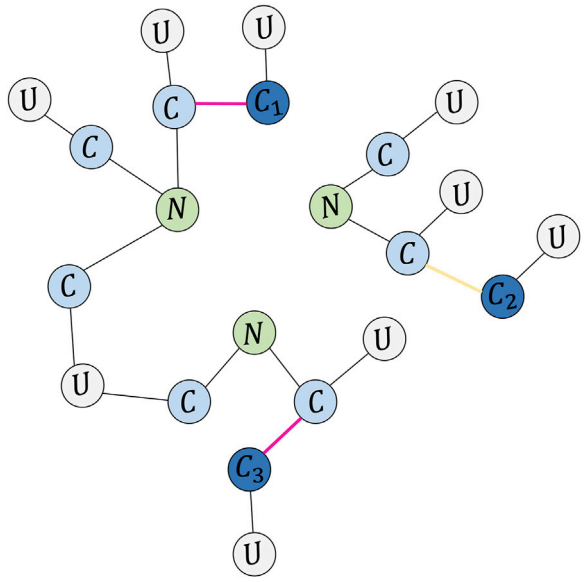

FIGURE 3
Example of a comment tree. *C* represents a comment, *N* means news, and *U* denotes a user. The red line from comment's node to comment's node means controversy, while the yellow line means non-controversy, and the node in deep blue C_1, C_2, C_3 are leaf nodes.

structure. Specifically, we construct a multiplex social comment network in which news, comments, and users act as nodes. As Figure 3 shows, these multiplex networks are composed of different entities and relationships. The entities can be classified into the following categories: comment entities, user entities, and news entities. The interactions between comment entities represent the reply relation between these two comments. The interactions between comment entities and user entities mean the related user proposes this comment. The interactions between comment entities and news entities represent the related comment replies to the current news. In the network, the comment nodes are labeled with three different types: positive, negative, and neutral. Regarding the types of these comments, we label the edges connected to two comment nodes into two types: controversial interaction and non-controversial interaction. Controversial interaction implies that the two endpoints of the edges are of positive and negative comments. Non-controversial interaction indicates the two endpoints of the edges are under the same type, which can be both positive and negative. Note that we ignore the links between neutral comments and other kinds of comments in the experiments. On the Toutiao platform, users comment on one or several pieces of news. Consequently, the news is connected to their comments, and comments are linked with their posters; in this way a piece of news and its comments naturally form a comment tree, and multiple comments form a network when they are connected with common users.

As a kind of edge in the network, do controversial edges show any significant structural patterns based on which we could distinguish them from others? This paper adopts the degree and betweenness centrality of two endpoint comment nodes to analyze the controversial edges. The degree of a comment node shows the number of its replies. Betweenness centrality describes the importance of a comment node in the network, which could show whether active yet aggressive users post the comment. Figure 4 presents the distribution of controversial edges for degree and between centrality. In Toutiao#1 and Toutiao#2, most controversial edges have larger betweenness centrality but a lower degree, and part of them has both relatively large betweenness centrality and degree. Toutiao#3 contains news items in both Toutiao#2 and Toutiao#1. The most controversial edges lie where both betweenness centrality and degree are large. It implies that structural patterns of controversial edges may exist, which motivates us to adopt graph convolution to learn such patterns. We use the time difference of two endpoint comment nodes to analyze controversial edges. Figure 5 presents the distribution of the time difference between the controversial interactions and non-controversial interactions. We observe that the reply time corresponding to controversial edges is shorter than that of non-controversial edges, which is the case in all three datasets.

3 Methods

In this section, we first briefly introduce the controversy detection problem and then show how to apply the proposed model, news–comment–user graph convolutional network (NCU-GCN) to solve the problem in detail.

3.1 Preliminaries

Our dataset consists of three types of nodes: news, comments, and users. On the platform, users could post their comments to the corresponding news or reply to others' comments, and we construct a news–comment–user network, denoted by $\mathcal{G} = (\mathcal{V}, \mathcal{E})$, to model such relationships. $\mathcal{V} = \mathcal{V}_n \cup \mathcal{V}_c \cup \mathcal{V}_u$ is the node set for all three types of nodes. $\mathcal{V}_n$, $\mathcal{V}_c$, and $\mathcal{V}_u$ correspond to news, comments, and users, respectively. For a comment c, it is associated with a timestamp t_c representing its post time, and each piece of news also has a publishing time t_n. $\mathcal{E} = \mathcal{E}_{u,c} \cup \mathcal{E}_{c,c} \cup \mathcal{E}_{c,n}$ represents the three types of relations among news, comments, and users. For $e_{u,c} = (u, c)$, where $u \in \mathcal{V}_u$, and $c \in \mathcal{V}_c$, it denotes that user u posts comments, and $e_{c_i,c_j} = (c_i, c_j)$, where $c_i, c_j \in \mathcal{V}_c$ represents that comment c_i replies to comment c_j. Likewise, $e_{c,n} = (c, n)$, where $n \in \mathcal{V}_n$ shows that comment c is the first-level comment of news n. Under the definition, we could obtain an undirected network $\mathcal{G}$ to model relationships between news, comments, and users.

Our solution to find controversy between comments is mainly based on the structure of the news–comment–user network. Mathematically, we aim to learn a mapping $\mathcal{T}: e_{c_i,c_j} \rightarrow 1$ or 0, where 1 means c_i and c_j, two controversial comments, and 0 represents the opposite.

3.2 Framework

In this part, we give a detailed description of the proposed model NCU-GCN.

GCN has proved its effectiveness in various areas. It aggregates the features of neighboring nodes to learn embeddings for nodes from the local structure perspective. The process is also known as message passing. For node i in a graph, the hidden representation of i of $(l+1)^{th}$ GCN layer, denoted as $h_i^{(l+1)}$, could be obtained by

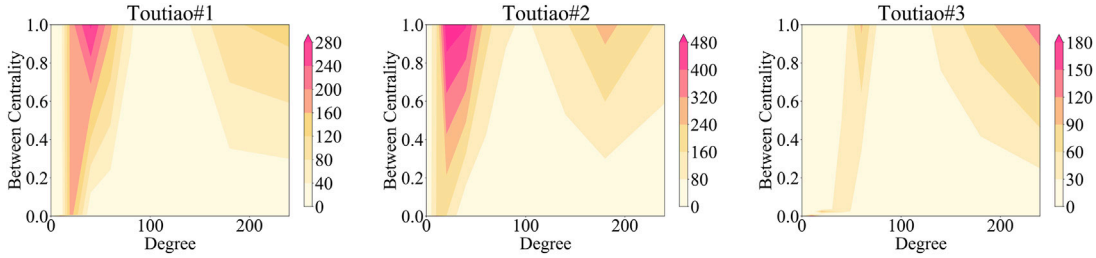

FIGURE 4
Illustration of heatmap distribution modulation consisting of two variables: node degrees and edge between centrality.

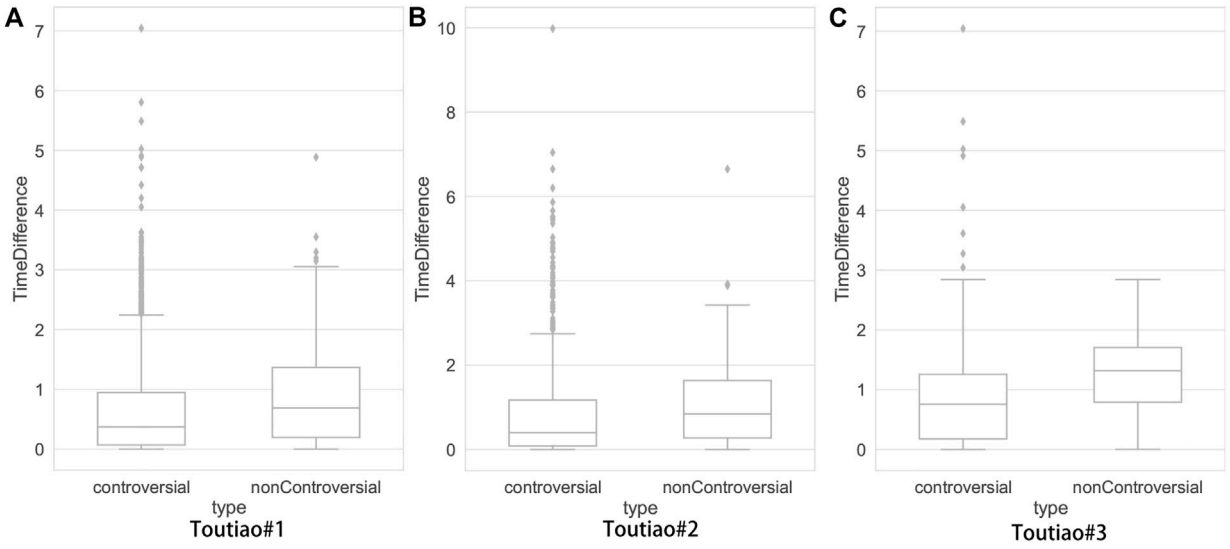

FIGURE 5
Distribution of reply time of comments and their replies. **(A–C)** represent the results of these three subsets: Toutiao#1, Toutiao#2 and Toutiao#3.

$$\boldsymbol{h}_i^{(l+1)} = \mathrm{ReLU}\left(\sum_{j\in\mathcal{N}_i\cup\{i\}} \mathbf{W}^{(l)}\boldsymbol{h}_j^{(l)} + \boldsymbol{b}^{(l)}\right), \tag{1}$$

where $\mathcal{N}_i$ is the neighbor of i. $\mathbf{W}$ is the trainable weights of *lth* GCN layer, and $\boldsymbol{b}^{(l)}$ is the corresponding bias. Incoming messages from $\mathcal{N}_i$ are aggregated after linear transformation and then passed to the central node. With $\mathrm{ReLU}(x) = \max(0, x)$ the activation function, a new representation is obtained.

In the message-passing framework, GCN works under the assumption of homogeneity. The comment network we discuss, however, consisted of nodes and edges with multiple types. Thus, we would adapt GCN to the comment network to achieve controversy detection. As presented in Figure 6, the NCU-GCN model is mainly composed of three types of layers: input layer, encoder layer, and decoder layer.

Input layer: NCU-GCN receives the comment network as the input. Considering the temporal information between comments and users, we propose to construct a temporal feature matrix $\boldsymbol{T} \in \mathbb{R}^{|\mathcal{V}|\times|\mathcal{V}|}$, which describes the temporal characteristics in the input layer. Specifically, we consider two types of edges: the edges between comments and the edges between comments and users. The structural patterns are considered, as shown in Section 2; we define the weight between comment i and another comment j by incorporating the degree and the post time interval of the two comments for an arbitrary comment i. Assuming the comment i and j belong to the news n, we normalize the weight of the two comments by the interval between the post time of the two comments. It is under the assumption that the closer a pair of comments are, the more influence they have on each other. For the relation between i and its poster, we use a hyper-parameter δ to adjust their closeness. For the edges of other types, we set their weights to 0 since they are out of the research scope of this paper. In summary, the construction of $\boldsymbol{T}$ goes as

$$\boldsymbol{T}_{i,j} = \begin{cases} \dfrac{\log_{10}\left(D_i * D_j\right)}{|t_i - t_j|}, & \textbf{if } \mathcal{E}_{i,j} \in \mathcal{E}_{c,c}, \\ \delta, & \textbf{if } \mathcal{E}_{i,j} \in \mathcal{E}_{c,u}, \\ 0, & \textbf{otherwise}. \end{cases} \tag{2}$$

where D_i means the degree of comment node i, and t_i represents the dynamic features of comment node i, which is calculated by $t_i = \log_{10}(\mathbb{T}_i - \mathbb{T}_n + 1) + 1$, $\mathbb{T}_i$ is the post time of comment node i, and $\mathbb{T}_n$ is the post time of news which contains comment i.

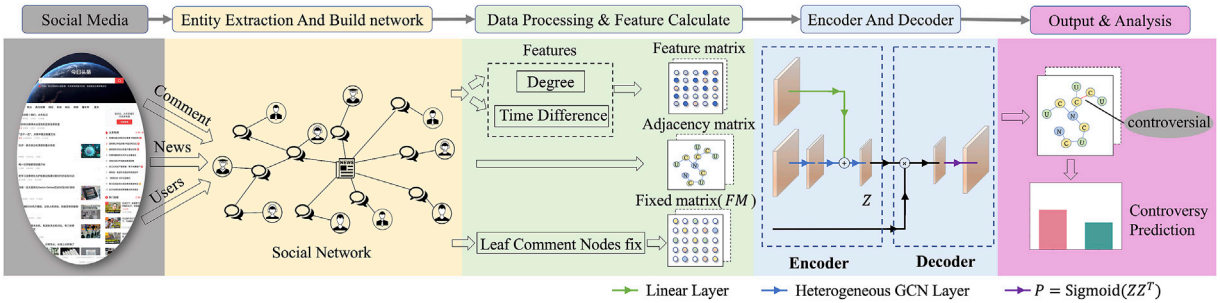

FIGURE 6
Architecture of our framework, including graph constructing and model of the news–comment–user graph convolutional network (NCU-GCN). Z represents the embedding vectors obtained from the encoder layer.

Encoder layer: After obtaining the constructed temporal feature matrix $\boldsymbol{T}$, we learn the representations of the nodes, denoted as $\boldsymbol{Z} \in \mathbb{R}^{|\mathcal{V}|\times d}$, by a GCN-inspired encoder, and d is the embedding dimension. $\boldsymbol{Z}$ is designed to incorporate $\boldsymbol{T}$, which describes the temporal characteristics and the structural features learned by neighborhood aggregation. Hence, the encoder consists of GCN-inspired structure learning and temporal feature fusion.

Different from the learning process of GCN, which acts on homogeneous networks, the structure learning module in the encoder layer considers three different kinds of neighbors. As we have introduced, for an arbitrary node in the network, its neighbors could be comment, news, or user nodes. We treat the neighbors separately when learning structural features and then integrate them to obtain the representation. In addition, due to the comment network's sparsity, we consider all the nodes in a two-hop neighborhood to ensure the abundance of structural features. Mathematically, GCN-inspired structure learning could be described as

$$\boldsymbol{h}_i = \sum_{j\in\mathcal{N}_i^2\cap\mathcal{V}_n} \boldsymbol{W}_n\boldsymbol{x}_j + \sum_{j\in\mathcal{N}_j^2\cap\mathcal{V}_c} \boldsymbol{W}_c\boldsymbol{x}_j + \sum_{j\in\mathcal{N}_i^2\cap\mathcal{V}_u} \boldsymbol{W}_u\boldsymbol{x}_j, \tag{3}$$

where $\boldsymbol{h}_i \in \mathbb{R}^{|\mathcal{V}|\times d}$ is the representation of node i. $\boldsymbol{W}_n$, W_c, and W_u are the trainable weights for encoding the features of the news, comment, and user node neighbors of i, respectively. For encoding, $\mathcal{N}_i^2$ denotes the node set of i's two-hop neighborhood, and thus, $\mathcal{N}_i^2 \cap \mathcal{V}_n$ is comment node in i's two-hop neighborhood. x_i is the initial feature of node i, and we set the initial feature of all nodes as an identity matrix since no other information other than the graph structure is available. Each part in Eq. 3 characterizes corresponding structural features, which performs better than mixing them in a single GCN layer. As for the parts of $\sum_{j\in\mathcal{N}_i^2\cap\mathcal{V}_n}\boldsymbol{W}_n\boldsymbol{x}_j$, $\sum_{j\in\mathcal{N}_j^2\cap\mathcal{V}_c}\boldsymbol{W}_c\boldsymbol{x}_j$, and $\sum_{j\in\mathcal{N}_i^2\cap\mathcal{V}_u}\boldsymbol{W}_u\boldsymbol{x}_j$, they aggregate the features of news nodes, comment nodes, and user nodes in two-hop neighborhood. The features of different nodes in the graph embedding process of multiplex networks have varying importance to the target node in the feature-aggregation process. In the process, NCU-GCN performs feature extraction by different trainable weight matrices and sums up the computed results. After obtaining the result, we then stack all the embeddings of nodes to obtain the structure feature matrix $\boldsymbol{H} \in \mathbb{R}^{|\mathcal{V}|\times d}$:

$$\boldsymbol{H} = [\boldsymbol{h}_0, \boldsymbol{h}_1, \ldots, \boldsymbol{h}_{|\mathcal{V}|}]^\top. \tag{4}$$

After obtaining the structural feature matrix $\boldsymbol{H}$, we further combine the temporal features $\boldsymbol{T}$ to obtain final representations $\boldsymbol{Z} \in \mathbb{R}^{|\mathcal{V}|\times d}$. To achieve the combination, we first map the temporal information with a linear layer to $\mathbb{R}^{|\mathcal{V}|\times d}$ and then apply the element-wise product over the encoded temporal feature and $\boldsymbol{H}$. After the combination, we use a fully connected layer f_H to smooth the embedding vectors. The process is shown as

$$\boldsymbol{Z} = f_H(\mathbf{concat}(f_L(\boldsymbol{T}), \boldsymbol{H})). \tag{5}$$

Decoder layer: The decoder layer re-transforms the hidden representations of nodes from embedding space to the original network. The edges whose endpoint nodes are close in the embedding space will be reconstructed. In the learning process, the model enlarges the distance of the representations of controversial and non-controversial edges, and they will not be reconstructed when decoding. In this study, we propose to use the inner product as the decoder and the probability matrix $\boldsymbol{P}$ = Sigmoid $(\boldsymbol{Z}\boldsymbol{Z}^T)$. In the comment network, there always exist comments without replies. Such comment nodes carry little structural information, which gets in the way of identifying the relations between them and their parent comments. To cope with the situation, we adopt a FIXMATRIX $\boldsymbol{F}$ in the decoder layer:

$$\boldsymbol{F}_{i,j} = \begin{cases} 1/D_i & \textbf{if } j \in \mathcal{N}_i, \\ 1 & \textbf{otherwise}, \end{cases}, \tag{6}$$

where D_i is the out-degree of comment i's parent comment and $\mathcal{N}_i$ represents the neighbor nodes of the parent node of comment i. As the definition indicates, the FIXMATRIX enhances the representations of leaf comment with other comments being to the same parent comment. We apply a Sigmoid function to the fusion vectors to get the final results:

$$\boldsymbol{P} = \mathrm{Sigmoid}\big((\boldsymbol{F}^\top\boldsymbol{Z})(\boldsymbol{F}^\top\boldsymbol{Z})^\top\big). \tag{7}$$

$\boldsymbol{P}$ is the possibility matrix, which indicates the prediction result of whether the interaction is controversial or not. To optimize the parameters in the model, we use cross-entropy as the objective:

$$\mathcal{L} = -\frac{1}{|\mathcal{E}'|}\sum_{(i,j)\epsilon\mathcal{E}'}\big(1-\boldsymbol{Y}_{i,j}\big)\log\big(1-\boldsymbol{P}_{i,j}\big) + \boldsymbol{Y}_{i,j}\log\big(\boldsymbol{P}_{i,j}\big), \tag{8}$$

where $\mathcal{E}'$ is the edges used for training. $Y_{i,j}$ is the label with 1 representing controversy and 0 representing the opposite. The framework of NCU-GCN is shown in Algorithm 1.

Require: the network $\mathcal{G} = (\mathcal{V}, \mathcal{E})$ with the adjacency matrix A
Pretrain the model through deep belief network to obtain the initialized parameters $\theta = \{\theta^{(1)}, \ldots, \theta^{(k)}\}$
Obtain the dynamic feature matrix $\boldsymbol{T}$, apply Eq. 2.
Obtain FixMatrix $\boldsymbol{F}$, apply Eq. 6.
while not convergence **do**
Based on Eq. 3, obtain structural embedding result $\boldsymbol{H}$.
Based on Eq. 5, use $\boldsymbol{T}$ and $\boldsymbol{H}$ to obtain node presentation embedding results $\boldsymbol{Z}$.
Based on Eq. 7, use $\boldsymbol{F}$ to obtain the probability matrix $\boldsymbol{P}$.
Based on Eq. 8, obtain $\mathcal{L}$
Use $\partial\mathcal{L}/\partial\theta$ to back-propagate through the entire network to get updated parameters θ.
end while
return $\boldsymbol{P}$

Algorithm 1. NCU-GCN.

3.3 Time complexity

To use NCU-GCN for controversy detection, one has to first calculate the dynamic and structural features and accumulate the result counts to a $N \times N$ matrix, where N is the number of nodes. Thus, the time complexity is $\mathcal{O}(N_{neighbr}N)$, where $N_{neighbr}$ is the number of neighbors of one node. The complexity required for a single iteration of NCU-GCN is divided into two main components, encoding operation and decoding operation. The encoder has a time complexity of $\mathcal{O}(3N^2\mathcal{H}^l) + \mathcal{O}(N^2L)$, where $\mathcal{H}$ is the size of the trainable graph filter. We have $l = 2$. L is the output dimension of the linear layer. Assuming that the adjacency matrix is sparse, we can have an encoder with a complexity of $\mathcal{O}(E\mathcal{H}^2) + \mathcal{O}(EL)$, where E is the number of edges from the inputting graph. The complexity of the decoding operation is $\mathcal{O}((L + \mathcal{H})NF) + \mathcal{O}(3N^2F)$, where F is the output dimension of the fully connected layer. Overall, the final time complexity for one epoch is $\mathcal{O}(E\mathcal{H}^2) + \mathcal{O}(EL) + \mathcal{O}((L + \mathcal{H})NF) + \mathcal{O}(N^2F)$.

4 Results

In this section, we conduct extensive experiments to compare our proposed model with other baselines to show the effectiveness.

4.1 Baselines

To validate the effectiveness of our method, we compare NCU-GCN with four representative baselines, which include network embedding approaches and graph neural networks.

- **node2vec** [33] keeps the neighborhood of vertices to learn the vertex representation among networks, and it achieves a balance between homophily and structural equivalence.
- **CTDNE** [42] is a general framework for incorporating temporal information into network embedding methods, which is based on random walk and stipulates that the timestamp of the next edge in the walk must be larger than that of the current edge.
- **GAE** [40] aims at using a structure based on encoder–decoder to get the vertex's embedding vector of the networks, and then the embedding vectors are used to finish the next purpose. The encoder consists of several GCN layers.
- **metapath2vec** [34] is used for heterogeneous graph embedding based on the meta-path walk to get a series of vertex containing various labels, then heterogeneous skip-gram is used to generate the embedding vectors. The meta-path strategy is set previously, and it is always symmetrical.
- **GAT** [43] achieves advanced performance on graph embedding problems. It uses the attention mechanism to learn the relative weights between two connected nodes. Moreover, GAT further uses multi-head attention to increase the model's expressive capability

4.2 Implementation details

As for baselines, the embedding dimension of node2vec and CTDNE is set to 128, and the optimal key parameters p and q of node2vec are obtained through grid search over {0.5, 1, 2}. For the metapath2vec method, the process to classify nodes is as follows: first, we divide all nodes into three types: news, comments, and users, and then we subdivide comment nodes; second, we formulate five meta-paths: including *comments* → *news* → *comments*, *comments* → *comments*, *comments* → *users* → *comments*, *comments* → *comments* → *news* → *comments*, and *comments* → *comments* → *users* → *comments*. Based on these meta-paths, we use the metapath2vec method to map the original network to a 128-dimensional vector space for quantization. For all embedding-based methods, we adopt logistic regression (LR) and random forest (RF) as the classifier for controversy detection. In the NCU-GCN model, we use 32-dim latent vectors to represent nodes and we use ReLU for our encoder layer. The optimizer used by NCU-GCN is Adam, and the learning rate is set 1e − 2 with a weight decay value, the value is 1e − 4. All the experiments are implemented on the platform equipped with an Intel(R) Xeon(R) Gold 5218 CPU and an NVIDIA Tesla V100S GPU.

Before conducting experiments, we split our dataset into training and testing sets. We divide total edges into two types: controversial and non-controversial. Then, we randomly sample n edges from the edges labeling controversial and randomly sample the same number of edges from the non-controversial edges. Then, we split into training and testing sets at the ratio of 4:1. Specifically, we choose 80% edges labeling controversial as positive samples of the training set and randomly sample the same number of edges from non-controversial edges. The remaining edges are positive testing data, and the same amount of non-controversial edges are sampled as negative testing data.

4.3 Performance comparison

We compare the performance of NCU-GCN with the competitive models on the dataset with AUC and average precision (AP) as the evaluation metrics.

TABLE 3 Performance of different methods among three subsets with respect to AUC and AP.

Method	Classifier	Toutiao#1		Toutiao#2		Toutiao#3	
		AUC	AP	AUC	AP	AUC	AP
node2vec	LR	0.6924	0.6306	0.7266	0.6625	0.7641	0.6973
	RF	0.7559	0.6988	0.8036	0.7386	0.7758	0.7153
CTDNE	LR	0.7066	0.6454	0.7241	0.6589	0.7531	0.6869
	RF	0.7692	0.7044	0.8131	0.7502	0.7878	0.7253
metapath2vec	LR	0.7114	0.6479	0.7191	0.6553	0.7673	0.7032
	RF	0.7621	0.6976	0.8098	0.7396	0.7835	0.7362
GAE		0.7846	0.7694	0.8372	0.8065	0.8051	0.7854
GAT		0.8270	**0.8095**	0.8490	0.8261	0.8230	0.7992
NCU-GCN(Homo)		0.8215	0.8004	0.8545	0.8201	**0.8697**	**0.8521**
NCU-GCN		**0.8324**	0.8010	**0.8671**	**0.8353**	0.8647	0.8457

The bold values stand for the best performance given by the aimed methods.

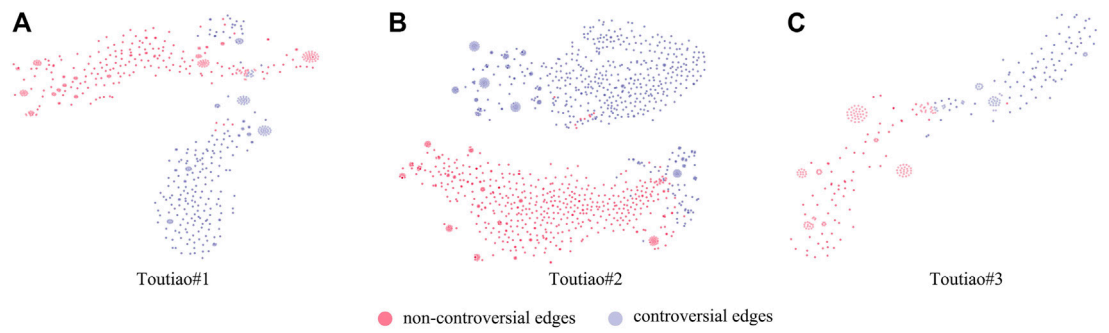

FIGURE 7
Comment-embeddings visualization. **(A–C)** represent the results of these three subsets: Toutiao#1, Toutiao#2 and Toutiao#3.

As presented in Table 3, NCU-GCN outperforms other models on the three Toutiao datasets. As a method only based on random walk, node2vec performs the worst among all methods. CTDNE have better performance than node2vec due to the integration of temporal information when conducting random walk, and metapath2vec makes use of the heterogeneity information in the comment network, which contributes to its better performance compared with node2vec. The performance gap between different classifiers, i.e., LR and RF, indicates that it is also important to choose a proper classifier even for state-of-the-art embedding-based methods. The results of the four GNN (graph neural network) methods show that end-to-end frameworks are always better than making inference by two-step methods, which usually obtain representations first. The NCU-GCN (Homo) method represents a method of graph embedding based on the homogeneity of network nodes, i.e., based on the structure of the NCU-GCN model by modifying Equation (3) as $\boldsymbol{h}_i = \sum_{j \in \mathcal{N}_i^2 \cap \mathcal{V}} \boldsymbol{W}_n \boldsymbol{x}_j$. Overall, NCU-GCN has better performance than other graph neural network methods, which is due to the consideration of temporal and heterogeneous information when designing the model. Moreover, the results of NCU-GCN are better than NCU-GCN(Homo). This shows that the graph-embedding results are improved by separating the nodes according to their neighborhood node types than by not separating the types.

Moreover, we notice that NCU-GCN performs better on Toutiao#2 than on Toutiao#1 and Toutiao#3. The different expressiveness of the obtained embeddings may cause it. Thus, we visualize the embedding vectors of edges with t-SNE. In order to generate feature representations for an edge, we compose the learned feature representations of the two endpoint comment nodes by element-wise production. As shown in Figure 7, the red points represent non-controversial edges, and the points in blue denote the opposite. Generally, the embeddings of controversial and non-controversial edges could be separated according to the visualizations, and some edges are mixed in the cluster that is not of their type, especially for Toutiao#1 and Toutiao#3. Such edges might result in the decrease of NCU-GCN's performance. The boundary of the two clusters in the visualization of Toutiao#2 is clearer than that in Toutiao#1 and Toutiao#3. It is consistent with the performance recorded in Table 3.

4.4 Parameter sensitivity

Here, we mainly focus on the influence of the three parameters, δ, D, and T, on the performance of NCU-GCN. The results are shown in

TABLE 4 Performance of different parameters of the NCU-GCN method among three subsets with respect to AUC and AP.

Parameter			Toutiao#1		Toutiao#2		Toutiao#3	
δ	D	T	AUC	AP	AUC	AP	AUC	AP
0	✓	×	0.8029	0.7343	0.8278	0.7635	0.8569	0.8002
0	×	✓	0.8347	0.7864	0.8609	0.8264	0.8643	0.8389
0.01	✓	×	0.8035	0.7331	0.8224	0.7527	**0.8659**	0.8160
0.01	×	✓	**0.8356**	0.7889	0.8623	0.8265	0.8582	0.8456
0.1	✓	✓	0.8284	0.7981	0.8623	0.8265	0.8610	0.8407
0.01	✓	✓	0.8281	**0.8071**	0.8626	0.8331	0.8626	0.8417
0	✓	✓	0.8324	0.8010	**0.8671**	**0.8353**	0.8647	**0.8457**

The bold values stand for the best performance given by the value of the aimed parameter.

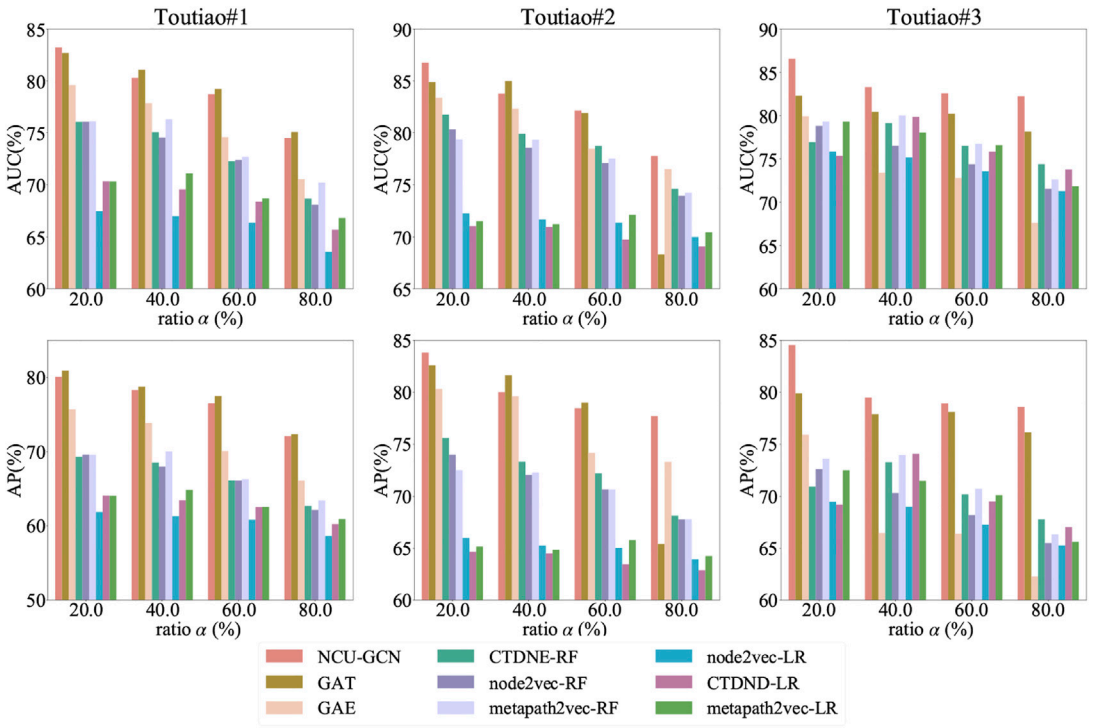

FIGURE 8
Performance of different methods on three different datasets when α changes.

Table 4 where we can see that the performance improves as δ decreases. Smaller δ represents the shorter time difference between comment nodes and user nodes. It validates that in our Chinese Toutiao datasets, the time difference between comment nodes and user nodes is relatively small. It is also coincidental that there is almost no time difference between the posting and release of a comment on social media. Moreover, the combination of features D and T in feature calculation achieves better performance than solely using D or T. The larger D represents that a comment has more replies, which indicates this comment is more important in the network. The results show that the importance of the comment nodes and the reply time difference can help controversy identification. It is consistent with the conclusions presented in [44].

In addition, we further vary the proportion of test set α to investigate whether NCU-GCN still performs better when only a small amount of labeled data is available. As shown in Figure 8, the performances of all methods decrease when the amount of training sample reduces. However, NCU-GCN still has the best performance compared to the baselines, showing its superior controversy detection ability. We also notice that the performance of GAE significantly decreases when $\alpha > 20\%$ on Toutiao#3, and the performance of GAT significantly decreases when $\alpha = 80\%$ on Toutiao#2. This is because the

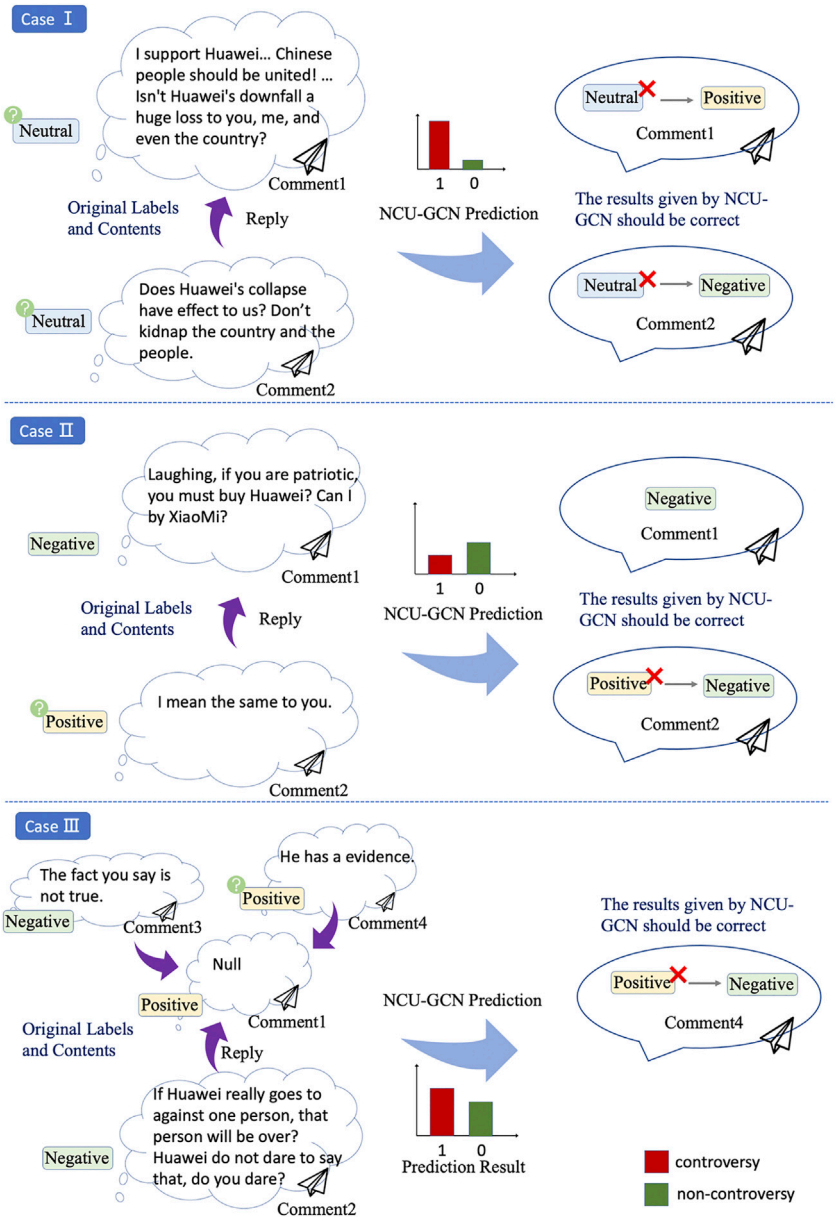

FIGURE 9
Samples of the comments which may get a wrong label.

risk of overfitting the model increases as the number of training sets decreases. As a model which also develops from GCN, NCU-GCN adopts the FixMatrix and the temporal feature matrix $\boldsymbol{T}$ to cope with the problem.

4.5 Misjudged cases

In addition to pursuing better performance, we also investigate the false positive edges to find why NCU-GCN fails on these samples. Statistically, a part of error detected edges occur due to the low depth of the endpoint comments in the comment tree. In other words, they possess less structural information than other comments. Although we propose to use FIXMATRIX to alleviate the influence, it is still hard to make precise detection under this circumstance.

Also, we find the edges with wrong labels in the misjudged samples, which are more common in real-world applications, especially in semantic-related tasks. As we introduced in Sec. 1, the obscurity of linguistics leads to the difficulty of comment labeling, even for human annotators, and the lack of comment content may also result in wrong labels. Figure 9 shows the three different kinds of misdetection, in which the comments are assigned with wrong labels. In case I, both of the comments are labeled as neutral, and the relation between the two comments is non-controversial consequently, which is opposed to the result given by NCU-GCN. However, the parent's comment is positive and the reply is negative according to their texts, implying that the relationship is controversial. The actual label is

identical to the model's judgment. It is a false-positive case where a non-controversial edge is considered a controversial one by the model. Similarly, case II is a truly negative one under the same situation. In case III, the label of the parent comment is obtained by annotators' inference according to its replies due to the lack of content. It may also lead to wrong comment labels. In these cases, the model makes the right judgments despite the wrong labels. It is because the model learns the structural patterns of controversial comments in the network, again showing the benefits of graph-based learning for controversy detection against the approaches solely based on semantics. It also reveals the dilemma that high-quality annotation is essential but always deficient in real-world applications. We may integrate semantics into the detection model in future works to give human-readable results, which is a possible solution to the aforementioned dilemma.

5 Discussion

In this paper, we collect a real-world dataset from a Chinese social media platform and construct multiplex networks connected by multiple links. After obtaining the networks, we propose NCU-GCN to detect controversial interactions between a comment and its replies. Unlike the existing works, we focus on detecting controversial interactions in social comment networks and exploit the information from related news under the same topic and the reply structure for more effective detection. Our paper proposes a novel strategy for multiplex social comment networks based on the graph convolutional network. Through training, NCU-GCN can fully exploit the multiplex social comment network's structural information and dynamic features and gain an improvement compared to competitive models. Moreover, the extensive experiments present NCU-GCN achieving good performance with a low train–test ratio of multiplex social comment networks. Moreover, our method can also find some mislabeled comments. The labels of some comments may be mislabeled, but NCU-GCN can identify them through the graph-embedding method.

This work opens several avenues for future research. First, our solution takes the graph-embedding method to solve the problem of controversial detection. Though some text information is lost, it avoids the problem of inaccurate prediction caused by semantic diversity. Second, we incorporated time information, node importance, and related node information into our model and achieved specific results.

Data availability statement

The raw data supporting the conclusion of this article will be made available by the authors, without undue reservation.

Author contributions

All authors contributed to the study conception and design. Material preparation, data collection, and analysis were performed by ZL, JZ, and YM. The first draft of the manuscript was written by ZL and checked by JZ, QX, XQ, and YM. All authors commented on previous versions of the manuscript. All authors read and approved the final manuscript.

Funding

This work was supported in part by the Key Research and Development Programs of Zhejiang Province under Grant 2022C01018, by the National Natural Science Foundation of China under Grants 61973273 and U21B2001, by the Zhejiang Provincial Natural Science Foundation of China under Grants LGF21G010003 and LR19F030001, by the National Social Science Foundation of China under Grant 18BGL231, and by the National Key R&D Program of China under Grant 2021YFB3101305.

Conflict of interest

The authors declare that the research was conducted in the absence of any commercial or financial relationships that could be construed as a potential conflict of interest.

Publisher's note

References

1. Coletto M, Garimella K, Gionis A, Lucchese C. Automatic controversy detection in social media: A content-independent motif-based approach. *Online Soc Networks Media* (2017) 3:22–31. doi:10.1016/j.osnem.2017.10.001

2. Garimella K, Morales GDF, Gionis A, Mathioudakis M. Quantifying controversy on social media. *ACM Trans Soc Comput* (2018) 1:1–27. doi:10.1145/3140565

3. Guerra P, Meira W, Jr, Cardie C, Kleinberg R. A measure of polarization on social media networks based on community boundaries. *Proc Int AAAI Conf Web Soc Media* (2013) 7:215–24. doi:10.1609/icwsm.v7i1.14421

4. Hessel J, Lee L. Something's brewing! early prediction of controversy-causing posts from discussion features. In: J Burstein, C Doran, T Solorio, editors. Proceedings of the 2019 Conference of the North American Chapter of the Association for Computational Linguistics: Human Language Technologies, NAACL-HLT 2019; June 2-7, 2019; Minneapolis, MN, USA. Association for Computational Linguistics (2019). p. 1648–59. Long and Short Papers.

5. Lu H, Caverlee J, Niu W. Biaswatch: A lightweight system for discovering and tracking topic-sensitive opinion bias in social media. In: Proceedings of the 24th ACM International on Conference on Information and Knowledge Management, Melbourne, VIC, October 19–23, 2015. (2015). p. 213–22.

6. Yin Z, Fan L, Yu H, Gilliland AJ. Using a three-step social media similarity (TSMS) mapping method to analyze controversial speech relating to COVID-19 in twitter collections. In: 2020 IEEE International Conference on Big Data; December 10-13, 2020; Atlanta, GA, USA. IEEE (2020). p. 1949–53.

7. Garimella K, Morales GDF, Gionis A, Mathioudakis M. Reducing controversy by connecting opposing views. In: Proceedings of the Twenty-Seventh International Joint Conference on Artificial Intelligence, IJCAI 2018; July 13-19, 2018; Stockholm, Sweden (2018). p. 5249–53. (ijcai.org).

8. Conover M, Ratkiewicz J, Francisco M, Gonçalves B, Menczer F, Flammini A. Political polarization on twitter. *Proc Int AAAI Conf Web Soc Media* (2011) 5:89–96. doi:10.1609/icwsm.v5i1.14126

9. Dori-Hacohen S, Allan J. Detecting controversy on the web. In: Proceedings of the 22nd ACM International Conference on Information & Knowledge Management, San Francisco, CA, October 28, 2013. (2013). p. 1845–8.

10. Choi Y, Jung Y, Myaeng SH. *Identifying controversial issues and their sub-topics in news articles*. Pacific-Asia Workshop on Intelligence and Security Informatics Springer, Hyderabad, India, June 21, 2010 (2010). p. 140–53.

11. Yasseri T, Sumi R, Rung A, Kornai A, Kertész J. Dynamics of conflicts in wikipedia. *PloS one* (2012) 7:e38869. doi:10.1371/journal.pone.0038869

12. Awadallah R, Ramanath M, Weikum G. Harmony and dissonance: Organizing the people's voices on political controversies. In: Proceedings of the fifth ACM International Conference on Web search and Data mining, Seattle, Washington, February 8–12, 2012. (2012). p. 523–32.

13. Kittur A, Suh B, Pendleton BA, Chi EH. He says, she says: Conflict and coordination in wikipedia. In: Proceedings of the SIGCHI conference on Human factors in computing systems, San Jose CA, April 28–May 3, 2007. (2007). p. 453–62.

14. Zhong L, Cao J, Sheng Q, Guo J, Wang Z. Integrating semantic and structural information with graph convolutional network for controversy detection. In: D Jurafsky, J Chai, N Schluter, JR Tetreault, editors. Proceedings of the 58th Annual Meeting of the Association for Computational Linguistics, ACL 2020, Seattle, WA, July 6–10, 2020. Association for Computational Linguistics (2020). p. 515–26. Online, July 5-10, 2020.

15. Mei Q, Ling X, Wondra M, Su H, Zhai C. Topic sentiment mixture: Modeling facets and opinions in weblogs. In: Proceedings of the 16th International Conference on World Wide Web (2007). p. 171–80.

16. Adamic LA, Glance N. The political blogosphere and the 2004 us election: Divided they blog. In: Proceedings of the 3rd International Workshop on Link discovery, Chicago, IL, August 21–25, 2005. (2005). p. 36–43.

17. Vuong BQ, Lim EP, Sun A, Le MT, Lauw HW, Chang K. On ranking controversies in wikipedia: Models and evaluation. In: Proceedings of the 2008 International Conference on Web search and Data mining, Palo Alto CA, February 11–12, 2008 (2008). p. 171–82.

18. Rad HS, Barbosa D. Identifying controversial articles in wikipedia: A comparative study. In: Proceedings of the eighth annual International Symposium on Wikis and Open collaboration, Linz, Austria, August 27–29, 2017 (2012). p. 1–10.

19. Linmans J, van de Velde B, Kanoulas E. Improved and robust controversy detection in general web pages using semantic approaches under large scale conditions. In: Proceedings of the 27th ACM International Conference on Information and Knowledge Management, Torino, Italy, October 22–26, 2018 (2018). p. 1647–50.

20. Koncar P, Walk S, Helic D. Analysis and prediction of multilingual controversy on reddit. In: 13th ACM Web Science Conference 2021, Virtual Event United Kingdom, June 21–25, 2021 (2021). p. 215–24.

21. Rethmeier N, Hübner M, Hennig L. Learning comment controversy prediction in web discussions using incidentally supervised multi-task cnns. In: Proceedings of the 9th Workshop on Computational Approaches to Subjectivity, Sentiment and Social Media Analysis, Brussels, Belgium, October 31, 2018 (2018). p. 316–21.

22. Addawood A, Rezapour R, Abdar O, Diesner J. Telling apart tweets associated with controversial versus non-controversial topics. In: Proceedings of the Second Workshop on NLP and Computational Social Science, Vancouver, Canada, August 3, 2017 (2017). p. 32–41.

23. Guimarães A, Weikum G. X-posts explained: Analyzing and predicting controversial contributions in thematically diverse reddit forums. In: C Budak, M Cha, D Quercia, L Xie, editors. Proceedings of the Fifteenth International AAAI Conference on Web and Social Media, ICWSM 2021; June 7-10, 2021; Held virtually. AAAI Press (2021). p. 163–72.

24. Levy S, Kraut RE, Yu JA, Altenburger KM, Wang YC. Understanding conflicts in online conversations. In: Proceedings of the ACM Web Conference 2022, Lyon, France, April 25–29, 2022 (2022). p. 2592–602.

25. Popescu AM, Pennacchiotti M. Detecting controversial events from twitter. In: Proceedings of the 19th ACM International Conference on Information and Knowledge Management, Toronto, ON, October 26–30, 2010 (2010). p. 1873–6.

26. Choi M, Aiello LM, Varga KZ, Quercia D. Ten social dimensions of conversations and relationships. In: Y Huang, I King, T Liu, M van Steen, editors. WWW '20: The Web Conference 2020; April 20-24, 2020; Taipei, Taiwan. ACM/IW3C2 (2020). p. 1514–25. doi:10.1145/3366423.3380224

27. Kumar S, Hamilton WL, Leskovec J, Jurafsky D. Community interaction and conflict on the web. In: P Champin, F Gandon, M Lalmas, PG Ipeirotis, editors. Proceedings of the 2018 World Wide Web Conference on World Wide Web, WWW 2018; April 23-27, 2018; Lyon, France. ACM (2018). p. 933–43. doi:10.1145/3178876.3186141

28. Wang X, Cui P, Wang J, Pei J, Zhu W, Yang S. Community preserving network embedding. Singh S. In: S Markovitch, editor. Proceedings of the Thirty-First AAAI Conference on Artificial Intelligence; February 4-9, 2017; San Francisco, California, USA. AAAI Press (2017). p. 203–9.

29. Zhang M, Chen Y. Link prediction based on graph neural networks. In: S Bengio, HM Wallach, H Larochelle, K Grauman, N Cesa-Bianchi, R Garnett, editors. Advances in Neural Information Processing Systems 31: Annual Conference on Neural Information Processing Systems 2018; December 3-8, 2018; Montréal, Canada. NeurIPS (2018). p. 5171–81.

30. Fu C, Zhao M, Fan L, Chen X, Chen J, Wu Z, et al. Link weight prediction using supervised learning methods and its application to yelp layered network. *IEEE Trans Knowledge Data Eng* (2018) 30:1507–18. doi:10.1109/tkde.2018.2801854

31. Lee JB, Rossi R, Kong X. Graph classification using structural attention. In: Proceedings of the 24th ACM SIGKDD international conference on Knowledge Discovery & Data Mining, London, United Kingdom, August 19–23, 2018. (2018). p. 1666–74.

32. Perozzi B, Al-Rfou R, Skiena S. Deepwalk: Online learning of social representations. In: Proceedings of the 20th ACM SIGKDD International Conference on Knowledge Discovery and Data mining, New York, NJ, August 24–27, 2014. (2014). p. 701–10.

33. Grover A, Leskovec J. node2vec: Scalable feature learning for networks. In: Proceedings of the 22nd ACM SIGKDD International Conference on Knowledge discovery and data mining, San Francisco CA, August 13–17, 2016 (2016). p. 855–64. doi:10.1145/2939672.2939754

34. Dong Y, Chawla NV, Swami A. metapath2vec: Scalable representation learning for heterogeneous networks. In: Proceedings of the 23rd ACM SIGKDD International Conference on Knowledge Discovery and Data mining, Halifax, NS, August 13–17, 2017 (2017). p. 135–44.

35. Wang J, Huang P, Zhao H, Zhang Z, Zhao B, Lee DL. Billion-scale commodity embedding for e-commerce recommendation in alibaba. In: Proceedings of the 24th ACM SIGKDD International Conference on Knowledge Discovery & Data Mining, London, United Kingdom, August 19–23, 2018 (2018). p. 839–48.

36. Xuan Q, Wang J, Zhao M, Yuan J, Fu C, Ruan Z, et al. Subgraph networks with application to structural feature space expansion. *IEEE Trans Knowledge Data Eng* (2019) 33:2776–89. doi:10.1109/tkde.2019.2957755

37. Jiang Z, Gao Z, Lan J, Yang H, Lu Y, Liu X. Task-oriented genetic activation for large-scale complex heterogeneous graph embedding. In: Proceedings of The Web Conference 2020, TaiPei, Taiwan, April 20–24, 2020 (2020). p. 1581–91.

38. Hu B, Fang Y, Shi C. Adversarial learning on heterogeneous information networks. In: Proceedings of the 25th ACM SIGKDD International Conference on Knowledge Discovery & Data Mining, Anchorage, AK, August 4–8, 2019. (2019). p. 120–9.

39. Kipf TN, Welling M. Semi-supervised classification with graph convolutional networks. In: 5th International Conference on Learning Representations, ICLR 2017; April 24-26, 2017; Toulon, France. Conference Track Proceedings (2017). (OpenReview.net).

40. Kipf TN, Welling M. *Variational graph auto-encoders* (2016). arXiv preprint arXiv: 1611.07308.

41. Yeomans M, Minson J, Collins H, Chen F, Gino F. Conversational receptiveness: Improving engagement with opposing views. *Organizational Behav Hum Decis Process* (2020) 160:131–48. doi:10.1016/j.obhdp.2020.03.011

42. Nguyen GH, Lee JB, Rossi RA, Ahmed NK, Koh E, Kim S. Dynamic network embeddings: From random walks to temporal random walks. In: 2018 IEEE International Conference on Big Data (Big Data); 10-13 December 2018; Seattle, WA, USA. IEEE (2018). p. 1085–92.

43. Velickovic P, Cucurull G, Casanova A, Romero A, Liò P, Bengio Y. Graph attention networks. In: 6th International Conference on Learning Representations, ICLR 2018; April 30 - May 3, 2018; Vancouver, BC, Canada. Conference Track Proceedings (2018).

44. Coletto M, Garimella K, Gionis A, Lucchese C. A motif-based approach for identifying controversy. *Proc Int AAAI Conf Web Soc Media* (2017) 11:496–9. doi:10.1609/icwsm.v11i1.14949

frontiers | Frontiers in Physics

TYPE Original Research
PUBLISHED 19 January 2023
DOI 10.3389/fphy.2023.1107446

OPEN ACCESS

EDITED BY
Ye Wu,
Beijing Normal University, China

REVIEWED BY
Peng Ji,
Fudan University, China
Siew Ann Cheong,
Nanyang Technological University, Singapore

*CORRESPONDENCE
Chenbo Fu,
cbfu@zjut.edu.cn
Shanqing Yu,
yushanqing@zjut.edu.cn

SPECIALTY SECTION
This article was submitted to Interdisciplinary Physics, a section of the journal Frontiers in Physics

RECEIVED 24 November 2022
ACCEPTED 09 January 2023
PUBLISHED 19 January 2023

CITATION
Fu C, Luo H, Liang X and Yu S (2023), The profit and risk in the interdisciplinary behavior.
Front. Phys. 11:1107446.
doi: 10.3389/fphy.2023.1107446

The profit and risk in the interdisciplinary behavior

Chenbo Fu[1,2]*, Haogeng Luo[1,2], Xuejiao Liang[1,2] and Shanqing Yu[1,2]*

[1]Institute of Cyberspace Security, Zhejiang University of Technology, Hangzhou, China, [2]College of Information Engineering, Zhejiang University of Technology, Hangzhou, China

Evaluating the influence of interdisciplinary research is important to the development of science. This work considers the large and small disciplines, calculates the interdisciplinary distance, and analyzes the influence of interdisciplinary behavior and interdisciplinary distance in the academic network. The results show that the risk of interdisciplinary behavior in the large discipline is more significant than the benefits. The peer in the small disciplines will tend to agree with the results of the small discipline across the large discipline. We further confirmed this conclusion by utilizing PSM-DID. The analysis between interdisciplinary distance and scientists' influence shows that certain risks will accompany any distance between disciplines. However, there still exists a "Sweet Spot" which could bring significant rewards. Overall, this work provides a feasible approach to studying and understanding interdisciplinary behaviors in science.

KEYWORDS

interdisciplinary behavior, scientific influence, large and small disciplines, interdisciplinary distance, causal inference

1 Introduction

Modern science aims to solve complex and large-scale social and natural problems [1, 2]. These systematic researches raises higher requirements on participating research team [3–5], which raises higher requirements on participating research teams. For example, collaborators may need expertise in different disciplines [6]. Furthermore, with the in-depth penetration of interdisciplinary expertise, the inherent boundaries of science have been broken, and interdisciplinary behavior has become more popular in modern science [7]. In addition, some pioneering researches involve expertise that often exceeds the scope of knowledge of a single discipline [8, 9]. Nowadays, interdisciplinary research achieves knowledge breakthroughs and innovations through colliding ideas between different disciplines, which is considered a significant feature and future trend of science society [10]. However, the study and the underlying operation mechanisms of interdisciplinarity are still in their infancy. With the successive emergence of academic databases, e.g., Web of Science, Scopus, PubMed, and Microsoft Academic Graph, these databases provide data support for interdisciplinary research. Currently, interdisciplinary research mainly focuses on three aspects: 1) interdisciplinary metrics; 2) interdisciplinary-related policies and funding; and 3) interdisciplinary influence.

The most commonly used measurements to evaluate interdisciplinarity are publications and citations. And the derived index of interdisciplinarity quantifies the diversity of disciplines involved in a paper [11, 12]. Based on the publications, interdisciplinary diversity can define with three dimensions [13], i.e., variety, balance, and disparity. Subsequent research has expanded the measurement dimensions by adding the concept of similarity and adopting cohesiveness [14]. Meanwhile, interdisciplinary research related to citation has also been explored and discovered. For example, the analysis based on citation showed that the knowledge structure of literature has changed and became increasingly interdisciplinary [15]. Furthermore,

a recent study further explored the interdisciplinary citation index and the weighted forms, and conducted verification in different disciplines [16].

Interdisciplinary research has attracted more and more attention and one of these foci is to investigate the policy and funding of interdisciplinary research [17–20]. Several prominent institutions have begun to emphasize and encourage the development of interdisciplinary research, such as the interdisciplinary development program of the National Academy of Sciences [21]. However, the evaluation of interdisciplinary funding in the academic field is mixed. One voice says interdisciplinary research is merely a policy incentive without financial support [22], i.e., interdisciplinary research is often unrewarding. For example, researchers have shown that interdisciplinary research has a lower citation and funding success rate [23]. On the contrary, another voice against this conclusion [24] showed that interdisciplinary scientists play an essential role in knowledge dissemination and are superior to scientists in traditional research for both the amount and scale of funding.

Furthermore, the underlying relationship between interdisciplinarity and scientists' influence [25–27] remains to be investigated. Previous researches provide conflicting evidence. On the one hand, it may be caused by the different definitions of interdisciplinarity. For example, scientists find that interdisciplinarity in physics has a negative influence when they measure the interdisciplinary by calculating the proportion of papers published in other disciplines [28]. Meanwhile, studies on biomedical disciplines show a negative correlation between interdisciplinarity and citation growth [29]. However, a recent study indicates that interdisciplinary papers receive more citations when interdisciplinarity is combined with novelty [30]. Furthermore, research about journals' analysis shows that papers published in journals with multiple disciplinary classifications receive fewer citations than papers published in disciplinary journals with clear disciplinary boundaries [31]. On the other hand, interdisciplinary analysis based on specific disciplines may lead to deviations. For example, biology and chemistry have a high degree of overlap in expertise, and collaborations among these disciplines tend to receive high citations in target disciplines, both for biology and chemistry. Meanwhile, low citation rates in computer science and humanities interdisciplinary may be caused by the low coverage of literature published in the interdisciplinary disciplines [32].

Although academic fields spend an enormous amount of time and energy on analyzing interdisciplinary behavior, the relationship between interdisciplinary and scientists' influence is still in its infancy. In this work, we propose the concepts of large and small disciplines and compare the changes in the influence of papers and scientists under interdisciplinary behavior. The main contributions of this work are summarized as follows.

- Our work examines a total of 4.9 million papers over the last 20 years and utilizes statistics and causal inference to quantify scientists' influence on interdisciplinary behavior.
- We find that the risk is greater than the benefit for the large across small discipline, and the opposite trend in the small discipline. Furthermore, we explore the relationship between scientists' influence and interdisciplinary distance. The results suggest that there exists a "Sweet Spot" which could bring significant rewards.
- We reveal and analyze the causal relationship between scientists' influence and interdisciplinary behavior.

The rest of the paper is organized as follows. Section 2 introduces the data preparation and the methods. Section 3 demonstrates the results of scientists' influence on interdisciplinary behavior. Finally, Section 4 concludes the investigation with some discussions.

2 Dataset and methods

2.1 Data preparation

This work uses the dataset from Aminer 1. As the release dataset version continues to update, it has become more popular and used for analyzing the information spread [33], studying the scientific influence [34–36], building recommendations in academic networks [37, 38], researching citation and cooperation networks [39–42], and developing the prediction in academic networks [43, 44]. This work adopts the 12*th* version of the dataset, which includes 4.9 million papers from 113,887 disciplines. The majority of papers contain the paper number, title, scientists, publication, citation, and field information [45]. Specifically, the field information is extracted from Mircosoft Academic Graph (MAG) [46], which contains field names and the weight w for fields of study. We selected 3,054,175 papers from 2000 to 2019, including 3,052,873 papers containing field information and 3,051,022 papers containing more than two fields information. For papers without two fields' information, we consider the field information according to the fields' proportion of the reference list, e.g., for paper P, the field A, B and C is 50%, 40% and 10% in the reference list, we attribute field A and B to the paper P.

2.2 Field-normalization

The influence meaning of citations in different fields is different. In order to avoid the bias, field-normalization is needed. In this work, we introduce the method in [47], and use a weight of the paper given by the dataset to eliminate the impact of the field. Specifically, we define the citation C_f of paper p by,

$$C_f = \sum_{i=1}^{k} \frac{w_i}{w_1 + w_2 + \cdots + w_k} * \frac{C_p}{\overline{C_i}} \tag{1}$$

Here, k is the total number of fields covered by paper p, i is one of the fields ($i = 1, 2, 3, \ldots, k$), and w_i is the weight of the i-th field; the field of research with weight w are given by the dataset; C_p is the number of citations we counted in the dataset; $\overline{C_i}$ is the total number of citations received in the i-th field.

2.3 Classification and distance for discipline

Our work explores the influence of interdisciplinary behavior based on large and small disciplines on scientists. Specifically, we extract the major and minor disciplines for the paper according to the field weight w and define the top 5% as the large discipline and the bottom 50% as the small discipline. Then, we map the relationship

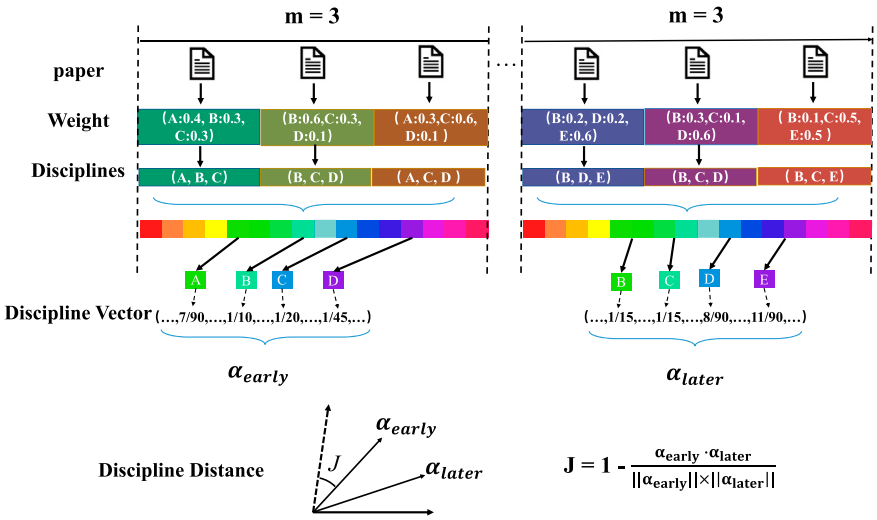

FIGURE 1
An example to calculate the interdisciplinary distance $J(m = 3)$. The early careers' discipline vector α_{early} and the later careers' discipline vector α_{later} are generated based on the early and later m papers. Finally, the interdisciplinary distance J is measured according to the complementary cosine similarity between discipline vectors.

between each paper and large or small disciplines according to citations. For example, paper A has received 10, 5, and two citations in F1, F2, and F3 disciplines, respectively. We can determine that the major discipline of paper A is F1, and the minor is F2. Finally, according to the major and minor disciplines, all papers in the data set can be classified as the large discipline set P_{l-l}, the large cross the small discipline set P_{l-s}, the small discipline set P_{s-s}, and the small cross the large discipline set P_{s-l}.

To quantify the discipline distance of inter-discipline, we utilize the method proposed by recent literature to measure the research interest evolution [48]. Specifically, all papers are attributed to the first scientist, and we have counted all authors in the data set who have continuously published papers for more than 6 years, and the maximum "tolerance year" is 2 years. For example, a scientist who has continuously published papers in 2000 and 2001, and then continued to publish papers in 2003, is also considered as consecutive publisher. Then we consider paper series for each consecutive publishing scientist as sorted by the publication period. We select three papers at the beginning and the end of the paper series for each scientist, regarded as the scientific outputs of the early and later careers, respectively. It should be noted that the early and late career we defined is not the scientists' career period, but the period before and after in a long time series. The dataset provides the discipline information representation of each paper, and we calculate the early and later discipline vector according to the discipline weight w. Finally, we can quantify the distance between the early and later career disciplines by calculating the cosine similarity of early and later career discipline vectors J. Figure 1 demonstrates an example of the specific calculation.

2.4 Causal inference

Different from correlation analysis, causal inference is not only based on correlation but also requires the temporal order of causality. Thus, correlation is only a necessary and insufficient condition for causal inference. In recent decades, causal inference has been dramatically applied in various fields, especially in finance [49] and education [50]. With the development of artificial intelligence [51–53], causal inference has new developments and applications [54, 55]. Currently, the most basic causal inference is to estimate the treatment effect by comparing the differences between the observation results of the control and treatment groups. the expected value of the treatment effect of all individuals receiving treatment, i.e., Average Treatment Effect on the Treated (ATT), can be defined as,

$$ATT = E[Y_i(1) - Y_i(0) \mid D_i = 1] \quad (2)$$

where $D_i = 1$ means individual i is disposed, $Y_i(1)$ represents the observed value of individual i after treatment, $Y_i(0)$ represents the observed value of individual i in the control group. However, randomized controlled trials will consume a lot of time and resources, individuals participating in the experiment can only be grouped into the control or treatment group. Therefore, the current causal inference tends to analyze causal relationships from statistical data [56], e.g., Differences in Differences (DID) [57], Granger Causality [58], Propensity Score Matching (PSM) [59], Generalized Propensity Score Matching (GPS) [60], Instrumental Variable [61], and Regression Discontinuity Design [62]. Compared with the above causal inference methods, DID is more suitable for panel data [63]. Specifically, we conduct the scientists into treatment and control groups according to whether they have interdisciplinary behavior, and the regression equation for DID can be written as,

$$Y_{it} = \beta_0 + \beta_1 treat_i + \beta_2 period_t + \beta_3 treat_i \times period_t + \varepsilon_{it} \quad (3)$$

where Y_{it} is a measurement of the influence (citations) of scientist i. $treat_i$ is a dummy variable for group membership and ε_{it} is the error term. If scientist i has interdisciplinary behavior, then scientist i belongs to the treated group, $treat_i = 1$; otherwise, $treat_i = 0$. $period_t$ is a dummy variable for the period. Assume that the time

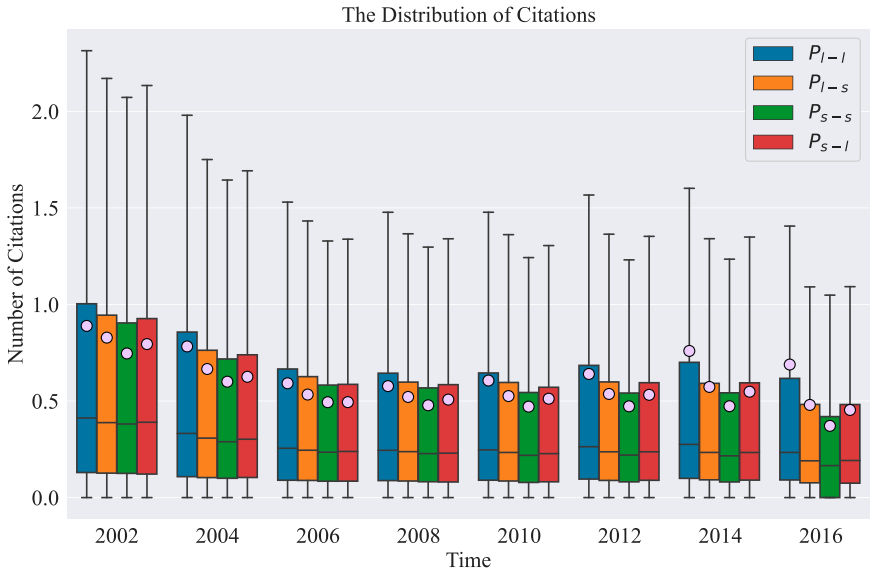

FIGURE 2
The evolution of citations of papers within different interdisciplinary types. We classify papers as the large discipline (blue box), the large across the small discipline (orange box), the small discipline (green box), and the small across large discipline (red box). The solid line and the pink dot in box represent the median and average number of citations, respectively.

for the interdisciplinary is t, and the observe time $t_i < t$ ($|t - t_i| <= 2$), $period_t = 0$, otherwise $period_t = 1$. The composite variable $treat_i \times period_t$ is a dummy variable, indicating whether the individual of the treated group is in the treated period, and the coefficient β_3 represents the treated effects for interdisciplinary behavior. It is worth noting that DID requires the treated and control group to be entirely in accord with the parallel trend assumption before the treatment, i.e., the influence of scientists should increase at the same rate, whatever in treated and control groups. In addition, even if the parallel trend assumption is satisfied, it is still necessary to control features that may affect scientists' influence, e.g., the career years of the scientist, the number of cooperation scientists, and the total number of publications. Thus, this work investigates the relationship between interdisciplinary behavior and scientists' influence by utilizing PSM-DID. PSM transforms multi-dimensional features into one-dimensional propensity scores through a functional relationship, and matches individuals in the treatment group with the control group according to the propensity score. Specifically, we select four observable features (covariates) for 2 years before and after scientists' interdisciplinary behavior: 1) the total number of publications; 2) the total number of disciplines of the scientist; 3) the career ages of the scientist; 4) the number of collaborators in each paper. Then, we calculate the propensity score of each scientist and conduct the match. The result of PSM provides supporting evidence for the parallel trend assumption. Finally, we consider citations and whether the scientist has interdisciplinary behavior as dependent and independent variables, respectively, and evaluate the treated effects of the treated group by utilizing DID.

Another goal of this work is to quantify the causal relationship between interdisciplinary distance and scientists' influence, i.e., the treated effect of continuous variables. However, the usual causal inference models allow only binary variables, i.e., the treated variable = 0 (1) in the control (treated). Thus, we consider utilizing the GPSM to evaluate the treated effect of interdisciplinary distance. GPSM is an extension of PSM and is widely used in many different fields, such as economics [64], education [65], and medicine [66]. Furthermore, compared with the PSM, GPSM inherits the core concept and has similar covariate balancing properties. The most significant advantage is that it breaks the PSM constraint that the treated variable only allows binary variables. We consider the relative citation growth rate in early and late careers as the quantification of scientists' influence (dependent variable). The independent variable is the interdisciplinary distance, and covariates are consistent in PSM.

3 Results

3.1 Citation dynamic of interdisciplinary paper

Papers play an essential role in academic society, it is interesting to investigate the influence caused by interdisciplinary behavior. To investigate this, our work considers 2 years as the observed time (t_i) and 3 years as the citation period to explore the citations of different types of interdisciplinary papers. Figure 2 compares the evolution of citations for papers with different interdisciplinary types. Compared with papers published in the large discipline (P_{l-l}), papers published in the large across small discipline (P_{l-s}) receive lower average citations (pink dot) in each interval. However, the papers in the small across large discipline (P_{s-l}) receive more average citations (pink dot) than that in the small discipline (P_{s-s}). On the one hand, it may be caused by the different citation dynamics in the inter-discipline and a single discipline, i.e., interdisciplinary papers need more than 3 years to reach peak citations. On the other hand, the large discipline cross to the small discipline receives less recognition and attention, and peers agree more with papers of the small cross to the large discipline.

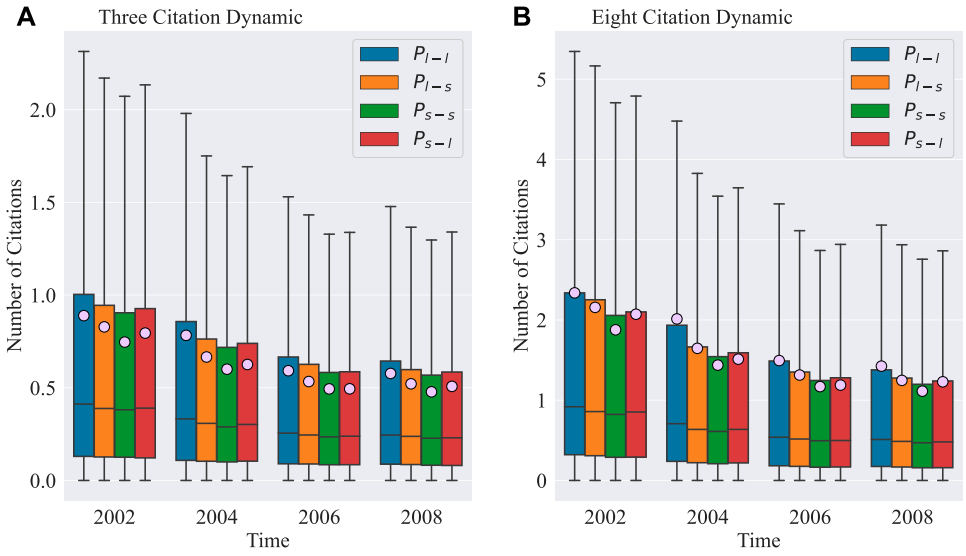

FIGURE 3
The evolution of citations of papers within different interdisciplinary types. We compare the number of citations with three **(A)** and eight **(B)** years citation period, and other elements are consistent with Figure 2.

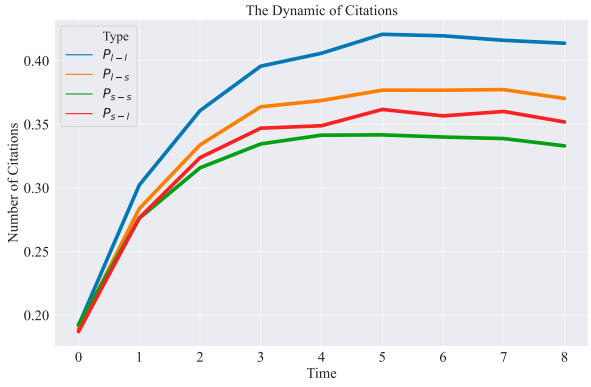

FIGURE 4
The dynamic of citations of papers for different interdisciplinary types. We select paper published before 2008, and calculate the average number of citations for different interdisciplinary types, i.e., the large discipline (blue line), the large across the small discipline (orange line), the small discipline (green line), and the small across large discipline (red line).

TABLE 1 The result of Z-test and K-S test.

	Z-test	K-S test
$P_(l-l)$ Vs. $P_(l-s)$	−0.96(0.34)	0.67(0.35)
$P_(s-l)$ Vs. $P_(s-s)$	0.43(0.66)	0.66(0.38)

In order to explore the underlying reasons for the different trends in the dynamic of papers with different types of interdisciplinary behaviors. We first investigate whether the interdisciplinary papers presented different citation dynamics from others by changing the citation period for papers. Figure 3 compares the citation period in three and 8 years in different disciplinary types. Papers published before 2008 are selected to avoid partial papers without 8 years citation period. When the citation period extends from 3 years (Figure 3A) to 8 years (Figure 3B), the citation of papers in the large cross the small discipline is less than that in the large disciplines, whatever three and eight citation period. Furthermore, citations of papers in the small cross the large discipline exhibit similar trends. This result indicates that the short- and long-term influence of interdisciplinary papers is similar to that of other papers, i.e., the increasing or decreasing of citations for interdisciplinary papers is irrelevant to the citation period. In particular, we further investigate the citation dynamics of papers in different disciplinary types published before 2008 in each year after publication. The average number of citation distribution is almost the same in different disciplines in Figure 4. We adopt the Z-test and Kolmogorov-Smirnov (K-S) test to examine distributions' differences. Our null hypothesis is that the distribution of average citations of interdisciplinary papers is different from that of single-discipline papers. The result in Table 1 shows that P - value $>$ 0.05, whatever P_{l-l} Vs. P_{l-s} and P_{s-l} Vs. P_{s-s}, which refuses the null hypothesis, and indicates that the citation dynamics of interdisciplinary and single discipline are the same distribution. It further indicates that interdisciplinary behavior will increase or decrease the citations, but the citation dynamics for interdisciplinary papers are similar to others.

One possible reason for the different trends in the citation of different types of interdisciplinary papers is the different recognition of scientific outputs. We analyze the citation sources for the different types of interdisciplinary papers within 8 years after publication in Figure 5. The disciplines with the most cited papers published by the large discipline (Figure 5A) and the small discipline (Figure 5C) are the large discipline (44%–46%) and small disciplines (41%–51%), respectively. It indicates that papers without interdisciplinary behavior have been widely recognized in self-discipline. Papers

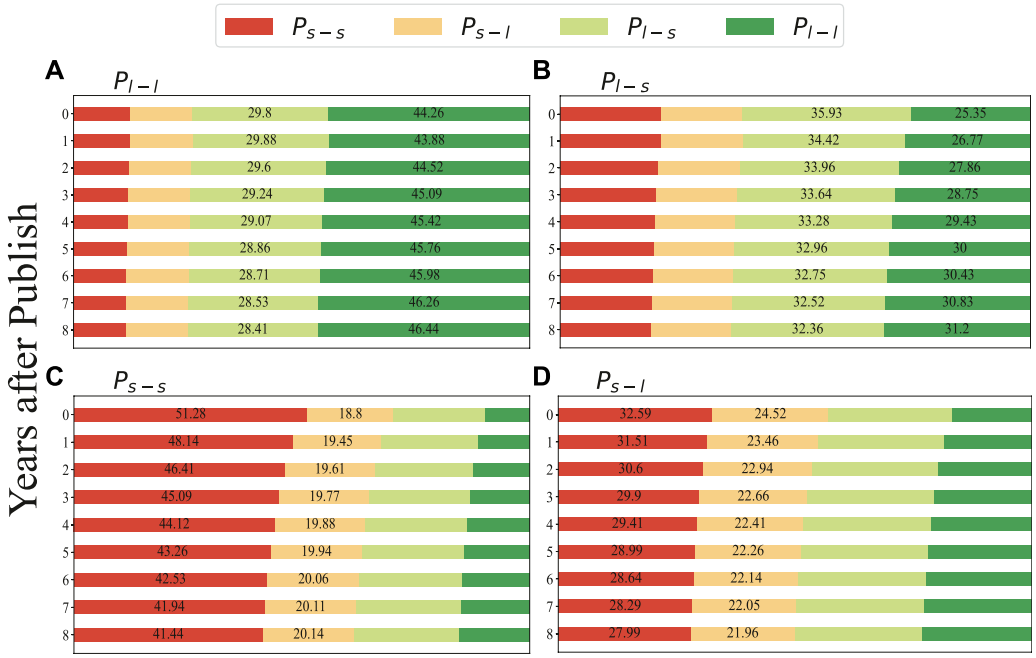

FIGURE 5
The citations attribution for different interdisciplinary types. We select the papers published after 2008, and the vertical axis represent the years after publish. The target disciplines are considered as the large discipline P_{l-l} (dark green column) across small discipline P_{l-s} (light green column), and the small P_{s-s} (red column) across large discipline P_{s-l} (pink column). **(A)** The large discipline (P_{l-l}). **(B)** The large across small discipline P_{l-s}. **(C)** The small discipline P_{s-s}. **(D)** The small across large discipline P_{s-l}.

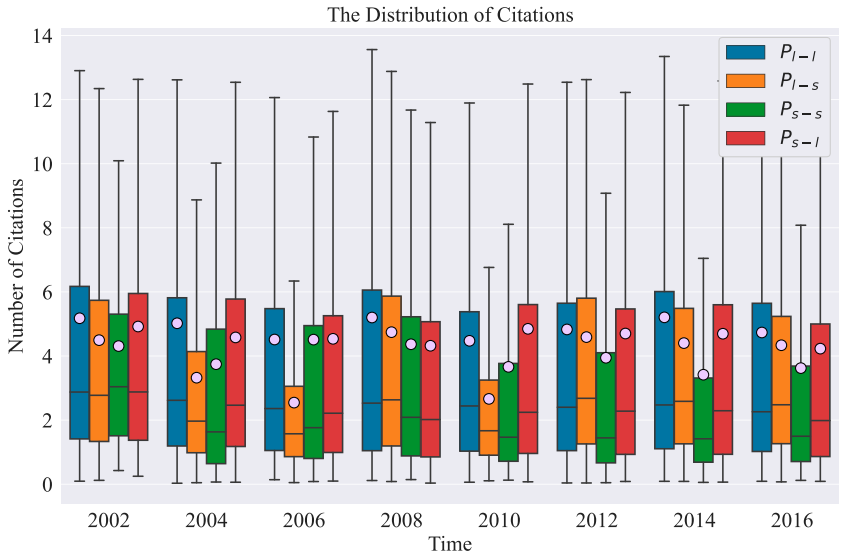

FIGURE 6
The evolution of citations for scientists within different interdisciplinary types. We classify scientists as the large discipline (blue box), the large across the small discipline (orange box), the small discipline (green box), and the small across large discipline (red box). The solid line and the pink dot in the box represent the median and the average number of citations for scientists, respectively.

published in P_{l-s} (Figure 5B) receive more citations in the same interdisciplinary type (32%–36%), while papers in P_{s-l} (Figure 5D) are cited most in the small discipline (28%–33%). Compered Figure 5C with Figure 5D, despite the proportion of citations in the small across large discipline having decreased in the small disciplines, the proportion is the highest in different disciplines, i.e., the initial disciplines (the small disciplines) tend to accept the scientific outputs in the small across large discipline.

TABLE 2 The result of DID.

Year	S_{l-s}			S_{s-l}		
	β_3	P-Value	Obs	β_3	P-Value	Obs
2002	−2.643	0.162	693	5.047***	0.007	1,471
2004	−2.583**	0.031	1858	7.117***	0.023	3,363
2006	−2.215***	0.002	3,723	5.793***	0.001	5,555
2008	−1.999***	0.000	5,871	6.067***	0.000	7,364
2010	−1.153*	0.076	8,248	5.696***	0.000	8,892
2012	−1.438**	0.024	10,350	6.144***	0.000	9,679
2014	−0.933	0.127	10,903	5.915***	0.000	8,870
2016	−1.412***	0.000	8,814	7.209***	0.004	6,307

3.2 The effect of different interdisciplinary types

We further explore the influence of interdisciplinary behavior on scientists. Specifically, according to the interdisciplinary types and attributing each paper to the first scientist, we can define an interdisciplinary type for the scientist, including the large discipline scientist (S_{l-l}), the large cross small discipline scientist (S_{l-s}), the small discipline scientists (S_{s-s}), and the small cross large discipline scientists (S_{s-l}).

Since the dynamic distribution of citations in interdisciplinary papers is similar to that in others (Figure 4), we consider citations received within 3 years after publication to measure the scientists' influence. Figure 6 compares the citations of scientists in different interdisciplinary types. In total periods, the influence of scientists in the large across small discipline (S_{l-s}) is lower than that of scientists in the large discipline (S_{l-l}) except in 2000. A different phenomenon is that scientists in the small across large discipline (S_{s-l}) receive more positive impacts from interdisciplinary behaviors. This finding indicates that the risk of interdisciplinary behavior of large disciplinary scientists is more significant than the rewards. In contrast, scientists in small disciplines can enhance their influence through interdisciplinary behavior, which benefits the sustainable development of their careers.

Table 2 demonstrates the result of DID in the different interdisciplinary types. As shown in Table 2, the interdisciplinary behavior of scientists in S_{l-s} significantly reduces their influence, especially in 2004, nearly reduced 2.6 citations. However, scientists in S_{s-l} increase their influence on interdisciplinary behavior, and the most significant increase occurred in 2016, with an increase of about 7.2 citations. In general, our results exhibit a causal perspective for developing scientists' careers, especially for scientists in the small discipline.

3.3 The effect of interdisciplinary distance

Interdisciplinary research is a tough career challenge for scientists, i.e., the trade-off between the new research field and influence [67]. Thus, the scientist may balance the risks and benefits of interdisciplinary behavior. To find out the "Sweet Spot" in the transition, this work further explores the relationship between interdisciplinary distance and scientists' influence. Specifically, We consider J as the interdisciplinary distance and use the growth of citations to evaluate the scientists' influence. The growth of citations is defined as $G_c = (C_{after} - C_{before})/C_{before}$, where C_{after} and C_{after} is the citations for scientists in early and later careers, respectively.

Figure 7 compares the relationship between inter-discipline distance J and the growth of citations. We find that both long and short inter-disciplinary distances limit scientists' benefits and that only appropriate interdisciplinary distances could enhance the influence of scientists. Furthermore, the interdisciplinary also may introduce negative influence, which displays a uniform distribution (inserted figure in Figure 7), which indicates that inter-disciplinary behavior may reduce the influence of scientists, whatever the interdisciplinary distance. This phenomenon suggests that scientists need to bear the risks through interdisciplinary behavior and turn an appropriate interdisciplinary distance if they want to increase their influence.

We further investigate the underlying relationship between interdisciplinary distance and scientists' influence by utilizing GPSM.

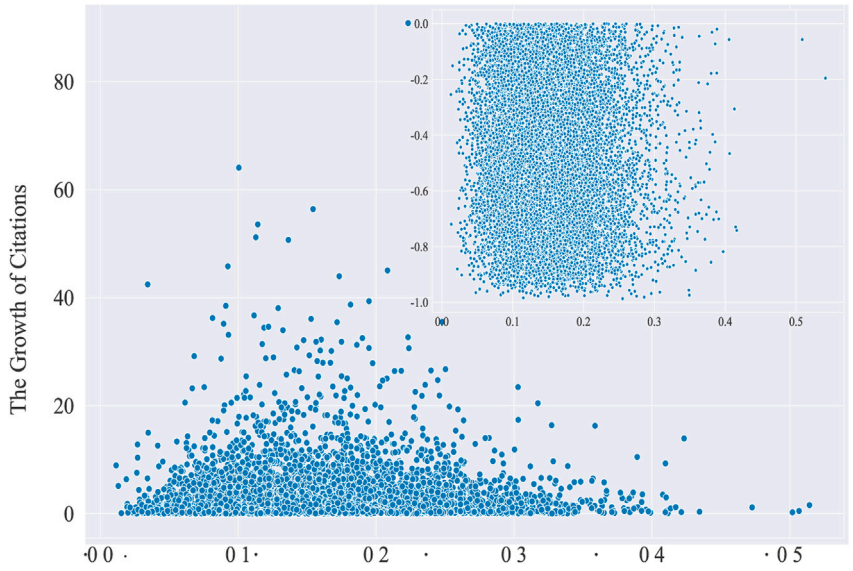

FIGURE 7
The distribution of citations' growth for the interdisciplinary scientists. The blue dot is G_c for each scientist. The insert picture shows the negative growth for citations.

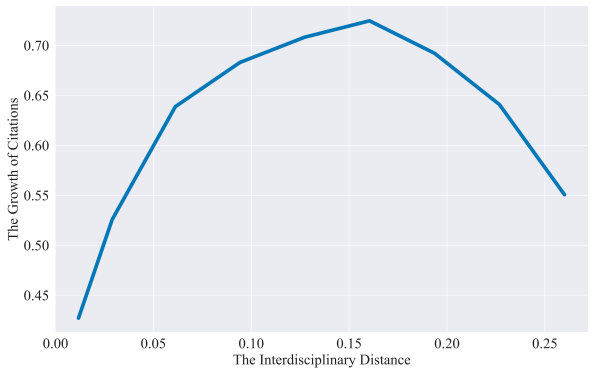

FIGURE 8
The evolution of treatment effect for GPSM. The blue line is the growth of citations G_c, which is the same as Figure 7. The horizontal and vertical axis represents the interdisciplinary distance and the growth of citations, respectively.

As shown in Figure 8, scientists' influence increases have a non-monotonic behavior: it increases for small inter-disciplinary distances and decreases (i.e., $J > 0.16$) for large inter-disciplinary distances (i.e., $J < 0.152$). The result implies that interdisciplinary behavior is an effective way to enhance scientists' influence. Furthermore, there exists a "Sweet spot" for the influence introduced by interdisciplinary behavior, that is, the interdisciplinary distance is 0.16.

4 Conclusion and discussion

This work studies the underlying relationship between interdisciplinary and influence. By introducing the concept of the large and small disciplines, we first investigate the relationship between interdisciplinary behavior and citations. The results show that different types of interdisciplinary behaviors will have different effects on the citations, i.e., the citations of papers from the large discipline across the small discipline will decrease, and the opposite trend in the small discipline. Then, we find that papers of the large discipline across the small discipline have been high-cited in the same interdisciplinary type papers, while peers in the small discipline will widely accept the paper of the small across the large discipline. The analysis of the relationship between interdisciplinary behavior and scientists' influence and the result of DID-PSM confirm this phenomenon. The previous study also confirmed that interdisciplinary research might have a high impact, but they may encounter challenges in collaboration and more obstacles in peer review [68]. Furthermore, the analysis of interdisciplinary distance and scientists' influence finds that interdisciplinary behavior will bring risks, and there exists a "Sweet spot" for the influence introduced by interdisciplinary behavior. It is important for scientists to choose the appropriate interdisciplinary distance while undertaking the risks. The short interdisciplinary distance may lead to a low impact caused by the lack of novelty, and excessive interdisciplinary distance may lead scientists to work in entirely unfamiliar disciplines and descend the scientific influence. Furthermore, this work only considers the first author, i.e., the credit of the paper attributes to the first author. With the increase of the number of co-authors of each publication, the scientific credit system is also facing the pressure of development [69–71]. Our future work will find a more reasonable credit allocation method to further reveal the potential influence of interdisciplinary behavior. In general, causality is the focus of research in the future academic network. Our research introduced causal inference into practice in the academic field. This work analyzes the correlation between interdisciplinary behavior and scientists' influence and reveals its potential impact mechanism by quantifying the causal relationship among them, which provides a new perspective for future related research in the academic field.

Data availability statement

Publicly available datasets were analyzed in this study. This data can be found here: https://www.aminer.cn/citation.

Author contributions

CF and HL wrote the main manuscript text. CF and SY conceived the experiments. CF, XL, and HL conducted the experiments. All authors analyzed the results and reviewed the manuscript.

Funding

This work was supported by the National Natural Science Foundation of China under Grant (62103374) and the Basic Public Welfare Research Project of Zhejiang Province under Grant (LGF20F020016).

Conflict of interest

The authors declare that the research was conducted in the absence of any commercial or financial relationships that could be construed as a potential conflict of interest.

Publisher's note

All claims expressed in this article are solely those of the authors and do not necessarily represent those of their affiliated organizations, or those of the publisher, the editors and the reviewers. Any product that may be evaluated in this article, or claim that may be made by its manufacturer, is not guaranteed or endorsed by the publisher.

References

1. Read EK, O'Rourke M, Hong GS, Hanson PC, Winslow LA, Crowley S, et al. Building the team for team science. *Ecosphere* (2016) 7:e01291. doi:10.1002/ecs2.1291

2. Stokols D, Misra S, Moser RP, Hall KL, Taylor BK. The ecology of team science: Understanding contextual influences on transdisciplinary collaboration. *Am J Prev Med* (2008) 35:S96–S115. S96–S115. doi:10.1016/j.amepre.2008.05.003

3. Barge JK, Shockley-Zalabak P. Engaged scholarship and the creation of useful organizational knowledge. *J Appl Commun Res* (2008) 36:251–65. doi:10.1080/00909880802172277

4. De Montjoye YA, Stopczynski A, Shmueli E, Pentland A, Lehmann S. The strength of the strongest ties in collaborative problem solving. *Scientific Rep* (2014) 4:5277–6. doi:10.1038/srep05277

5. Fiore SM. Interdisciplinarity as teamwork: How the science of teams can inform team science. *Small Group Res* (2008) 39:251–77. doi:10.1177/1046496408317797

6. Matthews NE, Cizauskas CA, Layton DS, Stamford L, Shapira P. Collaborating constructively for sustainable biotechnology. *Scientific Rep* (2019) 9:19033–15. doi:10.1038/s41598-019-54331-7

7. Gaff JG, Ratcliff JL. *Handbook of the undergraduate curriculum: A comprehensive guide to the purposes, structures, practices, and change*. Jossey-Bass Higher and Adult Education Series. ERIC (1997).

8. Chang YW, Huang MH. A study of the evolution of interdisciplinarity in library and information science: Using three bibliometric methods. *J Am Soc Inf Sci Technol* (2012) 63:22–33. doi:10.1002/asi.21649

9. Zhang L, Sun B, Chinchilla-Rodríguez Z, Chen L, Huang Y. Interdisciplinarity and collaboration: On the relationship between disciplinary diversity in departmental affiliations and reference lists. *Scientometrics* (2018) 117:271–91. doi:10.1007/s11192-018-2853-0

10. Repko AF, Szostak R. *Interdisciplinary research: Process and theory*. Sage Publications (2020).

11. Ding Y, Rousseau R, Wolfram D. *Measuring scholarly impact*. Springer (2016).

12. Wagner CS, Roessner JD, Bobb K, Klein JT, Boyack KW, Keyton J, et al. Approaches to understanding and measuring interdisciplinary scientific research (idr): A review of the literature. *J Informetrics* (2011) 5:14–26. doi:10.1016/j.joi.2010.06.004

13. Stirling A. A general framework for analysing diversity in science, technology and society. *J R Soc Interf* (2007) 4:707–19. doi:10.1098/rsif.2007.0213

14. Rafols I, Meyer M. Diversity and network coherence as indicators of interdisciplinarity: Case studies in bionanoscience. *Scientometrics* (2010) 82:263–87. doi:10.1007/s11192-009-0041-y

15. Hammarfelt B. Interdisciplinarity and the intellectual base of literature studies: Citation analysis of highly cited monographs. *Scientometrics* (2011) 86:705–25. doi:10.1007/s11192-010-0314-5

16. Porter A, Chubin D. An indicator of cross-disciplinary research. *Scientometrics* (1985) 8:161–76. doi:10.1007/bf02016934

17. Lyall C, Bruce A, Marsden W, Meagher L. The role of funding agencies in creating interdisciplinary knowledge. *Sci Public Pol* (2013) 40:62–71. doi:10.1093/scipol/scs121

18. Limoges C, Scott P, Schwartzman S, Nowotny H, Gibbons M. The new production of knowledge: The dynamics of science and research in contemporary societies. *The New Prod Knowledge* (1994) 1–192.

19. Stehr N, Weingart P. *Practising interdisciplinarity*. Toronto, ON: University of Toronto Press Inc (2000).

20. Frodeman R, Klein JT, Pacheco RCDS. *The Oxford handbook of interdisciplinarity*. Oxford: Oxford University Press (2017).

21. Porter AL, Roessner JD, Cohen AS, Perreault M. Interdisciplinary research: Meaning, metrics and nurture. *Res Eval* (2006) 15:187–96. doi:10.3152/147154406781775841

22. Woelert P, Millar V. The 'paradox of interdisciplinarity'in Australian research governance. *Higher Educ* (2013) 66:755–67. doi:10.1007/s10734-013-9634-8

23. Bromham L, Dinnage R, Hua X. Interdisciplinary research has consistently lower funding success. *Nature* (2016) 534:684–7. doi:10.1038/nature18315

24. Sun Y, Livan G, Ma A, Latora V. *Interdisciplinary researchers attain better performance in funding* (2021). *arXiv preprint arXiv:2104.13091*.

25. Wang J, Thijs B, Glänzel W. Interdisciplinarity and impact: Distinct effects of variety, balance, and disparity. *PloS one* (2015) 10:e0127298. doi:10.1371/journal.pone.0127298

26. Sunahara AS, Perc M, Ribeiro HV. Association between productivity and journal impact across disciplines and career age. *Phys Rev Res* (2021) 3:033158. doi:10.1103/physrevresearch.3.033158

27. Yegros-Yegros A, Rafols I, D'este P. Does interdisciplinary research lead to higher citation impact? The different effect of proximal and distal interdisciplinarity. *PloS one* (2015) 10:e0135095. doi:10.1371/journal.pone.0135095

28. Rinia E, van Leeuwen T, van Raan A. Impact measures of interdisciplinary research in physics. *Scientometrics* (2002) 53:241–8. doi:10.1023/a:1014856625623

29. Larivière V, Gingras Y. On the relationship between interdisciplinarity and scientific impact. *J Am Soc Inf Sci Technol* (2010) 61:126–31. doi:10.1002/asi.21226

30. Uzzi B, Mukherjee S, Stringer M, Jones B. Atypical combinations and scientific impact. *Science* (2013) 342:468–72. doi:10.1126/science.1240474

31. Levitt JM, Thelwall M. Is multidisciplinary research more highly cited? A macrolevel study. *J Am Soc Inf Sci Technol* (2008) 59:1973–84. doi:10.1002/asi.20914

32. Larivière V, Haustein S, Börner K. Long-distance interdisciplinarity leads to higher scientific impact. *Plos one* (2015) 10:e0122565. doi:10.1371/journal.pone.0122565

33. Molaei S, Babaei S, Salehi M, Jalili M. Information spread and topic diffusion in heterogeneous information networks. *Scientific Rep* (2018) 8:9549–14. doi:10.1038/s41598-018-27385-2

34. Fronczak A, Mrowinski MJ, Fronczak P. Scientific success from the perspective of the strength of weak ties. *Scientific Rep* (2022) 12:5074–10. doi:10.1038/s41598-022-09118-8

35. Amjad T, Rehmat Y, Daud A, Abbasi RA. Scientific impact of an author and role of self-citations. *Scientometrics* (2020) 122:915–32. doi:10.1007/s11192-019-03334-2

36. Wan L, Zhang M, Li X, Sun L, Wang X, Liu K. Identification of important nodes in multilayer heterogeneous networks incorporating multirelational information. *IEEE Trans Comput Soc Syst* (2022) 9:1715–24. doi:10.1109/tcss.2022.3161305

37. Liu X, Wu K, Liu B, Qian R. Hnerec: Scientific collaborator recommendation model based on heterogeneous network embedding. *Inf Process Manage* (2023) 60:103253. doi:10.1016/j.ipm.2022.103253

38. Li Y, Wang R, Nan G, Li D, Li M. A personalized paper recommendation method considering diverse user preferences. *Decis Support Syst* (2021) 146:113546. doi:10.1016/j.dss.2021.113546

39. Wang RW, Ye FY. Simplifying weighted heterogeneous networks by extracting h-structure via s-degree. *Scientific Rep* (2019) 9:18819–8. doi:10.1038/s41598-019-55399-x

40. Siudem G, Żogała-Siudem B, Cena A, Gagolewski M. Three dimensions of scientific impact. *Proc Natl Acad Sci* (2020) 117:13896–900. doi:10.1073/pnas.2001064117

41. Mercorio F, Mezzanzanica M, Moscato V, Picariello A, Sperlí G. Dico: A graph-db framework for community detection on big scholarly data. *IEEE Trans Emerging Top Comput* (2019) 9:1987–2003. doi:10.1109/tetc.2019.2952765

42. Shakibian H, Moghadam Charkari N. Mutual information model for link prediction in heterogeneous complex networks. *Scientific Rep* (2017) 7:44981–16. doi:10.1038/srep44981

43. Bütün E, Kaya M, Alhajj R. A supervised learning method for prediction citation count of scientists in citation networks" in 2017 IEEE/ACM International Conference on Advances in Social Networks Analysis and Mining (ASONAM). IEEE (2017). p. 952.

44. Mo X, Tang R, Liu H. A relation-aware heterogeneous graph convolutional network for relationship prediction. *Inf. Sci.* (2022) 623:311–23. doi:10.1016/j.ins.2022.12.059

45. Tang J, Zhang J, Yao L, Li J, Zhang L, Su Z. Arnetminer: Extraction and mining of academic social networks. In: *Proceedings of the 14th ACM SIGKDD international conference on Knowledge discovery and data mining* (2008). p. 990.

46. Wang K, Shen Z, Huang C, Wu CH, Dong Y, Kanakia A. Microsoft academic graph: When experts are not enough. *Quantitative Sci Stud* (2020) 1:396–413. doi:10.1162/qss_a_00021

47. Radicchi F, Fortunato S, Castellano C. Universality of citation distributions: Toward an objective measure of scientific impact. *Proc Natl Acad Sci* (2008) 105:17268–72. doi:10.1073/pnas.0806977105

48. Jia T, Wang D, Szymanski BK. Quantifying patterns of research-interest evolution. *Nat Hum Behav* (2017) 1:0078–7. doi:10.1038/s41562-017-0078

49. Darrat AF. Are financial deepening and economic growth causally related? Another look at the evidence. *Int Econ J* (1999) 13:19–35. doi:10.1080/10168739900000002

50. Weiner B. 5: An attributional approach for educational psychology. *Rev Res Educ* (1976) 4:179–209. doi:10.2307/1167116

51. Fu C, Xia Y, Yue X, Yu S, Min Y, Zhang Q, et al. A novel spatiotemporal behavior-enabled random walk strategy on online social platforms. *IEEE Trans Comput Soc Syst* (2021) 9:807–17. doi:10.1109/tcss.2021.3105381

52. Fu C, Zhao M, Fan L, Chen X, Chen J, Wu Z, et al. Link weight prediction using supervised learning methods and its application to yelp layered network. *IEEE Trans Knowledge Data Eng* (2018) 30:1507–18. doi:10.1109/tkde.2018.2801854

53. Fu C, Zheng Y, Liu Y, Xuan Q, Chen G. Nes-tl: Network embedding similarity-based transfer learning. *IEEE Trans Netw Sci Eng* (2019) 7:1607–18. doi:10.1109/tnse.2019.2942341

54. Schwab P, Miladinovic D, Karlen W. Granger-causal attentive mixtures of experts: Learning important features with neural networks. *Proc AAAI Conf Artif Intelligence* (2019) 33:4846–53. doi:10.1609/aaai.v33i01.33014846

55. Madumal P, Miller T, Sonenberg L, Vetere F. Explainable reinforcement learning through a causal lens. *Proc AAAI Conf Artif intelligence* (2020) 34:2493–500. doi:10.1609/aaai.v34i03.5631

56. Yao L, Chu Z, Li S, Li Y, Gao J, Zhang A. A survey on causal inference. *ACM Trans Knowledge Discov Data (Tkdd)* (2021) 15:1–46.

57. Abadie A. Semiparametric difference-in-differences estimators. *Rev Econ Stud* (2005) 72:1–19. doi:10.1111/0034-6527.00321

58. Granger CW. Investigating causal relations by econometric models and cross-spectral methods. *Econometrica: J Econometric Soc* (1969) 37:424–38. doi:10.2307/1912791

59. Rosenbaum PR, Rubin DB. The central role of the propensity score in observational studies for causal effects. *Biometrika* (1983) 70:41–55. doi:10.1093/biomet/70.1.41

60. Hirano K, Imbens GW. The propensity score with continuous treatments. *Appl Bayesian Model causal inference incomplete-data Perspect* (2004) 226164:73–84. doi:10.1002/0470090456.ch7

61. Angrist J, Imbens G. *Identification and estimation of local average treatment effects* (1995).

62. Thistlethwaite DL, Campbell DT. Regression-discontinuity analysis: An alternative to the ex post facto experiment. *J Educ Psychol* (1960) 51:309–17. doi:10.1037/h0044319

63. Hsiao C. *Analysis of panel data*. Cambridge University Press (2022).

64. Dai X, Cheng L. The effect of public subsidies on corporate r&d investment: An application of the generalized propensity score. *Technol Forecast Soc Change* (2015) 90:410–9. doi:10.1016/j.techfore.2014.04.014

65. Doyle WR. Effect of increased academic momentum on transfer rates: An application of the generalized propensity score. *Econ Educ Rev* (2011) 30:191–200. doi:10.1016/j.econedurev.2010.08.004

66. McCaffrey DF, Griffin BA, Almirall D, Slaughter ME, Ramchand R, Burgette LF. A tutorial on propensity score estimation for multiple treatments using generalized boosted models. *Stat Med* (2013) 32:3388–414. doi:10.1002/sim.5753

67. Funk RJ, Owen-Smith J. A dynamic network measure of technological change. *Manage Sci* (2017) 63:791–817. doi:10.1287/mnsc.2015.2366

68. Leahey E, Beckman CM, Stanko TL. Prominent but less productive: The impact of interdisciplinarity on scientists' research. *Administrative Sci Q* (2017) 62:105–39. doi:10.1177/0001839216665364

69. Hodge SE, Greenberg DA. Publication credit. *Science* (1981) 213:950–2. doi:10.1126/science.213.4511.950.c

70. Kennedy D. Multiple authors, multiple problems. *Science* (2003) 301(2003):733. doi:10.1126/science.301.5634.733

71. Allen L, Scott J, Brand A, Hlava M, Altman M. Publishing: Credit where credit is due. *Nature* (2014) 508:312–3. doi:10.1038/508312a

frontiers | Frontiers in Physics

TYPE Original Research
PUBLISHED 10 March 2023
DOI 10.3389/fphy.2023.1139475

OPEN ACCESS

EDITED BY
Ye Wu,
Beijing Normal University, China

REVIEWED BY
Fatao Wang,
Hebei University of Economics and Business, China
Lili Feng,
Hebei GEO University, China

*CORRESPONDENCE
Hongjing Ma,
251271437@qq.com

SPECIALTY SECTION
This article was submitted to Interdisciplinary Physics, a section of the journal Frontiers in Physics

RECEIVED 07 January 2023
ACCEPTED 28 February 2023
PUBLISHED 10 March 2023

CITATION
Li W, Chen J, Ma H and Feng X (2023), Research on emotional polarization mechanism of knowledge community from the perspective of social network structure —An empirical study on 'Zhihu' question and answer learning community.
Front. Phys. 11:1139475.
doi: 10.3389/fphy.2023.1139475

Research on emotional polarization mechanism of knowledge community from the perspective of social network structure —An empirical study on 'Zhihu' question and answer learning community

Wenzhu Li[1], Jiangfei Chen[2], Hongjing Ma[3]* and Xin Feng[4]

[1]School of Economics and Management, Beijing University of Posts and Telecommunications, Beijing, China, [2]School of Arts & Design, Yanshan University, Qinhuangdao, China, [3]Shijiazhuang Posts and Telecommunications Technical College, Shijiazhuang, China, [4]School of Management, Shijiazhuang Tiedao University, Shijiazhuang, China

Information overload and cocoon effect make the phenomenon of emotional polarization easily appear in online knowledge community. The mechanism of emotional polarization of users in knowledge community is analyzed, so as to reveal the formation rule of users' emotional polarization in knowledge community and summarize the intervention measures, provide a theoretical basis for further effective control of polarized emotions of knowledge community users. Starting from the theory of social network structure, based on the PAD emotional model, starting from the dimensions of Pleasure, Arousal and Dominance, focusing on the degree of user centrality, an index framework of emotional polarization is constructed around three behavioral patterns of information retrieval, information selection and information interaction. SOR model is used to dynamically explore the polarization mechanism under this framework. The results show that the heterogeneity of social network structure has an effect on participants' emotional perception and information behavior. The polarization of Pleasure has a positive effect on user centrality, and the polarization of Arousal and Dominance have a negative effect. User centrality positively affects their information selection and interaction behavior, but has no significant effect on retrieval behavior. The emotional polarization in the process of community knowledge sharing is decomposed from different perspectives, and the polarization mechanism is shared by combining social network structure and information behavior. From the perspective of application, this is conducive to promoting knowledge sharing, communication learning and information value chain remodeling, and also provides a kind of insightful analysis paradigm for this field.

KEYWORDS

knowledge community, social network structure, emotional polarization, mechanism, Zhihu

1 Introduction

With the popularization of online knowledge community, the relationship between different individuals within it has formed a specific social network. From the perspective of social network structure, there are differences in the opportunities and abilities of audiences to obtain information, and information stratification has emerged in the digital society [1], that is, different network structures in the community have different channels and contents to obtain information, and the ability to effectively use information has an impact on the status of the network society. Users have different status in the network society, and their importance and influence are also different, which will lead to corresponding changes in user behavior.

Emotional polarization refers to the extreme situation in which individual emotion deviates from the normal state, and it is an important influencing factor to induce individual extreme behavior. Multiple values and complex interest demands make users often contain emotional views when commenting on information, such as joy, sadness, anger, criticism, praise, etc. These views have a strong personal subjective color. In the network environment, "dematerialization" and "decentralization" coexist at the same time. On the one hand, online people do not have to be forced to submit to elite views, and on the other hand, online people have no real identity background restrictions [2], which makes extreme emotional consequences invisible. In the online knowledge community, the emotional state of users is closely related to the community network structure. The emotional polarization of users will affect the overall public opinion guidance of the community, and even cause the platform to fall into a bad atmosphere in serious cases.

Therefore, this paper takes online knowledge community 'Zhihu' as sample data to conduct research, explore the interaction of emotional polarization, network structure and information behavior, dynamically describe the polarization mechanism of users in the community, provide effective suggestions for better dissemination, use and sharing of content in online knowledge community, and promote the further extension and development of content value chain in online knowledge community. At the practical application level, it provides an insightful reference paradigm for expanding the depth and breadth of content services on the Internet platform, effectively controls and guides the emotions of Internet users, promote the sound development of the knowledge ecology of community platform, provide guarantee for the establishment of a more stable user emotional world and knowledge community platform, promote the feasibility construction of emotional polarization mechanism, and realize the sustainable progress and development of cyberspace.

2 Analysis of research status

This paper uses "social network structure", "emotional polarization", "user information behavior" as the subject words to conduct literature retrieval and sorting, summarize and analyze the current theoretical research, and quickly and comprehensively understand the research trends and results of scholars in related fields.

2.1 Research status of social network structure

Online community is a virtual organization form that uses digital technology to jointly create data, information and knowledge [3]. In this form of organization, knowledge collaboration takes place in an unprecedented scale and scope, helping those seeking answers to questions to obtain guidance. Participants improve their professional knowledge by learning from others, so that users can transform between content producers and content consumers.

Social network structure refers to the direct or indirect association mode between social members and the association mode existing in the individual set. It is a type of social network based on individual characteristics and group relations [4]. The essence of online community is the collection of community members and their organizational relationships [5], which divides the structure into three aspects: actors, relationships and connections. The social network structure in the online community can be expanded from the overall network measurement and network centrality analysis. The indicators of the overall network measurement include the density of individuals and community centers, the level of network density, clustering coefficient, etc., which are mainly used to measure the degree of tightness between nodes in the community network [6]. Simpson [7] found that there is direct dynamic feedback between social networks and organizational levels. The intimate relationship and reciprocal relationship between members of organizations promote the emergence of the whole network supporting social ties. The types and attributes of organizational levels in social networks, as well as the relative position of individuals in them, will affect and be affected by status differences; Li Zhuoyu [4] analyzed the social network structure based on the knowledge map theory, and the research results revealed the association relationship and path distance of each node in the online community; Deng Jun et al. [8] found the user size of the online knowledge community is positively related to the value users feel from within the community through the structural equation model. A perfect social network structure is conducive to users' obtaining a higher sense of self-worth; Gao Xiaoyu [9] took the international students as the node to form a new social network relationship through social media, and explored the relationship between the density and type of social network relationship of international students in the host country and cultural identity from the perspective of social network relationship; Wang Feifei et al. [53] believed that the enterprise decision-making under the leadership of the successor is affected by the social network embedded in it, which is reflected in the structural characteristics and relationship characteristics.

Based on previous studies, it can be found that there is a certain correlation between the social network structure of online knowledge community and user behavior, and the social network structure has become an important factor affecting the polarization mechanism of user behavior. At the same time, the social network

structure relationship has more far-reaching application value that is worth exploring.

2.2 Research status of emotional polarization

Scholars have various views on the definition of emotion: Shui et al. [10] believed that emotion is an important research topic in psychology, cognitive neuroscience and many other fields; Ye and Ho [11] believed that the actual change of the individual's environment is an effective reflection of emotion; Cui Xiaomiao and Wang Yi [12] believed that emotion is a state of emotional arousal with a fixed configuration in the human neuroanatomical system, including four basic emotions: anger, fear, sadness and happiness; Wu Weihua et al. [13] defined emotion as people's general feelings about real life in a specific era, full of shared values and social psychology; Guo Xiaoan et al. [14] believed that there are differences between emotion and sentiment, specifically, emotion emphasized the external performance of the subject's reaction to things, and sentiment emphasized the endogenous feelings of the subject. In this regard, this paper believes that emotion and sentiment have the same role in controlling behavior, so this paper makes no distinction between emotion and sentiment.

The emergence of social media and online communities has made people's communication more convenient. People communicate and express their views through the Internet, which has become an important channel for the public to vent their emotions due to its convenience and inclusiveness. However, due to the anonymity and fragmentation of network information, netizens' comments are more likely to be distorted or extreme. Users in the network tend to communicate with users with similar views rather than users with opposite positions, so information overload and cocoon room effect make these views extreme [15]. Xing et al. [16] found that social network users with the same opinion have gathered. These users identify with each other and form a group, refusing to accept other different views, which leads to the intensification of group emotional polarization. When the average value of emotions generated by public opinion is greater than the initial value, it indicates that the phenomenon of group emotional polarization has occurred [17]. Yang Guang [19] found that the intensification of emotional polarization is affected by the highly consistent online platform technology with people's selective contact, motivation reasoning, social identity and social identity mechanism. In addition, Sunstein [20] found that when individuals interact with each other within a group, their emotions and those of the group they belong to will be more extreme, and explained the causes of the irrational network phenomenon; Zhao Wanli et al. [21] believed that emotional polarization is closely related to group polarization, that is, group members have a certain bias at the beginning, after discussion, people continue to move in the direction of bias, and finally form extreme views, so that the groups involved in the discussion fall into an emotional polarization state. At the same time, emotional polarization is also shown in a more macroscopic way: Hobolt et al. [18] carried out an exploration of the western society of emotional polarization. They used surveys and experiments to measure the intensity of the emotional polarization of the parties and the Brexit countries, indicating that emotional polarization can come from identities other than party relations.

As a subjective factor, user emotion affects the direction and atmosphere of community public opinion, and the group emotional polarization has become the focus of scholars' research.

2.3 Research status of user information behavior

User information behavior includes information retrieval, information selection, information interaction, etc. Information retrieval refers to the process of retrieving effective information according to needs after information is organized, that is, the process of using search engines to find needed information [22]. Generally speaking, users' demand for information directly leads to their information retrieval behavior. Tan Chunhui et al. [23] built an influencing factor model of information retrieval behavior based on the motivation opportunity capability model, and found that when the motivation, opportunity and capability factors are met at the same time, online knowledge community users are more likely to conduct information retrieval behavior; Deng Shengli et al. [24] concluded that users' information needs indirectly affect information retrieval behavior by building an information retrieval influencing factor model; Chen Xiaoyu et al. [25] found that information requirements, information satisfaction and affinity will have an impact on information retrieval behavior through regression analysis.

From the perspective of information selection, ensuring the correct adoption of information is critical to successful information seeking, and the benchmark for adoption is whether information is based on needs and can help users make the best decisions [26]. Osatuyi et al. [27] pointed out that the reputation and information quality of contributors are important determinants of the choice of the best answer; Elwalda et al. [28] formed an information adoption model based on information quality and credibility, and proved that social support is the key prerequisite for information quality and credibility by using social support theory and information adoption model; Oliveira et al. [29] studied information adoption characterized by diversification and repeated influence stimuli, and confirmed that labels, forwarding, and influential publishers have significant positive effects on information adoption behavior; Han Zhengbiao et al. [30] revealed the mechanism of emotion in user information behavior model by analyzing literatures related to emotion.

From the perspective of information interaction, Xing Bianbian et al. [31] believed that information interaction includes the acceptance and distribution of information by individuals, which is a two-way information behavior; Tara [32] found that creating personal reputation, establishing or maintaining relationships, and pursuing important commitments in the community will affect users' observable information interaction behavior.

2.4 Overview of research status

It can be seen from the above domestic and foreign research status that most of the research on online knowledge community

users' emotions and emotional polarization focuses on the overall emotional polarization, that is, emotions are analyzed as a single variable. Few scholars separate emotions into different dimensions, and study the dynamic polarization mechanism of the emotional polarization of each dimension. The existing literature shows that there is a certain correlation between users' emotions and behavior patterns in the online knowledge community, and the network structure in the community will also affect users' behavior, but few articles combine the three for research. At the same time, in the research on behavior patterns, domestic and foreign scholars usually study each behavior pattern separately, and few scholars summarize and analyze the behavior pattern as a whole. Based on the above background, this paper explores the emotional polarization indicator framework under the interaction of different dimensions of emotional polarization, network structure and overall users' behavior mode, dynamically describes the polarization mechanism under this framework, and puts forward relevant suggestions for platform managers and community users.

3 Main concepts and theoretical foundations

This paper analyzes emotional polarization based on the PAD emotional model from Pleasure, Arousal, and Dominance dimensions, taking user centrality as the core and information retrieval, information selection, and information interaction as the three behavioral models to build an indicator framework to describe emotional polarization, so as to determine the background and theoretical basis of the operation mechanism of this paper.

3.1 PAD emotion model theory

Emotion models can be used to describe the types of emotions that arise in humans along the emotional dimension. Good emotion models tend to describe the vast majority of emotional states with a relatively small number of observations. Osgood [33] found that emotional experience can be measured in terms of Evaluation, Potency, and Activity. Mehrabian [34, 35] proposed the PAD emotional model based on this research base for generalization. The PAD three-dimensional emotion space can represent different categories of emotions continuously and smoothly, which in turn can represent the relationship between emotions [36]. It consists of three independent dimensions of Pleasure, Arousal and Dominance. According to the "+" or "-" values of the three descriptive dimensions, 8 kinds of 3D emotion models of 2*2*2 can be generated. In addition, the PAD model can be used in many ways and has the advantages of being fast and intuitive, fault-tolerant, and widely applicable. For example, Guo Yan [37] combined the PAD model to study its role in influencing users' information behavior; Jiang Ni et al. [38] used the PAD model to assess users' emotional experience during product use, which can be used to assess task usability, immersiveness, etc., Song Ying [39] constructed a text-oriented 3D emotion computing model for PAD in order to extract the service experience emotion information contained in UGC text. It can be seen that PAD model is more suitable for emotion measurement and can make qualitative judgment on user emotion. Therefore, PAD emotion model is chosen as the theoretical basis in this paper.

3.2 Social network structure

Social network structure can be considered as an organizational structure within a community. It combines micro factors such as individual behavior and individual relationships with the macro world such as social systems and organizational structures through the relationship of networks. Therefore, social network analysis method is widely used in the study of network structure. Social network analysis is a method established for studying the relationships between individuals, informal groups and formal groups. It is often used to reveal the characteristics of interactions between actors [40]. In social network analysis, an individual is regarded as a node in a social network. The connections between different individuals are regarded as the threads connecting the nodes in the social network. The intricate relationships between nodes and threads form the social network.

In this paper, we choose the model constructed by Li et al. [41], which divides the social network into two dimensions: relational dimension and structural dimension. Since this paper focuses on the network structure in online communities and explores where users are in the social network of online communities, this paper selects the structural dimension in social networks. User centrality in the structure dimension is chosen as a variable to measure the structure of the network because it is an indicator of the importance of the individual at the center of the network. According to Wang Lu [42], user centrality indicates the user's ability to engage with others in the network. This indicates that when a user has a high centrality, he or she is in the center of the entire social network and has more connections with the rest of the information nodes and user nodes, i.e., the user has a "star" effect in the online knowledge community. When the centrality of a user is low, the user is at the edge node of the community location, and the user has little or no connection with the rest of the information nodes and user nodes, so the user can be regarded as non-important and an "orphan" in the online knowledge community network structure.

3.3 User information behavior

User information behavior refers to the user's behavior related to the acquisition, retrieval, utilization, and proliferation of information. However, because there are many factors affecting information behavior, and the definition of information behavior from different perspectives is also different. Therefore, domestic and foreign scholars do not have a unified view on the concept of information behavior. Vanscoy et al. [43] considered information behavior as an important area of knowledge for consulting service providers because it provides structure for understanding user information seeking and use. Zhang Yaxin [44] defined information behavior as the activities of information acquisition, selection, and utilization carried out by users based on the needs of knowledge resources. Qu et al. [45] argued that user information behavior refers to the user's use of information technology services to efficiently obtain the information they want, as well as their

behaviors of selecting and optimizing information. In general, the specific behaviors of users in online knowledge communities include posting for questioning and sharing purposes, information retrieval and browsing, post selection, commenting and liking, and retweeting. In summary, combined with the characteristics of users' use of online knowledge communities, this paper argues that users' information behavior is based on users' need for certain information, spontaneous information search on the platform, and selection based on the validity of the retrieved information, and finally users will interact with other users for information activities. Therefore, information retrieval, information selection, and information interaction are selected as research indicators in this study.

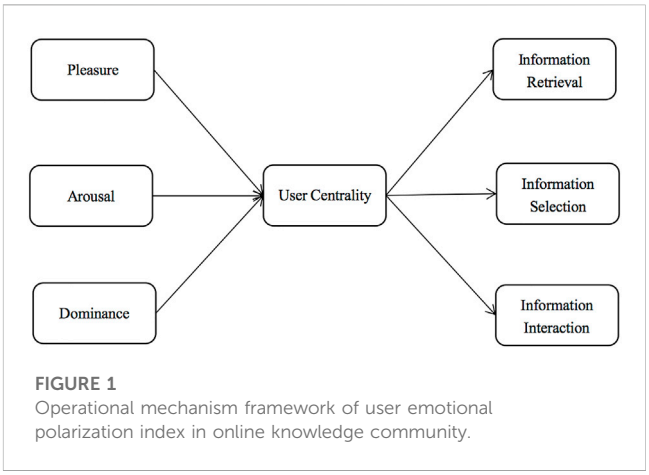

FIGURE 1
Operational mechanism framework of user emotional polarization index in online knowledge community.

4 Model construction and research hypothesis

4.1 Stimulus-organism-response model

Mehrabian [46] proposed the stimulus-organism-response model (SOR model), which is used to explain the effect of external stimuli on the organism, which will further stimulate individual behavior. Among them, the stimulus factor represents the external factors. From the macroscopic point of view, the external stimulus to the individual can be political, economic, cultural and other factors. From the microscopic point of view, it can be the individual's current psycho-emotional, physiological state, etc. The organism factor represents the state of the individual in the macro organization, i.e., the user's position in the macro network. The response factor represents the individual response, including the feedback given by the user psychologically and physiologically. Individuals are stimulated to change their current state, and the difference in state leads to a difference in individual behavior, which is the main generative principle of this model. Since it was proposed, the SOR model has been widely used in many fields such as sociology and management to study user behavior. Pan et al. [47] explored the impact of social support based on emotion-mediated mechanisms on user engagement behavior in online health communities based on the SOR model. Tian et al. [48] used the SOR model to investigate the impact of users' use of social e-commerce fashion products on their continuous purchase intention.

In this paper, the PAD emotional model theory, network structure, and theories related to user information behavior are incorporated into the SOR model. Among them, the PAD emotional model corresponds to the stimulus factors of the SOR model, and the polarization of pleasure, arousal and dominance in the emotional model all trigger individuals to be stimulated. The network structure corresponds to the organism factors of the SOR model, and the user centrality measures the user's position in the network structure, while the user network structure position is the external expression of the organism. User information behavior corresponds to the response factor of SOR model, and information retrieval, information selection, and information interaction in user information model as representative behaviors can reflect the response done by users. For users in online knowledge community, their degree of user centrality in the community is affected by their different degrees of pleasure, arousal and dominance. Individuals with different degrees of user centrality will also show different information behaviors in the community. The framework of the final emotional polarization indicator operating mechanism is shown in Figure 1.

4.2 Variable definition and measurement

4.2.1 Pleasure—Arousal—Dominance

Pleasure-P (Pleasure-displeasure) in the PAD three-dimensional emotional model represents the degree to which an individual's emotional state is positive or negative. Among the many external manifestations of emotional states, "extreme liking" is a state when the degree of pleasure is positively polarized; "extreme disliking" is a state when the degree of pleasure is negatively polarized, both of which can be regarded as having polarized pleasure. The state of "no feeling", which is neither liked nor disliked, can be regarded as zero pleasure, i.e., the degree of pleasure is not polarized.

Arousal-A (Arousal-nonarousal) in the PAD three-dimensional emotional model indicates the degree of physiological and psychological involvement of the individual. The higher the arousal of the individual, the higher the level of physiological arousal on the nerves and the greater the attentional nature, and *vice versa*. Among many external manifestations of emotional states, "active participation" is an emotional state in which arousal is positively polarized; "strong resistance" is an emotional state in which arousal is negatively polarized, both of which can be regarded as having polarized arousal. The state of "indifference", which is neither positive nor negative, is seen as zero arousal, i.e., arousal is not polarized.

Dominance-D (Dominance-submissiveness) in the PAD three-dimensional emotional model indicates the individual's state of control over situations and others, control and influence over others and the external environment. Among many external manifestations of emotional states, "extreme conceit" is an emotional manifestation with a positive degree of dominance, while "people follow the crowd" is an emotional manifestation with a negative degree of dominance. The emotional state that achieves equality of trust and control between oneself and the surroundings can be considered to have zero dominance.

TABLE 1 PAD three-dimensional emotional model measurement items.

Variable name	Number	Measurement indicators	References
Pleasure	PD1	I feel happy when using	[Mehrabian(1974) & Lunardo(2009)]
	PD2	I feel satisfied when using	
	PD3	My bad mood is improved when using	
Arousal	AN1	Sometimes I give it my full attention	
	AN2	Sometimes I feel excited and nervous	
	AN3	I will go over and over the content of a topic	
Dominance	DS1	I understand all the function points and how to use them	
	DS2	I do not change my opinion easily	
	DS3	My points are mostly correct	

TABLE 2 User centrality measurement items.

Variable name	Number	Measurement indicators	References
User centrality	CE1	I pay attention to a lot of topics in the community	[Hongseok(2008) & Tsai(1998)]
	CE2	I often receive replies to my posts	
	CE3	My answers are often viewed and liked	

Based on the research of Mehrabian [46] and Lunardo [49] on emotional states, this paper measured three dimensions by referring to the characteristics of online knowledge communities. As shown in Table 1.

4.2.2 User centrality

User centrality indicates the degree of importance of users in the online knowledge community network structure. When a user is in the central node of the community location, it means that the user has more connections with the rest of the information nodes, user nodes, etc., on the contrary, it means that the user has less connections or even no connections with the rest of the information nodes. Users with high centrality in online knowledge communities often show high extroversion, frequent interaction, high self-monitoring scores, and many direct and indirect relationships. Overall, individuals with higher prestige or social and leadership skills are the ones who have higher user centrality.

Based on the research of Hongseok [50] and Tsai [51] on user network structure centrality, this paper measured user centrality by referring to the characteristics of online knowledge communities. As shown in Table 2.

4.2.3 Information retrieval—Information selection—Information interaction

Information retrieval is the most basic behavior of users in online knowledge communities. Users enter the keywords of the topics they want to retrieve through the retrieval portal in the community to get the posts that meet their retrieval expectations. Information retrieval is one of the three user information behaviors that can best reflect current user topic concerns. Online knowledge communities usually provide users with hot lists below the search bar so that users can quickly search and understand recent hot topics.

Information selection is a kind of behavior that users filter and screen all the information they get when using online knowledge communities. Information selection behavior changes based on factors such as user's current needs or information matching, and selection behavior is the most persistent behavior among user information behavior. As long as users are still using online knowledge communities, information selection will continue to occur. Based on big data, the online knowledge community platform has added the "Guess Your Favorite" function, which will push different content to different users based on their past information selection behavior.

Information interaction is an act of user participation in topic interaction, which is reflected in adding specified people and topics to the following list, and liking, commenting and retweeting posts in the community. Online knowledge communities often use electronic text format to achieve information interaction. This form can maximize the preservation of document records, ensure the security and readability of information, and effectively avoid information distortion during the interaction process.

Based on the research of Shao [52] on user information behavior, this paper measured user information behavior by referring to the characteristics of online knowledge communities. As shown in Table 3.

4.3 Research hypotheses

4.3.1 Pleasure and user centrality

The polarization of pleasure is manifested as a strong liking or dislike for a topic or user. Polarized pleasure is usually

TABLE 3 Information behavior measurement items.

Variable name	Number	Measurement indicators	References
Information retrieval	SE1	I often check the content that I follow or recommend	[Shao(2009)]
	SE2	I always check the hot content	
	SE3	I often search for problems	
Information selection	CH1	I will select posts with high quality content and answers	
	CH2	I will choose the most current posts and answers	
	CH3	I will choose posts and answers that are relevant to my interests	
Information interaction	IN1	I will follow the people and topics that interest me	
	IN2	I often comment on topics	
	IN3	I often like and repost some topics	

accompanied by the publication of some extreme remarks. The participation process has too strong emotional color, and such too strong self-emotional expression will lead to alienation of other users. The importance of users in the community has decreased, that is to say, the polarization of pleasure is related to the centrality of the user's knowledge network, and this relationship is reverse. Based on such phenomena, this paper proposed the following assumption:

Hypothesis 1: The polarization of pleasure negatively affects user centrality.

4.3.2 Arousal and user centrality

The polarization of arousal is manifested as excessive attention or resistance to some topics and users. Such behavior will lead to overly one-sided information of users, who tend to wander away from the topic of concern at a low level of information acquisition, and thus cannot undertake the task of leading and coordinating other users and sharing information. Therefore, the polarization of arousal degree is related to the centrality of user's knowledge network, and this relationship is reverse. Based on such phenomena, this paper proposed the following assumption:

Hypothesis 2: The polarization of arousal negatively affects user centrality.

4.3.3 Dominance and user centrality

The polarization of dominance is manifested as extreme self-confidence or inferiority. The overconfident person will not accept the suggestions of others and are relatively strong, which makes most users resist and isolate the overconfident users. The extreme inferiority will reduce the social attributes and values of users in others' eyes, and will gradually be marginalized in the community. Therefore, the polarization of dominance has a relationship with the centrality of user's knowledge networks, and this relationship is reverse. Based on such phenomena, this paper proposed the following assumption:

Hypothesis 3: The polarization of dominance negatively affects user centrality.

4.3.4 User centrality and information retrieval

When the user centrality is high, the user is at the central node of the knowledge network structure. In order to consolidate their importance, users will obtain more information through information retrieval. Therefore, there is a positive relationship between user's knowledge network centrality and their retrieval behavior. Based on such phenomena, this paper proposed the following assumption:

Hypothesis 4: User centrality positively affects user information retrieval.

4.3.5 User centrality and information selection

With the improvement of user centrality, the importance of users has also been increasing, which has prompted users to strengthen their ability to filter and screen information obtained. At the same time, users with high centrality are more inclined to obtain high-quality information to consolidate their central position. Therefore, there is a positive correlation between user's knowledge network centrality and user's choice behavior. Based on such phenomena, this paper proposed the following assumption:

Hypothesis 5: User centrality positively affects user information selection.

4.3.6 User centrality and information interaction

When the user centrality is high, users will have more connections with other user nodes. Because the node has a large interpersonal network, it also generates more interactive behaviors. That is, there is a positive correlation between user's knowledge network centrality and user's interaction behavior. Based on such phenomena, this paper proposed the following assumption:

Hypothesis 6: User centrality positively affects user information interaction.

5 Research design and empirical analysis

Based on the SOR model with emotional polarization, network structure, and user information behavior as indicators, and under

TABLE 4 Sample characteristics of online knowledge community user behavior survey.

Project	Category	Number of samples	Proportion (%)
Gender	Male	208	52.26
	Female	190	47.74
Age	Under 18	13	3.27
	18–25	186	46.73
	26–35	114	28.64
	36–45	61	15.33
	Over 46	24	6.03
Educational background	High school and below	34	8.54
	Specialty	85	21.36
	Undergraduate	163	40.95
	Master or above	116	29.15
Occupation	Student	162	40.7
	College staff	16	4.02
	Personnel of government and public institutions	32	8.04
	Enterprise personnel	129	32.41
	Professional	47	11.81
	Other	12	3.02
Frequently browse the online knowledge community	Zhihu	287	72.11
	Baidu Knows	255	64.07
	Sogou asks	127	31.91
	360 Q&A	54	13.57
	Other	22	5.53
Registration usage time	Within half a year	43	10.8
	Half a year to one year	119	29.9
	One to three years	147	36.93
	Three to five years	68	17.09
	More than five years	21	5.28
Frequency of using online knowledge community	Used almost every day	133	33.42
	3–5 times a week	102	25.63
	1–3 times a week	94	23.62
	Less than once a week	69	17.34
Time of each use of online knowledge community	Within 30 min	226	56.78
	30 min to 1 h	104	26.13
	1 h to 2 h	42	10.55
	More than 2 h	26	6.53
Behavior interaction form of participating in online knowledge community	Browse Only	93	23.37
	Browse, collect and occasionally like	138	34.67

(Continued on following page)

TABLE 4 (*Continued*) Sample characteristics of online knowledge community user behavior survey.

Project	Category	Number of samples	Proportion (%)
	Search for questions and occasionally participate in answering	86	21.61
	Frequently ask questions and participate in answering questions	52	13.07
	Actively express experience and views, and actively interact	29	7.29

the guidance of the operating mechanism framework of user emotional polarization indicators of online knowledge community constructed above, the questionnaire designed includes seven variables, namely, pleasure, arousal, dominance, user centrality, retrieval behavior, selection behavior, and interaction behavior. The questionnaire design is divided into two parts: the influence of user's basic information and emotion on user behavior. In the second part, the Likert five-level scale is used to evaluate the emotional state, network structure, location and behavior of the users in the Q&A community. The respondents were required to score 1–5 levels according to their own experience. The corresponding levels are very disapproval, disapproval, meaningless, approval and very approval.

Taking into account the time cost, economic cost, convenience and other factors, the questionnaire was completed through the online questionnaire production platform "Questionstar". The distribution and recovery of questionnaires to online knowledge community users through the Internet mainly involve the following channels: Zhihu Community Post Bar, Baidu Knows Community, relevant users' QQ groups and WeChat groups. From 1 March 2022 to 15 April 2022, a total of 462 questionnaires were collected. Based on the comprehensive consideration of filling time, filling profile and filling IP, 398 valid questionnaires were obtained after strict screening, with an effective rate of 86.1%.

5.1 Descriptive statistics, reliability and validity analysis

This study uses R Studio 4.1.3 software to process the sample data obtained from the questionnaire survey, so as to obtain the basic information of the sample and the mean variance of the variables, and complete the reliability and validity analysis of the sample data.

5.1.1 Sample characteristics

Based on the statistics of the above survey results (Table 4), we can conclude that the survey objects have the following characteristics:

In terms of gender, men accounted for 52.26% of the total number, and women accounted for 47.74% of the total number; In terms of age, users aged from 18 to 25 account for the highest proportion. Such users are generally college students. They have more free time and no life pressure, so they will increase the investment in entertainment. Next are users aged from 26 to 35, accounting for about 1/3 of the total, and users aged from 36 to 45 account for 15% of the total. These two types of users are generally young and middle-aged groups who have already worked. Because of various factors such as personal curiosity and social needs, they will choose to use online knowledge communities to enrich their personal experience and solve work problems in addition to daily work. There are few users under the age of 18 and over the age of 46. Users under the age of 18 are minors. The use of the Internet will be controlled by family, society, software and other aspects. The personal ability of users over the age of 46 tends to be saturated, and the demand for using online knowledge communities decreases. This reflects the youth characteristics of the community; In terms of educational background, about 70% of the people have bachelor's degree or above, indicating that the groups using online knowledge communities are generally highly educated and users have good knowledge reserves; In terms of occupation, students accounted for the highest proportion, followed by enterprise employees. It can be seen from the age structure that the number of users under the age of 18 is small, but the overall proportion of users is high among middle school students, which indicates that most users of online knowledge communities are college students, masters and doctors. The number of employees in the social structure is large, so the proportion is also high.

Among the online knowledge communities that people frequently browse and use, Zhihu, as the first one, accounts for 72%, which can be mainly attributed to the popularity and authority of the community itself. Baidu Knows also uses more than half of them. The main source of traffic is the promotion function of Baidu Browser, which drives the development of Baidu Knows; In terms of registered use time, users from 1–3 years account for the most, and 90% of users have registered for more than half a year, indicating that the vast majority of users have a certain foundation for the use of online knowledge communities; In terms of the frequency of using online knowledge community, 1/3 of the users use it every day, followed by 3–5 times a week, which indicates that the online knowledge community is very sticky, and the number of times per person uses it every week can reach more than 3 days; In terms of the time spent each time using the online knowledge community, the number of people within 30 min is the largest, accounting for 56%; 30 min to 1 h accounts for 26%, 1 h to 2 h accounts for 11%, and more than 2 h accounts for 7%. It indicates that the average usage time is about half an hour, and the actual user activity is not high, which needs to be improved; In terms of interactive form, 34% of the people participated in browsing, collecting and liking, only 23% of the people browse, and 20% of the people frequently ask questions and actively express opinions.

Based on the above analysis, the main characteristics of the online knowledge community user sample are students aged

TABLE 5 Descriptive statistics of online knowledge community user behavior survey.

Dimension	Name	Mean value	Standard deviation
Variable	Pleasure	3.06	1.521
Item	PD1	3.17	1.567
	PD2	3.11	1.449
	PD3	2.9	1.541
Variable	Arousal	2.9	1.583
Item	AN1	3.17	1.535
	AN2	2.86	1.594
	AN3	2.65	1.585
Variable	Dominance	2.74	1.572
Item	DS1	2.77	1.582
	DS2	2.75	1.557
	DS3	2.69	1.585
Variable	User centrality	3.2	1.234
Item	CE1	3.39	1.127
	CE2	3.49	1.005
	CE3	2.72	1.398
Variable	Retrieval behavior	3.73	0.993
Item	SE1	3.71	1.013
	SE2	3.64	1.032
	SE3	3.84	0.925
Variable	Selection behavior	3.17	1.213
Item	CH1	3.15	1.167
	CH2	3.51	1.07
	CH3	2.85	1.307
Variable	Interaction behavior	3.04	1.233
Item	IN1	3.1	1.217
	IN2	3.09	1.218
	IN3	2.94	1.264

18–25 years old, and have a bachelor's degree or higher education background. The online knowledge community they use most often is Zhihu. The duration of use is concentrated in 1–3 years, and the duration of single use is concentrated in 30 min. The main form of user interaction still focus on basic browsing, collection and likes, but the process of uploading and sharing is lacking.

5.1.2 Descriptive statistics

The results of descriptive statistical analysis is based on the scale data are shown in Table 5. The dimensions are the variables and related item factors. The data range of is 1–5. The mean value of the item is the average user recognition of the item, and the standard deviation indicates the dispersion of user recognition.

It can be seen from Table 5 that the difference between the mean values of each item (PD, AN, DS, CE, SE, CH, IN) and the mean values of the corresponding variables (pleasure, arousal, dominance, user-centrality, retrieval behavior, selection behavior, and interaction behavior) remain within 0.5, indicating that the recognition of each observation variable is high. The standard deviation results of variables and items show that there are no abnormal items in the scale data. The volatility of data is large and the data is scattered. This is due to the data difference caused by the difference in the age, occupation, educational background and other foundations of users in the online knowledge community, which also shows that the online knowledge community is highly inclusive of users. To sum up, this survey data is suitable for testing the reliability and validity.

TABLE 6 Reliability and discrimination analysis data.

Variables	Item	General relevance	General relevance (After deletion of item)	Overall Cronbach's alpha value of the questionnaire
Pleasure	PD1	0.631	0.593	0.952
	PD2	0.650	0.616	
	PD3	0.702	0.670	
Arousal	AN1	0.757	0.732	
	AN2	0.783	0.760	
	AN3	0.820	0.798	
Dominance	DS1	0.727	0.698	
	DS2	0.606	0.568	
	DS3	0.732	0.701	
User centrality	CE1	0.780	0.752	
	CE2	0.770	0.744	
	CE3	0.745	0.705	
Retrieval behaviour	SE1	0.724	0.694	
	SE2	0.690	0.657	
	SE3	0.552	0.514	
Selection behaviour	CH1	0.842	0.820	
	CH2	0.754	0.723	
	CH3	0.774	0.739	
Interaction behaviour	IN1	0.796	0.766	
	IN2	0.826	0.801	
	IN3	0.856	0.833	

5.1.3 Reliability and discrimination analysis

Different items of the questionnaire in this study are different ways to describe the interaction of emotional polarization, information behavior and network structure, and to reveal the formation rule of emotional polarization of users in knowledge community. Therefore, there should be no significant differences between the different questions under the same variable. In order to test this indicator, reliability testing is often introduced in scientific research to confirm the reliability of the research data and the need for the study. Cronbach coefficient is the most commonly used reliability measurement method in academia, and when Cronbach's alpha > 0.8, the questionnaire was considered to have good reliability and research value. In this paper, the R language code was used to test the reliability of the questionnaire and the alpha coefficient was calculated as follows:

$$\alpha = (n/n-1)\left(1-\sum si^2/st^2\right)$$

The final overall Cronbach's Alpha value for the questionnaire was obtained as 0.952. In addition, a question-total correlation analysis, i.e., the differentiation of the items, is conducted on the questionnaire and the results are shown in Table 6. Generally speaking, if the correlation coefficient between a certain item and the total score is greater than 0.4, it means that the correlation between a certain item and the total score is high, and the differentiation of this question is good. Combined with the overall Alpha value of the questionnaire, this indicates that the overall reliability of the questionnaire is very high, the variables and items of the questionnaire are very reasonably designed, and the questionnaire is highly usable, stable and reliable.

5.1.4 Validity analysis

Validity analysis is used to reflect the corresponding relationship between structure and measurement value. Factor analysis is widely used in academia to measure the structural validity of the scale and questionnaire. The implementation logic of factor analysis is to extract some common factors from all variables and items. Each common factor is highly related to a certain group of specific variables, and these common factors represent the basic structure of the scale. Because the question-item scales used in this thesis are all well-established scales derived from the relevant literature and the reliability-tested data have high reliability, the validated factor analysis method was chosen to test the hypothesis model.

KMO and Buffett sphere tests should be conducted on the survey data before factor analysis. The closer the KMO value is

TABLE 7 KMO and buffett sphere test.

Observation index		Measured value
KMO test		0.92
Buffett sphere test	Approximate chi square	8,372.22
	Free degree	210
	Significance	0

TABLE 8 Factor convergent validity test results.

Route	AVE	CR
Factor 1 (Pleasure)	0.853	0.946
Factor 2 (Arousal)	0.770	0.909
Factor 3 (Dominance)	0.618	0.828
Factor 4 (User centrality)	0.646	0.842
Factor 5 (Retrieval behaviour)	0.634	0.834
Factor 6 (Selection behaviour)	0.684	0.864
Factor 7 (Interaction behaviour)	0.861	0.949

to 1, the stronger the partial correlation between factors, and the better the effect of factor analysis on data. The lower the significance of Buffett's sphere test results, the stronger the correlation between items. Academics generally believe that when the KMO value is greater than 0.7 and the significance *p*-value is less than 0.05, it is suitable for factor analysis. In this paper, using the R language code, the measured value of the scale KM test is 0.92, and the significance *p* is 0.000, as shown in Table 7, indicating that the scale data has passed the test and is suitable for factor analysis.

The mean extracted variance AVE and the combined reliability CR were calculated by RStudio software, where the mean extracted variance AVE was above 0.5 and the combined reliability CR was above 0.8, as shown in Table 8. The results indicate that the factor corresponds to a more representative topic setting and the convergent validity is ideal.

The analysis of the above data shows that the question options designed in the scale have a certain correlation, and the convergent validity is ideal; at the same time, different variables can be differentiated, and the discriminant validity is ideal; the scale meets the requirements of reasonable design and has a good structural effect; the overall validity of the questionnaire meets the requirements, and the measurement results are true and accurate.

5.2 Model empirical analysis

Based on the previous research samples and data analysis, the AMOS software was used to build a relevant model, and the path coefficients and significance coefficients of the variables were analysed according to the relationship between the variables in the model, so that the correctness of the model and the validity of the previous hypothesis could be verified. As shown in Figure 2:

5.2.1 Model fit

The fitting degree of the research model is obtained through R Studio software, as shown in Table 9.

According to the comparison between the coefficients in the table, model requirements and evaluation criteria, the model is ideal, and the fitting degree of sample data and hypothetical model is high.

5.2.2 Model path and research hypothesis analysis

When *p*-value of significance level< 0.05, this path can be considered as significant; When the S.E. value is > 0, it indicates that all variables under the assumption do not have the same linear relationship. When the variables are significantly correlated, the larger the path coefficient is, the closer the relationship between variables is. The specific values of this research model are shown in Table 10. According to the results, the degree of pleasure polarization has a positive impact on user centrality; dominance polarization adversely affects user centrality; user centrality has a positive impact on selection behavior and interaction behavior; Arousal polarization adversely affects user centrality; User centrality has no significant effect on retrieval behavior.

The path analysis and research assumptions of the model are as follows:

1) Pleasure and user centrality of online knowledge community

The relationship between the pleasure polarization of online knowledge community and user centrality is positive correlation, that is, the more extreme the pleasure in the emotional direction, the higher the user centrality. The model data results reject the original Hypothesis 1, and the results are contrary to the hypothesis. This is due to the anonymity and high openness of the online knowledge community. Users can hide their real identity and speak freely during the use process, so it is more likely to occur pleasure polarization. Extreme pleasure state is often accompanied by some extreme words, while other users will prefer these information that can intuitively judge the position rather than some absolutely neutral declarative statements in the process of information selection and use. In addition, users will also choose posts with more intense emotional expression to interact, thus increasing the centrality of the original post owner.

2) Arousal and user centrality of online knowledge community

The relationship between the arousal polarization of online knowledge community and user centrality is negative correlation, that is, the more extreme the arousal in the emotional direction, the lower the user's centrality. The model data results support the original Hypothesis 2. Users whose activeness is polarized tend to show excessive concern or resistance to some topics. Such users' knowledge is one-sided and tends to focus on specific topics. It is difficult to receive and disseminate various information at the intermediate nodes of the community, which leads to low centrality of such users.

3) Dominance and user centrality of online knowledge community

The relationship between dominance polarization and user centrality in online knowledge communities is negatively correlated, that is, the more extreme the dominance in the affective direction, the more the user centrality. The results of the model data support the original Hypothesis 3. Dominance indicates the degree of control over community topics and other users, and when dominance is too high, users tend to show arrogance, which is

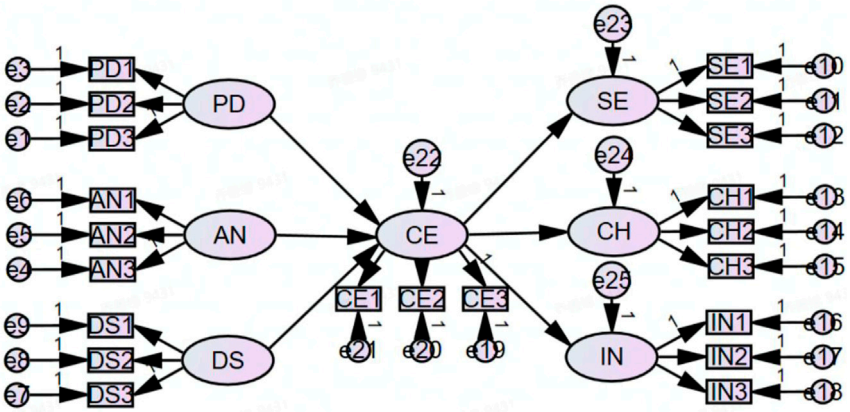

FIGURE 2
Structural equation model.

TABLE 9 Model fit.

Fitting index		χ2/df	RMSEA	CFI	NFI	TLI
Evaluation criterion	Ideal standard	< 3	< 0.05	> 0.9	> 0.9	> 0.9
	Acceptable standards	< 5	< 0.08	> 0.8	> 0.8	> 0.8
Actual value		2.216	0.069	0.928	0.861	0.911
Result		Ideal	Acceptable	Ideal	Acceptable	Ideal

TABLE 10 Model path inspection results.

Structural equation path	Normalized path coefficient	S.E.	*p*-value	Result
User centrality < – Pleasure	0.293	0.053	0.000	
User centrality < – arousal	−0.147	0.043	0.000	Remarkable
User centrality < – dominance	−0.415	0.049	0.000	
Retrieval behaviour < – user centrality	0.012	0.064	0.853	Remarkable
Selection behavior < – user centrality	0.232	0.05	0.000	
Interaction behavior < – user centrality	0.531	0.089	0.000	Remarkable

not conducive to maintaining interpersonal relationships; when dominance is too low, users tend to lack independent views, follow the crowd and are not valued, both of which lead to low centrality of the user in the community.

4) User centrality and information retrieval of online knowledge communities

The effect of online knowledge community user centrality on information retrieval is not significant, with little difference in retrieval behaviour when using the community between either star users with higher centrality or marginal users with lower centrality. The model data results reject the original Hypothesis 4. This is because information selection and interaction in online knowledge communities are based on retrieval behaviour, so information retrieval is the most basic information interaction. Users retrieve and browse information according to their own needs and hot tweets, and the results returned by retrieval do not differ according to user centrality, so user centrality does not affect the occurrence of information retrieval.

5) User centrality and information selection of online knowledge communities

User centrality and information selection in online knowledge communities are positively correlated, that is, the higher the centrality of users, the stronger the information selection. The model results support the original Hypothesis 5. Users with higher user centrality are in an important position in the network structure and play an important role in the reception and dissemination of information, and users with higher centrality tend to prefer topics and users with high quality, timeliness or relevance to their interests, so as to obtain higher

quality and relevant information and maintain their central position in the community network structure.

6) User centrality and information interaction of online knowledge communities

User centrality and information interaction in online knowledge communities are positively correlated, that is, the higher the centrality of users, the stronger the information interaction. The model data results support the original Hypothesis 6. When users are at the central node of the online knowledge community structure, they will frequently interact with other nodes, including but not limited to answering other users' questions, reposting posts, following and being followed, etc.

6 Research conclusion and emotional polarization intervention measures

6.1 Research conclusion

This paper takes existing research on online knowledge communities' emotions, network structure and users' information behaviour as the theoretical basis, combines the SOR model to establish the operational mechanism framework of online knowledge communities' users' emotional polarization index, collects data by means of questionnaires, and uses RStudio and AMOS 26.0 to complete the empirical analysis of the questionnaire data, and draws the following conclusions and recommendations.

(1) The polarization of users' pleasure has a positive impact on their centrality in the network structure, and when users have their own positions and attitudes in terms of emotions rather than absolute indifference and neutrality, it can strengthen their centrality in the community.
(2) The polarization of users' arousal and dominance has an inverse effect on their centrality in the network structure, and the polarization of users' dominance has a greater effect on centrality than the polarization of arousal. An excessive focus on one part of the problem or a strong ego or inferiority complex can reduce the importance of the user in the community as a whole and lead to the user being marginalized.
(3) The effect of user centrality on information retrieval is not significant. In online knowledge communities, information retrieval is the most basic interaction behaviour, and the same retrieval behaviour is generated regardless of the user's position in the network structure of the online community.
(4) The effect of user centrality on information selection and information interaction is positive, and the effect of user centrality on information interaction is greater than the effect on information selection. When users are at the centre of the online knowledge community network structure, they will enhance their selectivity of information and will also interact more with other nodes and information.

6.2 Emotional polarization intervention measures

According to the results of empirical analysis, the author puts forward suggestions on intervention measures of emotional polarization for users and platform managers in online knowledge communities:

Online knowledge communities are platforms where various users interact freely in the community under the supervision and control of the platform. Based on the above research findings, platform administrators should actively promote the community to connect to relevant software, archive all user information behavior and statistics, push information in the information pool differently for different users, control user speech through system control and correctly guide the community atmosphere; at the same time, introduce function points applicable to the community according to the basic elements of the community such as user network structure to meet the needs of different users. Platform administrator should use big data algorithms to manage and operate corresponding knowledge posts according to different network sizes. They can promote knowledge dissemination by setting the top, strengthening knowledge sharing rewards, and reducing the level required for comments [54]. In addition, the interaction mode of online knowledge communities is basically the same, which can be summarised as users posting questions in the community, answering and forwarding, etc. The singularity of the interaction mode limits the development of online knowledge communities, so new function points can be added or existing functions can be optimised to increase the playability and ease of use of the community. For example, the online knowledge community can be divided into a centralised mode and a distributed mode, and users can switch between the two modes freely. The diffusion mode favours the breadth of topics, mainly focusing on current social hotspots; the centralised mode favours the depth of the user's area of interest, which may involve some proper nouns or some industry terminology, thus satisfying the user's interests and personalised resources. In this way, the reliance and loyalty of users are enhanced and the economic value of the online knowledge community as a whole is increased.

For users of online knowledge communities, as arousal and dominance can have a significant impact on user centrality, it is necessary to strengthen the acquisition of all aspects of information in online knowledge community, do not pay too much attention to some topics and refuse to accept knowledge in other directions, and maintain a stable attitude. Online knowledge community is a highly inclusive community that everyone can participate in. We should accept all users and information in the community equally. In healthy communities with low level of community rewards and innovation knowledge, it is particularly important to improve emotional support. For example, maintain a civilized and friendly network order and guide users to respect the knowledge achievements of others; establish and improve the content review and user reporting mechanism to automatically delete or independently screen uncivilized content [55]. Reasonable control of their own emotional expression, under the premise of appropriate enhancement of emotional expression, friendly interaction with other users. In addition, the difference in centrality does not affect the user's information retrieval behaviour, so users should accurately control their own needs in the process of use, and improve their ability to express themselves when retrieving information, their ability to filter information and their own cultural literacy, so as to stop spreading bad information, thus enhancing the individual's fame and prestige in the online knowledge community, and attracting capital and traffic while enriching themselves.

6.3 Limitations of the study

The model was designed by integrating the existing research base, although some of the findings were achieved, there is still much room for improvement in the article as a whole. For example, the model uses the PAD 3D model of emotion, which is based on static emotions at specific points in time when users participate in filling out the questionnaire, but users' emotional states may change dynamically at different points in time when using online knowledge communities, so using static nodes to categorize them uniformly is obviously not comprehensive and accurate. In addition, there are many factors that influence the organizational structure of users other than centrality, and only the most obvious and easily statistically measurable centrality has been chosen as the indicator for consideration in this paper. In terms of theory, we can also start with the classical group polarization theory, summarize the connotation, dynamic mechanism and key influencing factors of the emotional polarization in the perspective of social network structure, and propose corresponding intervention measures of emotional polarization according to its generative mechanism and dynamic mechanism. In summary, this study will continue to improve and enhance the data optimization, model construction and theory in the future.

Data availability statement

The raw data supporting the conclusion of this article will be made available by the authors, without undue reservation.

Author contributions

XF and HM designed the study, WL collected the data, and JC performed calculations. WL and JC analyzed and interpreted the data and wrote the manuscript.

Acknowledgments

The authors acknowledge the financial support from the National Natural Science Foundation of China (No. 11905042), Natural Science Foundation of Hebei Province (No. G2021203011), Project of Social Science Development of Hebei Province (No. 20210501003).

Conflict of interest

The authors declare that the research was conducted in the absence of any commercial or financial relationships that could be construed as a potential conflict of interest.

Publisher's note

All claims expressed in this article are solely those of the authors and do not necessarily represent those of their affiliated organizations, or those of the publisher, the editors and the reviewers. Any product that may be evaluated in this article, or claim that may be made by its manufacturer, is not guaranteed or endorsed by the publisher.

References

1. Shen Y. Research on the emotional polarization of online public opinion in the "Cotton Age" from the perspective of Information Stratification. *Future Develop* (2022) 46(2):50–3.

2. Gao JF, Huang W. Estimation of emotional polarization of opinion clusters in network public opinion field. *Libr Inf Serv* (2019) 63(10):106–14.

3. Godinho MA, Borda A, Kariotis T, Molnar A, Kostkova P, Liaw ST. Knowledge co-creation in participatory policy and practice: Building community through data-driven direct democracy. *Big Data Soc* (2021) 8(1):205395172110194. doi:10.1177/20539517211019430

4. Li ZY. Social network structure of knowledge transmission: A case study of MOOC. *Inf Sci* (2022) 40(05):180–93.

5. Zhao D, Zhang Q, Ma F. Communication that changes lives: An exploratory research on a Chinese online hypertension community. *Libr Hi Tech* (2020) 38(4): 883–96. doi:10.1108/lht-08-2019-0172

6. Chen HL, Wei RB, Men XP. The Correlation analysis of Social network analysis methods and Research Topics. *Inf Sci* (2022) 40(09):38–46.

7. Simpson CR. Social support and network formation in a small-scale horticulturalist population. *Scientific Data* (2022) 9:570. doi:10.1038/s41597-022-01516-x

8. Deng J, Wei Y, Li J, Zhang ZS, Wang R. Intend to research the continuous use of online knowledge community of users, zhihu, for example. *J intelligence Sci* (2021) 33(05):138–55.

9. Gao XY. Connecting to other countries: The social network structure of students studying in China and the cultural identity of the host country. *J Xi'an Int Stud Univ* (2022) 30(02):119–23.

10. Shui X, Zhang M, Li Z. A dataset of daily ambulatory psychological and physiological recording for emotion research. *Scientifici Data* (2021) 8:161. doi:10.1038/s41597-021-00945-4

11. Ye S, Ho KKW. College students' twitter usage and psychological well-being from the perspective of generalised trust: Comparing changes before and during the COVID-19 pandemic. *Libr Hi Tech* (2022). ahead-of-print. doi:10.1108/LHT-06-2021-0178

12. Cui XM, Wang Y. *Red files show the emotional dimensions of communication*. Shanxi: Shanxi Files (2022).

13. Wu WH, Miao KP. Self-expression, collective memory and emotional linkage: A collage of short videos. *China Journalism Commun Res* (2021) 2021(03):187–99.

14. Guo XA, Li H. Emotional labor and emotional labor: Misuse, discrimination and its interpretation of the concept of. *Press* (2021) 2021:56–68. doi:10.15897/j.carolcarrollnki/g2.20211015.002cn51-1046

15. Jiang S, Wang H. Group polarization based on agent emotional characteristics and credibility. *Complexity* (2021). doi:10.1155/2021/9983541

16. Xing Y, Wang X, Qiu C, Li Y, He W. Research on opinion polarization by big data analytics capabilities in online social networks. *Technol Soc* (2022) 68:101902. doi:10.1016/j.techsoc.2022.101902

17. Carvalho VDH, Costa APCS. Towards corpora creation from social web in Brazilian Portuguese to support public security analyses and decisions. *Libr Hi Tech* (2022). ahead-of-print. doi:10.1108/LHT-08-2022-0401

18. Hobolt SB, Thomas J, Tilley J. Divided by the vote: Affective polarization in the wake of the Brexit referendum. *Br J Polit Sci* (2021) 51:1476–93. doi:10.1017/s0007123420000125

19. Yang G. Do intelligent media exacerbate the polarization of public opinion? - based on media technology, information characteristics and individual psychological analysis. *J youth press* (2022) 18:15–9. doi:10.15997/j.carolcarrollnkiQNJZ.2022.18.011

20. Sunstein CR. The law of group polarization. *J Polit Philos* (2002) 10(2):175–95. doi:10.1111/1467-9760.00148

21. Zhao WL, Xie R. Digital inequality and social stratification: The effect of information communication technology on social inequality. *Sci Soc* (2020) 10(01): 32–45.

22. Wu J, Hong R, Tian Q. Special issue on cross-modal retrieval and analysis. *Int J Multimedia Inf Retrieval* (2022) 11:523. doi:10.1007/s13735-022-00265-2

23. Tan CH, Ren JH. Research on the combination of factors influencing users' information searching behavior in virtual academic community: A qualitative comparative analysis method based on Fuzzy Sets. *Mod Inf* (2022) 42(04):39–51.

24. Deng SL, Chen XY, Fu SX. Research on the influence of users' information demand on information search in social question-and-answer community -- based on the mediating role of question-and-answer community involvement. *Inf Sci* (2017) 35(07):3–15.

25. Chen XY, Fu SX, Deng SL. Research on the influencing factors of social question and answer users' information search: A mixed approach perspective. *Libr Inf Serv* (2018) 62(20):102–11.

26. Sarthak C, Sabuj KC. Unfolding social learning parameters behind the selection of information sources against cyclones: A perspective of information seeking behavior research. *Libr Inf Sci Res* (2022) 44(4):101194. doi:10.1016/j.lisr.2022.101194

27. Osatuyi B, Passerini K, Turel O. Diminishing returns of information quality: Untangling the determinants of best answer selection. *Comput Hum Behav* (2022) 126:107009. doi:10.1016/j.chb.2021.107009

28. Elwalda A, Erkan İ, Rahman M, Zeren D. Understanding mobile users' information adoption behaviour: An extension of the information adoption model. *J Enterprise Inf Manage* (2022) 35(6):1789–811. doi:10.1108/jeim-04-2020-0129

29. Oliveira JF, Marques-Neto HT, Karsai M. Measuring the effects of repeated and diversified influence mechanism for information adoption on Twitter. *Soc Netw Anal Min* (2022) 12:16. doi:10.1007/s13278-021-00844-x

30. Han ZB, Zhai RR. Research on the mechanism of emotion in user information behavior model. *Inf Theor Pract* (2022) 45(12):103–10.

31. Xing DB, Zhang WN. Research on the emotional experience of archival we-media users based on information interaction behavior. *Arch Construction* (2019) 2019:35.

32. Zimmerman T. Social noise: The influence of observers on social media information behavior. *J Documentation* (2022) 78:1228–48. doi:10.1108/jd-08-2021-0165

33. Osgood CE. Dimensionality of the Semantic space for communication via Facial expressions. *Scand J Psychol* (1966) 7(1):1–30. doi:10.1111/j.1467-9450.1966.tb01334.x

34. Mehrabian A. Pleasure-arousal-dominance: A general framework for describing and measuring individual differences in temperament. *Curr Psychol* (1996) 14(4):261–92. doi:10.1007/bf02686918

35. Mehrabian A, LjunggrEn E. Emotional correlates of preferences for situation-activity combinations in everyday life. *Genet Soc Gen Psychol Monogr* (1997) 123(4):461–77.

36. Sun Y, Ma HJ, Zhang XY. PAD under the dimension of depth emotion associated modeling study. *J Electron Des Eng* (2022) 30(07):47–52. doi:10.14022/j.issn1674-6236.2022.07.010

37. Guo Y. *A study on the information behavior of users in social question-and-answer community based on PAD emotion model*. Mianyang, China: Southwest university of science and technology (2020).

38. Jiang N, Li RN, Liu CY, Fang H. PAD emotion model application in the user's emotional experience evaluation. *J packaging Eng* (2021) 22:413–20.

39. Song Y. *Research on multidimensional emotion computing model for user experience quality*. Shanghai, China: Donghua University (2022).

40. Zhang SH, Wu YT, Yu HS. Urban innovation correlation network in Shandong Province based on improved gravity model and social network analysis. *J Ludong Univ* (2022) 38(04):342–9.

41. Li YQ, Huang Y. Relationship between individual characteristics and social network: Its localization development. *Adv Psychol Sci* (2014) 22(11):1801–13. doi:10.3724/sp.j.1042.2014.01801

42. Wang L. Social network analysis of virtual learning community. *China E-Education* (2009) 2:5–11.

43. VanScoy A, Julien H, Harding A. Integration of information behavior into reference and information services education: A syllabus study. *J Educ Libr Inf Sci* (2022) 2022:20220.

44. Zhang YX. *Research on personal information network infringement*. Shenyang, China: Shenyang University of Technology (2016).

45. Qu NW, Xia ZJ, Wang YM. Based on users' information behavior of social media rumours effect research. *J intelligence Sci* (2021) 33(01):111–9. doi:10.13833/j.iSSN.1007-7634.2021.01.015

46. Mehrabian A, Russell JA. *An approach to environmental psychology*. Cambridge: MIT (1974).

47. Pan TT, Lv YJ. Study on the influence factors of user participation behavior in online health community based on SOR model. *Inf Serv* (2002) 43(02):76–83.

48. Hewei T, Youngsook L. Factors affecting continuous purchase intention of fashion products on social E-commerce: SOR model and the mediating effect. *Entertainment Comput* (2022) 41:100474. doi:10.1016/j.entcom.2021.100474

49. Lunardo R, Mbengue A. Perceived control and shopping behavior: The moderating role of the level of utilitarian motivational orientation. *J Retailing Consumer Serv* (2009) 16(6):434–41. doi:10.1016/j.jretconser.2009.06.004

50. Oh H, Kilduff M. The ripple effect of personality on social structure: Self-monitoring origins of network brokerage. *J Appl Psychol* (2008) 93(5):1155–64. doi:10.1037/0021-9010.93.5.1155

51. Tsai W, Ghohal S. Social capital and value creation: The role of intrafirm networks. *Acad Manage J* (1998) 41(4):464–76. doi:10.5465/257085

52. Shao G. Understanding the appeal of user-generated media: A uses and gratification perspective. *Internet Res* (2009) 19(1):7–25. doi:10.1108/10662240910927795

53. Wang FF, Wu J, Lu YZ, Zhu Y. Research on the impact of the characteristics of social network embedded by successors on inefficient investment -- an empirical analysis based on structural and relational embeddedness. *Investment Res* (2022) 41(11):4–24.

54. Chu JW, Li JX. Research on the evolution of user's knowledge sharing strategy in virtual knowledge community -- based on scale-free network theory. *Inf Sci* (2022) 2022:1–9.

55. Huang ZX, Xiong HX. Evolutionary game research on knowledge sharing and hidden behavior of online health community users. *Data Anal Knowledge Discov* (2022) 2022:1–21.

frontiers | Frontiers in Physics

TYPE Original Research
PUBLISHED 18 April 2023
DOI 10.3389/fphy.2023.1107178

OPEN ACCESS

EDITED BY
Ye Wu,
Beijing Normal University, China

REVIEWED BY
Zhongyuan Ruan,
Zhejiang University of Technology, China
Peng Ji,
Fudan University, China

*CORRESPONDENCE
Lin Zhang,
zhanglin2011@bupt.edu.cn

RECEIVED 24 November 2022
ACCEPTED 30 March 2023
PUBLISHED 18 April 2023

CITATION
Zhang J, Fang K, Zhu Y, Kang X and Zhang L (2023), Time tracing the earliest case of local pandemic resurgence. *Front. Phys.* 11:1107178. doi: 10.3389/fphy.2023.1107178

Time tracing the earliest case of local pandemic resurgence

Jianing Zhang[1], Kexin Fang[1], Yinhua Zhu[2], Xiaoyun Kang[3,4] and Lin Zhang[1]*

[1]School of Science, Beijing University of Posts and Telecommunications, Beijing, China, [2]Affiliated Zhejiang Hospital, Zhejianq Univerisity School of Medicine, Hangzhou, China, [3]Research Center of Computational Communication, Beijing Normal University, Zhuhai, China, [4]School of Journalism and Communication, Beijing Normal University, Beijing, China

Origin identification of the earliest cases during the pandemic is crucial in containing the transmission of the disease. The high infectiousness of the disease during its incubation period (no symptom yet) and underlying human interaction pattern make it difficult to capture the entire line of the spread. The hidden spreading period is when the disease is silently spreading, for the "silent spreaders" showing no symptoms yet can transmit the infection. Being uncertain of the hidden spreading period would bring a severe challenge to the contact tracing mission. To find the possible hidden spreading period span, we utilized the SEITR (susceptible–exposed–infected–tested positive–recovered) model on networks where the relation between E state and T state can implicitly model the hidden spreading mechanism. We calibrated the model with real local resurgence epidemic data. Through our study, we found that the hidden spreading period span of the possible earliest case of local resurgence could vary according to the people interaction networks. Our modeling results showed the clustering and shortcuts that exist in the human interaction network significantly affect the results in finding the hidden spreading period span. Our study can be a guide for understanding the pandemic and for contact tracing the origin of local resurgence.

KEYWORDS

SEITR, resurgence, origin identification, tracing, EPI, epidemiology

1 Introduction

Since December 2019, the newly recognized coronavirus known as severe acute respiratory syndrome–coronavirus 2 (SARS-CoV-2) has affected every individual. Globally, it has caused more than 623,000,396 confirmed cases, including 6,550,033 deaths, according to the WHO [1]. While the coronavirus has affected the healthcare system significantly, it is a greater challenge for the government to help people coordinate their daily lives living with the virus. One of the most used strategies, contact tracing, along with robust testing and isolation, is a key strategy for interrupting chains of transmission of SARS-CoV-2 and reducing COVID-19-associated mortality [1]. The virus was first reported in Wuhan, China, in late 2019. The doubt still unresolved as to when the virus actually started its spreading.

COVID-19 displays peculiar epidemiological traits when compared with previous coronavirus outbreaks [2]. A large number of transmissions occurred through human-to-human contact with individuals showing no or mild symptoms. High viral loads of SARS-CoV-2 were found in the upper respiratory samples of patients showing little or no symptoms, with a viral shedding pattern akin to that of influenza viruses [3]; hence, the

inapparent transmission, that is, the disease's hidden spread may play a major and underestimated role in sustaining the outbreak.

Origin identification requires detailed contact history records, which are not easily accessible [4]. Even now under the implemented mandatory COVID test that requires frequent detection, there is still unexpected local resurgence occurring with no clear sign. High cost and exhausted human labor are obvious problems in terms of tedious contact tracing missions, especially when the virus is rapidly evolving and there is no clear guidance on how many contacts should be isolated. The Omicron variant BA.5 remains dominant in the United States, people infected with COVID-19 can show symptoms as early as 2 days or as late as 14 days after infection, and people are generally contagious between 3 and 4 days before appearance of symptoms [5]. The BA.5 variant also causes long COVID-19 symptoms, and some can experience health problems for 4 or more weeks after first being infected [6].

To understand the complicated factors in predicting the spread of disease, stochastic mathematical epidemic modeling has been one of the main approaches in understanding the spreading dynamics of the virus. Commonly used models are SIR-inspired models, which describe the flow of individuals through three or more mutually exclusive stages of infection: susceptible, infected, and recovered. More complex models such as SEITR and SEIQR have been carried out to portray the dynamic spread of specific epidemics [7–11]. The SEITR model is a more complex and detailed infectious disease modeling framework than the SIR model [12, 13]. The SEITR model includes a more accurate representation of disease progression and allows for a better understanding of the transmission dynamics of the disease. It accounts for the latency period between exposure and onset of symptoms and can help in modeling diseases where individuals can spread the infection before showing symptoms [14].

In order to understand the local resurgence and find the possible hidden spreading period, we utilized a modified SEITR (susceptible–exposed–infected–tested positive–recovered) compartmental mathematical model for predictions of COVID-19 epidemic dynamics. Our main goal is to use the modified SEITR model to trace back the origin time of the spreading process, given a certain number of confirmed cases. In the following article, real local resurgence data from Xi'an, China, is used to calibrate the model to find the possible hidden spreading period of local resurgence. While homogeneous contact is not applicable in real life, we compared our model on different people interaction networks to observe the impact of clustering and shortcuts created by mobility. Our results showed that the existence of clustering and shortcuts does affect the speed of disease transmission, hence affecting our decision in finding the possible hidden spreading period span. Although local resurgence seems unpredictable, our model provides guidance for time spans of contact tracing and suggestions on modifications of control measures and testing abilities.

2 Methods

2.1 SEITR model

The SEITR model is a variation of the basic SIR (susceptible–infectious–recovered) model used for modeling the spread of infectious diseases in a population [14]. The SEITR model includes additional compartments to account for more complex disease transmission dynamics. Considering one population, as shown in Figure 1, the model subdivides the total human population size at time t denoted as $N(t)$ into susceptible $S(t)$, exposed $E(t)$, infected $I(t)$, tested positive $T(t)$, and the recovered $R(t)$. Hence, for the population, we have $N(t) = S(t) + E(t) + I(t) + T(t) + R(t)$.

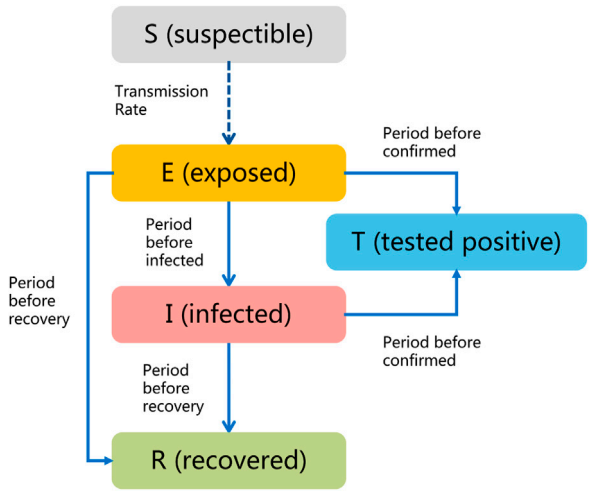

FIGURE 1
SEITR model transmission graph.

Since the beginning of the COVID-19 epidemic, SARS-CoV-2 has evolved and mutated continuously, producing variants with different transmissibility and virulence. Real data indicate that asymptomatic and symptomatic infected individuals can spread the virus to susceptible persons through close contact. Mwalili identified the difference between asymptomatic and symptomatic infected individuals by dividing the infected I(t) into these two subpopulations. Ottaviano provides analytical results for SAIRS (susceptible–asymptomatic infected–symptomatic infected–recovered–susceptible) model where asymptomatic infected is considered one compartment [15, 16]. While different approaches have been taken in considering the "silent spreaders"—those showing no symptoms and able to transmit the infection—here in our study, we included both the concept of incubation period along with the asymptomatic infected individuals into the compartment exposed $E(t)$. The hidden spreading period Φ is when the disease is silently spreading, for the "silent spreaders" showing no symptoms yet able to transmit the infection, and the uncertainty of the hidden spreading period would bring a severe challenge to the contact tracing mission. We define the hidden spreading period Φ as the time since the initial infectious individual [exposed individual $E(t)$ or infected individual $I(t)$] in the population until the time since the first confirmed case $T(t)$. In the process of disease spread, the susceptible individual first moves to the exposed population $E(t)$ when making contact with exposed or infected individuals since they both are infectious. During the incubation period, the exposed population may develop severe symptoms like shortness of breath, chest pain, or confusion

TABLE 1 Model parameters.

Parameter	Symbol	Value	References
Rate of transmission from S to E due to contact with E	β_E	$R_0\gamma$	[6]
Rate of transmission from S to I due to contact with I	β_I	$R_0\gamma$	[6]
Hardness of control measures	c	(0,1)	None
Rate of incubation period	σ	1/3.5 days	[6]
Rate of transmission from E to I	α	0.13	[17]
Proportion of successful COVID testing	p	(0,1)	None
Rate of COVID testing	ω	1/3 days	[18]
Rate of recovery of the infected population	γ	1/21 days	[5]

[these would move to the infected population $I(t)$], some may be self-immune to the virus [move to recovered $R(t)$], and some people may only have very mild or non-specific symptoms [some can be tested as confirmed cases $T(t)$]. $T(t)$ is the number of confirmed cases detected through the ordinary COVID tests at time t; this number can be significantly affected by the testing ability. Some infected individuals would be detected positive through ordinary screening, and some infected individuals would self-recover and move to the recovered human population $R(t)$.

The SEITR model is, thus, governed by the reactions:

$$\begin{aligned} S + E &\xrightarrow{c\beta_E} E + E \\ S + I &\xrightarrow{c\beta_I} E + I \\ E &\xrightarrow{\sigma\alpha} I \\ E &\xrightarrow{\sigma\omega p} T \\ E &\xrightarrow{\sigma(1-\alpha)} R \\ I &\xrightarrow{\omega p} T \\ I &\xrightarrow{\gamma} R \end{aligned}$$

where parameters used in the transmission model are given in Table 1.

The contagion process involves contact interaction. In this mean field approach, the effect of contact on susceptible individuals with exposed and infected individuals is considered in a homogeneously mixed population. So, the model culminates in the following systems of mean field equations:

$$\begin{aligned} S(t+1) &= S(t) - c\beta_E E(t)S(t) - c\beta_I I(t)S(t) \\ E(t+1) &= E(t) + c\beta_E E(t)S(t) + c\beta_I I(t)S(t) - \sigma\alpha E(t) \\ &\quad - \sigma(1-\alpha)E(t) - \sigma p E(t) \\ I(t+1) &= I(t) + \sigma\alpha E(t) - \gamma I(t) - \omega p I(t) \\ T(t+1) &= T(t) + \omega p I(t) + \sigma p E(t). \\ R(t+1) &= R(t) + \sigma(1-\alpha)E(t) + \gamma I(t). \end{aligned}$$

The basic reproduction number defines the average number of secondary infections caused by an individual in an entirely susceptible population. The derivation of R_0 in our model can be approximated by $R_0 = \beta_I/\gamma$. There is no death or birth in the process, and an individual would attain immunity after recovery and cannot be infected again.

During the hidden spreading period, the exposed population spread the virus "silently," wherein some would self-recover, some would transfer to infected individuals, and some would be detected as test positives. Real data showed that the transmission rate from asymptomatic to infected individuals during local resurgence in Shanghai in April is 1995/15284 = 13.05% [17]. In the model, β_I and β_E are generated from $R_0{*}\gamma$, which is around 0.88. $1/\sigma$ is the average latency period of the exposed individuals and $1/\gamma$ captures the average recovery time of the infected population.

In the model, two aspects of non-pharmaceutical intervention practices are introduced to model the effect of intervention policies. In facing a local resurgence of the disease, the hardness of control measures $c \in (0, 1)$ would be tightened to scale down the ability of transmission. This act could be explained by reduced contact interaction during city lockdown or suspended travel activities. For other non-pharmaceutical intervention practices, the testing ability would affect the number of tested positive $T(t)$ individuals, which consist of two latent parameters: rate of successful COVID testing $p \in (0, 1)$ and testing frequency ω. Depending on the quality of each throat swab, the rate of successful COVID testing p would vary and rely highly on those third-party organizations corresponding to the testing. The testing frequency ω describes how frequently the COVID test is implemented. The current standard in major cities for testing frequency is a COVID test in 3 days and one test per day during lockdowns.

Considering the aforementioned interaction measures, our model can capture the dynamics of the spreading process when restrictions are implemented during a local resurgence.

2.2 Model calibration and time tracing the earliest case

The data used to calibrate the model were real local resurgence data from Xi'an, China, from 09 August 2022 to 18 September 2022 [18]. The first BA.5 confirmed case was detected on August 9 in Xi'an, which then caused rapid increase in daily new cases, consisting daily new infected cases and daily new asymptomatic cases. In our simulation, we implemented the lockdown once the number of tested positive T(t) exceeds 18 by minimizing the control measure c to 0 and pushing the testing ability p to the highest 0.99 with a daily COVID test, as what really happened in July at Xi'an. The source of this local resurgence was still not clear.

The methodology of locating the earliest case in local resurgence is as follows: first, real data are used to calibrate the SEITR model,

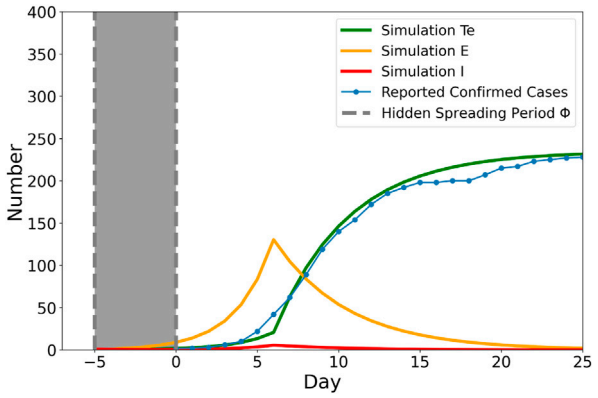

FIGURE 2
Simulation result with real Xi'an local resurgence data fitted. The blue dotted line shows the real recorded accumulated daily confirmed cases since Day 0. The green line is the simulated tested positive number with the implementation of lockdown once the number of reported confirmed case exceeds 40. $\beta_I = \beta_E = 0.88$, $c = 1$, $w = 1/3$, $p = 0.8$. The shaded area $\Phi = 5$ hidden spreading period span was added to the real data to capture the delay of growth in simulation, indicating the possible initial infected individual started its hidden spreading period around 5 days ago.

and then the control policies are added. This can be done by adjusting only control measures (c), rate of successful COVID testing (p), and testing frequency (w), while the remaining parameters are determined by real clinical report data. Since these parameters act directly on the transmission of the disease, different combinations of the aforementioned policy measures can simulate different control scenarios such as city lockdowns and restrictions on human travel. Normally in real life scenarios, control policies would be strengthened once the newly confirmed cases exceed a certain number. However, it is certain that the disease has been spreading hidden for a period, and this is why finding the possible hidden spreading period Φ span is crucial for the following contact tracing work.

A total population of $N = 13,000,000$ is considered to approximate the population of Xi'an city. As shown in Figure 2, initially, we added one infected (I) individual into the population, while the remaining population are susceptible (S) individuals. We can clearly see that even days before disease detection, a certain number of exposed (E) individuals in the population have been "silently" spreading the virus. During this hidden spreading period Φ, some exposed individuals are already infectious, yet due to the virus being still in its incubation period, they may escape from detection. The rapid increase in the number of either tested positive (T) or recovered (R) would occur once it is detectable or recovered, respectively. With the implementation of the lockdown, restrictions in control measures such as less travel or visiting ($c = 0.4$) and increasing the testing ability and the frequency ($p = 0.99$, $w = 1$), the increase in the confirmed case would soon reduce as what happened in Xi'an.

The hidden spreading period Φ is deduced by comparing the difference between the first reported case in real resurgence record and the simulated initial spreader. As shown in Figure 2, the shaded area $\Phi = 5$ hidden spreading period span was added to the real data to capture the delay of growth in simulation, indicating the possible initial infected individual started its hidden spreading period around 5 days ago. We define $Error_\Phi$ as the difference between the predicted and real data under different hidden spreading periods Φ since it is possible in real life that the disease has been "silently" spread in the population for a while until first reported. Different hidden spreading period Φ values are added before the first reported day. $Error_\Phi$ is then calculated for each possible Φ hidden spreading period to find the best result. As shown in Figure 2, a $\Phi = 5$ hidden spreading period span was selected as the best-fitted model with $Error_\Phi = 2.218/N$.

The mean field numerical results can provide us with the solution to the systems of equations; however, the real-case scenario is much more complicated than one system of equations. $\Phi = 5$ is the most possible hidden spreading period based on the strong assumption that the population is homogeneously mixed. However, in real life, social interactions are much more complicated, and the heterogeneity in human behavior would significantly affect the speed of transmission. The key to confronting the pandemic is to lower the rate of transmission of the disease. Our non-pharmaceutical intervention practice parameters in the model can provide a vague picture of modifying the transmission rate. Having $c = 0$ (city lockdown) is one of the worst-case scenarios since it bans people from moving.

Therefore, it is necessary to understand the trade-offs between restrictions and daily activities. Some regulations such as restricting certain types of transportation would decrease human mobility; hence, in turn, lowering the transmission rate may also be useful, but is it really efficient in controlling the spread of the disease? In the following section, we extended our model on human interaction networks to discuss the impact of clustering and shortcuts created by mobility.

2.3 SEITR on networks

Many studies have shown that human daily interactions and mobility can lead to construction of local communities and shortcuts in social networks [19]. Clustering is often simply described as the number of triangles (where the friend of my friend is also my friend) in a network, but usually also implies that links between nodes tend to be aggregated in well-connected, groups as shown in Figure 3. Hebert–Dufresne investigated the impact of contact structure clustering on the dynamics of multiple diseases interacting through the coinfection of a single individual and found the opposite effect of clustering. In addition, they showed that although clustering slows down the propagation of non-interacting diseases, it would speed up the propagation of synergistically interacting diseases [20].

Extensive studies on mobility within the pandemic revealed that population mobility is among the main drivers of the spatial spreading of the outbreak [19, 21, 22]. The complex social network structures created by heterogeneous mobility and contacts would affect the spread of the disease significantly [21]. At the modeling level, the network consists of a set of communities (node), connected by edges that capture daily short-range commuting and long-range mobility. The small-world network is one of the most basic representations of human interaction patterns

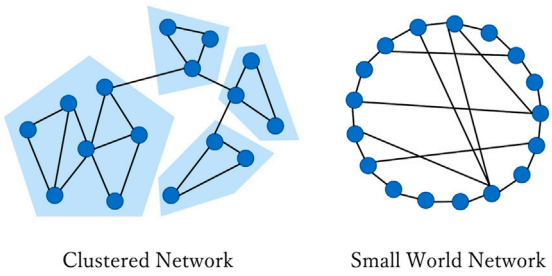

FIGURE 3
Different network structure.

in network science, by analogy with the small-world phenomenon [23]. We run our model on simple small-world networks by modifying initial rewiring probability to simulate the existence of shortcuts, an analogy of the shortcuts created by travel behavior.

The community structure network extended the description of propagation dynamics on a highly clustered network using overlapping community structures [20]. The arrangement of nodes leads to clustering of nodes into well-connected groups, which may represent the notion of a workplace or family. Every connection in this structure can be decomposed in terms of groups, where even single links between two individuals can be considered a group of size 2. Assuming that we know the distribution of group sizes (number of nodes per group) and of node memberships (number of groups per node), we can define a maximally random ensemble of clustered networks with a fixed community structure by randomly assigning nodes to groups. Hence, the entire network structure is solely defined by two probability distributions, p_n, and g_m, respectively, which are the probabilities that a randomly selected group will contain n members (size n) or that a randomly selected individual will participate in m groups (m memberships). This concept results in a network with highly connected communities and a sparser density of links between them. To highlight the effects of community structure (CS), an equivalent random network (RN) with exactly the same degree distribution but randomly rewired links is generated. Furthermore, description of the dynamics of the community structure can be found at [20].

The network-based SEITR model counts the changes in network contacts upon the presence of infected (I) and also allows for exposed (E), which could be used to simulate the likely changes in contact patterns of an individual in tested positives. The parameters discussed in previous sections are preserved during the Monte Carlo simulation. The one seed-infected individual was added randomly into the network of 2,000 nodes. At each time step, susceptible individuals S_i would be infected and transmit to exposed E_i when contacted with exposed individual E_j or infected individual I_j neighbors. The transmission rate could be expressed as $\beta = 1 - \sum_{j\in[1,N]}(1 - \beta_E E_j)(1 - \beta_I I_j)A_{ij}$, while A is the adjacency matrix of the network. During the incubation period, exposed individuals would transfer to infected individuals spontaneously, and some would self-recover. In both exposed and infected individuals, some would be detected as tested positive T_i. By modifying the control measures and test ability, we would see how these non-pharmaceutical intervention practices affect the time tracing of the earliest case.

We tested our model on both the community structure network and the equivalent random network introduced by Hebert–Dufresne [20], hoping to find the evidence of clustering speed up the propagation and hence influence our decision in finding the Φ hidden spreading period span. In addition, since the network models described by Hebert–Dufresne mainly focused on the effect of the existence of clustering, we also discussed the effect of the shortest path created by human mobility in the network. We addressed this by running the model on a small-world network, modifying the probability of rewiring an edge [23].

3 Results and discussion

The existence of community is a common feature of human interaction networks. The main goal of running the SEITR model on different network structures is to reconstruct the possible human interaction networks during disease propagation. Figure 4 shows the phase diagram of running simulation on the community structure network and the equivalent random network shows the number of tested positive (T) at its final steady state of each simulation. The control measures c and frequency of COVID test w are two non-pharmaceutical intervention practices that can be modified in our model to simulate real intervention conditions. Lower c means a lower level of transmission, and higher c means there are no restrictions to prevent the disease from spreading. The lowest frequency of COVID testing w means no COVID test is conducted; hence, all the exposed and infected individuals would remain in the population and spread the disease silently. Assuming a 100% success in COVID testing $p = 1$, we compared how the two intervention policies would affect the propagation. As shown in Figure 4, $w = 0$ means no COVID test is conducted; hence, no test positive exists in the population; $w = 1$ means any exposed or infected individuals would be detected once they are positive. Figure 4A shows the number of tested positive (T) at its final steady state on the community structure network of the 2,000 nodes. In Figure 4B, the equivalent random network result is presented. The random network is created from the community structure network, by randomly rewiring the links within the community to another node while keeping the same average degree. The resulting random network in our analysis has a clustering coefficient of around 0.05, while the coefficient of the structure community network is around 0.10. In Figure 4, we can see that although the average degree of both networks is relatively the same, the changes in the community structure network are smoother than those of the random network due to the randomness of Monte Carlo simulations. There are similarities between community structure and its equivalent random network, and the reason may be how the community structure network was constructed. Although the clustering coefficient is doubled for the community structure network, the relatively same average degree and average shortest path of the two networks would smooth out the effect of clustering on disease propagation. However, if we focus on a coarse-grained level of the heat map, the combined influence of the two intervention policies on disease transmission is clear and would be useful as guidance.

While the phase diagram provides thorough information about how the combined intervention would affect the results of the

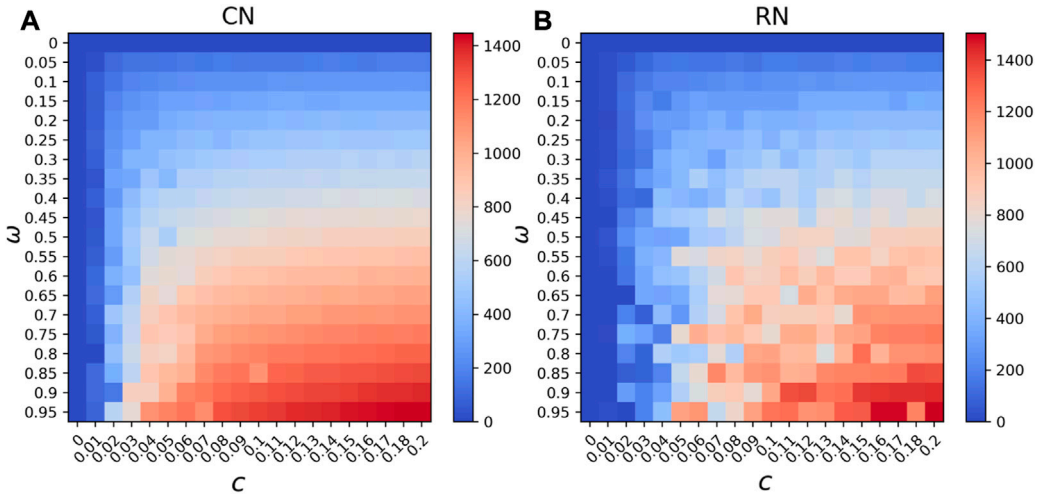

FIGURE 4
Phase diagram of steady state tested positives (*T*) **(A)** on the community structure network and **(B)** the equivalent random network under different combinations of control measures and testing frequency.

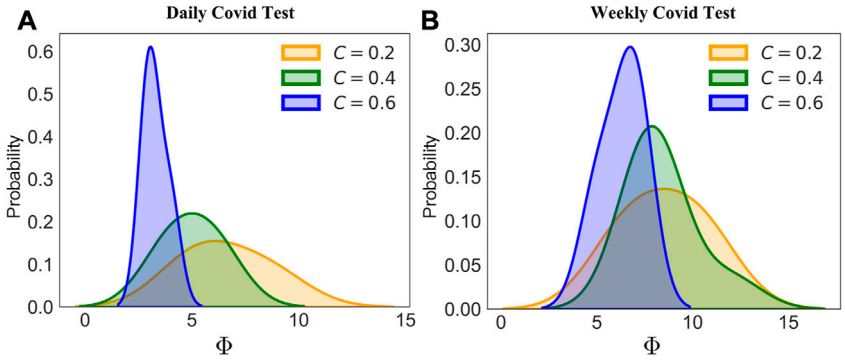

FIGURE 5
Probability density distribution of the hidden spreading period span Φ. Holding a control measure of c = 0.03, two testing frequencies are chosen, a test per day **(A)** and a test per 7 days **(B)**. Results under different clustering coefficient community structure networks (CNs) are provided.

disease spread, our main task is to locate possible hidden spreading period span Φ in a local pandemic resurgence. Through each simulation, we counted the number of days needed for a local resurgence, and the accumulated tested positive number exceeds 10. As shown in Figure 5, we provided a comparison between different community structures by varying its clustering coefficient C. With the increased clustering coefficient, the hidden spreading period span would shrink significantly, indicating that a higher clustering network provides a smaller hidden spreading period span Φ. We can conjecture that the clustering in the network does affect the speed of the propagation. As shown in Figure 5A, with a daily COVID test window, all the positives would be detected immediately. As shown in Figure 5B, a higher clustering coefficient of 0.6 would still provide a shorter span than that of a clustering coefficient of 0.2 and 0.4. In addition, Figure 6A shows the trend of how the average hidden spreading period span changes along with different clustering coefficients. The red line represents the result of Φ if the COVID test is conducted per week; it is obvious that a delayed test would shade the hidden spreading and, hence would cause more difficulty in conducting the contact tracing. Especially in the low clustering region (clustering coefficient of 0.05), a 1-week delayed test would lead up to 1 month of contact tracing. If the test is not conducted daily, but with a delay of few days, some exposed and infected individuals would self-recover, and some would still spread the disease 'silently' and not be tested on time. This is the reason the hidden spreading period spans are increased, hence increasing the tracing back time of the origin of disease propagation.

The time span results may vary according to the heterogeneity of human interaction behaviors. We showed the existence of a community provides a higher amount of interactions in the community, and the disease would spread faster, hence reducing the hidden spreading period span. Another effect of human interaction networks is the existence of a short path in the

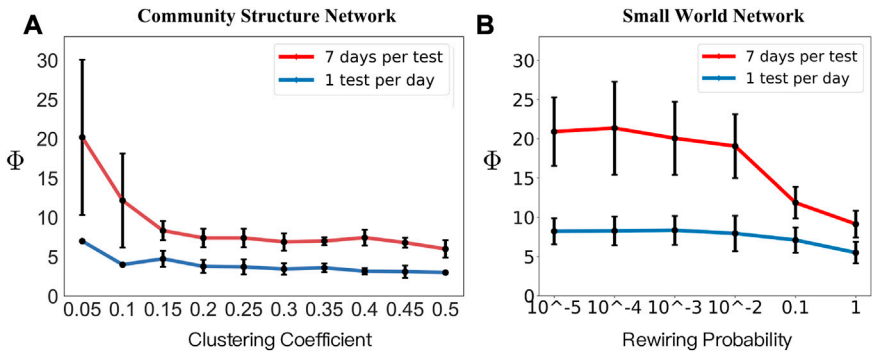

FIGURE 6
Hidden spreading period span Φ results. Holding a control measure of c = 0.03, two testing frequencies are chosen, a test per day (blue lines) and a test per 7 days (red lines). **(A)** A set of community structure networks has different clustering coefficients. **(B)** Small-world network with six sets of rewiring probability were chosen, providing the average shortest path from 20.49, 11.58, 5.58, 3.43, 2.72, and 2.25, respectively.

network. In our daily activities, a short journey to another city can create a short path for the contagious disease. To address the influence of human travel, we used the small-world network developed by Watt and Strogatz [23]. The network of 2,000 nodes has an average degree of 50, representing the number of people that an individual has regular physical contact with, e.g., family members, co-workers, and friends. We compared different sets of rewiring probability p, the probability that an edge is disconnected from one of its nodes and then randomly connected to another node anywhere in the network (vertex may have a long-range shortcut connected to a remote vertex).

As shown in Figure 6B, six sets of rewiring probability were chosen, providing different average shortest paths. Similar to that shown in Figure 6A, the trend of both lines steadily decreases, indicating a smaller average shortest path provides a shorter period of hidden spreading span. In general, the daily COVID test would capture both exposed and infected individuals immediately, but with delayed testing, the span of the possible period distribution would be increased. Through the aforementioned comparison, we conclude that the structure of how human interaction networks would have a great influence on how fast disease propagation is, and in turn, influence the time tracing mission finding the origin of the propagation.

It should be necessary to point out that rewiring probability p is meaningful only in a relative sense. For example, choosing a degree of 50 and p = 0.01 does not imply that each person in society interacts with 50 people in daily activities and knows only one person in far-away areas. But rather, the changes from p = 0.01 to p = 0.001 mean that, on average, each person reduces the daily infection-transmissible interactions by half and/or long-distance travel by 90%. Another point that needs to be made is that in real-world social networks, different individuals have different ways of interacting with others, for example, the contact frequency is usually different between the different contact patterns, and household contact is significantly more frequent than other scenarios. For example, it is unknown how individuals with different levels of social interactions respond to social distancing or lockdown orders. Figure 7 shows that different choices of the contact frequency distribution do not affect greatly tracing the possible hidden spreading span. In our study, the

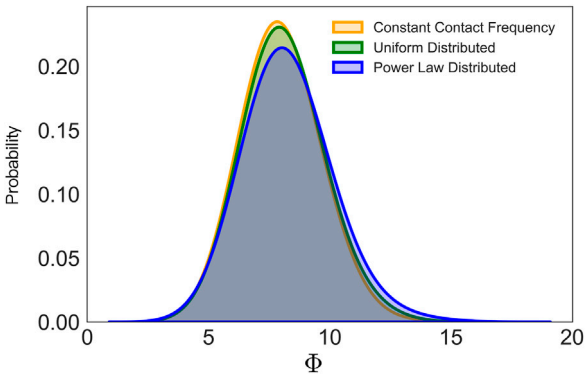

FIGURE 7
Probability density distribution of the possible hidden spreading span under the different choice of contact frequency. Holding the mean of the contact frequency as 0.05, we compared the influence of contact frequency on the possible hidden spreading span.

contact frequency is assumed to be the same for all the vertices because there is no adequate data on the real contact network. So in order to address the problem of the heterogeneity of contact frequency, except for the constant control measure c, we also tested both power-law distributed contact frequency and uniformly distributed contact frequency. Holding the mean of the distribution to the same constant number, we see no clear difference in finding the possible hidden spreading period. Hence, the use of the constant contact frequency with each individual represented as a vertex can still provide useful predictions.

4 Conclusion

Till today, SARS-CoV-2 has caused more than 623,000,396 confirmed cases, including 6,550,033 deaths. We need to understand how and what should we do to live with the disease. Origin identification of the earliest cases during the pandemic is crucial in terms of contact tracing. It is a key strategy for interrupting chains of transmission of SARS-CoV-

2 and reducing COVID-19-associated mortality. However, high cost and human labor are a problem in terms of contact tracing, especially when the virus is rapidly evolving and there is no clear guidance on how many contacts should be isolated. To help understand the disease propagation and to trace the earliest case, we utilized a modified SEITR compartmental mathematical model for prediction of COVID-19 epidemic dynamics. Our main goal was to use the data-driven simulation result to find the possible hidden spreading period span since the beginning of the spreading process. Real local resurgence data of Xi'an, China (August 2022) were used to fit the mean field model. Our result indicated the possible initial infected individual started its hidden spreading period around 5 days ago since the first recorded confirmed case.

Since a homogeneously mixed population is not applicable in real life, we then tested our model on different network structures to simulate human interaction patterns. The community structure network extended the description of propagation dynamics on a highly clustered network using overlapping community structure [20], and our results showed that in a local pandemic resurgence, given a certain amount of test positive cases, a high clustering network does minimize the possible hidden spreading span. We then discussed the effect of the short path created by human mobility. The results showed clear evidence that shorter average paths provide a shorter period of the hidden spreading results. In real-case scenarios, these together may infer the different human interaction patterns between big cities and rural areas. Where communities are very common and have constant interactions with remote individuals, a local resurgence in big cities always appears very suddenly and breaks out. If not with accurate control restrictions, a larger pandemic seems inevitable. However, in rural areas, where communities are normally sparse and lack interactions, the local resurgence is not very often and may not grow to a larger scale. Hence, in order to capture the "silent" spreaders in a timely manner, accurate contact tracing should be carried out as soon as a positive is detected to avoid further costs.

We discussed two aspects of non-pharmaceutical intervention practice in facing the local resurgence of the disease. The hardness of control measures scales down the ability of transmission and testing ability, consisting of the rate of successful COVID testing and testing frequency. Control measures could be interpreted as the restrictions policies such as city lockdowns, while the testing ability represents the detection quality. Based on these, our model provides insights into how the combination of the interventions could affect the speed of disease propagation. Our results present the possible distribution of the hidden spreading period span in terms of contact tracing.

There is a certain amount of mis-considerations when building up our SEITR model, for example, the birth and death rate of the population is not included, as well as the quarantine factor. The network structures we considered were all static rather than temporal. In real life, the spontaneous and temporal movement could modify human interaction networks. More studies need to be performed to address the real changing temporal characteristics of human mobility to better understand the propagation patterns. In addition, our study of disease propagation could also extend to subjects such as idea propagation [24–26], culture spreading [27], and signal propagation [28]. For example, signal propagation patterns on complex networks may be helpful in understanding the complex behavior of the contagion, especially how the social system would respond according to perturbation of the dynamics [28, 29]. Our work put forward the method to timing the earliest case, given real local resurgence data. Although local resurgence seems unpredictable, our model provides a guidance for time spans of contact tracing as well as suggestions on modifications of control measures and testing abilities.

Data availability statement

The datasets presented in this study can be found in online repositories. Epidemiological data for this study are available at http://www.nhc.gov.cn/xcs/yqtb/list_gzbd.shtml. The code used for the simulations is available at https://github.com/avecsally/Tracing-the-time-of-the-origin-in-local-epidemic-spreading-on-networks/tree/main.

Author contributions

JZ, KF, and LZ conceived and designed the research with inputs from all the authors. JZ and KF performed parameter identification and the numerical studies and wrote the first draft of the manuscript. JZ and LZ supervised the research and consolidated the manuscript in its present submission. JZ contributed to the interpretation and analysis of the results and to reviewing the current submission of the manuscript. All authors contributed to the article and approved the submitted version.

Funding

This work was jointly supported by the National Natural Science Foundation of China (Grant Nos. 11971074 and 61671005).

Conflict of interest

The authors declare that the research was conducted in the absence of any commercial or financial relationships that could be construed as a potential conflict of interest.

Publisher's note

References

1. World Health Organization. *Contact tracing in the context of covid-19. interim guidance*. Pediatria i Medycyna Rodzinna (2020). Available at: https://www.who.int/emergencies/diseases/novel-coronavirus-2019/global-research-on-novel-coronavirus-2019-ncov.

2. Giordano G, Blanchini F, Bruno R, Colaneri P, Filippo AD, Matteo AD, et al. Modelling the Covid-19 epidemic and implementation of population-wide interventions in Italy. *Nat Med* (2020) 26:855–60. doi:10.1038/s41591-020-0883-7

3. Read JM, Bridgen JR, Cummings DAT, Ho AYW, Jewell CP. *Novel coronavirus 2019-ncov: Early estimation of epidemiological parameters and epidemic predictions*. medRxiv (2020). Philosophical Transactions of the Royal Society B.

4. Xia Y, Lee G. *How to return to normalcy: Fast and comprehensive contact tracing of covid-19 through proximity sensing using mobile devices* (2020). arXiv preprint. ArXiv: 2004.12576.

5. CDC. *Nsars-cov-2 variant classifications and definitions*. Centers for Disease Control and Prevention (2022). Available at: https://www.cdc.gov/coronavirus/2019-ncov/variants/variant-classifications.html.

6. UC DAVIS HEALTH. *Omicron ba.5: What we know about this covid-19 strain* (2023). Available at: https://health.ucdavis.edu/coronavirus/covid-19-information/omicron-variant.

7. Prabakaran R, Jemimah S, Rawat P, Sharma D, Gromiha MM. A novel hybrid seiqr model incorporating the effect of quarantine and lockdown regulations for Covid-19. *Scientific Rep* (2021) 11:24073. doi:10.1038/s41598-021-03436-z

8. Huang Q, Ma J, Xu Z, Gu X, Yang M. A staging prediction model for Covid-19 pandemic under strong public health interventions. In: 2022 Tenth International Conference on Advanced Cloud and Big Data (CBD); 04-05 November 2022; Guilin, China (2022). p. 184–9. doi:10.1109/CBD58033.2022.00040

9. Yang Z-F, Zeng Z, Wang K, Wong S-S, Liang W, Zanin M, et al. Modified seir and ai prediction of the epidemics trend of Covid-19 in China under public health interventions. *J Thorac Dis* (2020) 12:165–74. doi:10.21037/jtd.2020.02.64

10. Cai M, Karniadakis GE, Li C. Fractional seir model and data-driven predictions of Covid-19 dynamics of omicron variant. *Chaos* (2022) 32:071101. doi:10.1063/5.0099450

11. Calafiore GC, Novara C, Possieri C. A modified sir model for the Covid-19 contagion in Italy. In: 2020 59th IEEE Conference on Decision and Control (CDC); 14-18 December 2020; Jeju, Korea (South) (2020). p. 3889–94. doi:10.1109/CDC42340.2020.9304142

12. Kucharski AJ, Russell TW, Diamond C, Liu Y, Edmunds JW, Funk S, et al. Early dynamics of transmission and control of Covid-19: A mathematical modelling study. *Lancet Infect Dis* (2020) 20:553–8. doi:10.1016/s1473-3099(20)30144-4

13. Hethcote HW. The mathematics of infectious diseases. *SIAM Rev* (2000) 42:599–653. doi:10.1137/s0036144500371907

14. Brauer F, Castillo-Chavez C. *Mathematical models in population biology and epidemiology New York: springe* (2001) 2:40.

15. Mwalili S, Kimathi M, Ojiambo V, Gathungu D, Mbogo R. Seir model for Covid-19 dynamics incorporating the environment and social distancing. *BMC Res Notes* (2020) 13:352. doi:10.1186/s13104-020-05192-1

16. Ottaviano S, Sensi M, Sottile S. Global stability of sairs epidemic models. *Nonlinear Anal Real World Appl* (2022) 65:103501. doi:10.1016/j.nonrwa.2021.103501

17. Hangzhou. Hangzhou (2022). Available at: https://news.hangzhou.com.cn/gnxw/content/2022-04/15/content_8228338.htm (Accessed on 04 15, 2022).

18. NHC. NHC (2022). Available at: http://www.nhc.gov.cn/xcs/yqtb/list_gzbd.shtml (Accessed on 11 13, 2022).

19. Parino F, Zino L, Porfiri M, Rizzo A. Modelling and predicting the effect of social distancing and travel restrictions on Covid-19 spreading. *J R Soc Interf* (2021) 18:20200875. doi:10.1098/rsif.2020.0875

20. Hébert-Dufresne L, Althouse B. Complex dynamics of synergistic coinfections on realistically clustered networks. *Proc Natl Acad Sci United States America* (2015) 112:10551–6. doi:10.1073/pnas.1507820112

21. Kraemer MUG, Yang C-H, Gutierrez B, Wu C-H, Klein B, Pigott DM, et al. The effect of human mobility and control measures on the Covid-19 epidemic in China. *Science* (2020) 368:493–7. doi:10.1126/science.abb4218

22. Jia J, Lu X, Yuan Y, Xu G, Jia J, Christakis N. Population flow drives spatio-temporal distribution of Covid-19 in China. *Nature* (2020) 582:389–94. doi:10.1038/s41586-020-2284-y

23. Watts D, Strogatz S. Collective dynamics of small world networks. *Nature* (1998) 393:440–2. doi:10.1038/30918

24. Watts DJ. A simple model of global cascades on random networks. *Proc Natl Acad Sci United States America* (2002) 99:5766–71. doi:10.1073/pnas.082090499

25. Granovetter MS. Threshold models of collective behavior. *Am J Sociol* (1978) 83:1420–43. doi:10.1086/226707

26. Leskovec J, Adamic LA, Huberman BA. The dynamics of viral marketing. *ACM Trans Web* (2005) 1:5. doi:10.1145/1232722.1232727

27. Kempe D, Kleinberg JM, Tardos É. Maximizing the spread of influence through a social network. In: *Knowledge discovery and data mining* (2003).

28. Bao X, Hu Q, Ji P, Lin W, Kurths J, Nagler J. Impact of basic network motifs on the collective response to perturbations. *Nat Commun* (2022) 13:5301. doi:10.1038/s41467-022-32913-w

29. Ji P, Lin W, Kurths J. Asymptotic scaling describing signal propagation in complex networks. *Nat Phys* (2020) 16:1082–3. doi:10.1038/s41567-020-1025-3

frontiers | Frontiers in Physics

TYPE Original Research
PUBLISHED 02 June 2023
DOI 10.3389/fphy.2023.1203665

OPEN ACCESS

EDITED BY
Cong Li,
Fudan University, China

REVIEWED BY
Qi Xuan,
Zhejiang University of Technology, China
Jun Wu,
Beijing Normal University, China

*CORRESPONDENCE
Yongxiang Xia,
xiayx@hdu.edu.cn

RECEIVED 11 April 2023
ACCEPTED 24 May 2023
PUBLISHED 02 June 2023

CITATION
Lin H, Xia Y, Li X and Gao X (2023), A routing strategy for spatial networks based on harmonic centrality.
Front. Phys. 11:1203665.
doi: 10.3389/fphy.2023.1203665

A routing strategy for spatial networks based on harmonic centrality

Hong Lin, Yongxiang Xia*, Xingyi Li and Xiaoxu Gao

School of Communication Engineering, Hangzhou Dianzi University, Hangzhou, China

With the rapid development of networks, the traffic in the networks has increased sharply, resulting in frequent congestion, especially in spatial networks, such as the railway network, aviation network, and sensor network, and congestion not only affects the user's experience but also causes serious economic losses. Therefore, in this paper, we effectively identify the high-load nodes in spatial networks by considering harmony centrality and degree. On this basis, we design the *HD* routing strategy by avoiding these key nodes, which can enhance the traffic throughput of spatial networks efficiently. The results provide new ideas and directions for the design of routing strategies for spatial networks.

KEYWORDS

spatial networks, routing strategy, harmony centrality, congestion, complex network

1 Introduction

At the end of the 20th century, the discoveries of the small-world phenomenon [1] and scale-free property [2] attracted much attention. Since then, complex networks have become a research hotspot in many fields, including communication, transportation, power grids, and social relations [3–13]. Many complex systems can be modeled into complex networks, for example, in some complex systems with transmission as their main function, such as communication networks, internet, and transport network. The constituent elements of these systems can be abstracted as nodes, and links can be used to describe the interrelationships between different elements, which can help us analyze traffic dynamics on these systems effectively. Among them, congestion is the most critical problems of such complex networks, which is related to network topology [14] and routing strategy [15]. However, it is too expensive to modify the network structure. Therefore, optimizing the routing strategy seems to be more practical to improve network transmission performance.

The shortest path (*SP*) routing strategy is the most common routing strategy, which is extensively adopted in various complex systems. However, it is easy to cause congestion at some hub nodes. To solve this problem, many efficient routing strategies have been proposed to avoid these hub nodes [16–26]. Yan et al. [24] realized the influence of network topology on traffic dynamics. They focused on the node degree and proposed an efficient routing strategy, which can enhance the network throughput more than 10 times. Jiang et al. [25] found that nodes with the largest betweenness are most likely to be congested, so they designed an *IE* strategy. The load can avoid these high-betweeness nodes during transmission, which can achieve high network throughput. Zhang et al. [26] considered both static and dynamic information and proposed an adaptive routing strategy. The load can select the appropriate path for transmission based on the waiting time and degree, which can reduce congestion effectively.

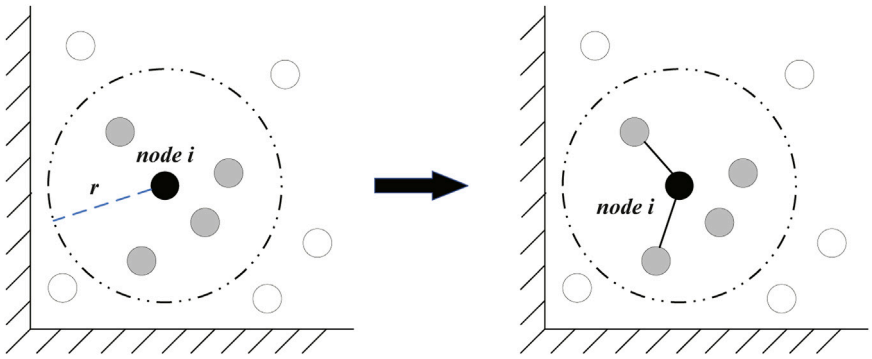

FIGURE 1
Node i build links with nodes in the set Ω_i with probability p.

However, most current works ignore the influence of a space factor. In fact, aviation networks [27], transportation networks [28], wireless sensor networks [29], and swarming networks [30] are all limited by spatial locations. In these networks, each node has a fixed spatial location, and link length is limited. We generally call these networks as spatial networks, which is a significant class of complex networks [31]. Due to the limitation of link length, the topological structure in spatial networks is quite different with topological networks. At the same time, the traffic dynamics on spatial networks will also vary due to distinct structures [32]. For example, in the topological networks, the node degrees often exhibit an obvious power-law relationship with the loads when adopting the *SP* routing strategy. However, Lin et al. [33] found that this power-law relationship is not obvious in spatial networks. Most of the existing routing strategies cannot achieve great results in spatial networks. Thus, there is an urgent need for an efficient routing strategy to alleviate congestion of spatial networks.

In this paper, we focus on traffic dynamics for spatial networks. Based on the harmony centrality and degree, we redefine the key nodes in the transmission. We find that the node with the high harmony centrality index and degree usually deals with more loads. Therefore, we design a harmony-degree (*HD*) routing strategy to bypass these key nodes. All simulations are made on the local-area and energy-efficient (*LAEE*) evolution model and improved the random geometric graph (*IRGG*) model, which are two spatial networks with different structures. According to the results of simulation, our *HD* routing strategy can help spatial networks obtain greater traffic throughput.

The outline of this paper is as follows. In Section 2, we describe the generation of spatial networks. In Section 3, we explain the traffic dynamic model. In Section 4, we introduce our *HD* routing strategy. Simulation results and discussions are given in Section 5. In Section 6, we summarize the conclusion of this paper.

2 Network models

It has been shown that the network structure is an important factor affecting load transmission. For an efficient routing strategy, it should ensure high performance on different spatial networks. Therefore, we will test the performance of the proposed routing strategy on two spatial networks with homogeneous and heterogeneous properties, respectively. The generation of these two models is as follows.

2.1 *IRGG* model

The *IRGG* model is a simple homogeneous spatial network, which has a uniform degree distribution.

The generation process of the *IRGG* model is as follows:

Step 1: N nodes are distributed randomly in the 1×1 square area S.

Step 2: We set a connection radius r for each node. As shown in Figure 1, any node i only can establish links with nodes located in its circular connected area. The set of these nodes can be represented by Ω_i.

Step 3: We set a connection probability p. Node i establishes links with the nodes in the set Ω_i with probability p.

Step 4: We repeat Step 3 until all nodes follow this rule to build links with nodes within their respective connected areas.

2.2 *LAEE* model

The study found that many practical networks follow the scale-free property. To explore the applicability of our proposed routing strategy on heterogeneous spatial networks, we adopt the *LAEE* evolution model proposed by Jiang et al. [34], which builds a spatial network with a power-law degree distribution.

The generation process of the *LAEE* evolution model is as follows [34]:

Step 1: N nodes are distributed randomly in the 1×1 square region S.

Step 2: We define the node closest to the origin as the sink node. At this point, all nodes are isolated. We set every node with the same connection radius r. If the scatter node A lies within the connection radius of node B, we call the scatter node A as the potential neighbor node of the node B.

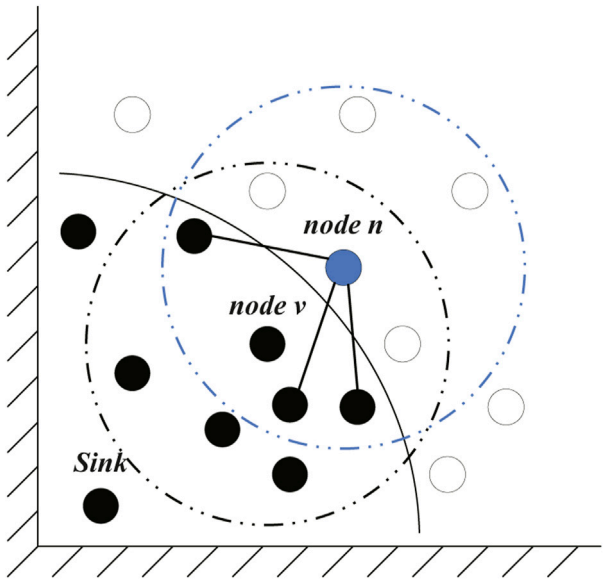

FIGURE 2
At every time step, node *n* builds links with nodes in the network.

Step 3: Sink node builds link with m_0 potential neighbor nodes to form the initial network.

Step 4: At time step i, we calculate the number of potential neighbor nodes owned by different nodes in the network separately. Next, we select the one with the most network and name it as node v. Then, we select one of its potential neighbor nodes randomly and call it as node n.

Step 5: As shown in Figure 2, the node n establishes links with m nodes in the network with the priority probability Π_i:

$$\Pi_i = \Pi_i^{'}(i \in local - area)\frac{\varphi(E_i)k_i}{\sum_{local-area}\varphi(E_j)k_j - qk_{max}}, \quad (1)$$

where the local-area is the set of node n's potential neighbor nodes. k_{max} represents the upper limit that the node's degree is allowed to reach, q indicates the number of nodes whose degrees arrive at k_{max}, and $\varphi(E)$ is a function. In this paper, we set $\varphi(E_i) = 1$ and $\varphi(E_j) = 1$.

Step 6: We repeat Step 4 and Step 5 until all nodes are connected to the network.

Based on the aforementioned generation methods, we can generate these two networks and observe the degree distribution. As shown in Figure 3, the degree distribution of the *IRGG* model is relatively even, but the *LAEE* model presents power-law distribution. Then, the *IRGG* model is a homogeneous spatial network and *LAEE* belongs to a heterogeneous spatial network.

3 Traffic dynamics

At every time step, every node can handle at most C units of load, and R units of load are generated in the whole system. We can randomly select pairs of nodes as the sources and destinations. At each time step, we select a neighbor node as the next hop for the load according to the routing strategy. Once the load arrives at its destination, it will disappear automatically. To better understand congestion, we shall introduce the order parameter [35] as follows:

$$\eta(R) = \lim_{t\to\infty}\frac{C}{R}\frac{<W(t+\triangle t) - W(t)>}{\triangle t}, \quad (2)$$

where $W(t)$ is denoted as the units of load in the network at time t and $<\cdots>$ indicates the average over time windows of the width $\triangle t$.

When R is small, the inflow and outflow of a node are balanced and no congestion occurs in the network, so $\eta(R) = 0$. We generally call this state as the free-flow state. However, with the increase of R, some load cannot be processed in time. At that time, $\eta(R) > 0$, and the congestion occurs. We always use the critical value R_c to describe this phase transition. When $R < R_c$, the network is in a free-flow state; when $R > R_c$, congestion occurs. We call R_c as the maximum network throughput. In this paper, our main work is to design an efficient routing strategy to help the spatial network obtain a higher value of throughput.

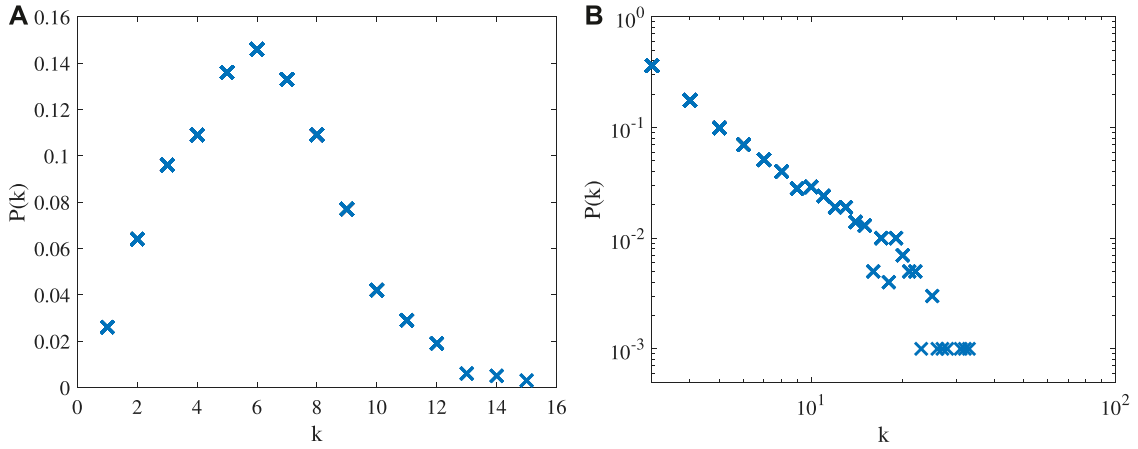

FIGURE 3
Degree distribution of the **(A)** *IRGG* network and **(B)** *LAEE* network. Parameters of the network are set as $N = 1000$, average degree $<k> = 6$, and connection radius $r = 0.12$.

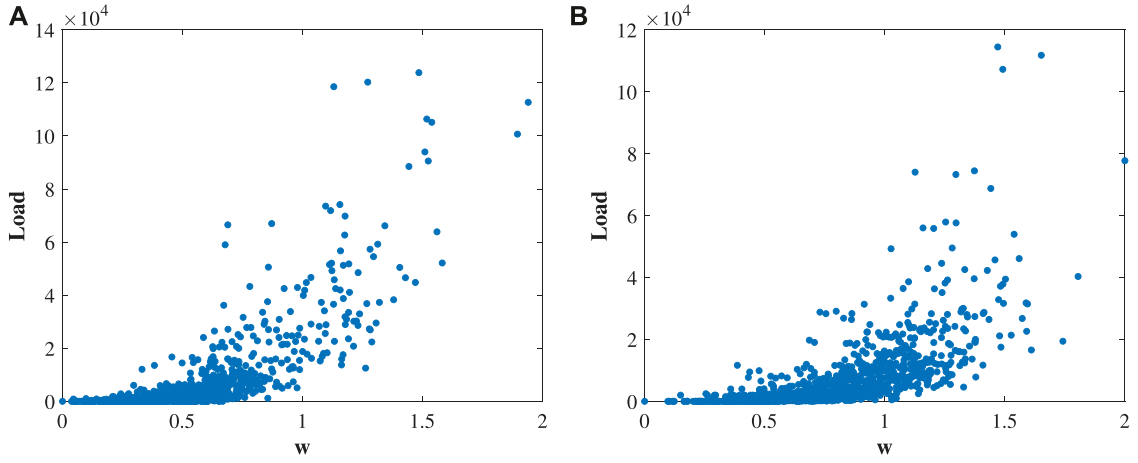

FIGURE 4
Load versus w of nodes under the shortest path (*SP*) routing strategy for the **(A)** *LAEE* network and **(B)** *IRGG* network with $\alpha = 1$ and $\beta = 1$, respectively. Parameters of the network are set as $N = 1000$, average degree $< k > = 4$, and connection radius $r = 0.12$.

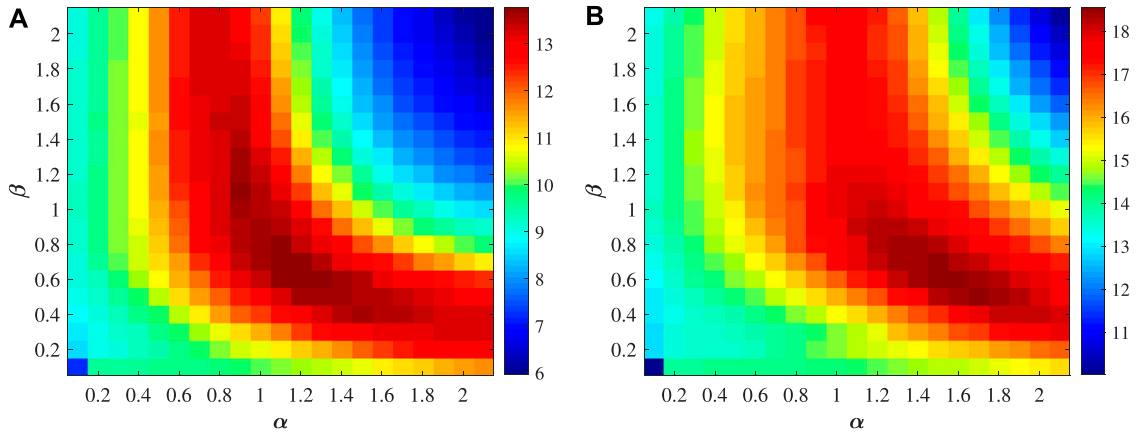

FIGURE 5
Network throughput R_c, determined by adjustable exponents α and β in the **(A)** *LAEE* network; **(B)** *IRGG* network. Parameters of the network are set as $N = 1000$, average degree $< k > = 4$, and connection radius $r = 0.12$. Experimental results are the averages over 10 independent simulations.

Betweeness is a significant indicator to describe the load of nodes. The betweeness of node n is calculated as follows:

$$b(v) = \sum_{s \neq t} \frac{\sigma_{st}(n)}{\sigma_{st}}, \tag{3}$$

where σ_{st} is the number of paths from node s to node t according to the adopted routing strategy and $\sigma_{st}(n)$ represents the number of paths from node s to node t through node n. Traffic congestion first occurs at the node with maximum betweeness. In addition, the throughput of the network can be calculated by

$$R_c = \frac{N(N-1)C}{b_{max}}, \tag{4}$$

where b_{max} is the maximum betweeness in the network. Therefore, in order to enhance the throughput of the network, we should minimize the value of b_{max}.

4 Routing strategy

For any pair of nodes $\{s, t\}$, the path between them is defined as follows:

$$P(s \to t): s \equiv x^{(0)}, x^{(1)}, \ldots, x^{(n)} \equiv t. \tag{5}$$

An efficient routing strategy attempts to find the optimal path to achieve a high network throughput R_c.

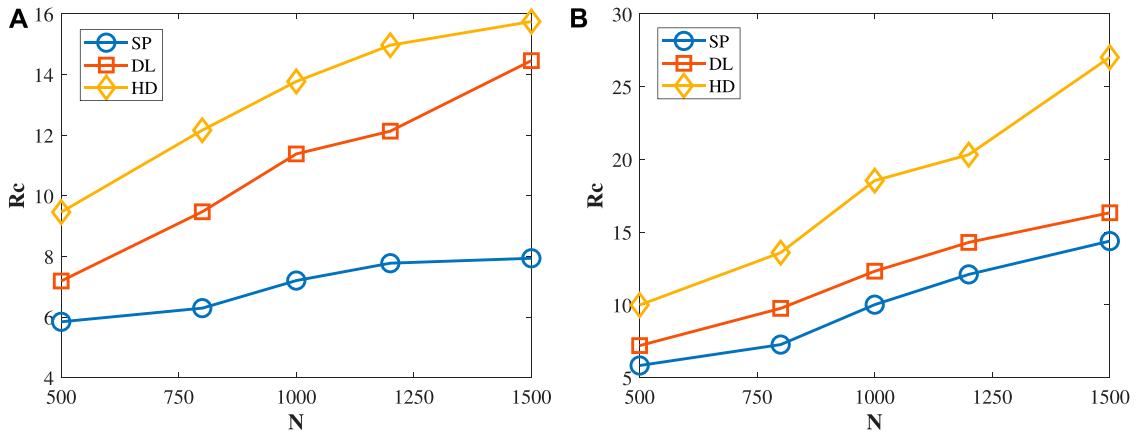

FIGURE 6
R_c of the three routing strategies on the **(A)** *LAEE* network and **(B)** *IRGG* network with different node sizes N. Parameters of the network are set as average degree $<k> = 4$ and connection radius $r = 0.12$. α and β are set to be optimal to maximize R_c. Experimental results are the averages over 10 independent simulations.

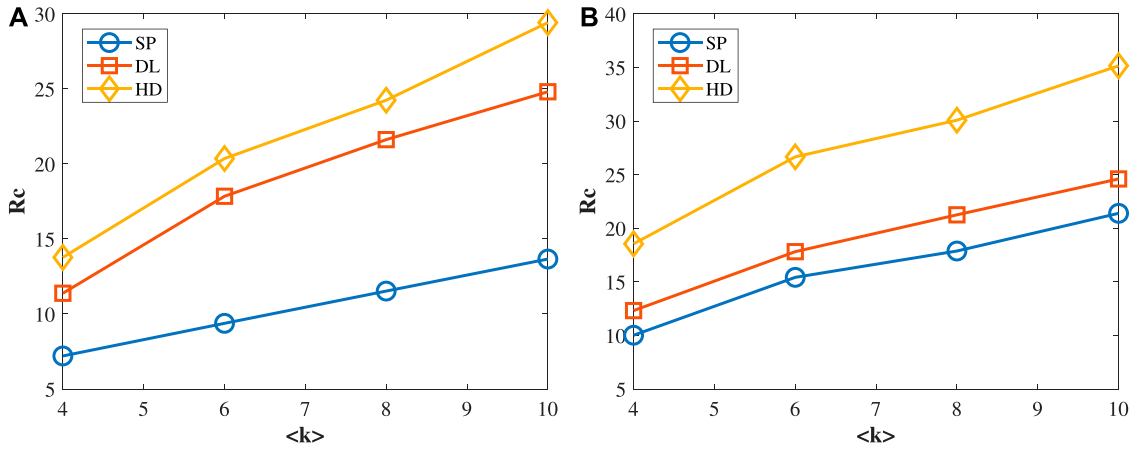

FIGURE 7
R_c of the three routing strategies on the **(A)** *LAEE* network and **(B)** *IRGG* network with different average degree $<k>$. Parameters of the network are set as $N = 1000$ and connection radius $r = 0.12$. α and β are set to be optimal to maximize R_c. Experimental results are the averages over 10 independent simulations.

4.1 *SP* routing strategy

The shortest path means the path with the minimum number of links between two nodes. In the *SP* routing strategy, load can be transmitted from its source to its destination with fewer hops. However, it easily causes congestion at hub nodes and the network has a low throughput.

4.2 Degree-location routing strategy

In the topological network, Yan et al. [24] found that the node with the larger degree always has to deal with more loads. However, in the spatial network, this relationship is not that obvious. Lin et al. [33] investigated the influence of network topology on load transmission. They found that the nodes with larger links and closer to the regional center usually process more loads. Based on this idea, they proposed the degree-location (*DL*) routing strategy, which is presented as follows.

Nodes are distributed in a two-dimensional region. Each node has its own coordinates. We set the center of the region as C, whose coordinate is (x^c, y^c). For any node v, we can calculate its Euclidean distance from the center C as

$$L_v = \sqrt{(x_v - x^c)^2 + (y_v - y^c)^2}, \tag{6}$$

where (x_v, y_v) represents the 2D coordinate of node v. Next, we normalize L_v to L_v':

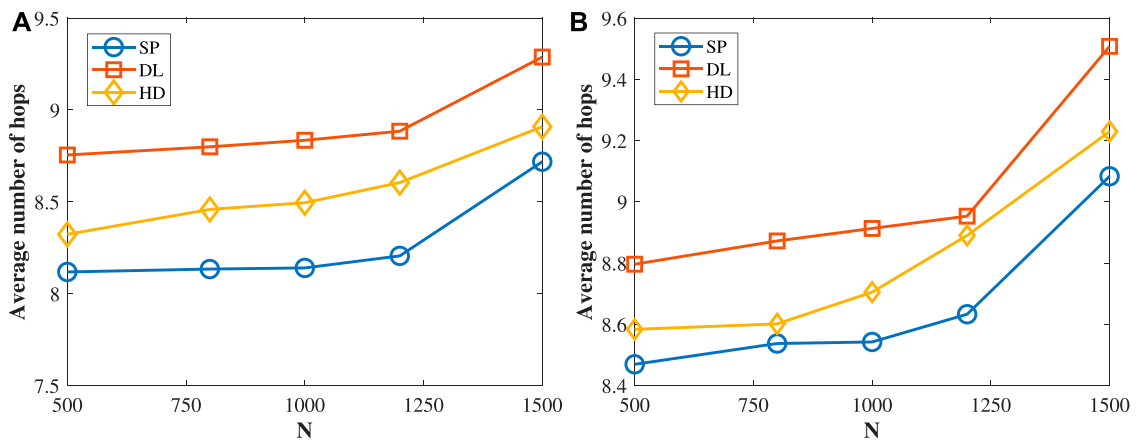

FIGURE 8
Average number of hops vs. N under three routing strategies on the **(A)** *LAEE* network and **(B)** *IRGG* network. Parameters of the network are set as average degree $<k> = 4$ and connection radius $r = 0.12$. α and β are set to be optimal to maximize R_c. Experimental results are the averages over 10 independent simulations.

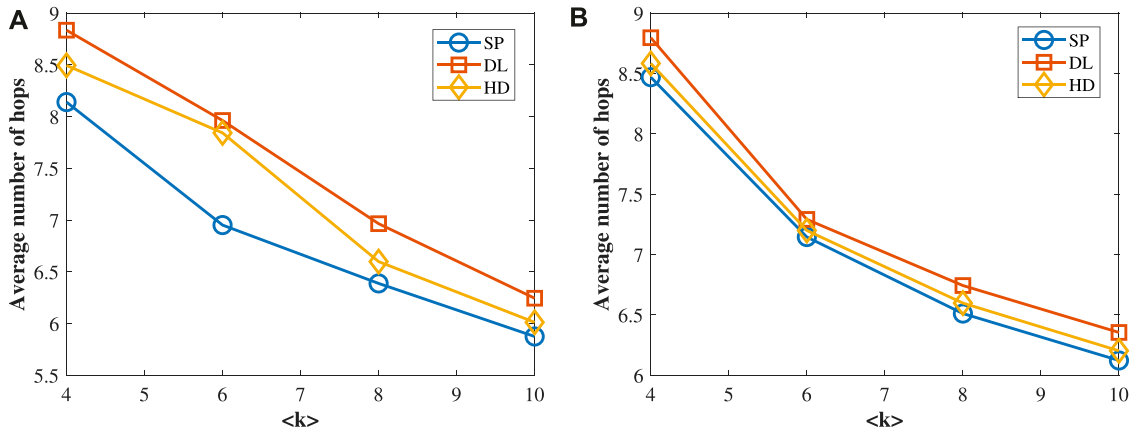

FIGURE 9
Average number of hops vs. $<k>$ under three routing strategies on the **(A)** *LAEE* network and **(B)** *IRGG* network. Parameters of the network are set as $N = 1000$ and connection radius $r = 0.12$. α and β are set to be optimal to maximize R_c. Experimental results are the averages over 10 independent simulations.

$$L'_v = 1 - \frac{L_v - min(L)}{max(L) - min(L)}. \tag{7}$$

Similarly, the normalized degree is defined as

$$k'_v = \frac{k_v - min(k)}{max(k) - min(k)}. \tag{8}$$

The weight of node v is denoted as follows:

$$Q_v = k'^{\alpha}_v + L'^{\beta}_v, \tag{9}$$

where α and β are two adjustable exponents, corresponding to degree and location, respectively.

Considering the node with a high Q value should have large load, the *DL* routing strategy tends to bypass these busy nodes to improve the network throughput. To perform that, the *DL* routing strategy attempts to use the path with the smallest sum of the Q value, i.e.,

$$G_Q(P(s \to t)) = min \sum_{m=0}^{n} Q_{x^{(m)}}. \tag{10}$$

4.3 Harmony-degree routing strategy

In 2000, Marchiori and Latora proposed the harmonic centrality [36] denoted as

$$H_i = \sum_{j \neq i} \frac{1}{d(j,i)}, \tag{11}$$

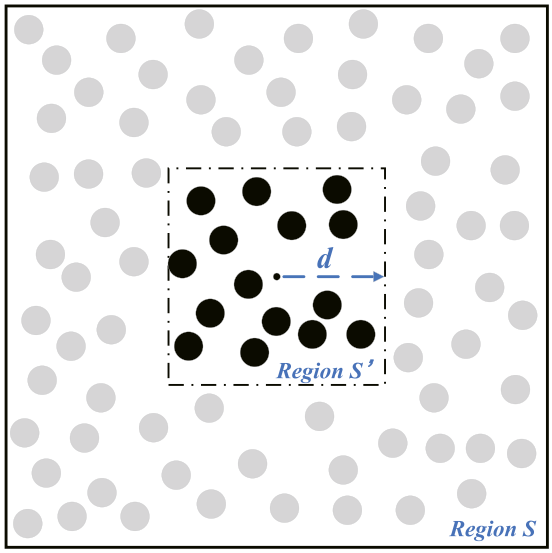

FIGURE 10
Demonstration of regions S' and S. They have the same center $(x^c, y^c) = (0.5, 0.5)$. Region S is a 1×1 region, and S' is its sub-region with the side length $2d$. $d \leq 0.5$.

where $d(i, j)$ represents the number of hops from node i to node j. If there is no path between node i and node j, then $d(i, j) = \infty$. We normalize H_i as follows:

$$H_i' = \frac{H_i - min(H)}{max(H) - min(H)}. \tag{12}$$

According to Eq. 11, if node i has a high harmonic centrality index, it means that this node establishes contact with other nodes through fewer hops. Therefore, this node is busy in load transmission. At the same time, degree is also a significant factor to identify high-load nodes. With the consideration of the aforementioned two factors, the node with a high harmonic centrality index and high degree should deal with high load. Next, we attempt to combine these two factors to form a new measurement as follows:

$$w_i = k_i'^{\alpha} + H_i'^{\beta}, \tag{13}$$

where α and β are two exponents, corresponding to degree and harmonic centrality, respectively.

Next, we investigate the load distribution in spatial networks. Figure 4 shows that this new measurement can help us easily identify the high-load nodes in the spatial networks. If the node has a high value of w, this node needs to process more loads.

In order to enhance the transmission efficiency of spatial networks, we redistribute the load from the nodes with high w to these with low. Since w depends on the harmonic centrality and degree of the node, this strategy is named as the *HD* routing strategy, which is defined as follows:

$$G_w(P(s \to t)) = min \sum_{m=0}^{n} w_{x^{(m)}}. \tag{14}$$

That is, the *HD* routing strategy attempts to seek a path with the minimal sum of the w value along the path.

5 Simulation results

To verify the effectiveness of *HD* routing strategies, we adopt R_c to measure the traffic capacity of spatial networks. If the network carries a large R_c, the congestion hardly occurs. All simulations are carried out on heterogeneous and homogeneous spatial networks, corresponding to the *LAEE* model and *IRGG* model, respectively, mentioned previously. Without the loss of generality, we set $C = 1$ in the following simulations.

The *HD* routing strategy is based on the harmonic centrality and degree, and we can use α and β to adjust their weights, respectively. Figure 5 shows the variation of R_c under different α and β. In the *LAEE* network, the peak value of R_c is observed at $\alpha = 1$ and $\beta = 0.6$; in the *IRGG* network, the maximum value is observed at $\alpha = 1.4$ and $\beta = 0.5$.

In order to further verify the efficiency of our routing strategy, we observe the change of R_c when adjusting the network size and average degree. In addition, we also compare with *SP* and *DL* routing strategies. Figure 6 shows the results of R_c in different scale networks. When N increases, R_c also increases. The *HD* strategy is always better than the *SP* and *DL* strategies in the *LAEE* and *IRGG* models.

Figure 7 shows the R_c increases almost linearly with the average degree $< k >$. With the growth of the $< k >$, the network connections become denser and the load has more path options during transmission. Therefore, the load distribution becomes more even, which also directly leads to the increase of R_c. R_c of the *HD* routing strategy is higher than that in the *SP* and *DL* routing strategies. For the aforementioned results, we observe that spatial networks can carry the highest network throughput under our *HD* routing strategy in all cases.

The number of hops is also an important factor to evaluate the performance of the routing strategy. As we all know, the aim of a good routing strategy is not only to enable the network to carry more load but also to allow loads to be transmitted from its source to its destination quickly. Therefore, we expect a smaller number of hops under an efficient routing strategy. Figure 8 shows the relationship between node size N and average number of hops under different routing strategies. As the name suggests, the *SP* routing strategy always has the minimum number of hops. In the *DL* strategy, the load tends to be transferred around the edge of the region. Therefore, it needs the highest number of hops.

Similarly, Figure 9 shows the effect of $< k >$ on the average number of hops under different routing strategies. No matter how the average degree $< k >$ changes, the *SP* routing strategy always has the smallest average number of hops, and the average number of hops under the *DL* routing strategy is always higher under than the *HD* strategy.

In order to better understand the performance of these routing strategies, we observe the average load per node under these routing strategies in different regions. As shown in Figure 10, all nodes are placed in the 1×1 square region S, and the region center $(x^c, y^c) = (0.5, 0.5)$. S' is a square sub-area of region S, which has the same center as the region S and side length $2d$.

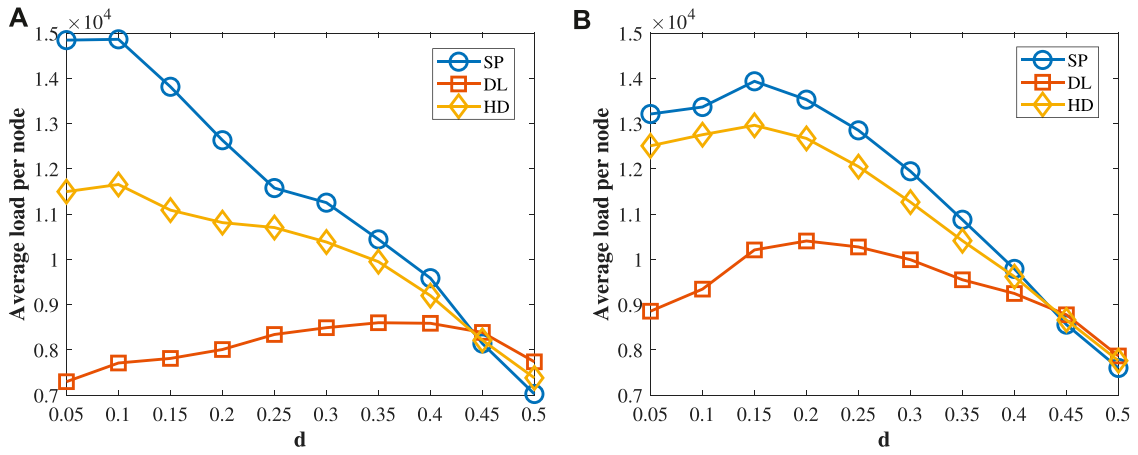

FIGURE 11
Average load per node vs. *d* under three routing strategies on the **(A)** *LAEE* network and **(B)** *IRGG* network. $N = 1000$ and $r = 0.12$. Center of a region is (0.5,0.5). Experimental results are the averages over 10 independent simulations.

Figure 11 shows the variation of the average load per node in the region S'. When d is small, nodes in region S' are close to the center. In this case, these nodes have high average load under the *SP* routing strategy. This is because the *SP* routing strategy finds the shortest path, which often goes through the central region. The high load leads to congestion at these nodes in the central region easily. That is why R_c is low under the *SP* routing strategy. On the contrary, when d is small, the average load is the lowest under the *DL* routing strategy. However, when d is large, the nodes need to deal with more loads under the *DL* routing strategy. Evidently, the load is more inclined to be transmitted along the edge of the region *S*. This load distribution makes the *DL* routing strategy always has the largest number of hops, as shown in Figures 8, 9. A high-detour cost becomes the main factor restricting the network throughput in the *DL* routing strategy. Compared with these two routing strategies, the load distribution is more even under the *HD* routing strategy. That is the main reason why the *HD* routing strategy performs better in spatial networks than other two routing strategies.

6 Conclusion

In this paper, we design an efficient routing strategy for spatial networks. To alleviate congestion, we attempt to find high-load nodes in spatial networks. Our routing strategy redefines the high-load nodes by considering both the harmony centrality and degree to improve the throughput significantly. Moreover, it not only ensures that the network can carry more load but also ensures that the load can be quickly transmitted to the destination. Therefore, our strategy can be adopted in spatial networks to help alleviate the congestion and provide a new thought for the design of routing strategies.

Data availability statement

The original contributions presented in the study are included in the article/Supplementary Material; further inquiries can be directed to the corresponding author.

Author contributions

All authors listed have made a substantial, direct, and intellectual contribution to the work and approved it for publication.

Conflict of interest

The authors declare that the research was conducted in the absence of any commercial or financial relationships that could be construed as a potential conflict of interest.

Publisher's note

All claims expressed in this article are solely those of the authors and do not necessarily represent those of their affiliated organizations, or those of the publisher, the editors, and the reviewers. Any product that may be evaluated in this article, or claim that may be made by its manufacturer, is not guaranteed or endorsed by the publisher.

References

1. Watts DJ, Strogatz SH. Collective dynamics of 'small-world' networks. *Nature* (1998) 393:440–2. doi:10.1038/30918

2. Barabasi AL, Albert R. Emergence of scaling in random networks. *Science* (1999) 286:509–12. doi:10.1126/science.286.5439.509

3. Rossa FD, DeLellis P. Stochastic master stability function for noisy complex networks. *Phys Rev E* (2020) 101:052211. doi:10.1103/PhysRevE.101.052211

4. Huang W, Zhang T, Wei Y. Optimization for sequential communication line attack in interdependent power-communication network. *Physica A* (2022) 592:126837. doi:10.1016/j.physa.2021.126837

5. Tatsuro M, Yuichi I. Optimizing travel routes using temporal networks constructed from global positioning system data in kyoto tourism. *Front Phys* (2022) 10:1158. doi:10.3389/fphy.2022.1001983

6. Rodriguez-Sanz A, Comendador FG, Valdes RA, Perez-Castan J, Montes RB, Serrano SC. Assessment of airport arrival congestion and delay: Prediction and reliability. *Transportation Res C: Emerging Tech* (2019) 98:255–83. doi:10.1016/j.trc.2018.11.015

7. Liu T, Bai G, Tao J, Zhang YA, Fang Y, Xu B. Modeling and evaluation method for resilience analysis of multi-state networks. *Reliability Eng Syst Saf* (2022) 226:108663. doi:10.1016/j.ress.2022.108663

8. Ferenc M, Takashi N, Motter AE. Asymmetry underlies stability in power grids. *Nat Commun* (2021) 12:1457. doi:10.1038/s41467-021-21290-5

9. Liang Y, Xia Y, Yang X. Hybrid-radius spatial network model and its robustness analysis. *Physica A* (2022) 591:126800. doi:10.1016/j.physa.2021.126800

10. Zou Y, Li H. Study on power grid partition and attack strategies based on complex networks. *Front Phys* (2022) 9:790218. doi:10.3389/fphy.2021.790218

11. Zhou F, Lu L, Mariani MS. Fast influencers in complex networks. *Commun Nonlinear Sci Numer Simulation* (2019) 74:69–83. doi:10.1016/j.cnsns.2019.01.032

12. Wang Y, Li H, Zhang L, Zhao L, Li W. Identifying influential nodes in social networks: Centripetal centrality and seed exclusion approach. *Chaos, Solitons and Fractals* (2022) 162:112513. doi:10.1016/j.chaos.2022.112513

13. Das K, Samanta S, Pal M. Study on centrality measures in social networks: A survey. *Social Netw Anal Mining* (2018) 8:13–1. doi:10.1007/s13278-018-0493-2

14. Mohseni A, Gharibzadeh S, Bakouie F. The effect of network structure on desynchronization dynamics. *Commun Nonlinear Sci Numer Simulation* (2018) 63:271–9. doi:10.1016/j.cnsns.2018.02.011

15. Tan F, Wu J, Xia Y, Tse CK. Traffic congestion in interconnected complex networks. *Phys Rev E* (2014) 89:062813. doi:10.1103/PhysRevE.89.062813

16. Echague J, Cholvi V, Kowalski DR. Effective use of congestion in complex networks. *Physica A* (2018) 494:574–80. doi:10.1016/j.physa.2017.11.159

17. Ling X, Wang X, Chen J, Liu D, Zhu K, Guo N. Major impact of queue-rule choice on the performance of dynamic networks with limited buffer size. *Chin Phys B* (2020) 29:018901. doi:10.1088/1674-1056/ab5935

18. Kirst C, Timme M, Battaglia D. Dynamic information routing in complex networks. *Nat Commun* (2016) 7:11061. doi:10.1038/ncomms11061

19. Wang C, Xia Y, Zhu L. A method for identifying the important node in multi-layer logistic networks. *Front Phys* (2016) 10:968645. doi:10.3389/fphy.2022.968645

20. Dong T, Hu W, Liao X. Dynamics of the congestion control model in underwater wireless sensor networks with time delay. *Chaos, Solitons and Fractals* (2016) 92:130–6. doi:10.1016/j.chaos.2016.09.019

21. Ohnishi M, Minamiguchi C, Ohsaki H. In: WK Chan, B Claycomb, H Takakura, JJ Yang, YT amd Dave Towey, S Segura, et al. editors. *On the performance of end-to-end routing in complex networks with intermittent links. 2020 IEEE 44th annual computers, software, and applications conference (COMPSAC)*. IEEE) (2020). p. 1157–62.

22. Almasan P, Suarez-Varela J, Rusek K, Barlet-Ros P, Cabellos-Aparicio A. Deep reinforcement learning meets graph neural networks: Exploring a routing optimization use case. *Comput Commun* (2016) 196:184–94. doi:10.1016/j.comcom.2022.09.029

23. Ma J, Wei J, Tang X, Zhao X. An improved efficient routing strategy on two-layer networks. *Pramana* (2022) 96:95. doi:10.1007/s12043-022-02344-9

24. Yan G, Zhou T, Hu B, Fu Z, Wang B. Efficient routing on complex networks. *Phys Rev E* (2006) 73:046108. doi:10.1103/PhysRevE.73.046108

25. Jiang Z, Liang M. Improved efficient routing strategy on scale-free networks. *Int J Mod Phys C* (2012) 23:1250016. doi:10.1142/S0129183112500167

26. Zhang H, Liu Z, Tang M, Hui P. An adaptive routing strategy for packet delivery in complex networks. *Phys Lett A* (2007) 364:177–82. doi:10.1016/j.physleta.2006.12.009

27. Donnet T, Ryley T, Lohmann G, Spasojevic B. Developing a queensland (Australia) aviation network strategy: Lessons from three international contexts. *J Air Transport Manage* (2018) 73:1–14. doi:10.1016/j.jairtraman.2018.08.003

28. Wang Y, Wu Q, Song J. Spatial network structure characteristics of green total factor productivity in transportation and its influencing factors: Evidence from China. *Front Environ Sci* (2022) 10:982245. doi:10.3389/fenvs.2022.982245

29. Li J, Wang Z, Lu R, Xu Y. Partial-nodes-based state estimation for complex networks with constrained bit rate. *IEEE Trans Netw Sci Eng* (2021) 8:1887–99. doi:10.1109/TNSE.2021.3076113

30. Xu B, Bai G, Liu T, Fang Y, an Zhang Y, Tao J. An improved swarm model with informed agents to prevent swarm-splitting. *Chaos, Solitons and Fractals* (2023) 169:113296. doi:10.1016/j.chaos.2023.113296

31. Barthelemy M. Spatial networks. *Phys Rep* (2011) 499:1–101. doi:10.1016/j.physrep.2010.11.002

32. Xia Y, Wang C, Shen HL, Song H. Cascading failures in spatial complex networks. *Physica A* (2020) 559:125071. doi:10.1016/j.physa.2020.125071

33. Lin H, Xia Y, Liang Y. Efficient routing for spatial networks. *Chaos: Interdiscip J Nonlinear Sci* (2022) 32:053110. doi:10.1063/5.0091976

34. Jiang L, Jin X, Xia Y, Ouyang B, Wu D, Chen X. A scale-free topology construction model for wireless sensor networks. *Int J Distributed Sensor Networks* (2014) 10:764698. doi:10.1155/2014/764698

35. Arenas A, Díaz-Guilera A, Guimerà R. Communication in networks with hierarchical branching. *Phys Rev Lett* (2001) 86:3196–9. doi:10.1103/PhysRevLett.86.3196

36. Marchiori M, Latora V. Harmony in the small-world. *Physica A* (2000) 285:539–46. doi:10.1016/S0378-4371(00)00311-3

Frontiers in Physics

Investigates complex questions in physics to understand the nature of the physical world

Addresses the biggest questions in physics, from macro to micro, and from theoretical to experimental and applied physics.

Discover the latest Research Topics

See more →

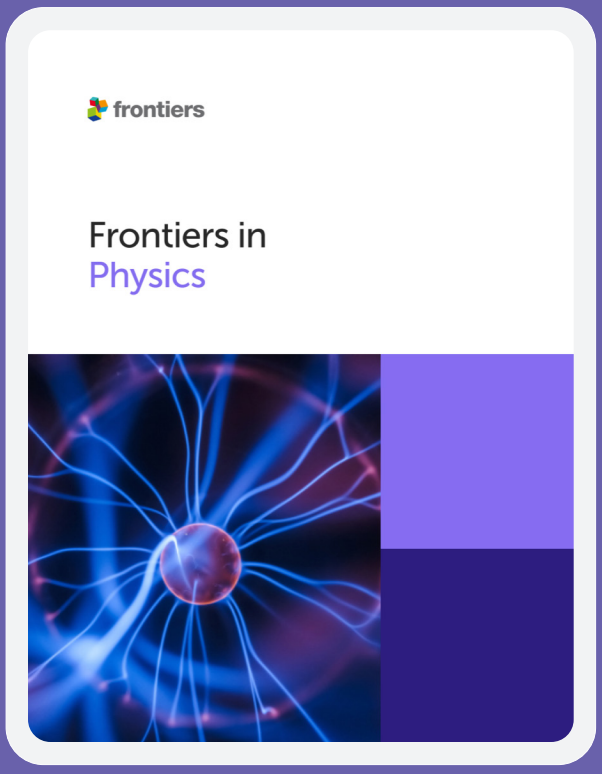

Frontiers

Avenue du Tribunal-Fédéral 34
1005 Lausanne, Switzerland
frontiersin.org

Contact us

+41 (0)21 510 17 00
frontiersin.org/about/contact